Ph.d. thesis in physics

Niels Bohr Institute, Faculty of Science
University of Copenhagen

Topological Phenomena in Periodically Driven Systems

May 4, 2018

Frederik Sønderby Nathan

Supervisor: Mark S. Rudner

Abstract

Periodic driving has recently been investigated as a mechanism for generating nontrivial topological phases of matter within otherwise ordinary systems. Periodic driving can even induce new, so-called *anomalous* topological phases, which have no counterpart in equilibrium. This thesis studies such topological phenomena and phases in periodically driven systems. The first part of the thesis introduces the concept of topological phases in periodically driven systems, and classifies the noninteracting topological phases that can arise in such systems, including the anomalous phases. The second part of the thesis studies the anomalous Floquet insulator (AFI), which is an example of an anomalous topological phase. The discussion here shows that the AFI is characterized by a quantized, nonzero bulk magnetization density, and demonstrates that strong disorder can stabilize the phase in the presence of interactions. The third part of the thesis explores driving-induced topological effects in other physical systems. The discussion here shows that periodic driving can lead to new, topologically-robust energy pumping effects. In some cases, these effects can be described as fully classical phenomena and have potentially useful applications. A novel master equation for dissipative, periodically driven quantum systems is derived in this connection.

Aknowledgements

I would like to express my gratitude to the people who have supported me during my three years as a ph.d., and contributed to the work in this thesis.

First and foremost, I would like to thank my supervisor Mark S. Rudner, for dedicated and insightful guidance in both scientific and professional aspects. I am also grateful to my supervisor for giving me the opportunity to work in this exciting field, and for sharing his ideas which form the basis for the work in this thesis.

I am deeply indebted to my collaborators, whose ideas form the basis of most of my work, and whose contributions feature on multiple occasions in this thesis. This includes (in chronological order) Mark S. Rudner, Netanel H. Lindner, Erez Berg, Gil Refael, Dmitry Abanin, Mike Kolodrubetz, Snir Gazit, Takahiro Morimoto, Joel E. Moore, and Ivar Martin.

I also thank the people at the condensed matter theory group at the Niels Bohr Institute for good discussions and a friendly atmosphere, which have made every-day life delightful during the last three years.

In the beginning of my ph.d., Mark encouraged me to apply for the EliteReserach travel grant, funded by the Danish Ministry of Higher Education. The grant, which allowed me to travel essentially freely, gave me opportunity to meet many colleagues around the world, become part of several new projects, and gave me some fantastic experiences, for which I am extremely grateful.

I would moreover like to thank the people who have hosted me during my visits for welcoming me. These visits gave me opportunity to be part in several new projects, widened my world as a scientist, and gave me some of my best experiences during my 3 years as a ph.d. student. I would like to thank Norman Yao for his hospitality, for welcoming me at Berkeley, and for introducing me to a lot of people during an intensive week in 2016. I also thank Mike Kolodrubetz and his collaborators for involving me in their project on the Floquet energy pump during my visit there. I am very grateful to Gil Refael and his group in Caltech, for their hospitality and friendliness during two stays at Caltech. I also thank Dmitry Abanin and his group at University of Geneva for their friendliness and hospitality, and for involving me in stimulating discussions there during a visit in 2017. I would finally like to thank Netanel H. Lindner and his group at the Technion, for their hospitality, warm and friendly atmosphere, and for introducing me to Israel during an enjoyable month's stay at the Technion.

Last, and most importantly, I would like to thank my family for love, patience and support during the last three years, which have included a lot of work and travel activity.

Frederik Nathan
Copenhagen, May 2018

Contents

Introduction to the thesis

This introductory section briefly presents the context and motivation for the work which is discussed in this thesis. The section moreover contains a short summary of the thesis' structure and results.

Background

In the last decade, topology has gained a new importance in physics, due to the theoretical prediction [9–11], and experimental discovery [12, 13] of new classes of materials known as topological insulators and superconductors. Topological insulators and superconductors exhibit exotic phenomena which are characterized by their universality and extreme robustness. Examples of such topological phenomena include topologically-protected Majorana end states, chiral edge modes, and quantized bulk Hall conductance [9, 11, 14–17]. A unified theoretical description of topological insulators and superconductors was developed shortly after the discoveries above [18,19]. These advances show that the nontrivial topological effects described above can be seen as intrinsic properties of the bulk material which supports the phenomena. However, while topological insulators and superconductors are theoretically well-understood, robust experimental signatures of these materials have been elusive, with the notable exception of the integer quantum Hall effect [14].

More recently, periodic driving has been studied extensively as a means for realizing such topological phases of matter. Periodic driving means subjecting the system to an externally oscillating force, such as the electromagnetic field induced by a laser. Such external oscillating forces can effectively modify the Hamiltonian of the system, thereby giving a way for driving an otherwise ordinary material into a nontrivial topological phase [20–40]. While the manipulation of a material's properties by a periodic drive has a huge potential for applications, the high intensity and frequency required to significantly affect solid-state Hamiltonians mean that realizations of the effect in such settings remain a challenge. However, the method has been used with success in gases of ultracold atoms in optical lattices, where it led to the experimental realization of the Haldane model [41].

The initial idea of realizing nontrivial topological phases with a periodic drive inspired extensive theoretical efforts in characterizing the topological phases of periodically driven systems. An important and surprising result has been the realization that periodically driven systems support a *richer* topological structure than their nondriven counterparts [1,2,5,42–56]. In particular, periodic driving may induce new topological phases of matter, that are of intrinsically nonequilibrium nature. These so-called *anomalous* phases are characterized by nontrivial topological properties of the dynamics that take place within a driving period. Examples of such anomalous phases include the anomalous Floquet insulator [2, 6], which exhibits quantized bulk magnetization (see Chapter 4), and the Floquet-time crystals [49, 50] which is characterized robust, period-doubled oscillations. Although the nonequilibrium nature of these systems lead to some complications – notably, the uncontrolled heating induced by periodic driving in isolated, thermalizing systems – theoretical work shows that such anomalous phases may in principle be realized in interacting

many-body systems when strong disorder is present (see Chapters 5-6). Floquet time-crystals have been realized in trapped-ion systems [52], while concrete experimental protocols have been proposed for realizing the anomalous Floquet insulator with ultracold atoms in optical lattices [53].

In addition to the topological phases of matter described above, other setups have been explored as platforms for realizing topological phenomena in periodically driven systems. Such platforms include optical systems [57, 58], and, notably, photonic crystals [59–61]. Another direction of current research is to use combinations of periodic driving fields to realize novel, topological pumping effects. [3, 8, 9, 62–64], analogous to Thouless' adiabatic charge pump [65].

Structure of thesis

The work discussed in this thesis explores topological phases and phenomena in periodically driven systems. The thesis is divided into three parts.

- Part 1, which contains Chapters 1-3 serves as the introduction of the thesis. Chapters 1 and 2 introduce the subject of topological insulators and topology in periodically driven systems, respectively. Chapter 3 explores the nature of the additional topological structure in periodically driven systems, and develops a general scheme for classifying the topological phases of (noninteracting) periodically driven systems.

- Part 2 of the thesis, which includes Chapters 4-6, studies the anomalous Floquet insulator (AFI). The AFI is a newly-discovered, driving-induced phase of matter that intriguingly has no counterpart in equilibrium [2]. Chapter 4 focuses the physical manifestations of the AFI in the absence of interactions, showing that the phase is characterized by a nonzero, quantized magnetization density in the bulk. Chapter 5 demonstrates the stability of the AFI in the presence of interactions, where many-body localization prevents the system from heating to infinity. Finally, Chapter 6 studies the topological properties of the AFI in the presence of interactions, showing that the AFI is characterized by an infinite family of topological invariants, linked to the magnetization density in the system.

- Part 3 of the thesis, which includes Chapters 7-8, explores the idea of realizing topological effects in driven systems beyond the solid-state settings considered in the previous chapters. Chapter 7 studies the dimensional reduction of the AFI to an adiabatic pump, analogously to Thouless' charge pump [65]; in the case studied in Chapter 7, the adiabatic pumping parameter, together with the periodic driving field, leads to a topologically-robust energy pumping effect. Chapter 8 explores an idea introduced Ref. [3], where a periodically driven magnetic particle effectuates a transfer of energy from the driving field to a cavity mode.

The appendices of this thesis contain technical derivations that support the discussion in the main text. These are primarily necessary if the reader wants further verification of the details in the main text. A notable exception is Appendix A, which contains a result which may have relevance beyond the discussion in this thesis. Specifically, Appendix A derives a master equation that describes the evolution of a periodically driven quantum system coupled to external bath, only making use of the Markov approximation. The resulting master equation is used in Chapter 8 to describe a driven system consisting of a magnetic particle and a cavity mode coupled to external

baths. However, the master equation derived in Appendix A can in principle be applied to any periodically driven quantum system coupled to external baths.

Part I

Topological Phases in Periodically Driven Systems

Chapter 1

Topological Insulators

This chapter is partially based on Chapter 2 from the author's master's thesis (2015). The master's thesis is cited as Ref. [4].

Topology has gained a major relevance in condensed matter physics in recent years. One major reason for this is the theoretical prediction and experimental detection of a new class of materials known as *topological insulators*. Topological insulators are characterized by universal, exotic and extremely robust phenomena with potentially useful applications. Such topological phenomena include the possible Majorana end states of proximity-coupled nanowires (Fig. 1.1a), the integer quantum Hall effect (Fig. 1.1b), or single Dirac cone at in the edge dispersion of Bismuth Selenide (Fig. 1.1c) [10, 15, 16]. Topology is a plays a major role in the theoretical description of these effects, and has been used as a guiding principle for predicting some of the new materials above [11, 16, 66]. This chapter introduces the concept of topology in physical systems, with a specific focus on topological insulators.

1.1 Topological phases of matter

The discussion of this thesis takes its starting point in a relatively simple, but powerful question: which properties of a system remain unaffected by perturbations that preserves its band gaps and symmetries? Properties that have this "invariance", if such exist, are referred to as *topological invariants* of the system. A priori, the existence of topological invariants in real-world materials might seem unlikely. However, the question above in many cases has a nontrivial answer: the defining feature of a topological insulator is a nontrivial value of one (or more) topological invariants.

The existence of topological invariants has profound implications. In particular, Hamiltonians with a given symmetry fall into distinct topological classes or phases: two Hamiltonians belong to the same *topological class* or *phase* if and only if they can be smoothly deformed into each other while preserving all energy gaps and symmetries of the system. By definition, two systems characterized by distinct values of one or more topological invariants must belong to different topological phases. A topological insulator is defined to be a system which belongs to a nontrivial topological phase. Topological phases by nature have some highly nontrivial properties. Since the

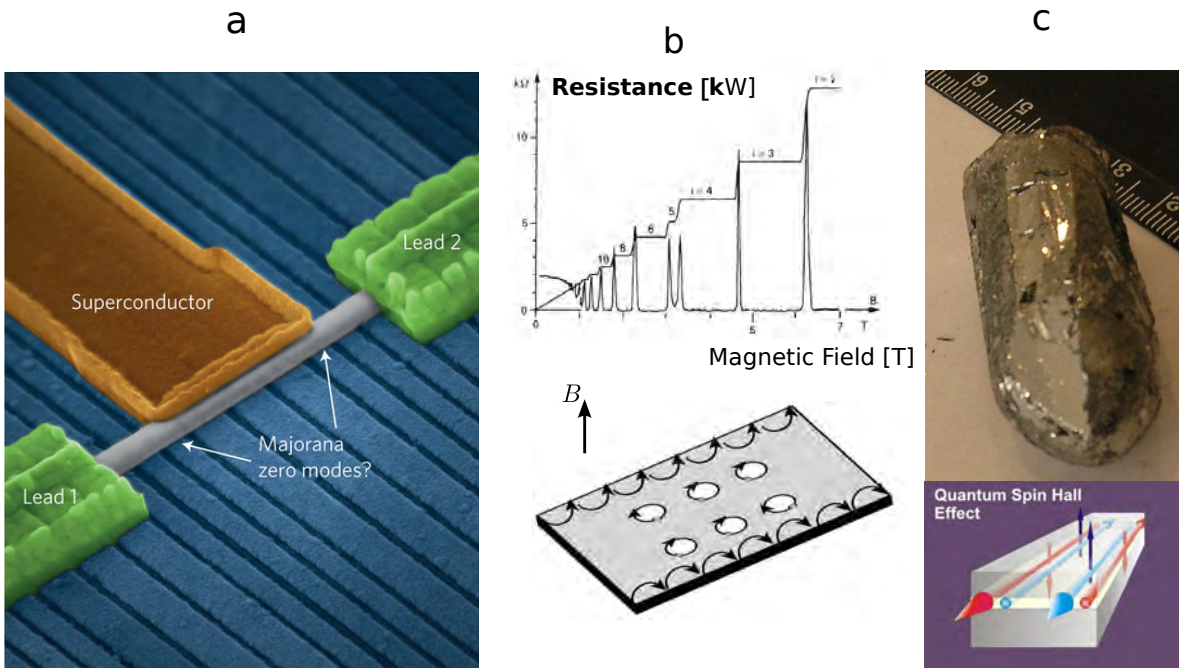

Figure 1.1: Examples of topological insulators and superconductors. a) Topological superconductor: experimental setup that may support Majorana fermions. b) A system exhibiting the integer quantum Hall effect (IQHE). Top panel shows the quantized Hall resistance in an IQHE system, as a function of the applied perpendicular magnetic field. Bottom panel depicts of the skipping orbits in an IQHE system. These can be seen as the classical analogue of the chiral edge modes described in Sec. 1.2. c) Topological insulators protected by time-reversal symmetry. Top panel shows a sample of BiSe, a time-reversal symmetry protected topological insulator. Bottom panel schematically depicts of the spin quantum Hall-effect, a manifestation of a 2D topological insulator with time-reversal symmetry. From Ref. [4].

defining properties of the phases by definition are identical for a wide class of systems (related by continuous, gap-preserving deformations), signatures of topological phases are *universal*: they lead to the same effects in a wide range of experimental setups. Moreover, due to their insensitivity to a wide class of perturbations, the novel phenomena arising from topological phases are extremely robust. In addition to these two facts, the topological phases of a system are often associated with exotic experimental signatures, although this is not always the case. The universality, robustness, and exotic nature of topological phenomena is what makes them interesting. The best example of these aspects is the universal, quantized Hall conductance in the integer Quantum Hall effect (see Fig. 1.1b), which is possible to detect to extremely high precision in relatively dirty and uncontrolled macroscopic systems [14]. The universality and extreme robustness of this effect means that it is used as an international standard for electrical resistance [67].

To exploit the powerful concept of topological invariance in the this thesis, we will make use of some terminology which is common in the literature: in the following, the term *topological*

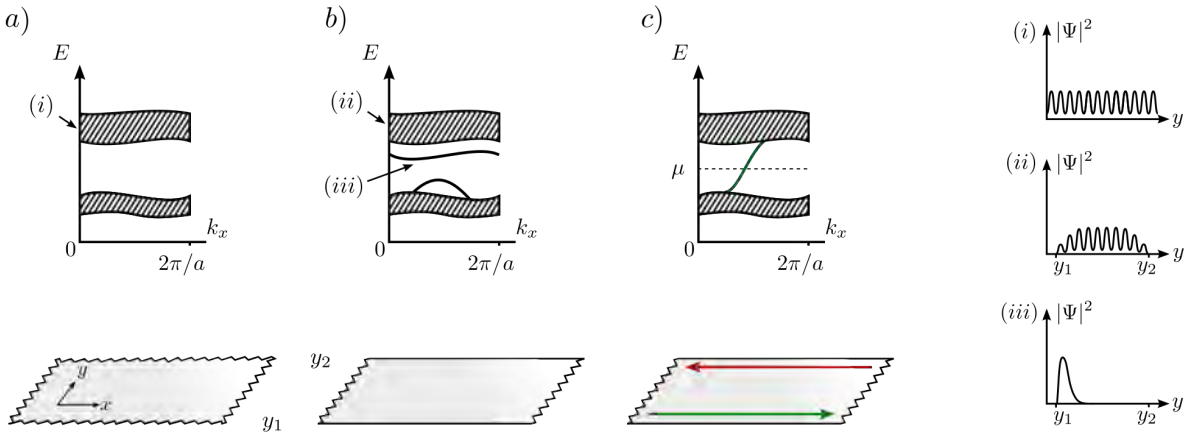

Figure 1.2: Schematic depiction of how topologically-invariant features can arise in a two-dimensional band insulator (see main text). Panel a) shows the energy spectrum of an infinitely-large band insulator as a function crystal momentum k_x. When confined to a strip geometry [panel b)], the system may host modes in the gaps of its bulk bands corresponding to localized states at the edges (*iii*). The system depicted in panel c) has a topologically-invariant feature: the single rightmoving mode on edge 1 (green) cannot be removed, unless the bulk gap closes. From Ref. [4].

refers to features of a system which are topologically invariant (by the definition we gave in the beginning of this section). The term *topology* refers to the topological properties of a system.

1.2 Topological features of two-dimensional band insulators

The ideas introduced above are best illustrated on a system of noninteracting fermions in a two-dimensional lattice.

For simplicity we assume the system to have discrete translational symmetry[1]. In this case, Bloch's theorem dictates that the eigenstates of the Hamiltonian H are plane waves with well-defined crystal momenta $\mathbf{k}$, as illustrated in Fig. 1.2(*i*). In the subspace with crystal momentum $\mathbf{k}$, the Hamiltonian is given by the Bloch space Hamiltonian $H(\mathbf{k})$. Note that locality implies that the Bloch Hamiltonian $H(\mathbf{k})$ is continuous in crystal momentum. The energy spectrum of the system is formed by the eigenvalues $E(\mathbf{k})$ of the Bloch Hamiltonian, and forms smooth bands as function of $\mathbf{k}$, as schematically depicted in Fig. 1.2a. We consider the case where the system has N bands, separated by finite gaps (as a function of $\mathbf{k}$). As discussed in the introduction above, the finiteness of the energy band gaps will play a major role in this chapter. Ordering the bands of $H(\mathbf{k})$ according to the energies, we refer to the gap above band n as the nth energy gap of the system.

To illustrate how topologically invariant features can arise in the system, we confine the system to the geometry of a strip with edges at $y = y_1$ and $y = y_2$ (where $y_1 < y_2$), such that

[1]Note that the results quoted in this section also hold in the presence of disorder

translational invariance along the x-direction remains unbroken, as depicted in Fig. 1.2b (we refer to the edge at $y = y_1$ as edge 1, and the edge at y_2 as edge 2 in the following). Since the x-component of crystal momentum k_x in this case remains a good quantum number, the system's energy spectrum still depends continuously on k_x, as depicted in Fig. 1.2b.

When the strip is wide enough, most of the system is not significantly affected by the presence of the edges: sufficiently far within the strip, the eigenstates are delocalized plane waves, and the energy bands from the infinite system are intact (*ii*). We refer to this part of the systems' energy spectrum as the *bulk* bands of the system. In addition to the bulk bands, the Hamiltonian can have localized eigenstates confined to either of the edges (*iii*). These are referred to as *edge modes*. The energies of the edge modes must lie in the gaps of the bulk bands: once the energy of an edge mode comes within the range of the bulk bands, the edge mode hybridizes with the continuum of bulk eigenstates[2], and is no longer confined to the edge [68].

Nontrivial topology arises when a mode on edge 1 connects two bands across a bulk gap gap, as depicted in Fig. 1.2c (green). If this is feature is present, it must persist under any continuous deformation of the system that keeps the bulk energy gap open[3]. By the definition in Sec. 1.1, this feature is *topologically invariant*. Generalizations of this argument show that number z_n of rightmoving edge modes in gap n (on edge 1) can only change under a continuous deformation of the system, if bulk gap n closes[4] . In this way, we identify the integer z_n as a topological invariant of of the system. Note that the existence of z_n rightmoving modes at edge 1 implies the existence of z_n leftmoving modes[5] localized around edge 2, as indicated by red in Fig. 1.2c. In the following we refer to the unidirectional modes described above as *chiral edge modes*.

The discussion above demonstrates that the simple two-dimensional model introduced in the beginning of this section supports nontrivial topological features. Specifically, the net number of chiral edge modes in each bulk gap z_n is a topological invariant of the system. Systems with a nonzero number z_n of chiral edge modes are known as *Chern insulators*. Such systems notably include two-dimensional electron gases subject to strong perpendicular magnetic fields. These systems exhibit the integer quantum Hall effect (Fig. 1.1b), and nonzero values of the invariants $\{z_n\}$ (i.e. the numbers of chiral edge modes) is a defining feature of this phenomenon [14, 15, 69].

Although the discussion above relies on unbroken translation symmetry, the robustness of the invariants $\{z_n\}$ even persist in the presence of disorder: since there are no leftmoving modes near y_1 at the fermi energy, a rightmoving particle at this edge cannot be backscattered by impurities [69]. The extreme robustness of the invariants $\{z_n\}$ allows for detection of their signatures at extremely high precision in macroscopic and relatively dirty systems. The physical signatures of these invariants and the integer quantum Hall effect are discussed in further detail below.

[2]Except in fine-tuned cases.

[3]Removing this feature in any other way than closing the bulk gap would require "ripping" the edge mode apart during the deformation, which implies breaking locality – a fundamental principle of nature.

[4] The invariant z_n can be rigorously defined as the number of edge modes at any given energy in the gap whose energies have positive slope, subtracted by the number of edge modes with negative slope. Fig. 1.2c depicts a situation where $z_n = 1$.

[5]See for example Ref. [65] for a proof.

1.2.1 Bulk-edge correspondence

The discussion above shows that the net number of chiral edge modes z_n is a topological invariant, and hence may only change if bulk gap n closes. This suggests that z_n is closely related with the properties of the bulk system. Here we confirm this intuition by demonstrating that the invariant z_n can be computed directly from the bulk Hamiltonian $H(\mathbf{k})$.

Specifically, theoretical results [70] show that there exist *exactly* $N-1$ independent topological invariants $\{C_n\}$ of a Hamiltonian with N bands[6]. Each of these invariants C_n can be expressed in terms of the spectral decomposition of the Hamiltonian $H(\mathbf{k})$:

$$H(\mathbf{k}) = \sum_{n=1}^{N} |\Psi_n(\mathbf{k})\rangle\langle\Psi_n(\mathbf{k})| E_n(\mathbf{k}). \tag{1.1}$$

Here $\{|\Psi_n(\mathbf{k})\rangle\}$ denote the eigenstates of $H(\mathbf{k})$, ordered according to their energies. The fact that $H(\mathbf{k})$ is continuous in $\mathbf{k}$ implies that each eigenspace projector $P_n(\mathbf{k}) \equiv |\Psi_n(\mathbf{k})\rangle\langle\Psi_n(\mathbf{k})|$ is also continuous as a function of $\mathbf{k}$ whenever the gaps above and below band n are finite. The invariant C_n can then be computed as $C_n = C[P_n]$, where

$$C[P] = \frac{1}{2\pi i} \int_0^{\frac{2\pi\hbar}{a}} \mathrm{d}^2\mathbf{k}\, \mathrm{Tr}(P\,[\partial_{k_x} P, \partial_{k_y} P]). \tag{1.2}$$

The number C_n is the so-called *Chern number* of band n[7]. Remarkably, the Chern number $C[P]$ is an integer and cannot change under any smooth deformation of the projector P, as long as P remains continuous in crystal momentum[8]. Thus, we identify the integers $\{C_n\}$ as topological invariants of the system.

The integers $C_1 \ldots C_{N-1}$ form a *complete* set of topological invariants of the system[9]. Specifically, two Hamiltonians with N bands can be smoothly deformed into each other while keeping all gaps open, if and only if the invariants $C_1 \ldots C_{N-1}$ take the same values for the two systems [70]. This completeness property implies that any topological invariant of the system is expressable as a function of the integers $\{C_n\}$. This in particular holds for the net number of chiral edge modes $\{z_n\}$, which were identified as a topological invariants of the system in the beginning of this section. Indeed, spectral flow arguments [65] show that

$$C_n = z_n - z_{n-1}. \tag{1.3}$$

Since there can be no chiral edge modes below the lowest band (i.e. $z_0 = 0$), we thus find

$$z_n = \sum_{m \le n} C_m. \tag{1.4}$$

This non-trivial relation establishes that the net number of chiral edge modes z_n is a property of the bulk system.

---

[6] See discussion below Eq. (1.2).

[7] Note that the Chern number is also defined for disordered systems, see e.g., Ref. [71].

[8] To show this, let $P(s)$ describe a continuous deformation of P, controlled by the parameter s. Using that $P(s)$ is a projector for all s, it follows that $\partial_s P(\mathbf{k}) = -i[X(\mathbf{k}), P(\mathbf{k})]$, where $X(\mathbf{k})$ is a Hermitian operator which is continuous in $\mathbf{k}$. Using this result, along with Eq. (1.2), one can show that $\partial_s C[P]$ vanishes.

[9] It can be shown that the sum of all N Chern numbers always vanishes [15]. Hence $C_N = -\sum_{n=1}^{N-1} C_n$.

A result that relates the topological invariants of the edge spectrum with the topological invariants of the bulk is known as a *bulk-edge correspondence*. The existence of such a relation is a key feature of topological insulators.

1.2.2 Physical signatures of nontrivial topology

The physical significance of the invariant z_n becomes apparent once the chemical potential of the system μ lies in gap n, as depicted in Fig. 1.2c. While a topologically trivial system would be insulating in this case, a nonzero value of z_n results in a quantized, nonzero transverse conductance. To show this, we consider the current carried by the edge modes in gap n at low temperatures. In this case, the current carried by a single edge mode is well-approximated by the formula $I = -e\int_{E_0}^{\mu} dE\, \rho(E)v(E)$. Here $v(E) = \frac{\partial E}{dk_x}$ is the group velocity of the mode, $\rho(E)$ is the density of states in the edge mode at energy E (i.e. the number of states at energy E, divided by the length of the system), and E_0 denotes the energy where the edge mode merges with the bulk band. The density of states in a single mode at x-momentum k_x is given by $(2\pi\hbar)^{-1}$ (here we assume no spin degeneracy), and thus $\rho(E)$ is given by $\rho(E) = (h\,\partial E/\partial k_x)^{-1}$, where we used $h = 2\pi\hbar$. Thus, letting μ_1 denote the chemical potential at edge 1, each rightmoving mode at edge 1 carries a current of $-\frac{e}{h}(\mu_1 - E_0)$, while each leftmoving mode at the same edge carries an opposite current. Suppressing the gap index n, the total rightmoving current running along edge 1

$$I_1 = -\frac{z_n e}{h}(\mu_1 - E_0). \tag{1.5}$$

The same considerations show that the chiral modes at edge 2 carry the current $I_2 = \frac{z_n e}{h}(\mu_2 - E_0)$, where μ_2 denotes the chemical potential at the edge near $y = y_2$. This value ensures that no current runs along the strip in equilibrium where $\mu_1 = \mu_2$.

To study the signatures of nontrivial topology, we consider the case where a nonzero electric field E_y is applied along the y-direction in the system. The electric field generates a voltage difference between the two edges of the strip, such that $\mu_1 - \mu_2 = eE_yL_y$, where $L_y = y_2 - y_1$ is the width of the strip. When the system is in equilibrium in the presence of the field E_y, more electrons occupy the rightmoving mode than the leftmoving mode. This results in a nonzero net current $I_{\text{edges}} \equiv I_1 + I_2$, carried by the edge modes along the x-direction:

$$I_{\text{edges}} = -\frac{z_n e^2}{h} E_y L_y. \tag{1.6}$$

We note that the current density *must* vanish everywhere when the system is in equilibrium, even in the presence of the field E_y. Thus, the field E_y, must generate a current of bulk particles I_{bulk} that exactly cancels the current from the edges:

$$I_{\text{bulk}} = \frac{z_n e^2}{h} E_y L_y. \tag{1.7}$$

Taking the derivative of I_{bulk} with respect to E_y, and dividing by the width of the strip, we obtain the associated transverse (Hall) conductance of the bulk system $\sigma_{xy} \equiv \frac{\partial j_x}{\partial E_y}$, where j_x denotes the current density along the x-direction. The result in Eq. (1.7) implies that the Hall conductance is *quantized*:

$$\sigma_{xy} = z_n \sigma_0/2. \tag{1.8}$$

where $\sigma_0 \equiv 2e^2/h \approx (12.91\,\mathrm{k\Omega})^{-1}$ is the conductance quantum[10].

The quantized Hall conductance is a topologically invariant property of the system: at low temperatures, the Hall conductance can only change if the chemical potential comes within the range of a bulk band, either due to a bulk gap closing, or due to the bulk bands being shifted in energy. Similarly to the chiral edge modes, the quantization of Hall conductance even persists in the presence of disorder.

1.2.3 Integer quantum Hall effect

The situation described above is the mechanism behind the integer quantum Hall effect (IQHE). The IQHE arises in 2-dimensional electron gases, such as for example GaAs/AlGaAs interfaces, subject to strong perpendicular magnetic fields [14]. The strong magnetic field induces discrete bands in energy spectrum of the electron gas, corresponding to distinct, quantized angular momenta of cyclotron orbits [72]. The bands, known as Landau levels, are flat and evenly spaced in energy. Their separation is given by the cyclotron frequency $\Delta E = \frac{eB\hbar}{m}$, where m is the carrier mass.

Remarkably[11], each Landau level has Chern number 2. Hence, when the system is confined to a geometry with edges, there are $2n$ chiral edge modes in the gap above the nth Landau level. Semiclassically, the chiral edge modes can be interpreted as "skipping orbits" of electrons that arise due to their circular motion in the magnetic field (see bottom of Fig. 1.1b for a schematic depiction of this effect). As the discussion in Sec. 1.2.2 shows, the nonzero Chern numbers and chiral edge modes implies a quantized Hall conductance in the bulk. Specifically, when the Fermi energy lies in the gap above the nth Landau level, the Hall conductance of the system is given by $n\sigma_0$. This quantized bulk response leads to one of the most noticeable features of the integer quantum Hall effect, namely the plateaus formed by the Hall conductance as a function of the magnetic field (see top panel of Fig. 1.1b)[12].

The topological robustness of the edge modes protects this effect against disorder (in fact, the quantum Hall effect would not exist without disorder [69]), which means the quantized conductance $n\sigma_0$ can be observed in wild and relatively uncontrolled solid state samples to a accuracy of a few parts per billion. Due to its universality and robustness, the Quantum hall conductance is used as an international standard for electrical resistance [67]. The integer quantum Hall effect is a prominent example of the robust and exotic effects that can arise from nontrivial topology.

[10] The factor of 1/2 arises since a two-fold spin degeneracy was not assumed.

[11] The factor of two arises because of the spin degeneracy of electrons, which is not lifted significantly unless the magnetic field is very strong.

[12] To see how the plateaus form, note that the spacing ΔE between the Landau levels depends linearly on the magnetic field. As the magnetic field B is increased, a Landau levels will therefore cross the chemical potential at certain strengths of B. Each time a Landau level crosses the chemical potential, the sum of Chern numbers of bands below the chemical potential decreases by 2, and hence the Hall conductance decreases by σ_0 (see Eqs. (1.8) and (1.4)). This leads to the plateau-structure of the Hall resistance as function of magnetic field shown in top panel of Fig. 1.1b (the figure depicts the Hall resistance on the y-axis, which is obtained by taking the inverse of the Hall conductance).

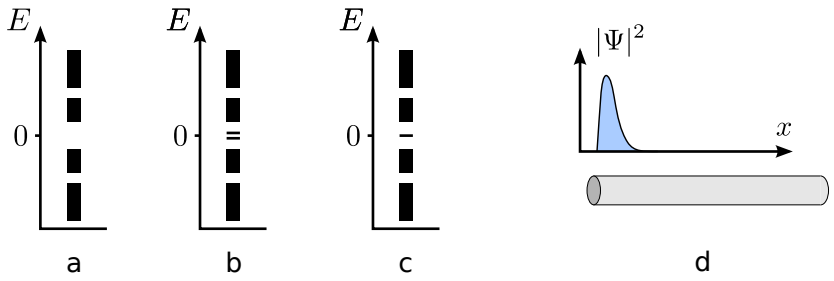

Figure 1.3: Schematic depiction of how particle-hole symmetry can lead to the topological protection of features in a one-dimensional system. Panel a) shows the energy spectrum of an infinite 1-dimensional system (wire) with particle-hole symmetry. Particle-hole symmetry implies that the energy spectrum is symmetric around zero. Panel b) shows the spectrum of the same system in a wire of finite length, with the spectrum of edge modes at one edge displayed (a schematic depiction of such an edge mode is shown in panel d)). This system has an even number of edge modes in the gap at $E = 0$, and is topologically trivial. c) Spectrum of a system with a single self-conjugate edge mode at energy zero. Due to particle-hole symmetry, the zero-energy mode can only disappear if the bulk gap closes, or the symmetry is broken; the zero-energy mode is thus a topologically-protected feature of the system.

1.3 Topological features of superconducting wires

Sec. 1.2 identified the numbers of chiral edge modes $\{z_n\}$ as topological invariants of two-dimensional systems. In this section, we give an example where the presence of a symmetry can also assist in protecting the topological features of a system.

Specifically, we consider a one-dimensional system with particle-hole symmetry[13]. Particle-hole symmetry is present when the Hamiltonian H is purely imaginary in some basis: $H = -H^*$. The symmetry $H = -H^*$ implies that the eigenstates of H come in pairs: if $|\Psi_n\rangle$ is an eigenstate of H with energy E_n, the state $|\Psi_n^*\rangle$ also is an eigenstate, but with energy $-E_n$[14]. The energy spectrum of the system is thus symmetric around $E = 0$, as schematically depicted in Fig. 1.3a for the infinite one-dimensional wire. We consider the case where the infinite system has an energy gap around $E = 0$.

As in Sec. 1.2, we study the system's topological properties by confining it to a geometry with edges, such that the wire has a finite extent. In this case, as in Sec. 1.2, the system may have localized edge modes in its bulk gaps, as depicted in Fig. 1.3d. Due to the symmetry described above, edge modes with nonzero energies come in pairs with opposite energies, as depicted in Fig. 1.3b.). Importantly, it is possible for zero-energy edge modes to be their own conjugates, as in Fig, 1.3c.

The localized edge modes can be eliminated under perturbations of the system, by shifting their energies until they merge with the bulk bands. Crucially, when the bulk gap is fixed, edge modes can only be eliminated pairwise in this fashion, due to the symmetry of the energy

[13]Specifically, we consider symmetry class D in the Altland-Zirnbauer classification (see Sec. 1.4).

[14]Here $|\Psi_n^*\rangle$ is obtained by complex-conjugating the components of $|\Psi_n\rangle$ in the basis where $H = -H^*$.

spectrum. Thus, if the number N_0 of self-conjugate edge modes on one edge is odd (this case is shown in Fig. 1.3c), at least one edge mode has to stay confined at $E = 0$ during any deformation of the system that preserves particle-hole symmetry and keeps the bulk gap at energy 0 open.

The above discussion shows that the parity of the number of zero-energy edge modes $(-1)^{N_0}$ as a topological invariant of the system (by the definition in Sec. 1.1). In contrast to Sec. 1.2, the invariant $(-1)^{N_0}$ is a $\mathbb{Z}_2$ index: it can only take two distinct values, corresponding to the topologically trivial and nontrivial cases.

Analogously to the Chern numbers the two-dimensional systems (see Sec. 1.2), it is also possible to identify a topological invariant directly from the Bloch-space Hamiltonian $H(k)$ of the system [16]. The bulk invariant is given by

$$p = \mathrm{sgn}\left(\mathrm{Pf}[H(0)]\,\mathrm{Pf}[H(\hbar\pi/a)]\right), \tag{1.9}$$

where $z = -1$ corresponds to the topologically nontrivial case, and a denotes the lattice constant. The so-called Pfaffian $\mathrm{Pf}(\cdot)$ is a scalar quantity defined for antisymmetric matrices which is invariant under orthogonal transformations[15] . Analogously to the Chern numbers, the index p gives a *complete* topological classification of the system [18]. As for the two-dimensional system in Sec. 1.2, the parity of the number of zero-energy edge modes must therefore be given by some function of p. Indeed, it was established by in Ref. [16] that

$$(-1)^{N_0} = p. \tag{1.10}$$

This constitutes the bulk-edge correspondence for the one-dimensional wire with particle-hole symmetry.

Majorana modes at the ends of superconducting wires

Particle hole-symmetry is notably found in Boguliubov-de Gennes (BdG) Hamiltonians that provide a mean-field description of fermionic systems with superconductivity. BdG-Hamiltonians act on a space that consists of two particle-hole conjugate copies of the same system. In this way, particle-hole symmetry is artificially present in BdG Hamiltonians. Nevertheless, such systems can have edge-modes that are their own conjugates [16]. The self-conjugate modes correspond to many-body excitations that are their own antiparticles. These excitations are known as Majorana fermions, and have non-trivial exchange statistics with potential applications in quantum computation. Majorana fermions have for instance been predicted in a 1-dimensional wire with strong spin-orbit coupling in the proximity of superconductivity (see e.g. Refs. [66, 74]). Fig. 1.1a shows a scanning electron microcopy (SEM) image of such an experimental setup. While the Majorana fermions' exotic topological properties have not yet been experimentally demonstrated, these excitations are subject of intensive studies [75–77].

1.4 Topological insulators

Sec. 1.3 demonstrates that particle-hole symmetry can lead to the topological protection of zero-energy edge modes in a one-dimensional system: these features cannot vanish under any

[15] More information about Pfaffians can e.g. be found in Ref. [73]. Note that the matrix representation of the Hamiltonian that enters in Eq. (1.9) should be given in a basis where that $H = -H^*$.

Symmetry				d							
AZ	Θ	Ξ	Π	1	2	3	4	5	6	7	8
A	0	0	0	0	$\mathbb{Z}$	0	$\mathbb{Z}$	0	$\mathbb{Z}$	0	$\mathbb{Z}$
AIII	0	0	1	$\mathbb{Z}$	0	$\mathbb{Z}$	0	$\mathbb{Z}$	0	$\mathbb{Z}$	0
AI	1	0	0	0	0	0	$\mathbb{Z}$	0	$\mathbb{Z}_2$	$\mathbb{Z}_2$	$\mathbb{Z}$
BDI	1	1	1	$\mathbb{Z}$	0	0	0	$\mathbb{Z}$	0	$\mathbb{Z}_2$	$\mathbb{Z}_2$
D	0	1	0	$\mathbb{Z}_2$	$\mathbb{Z}$	0	0	0	$\mathbb{Z}$	0	$\mathbb{Z}_2$
DIII	-1	1	1	$\mathbb{Z}_2$	$\mathbb{Z}_2$	$\mathbb{Z}$	0	0	0	$\mathbb{Z}$	0
AII	-1	0	0	0	$\mathbb{Z}_2$	$\mathbb{Z}_2$	$\mathbb{Z}$	0	0	0	$\mathbb{Z}$
CII	-1	-1	1	$\mathbb{Z}$	0	$\mathbb{Z}_2$	$\mathbb{Z}_2$	$\mathbb{Z}$	0	0	0
C	0	-1	0	0	$\mathbb{Z}$	0	$\mathbb{Z}_2$	$\mathbb{Z}_2$	$\mathbb{Z}$	0	0
CI	1	-1	1	0	0	$\mathbb{Z}$	0	$\mathbb{Z}_2$	$\mathbb{Z}_2$	$\mathbb{Z}$	0

Figure 1.4: Periodic table of topological insulators (see discussion in Sec. 1.4). The table classifies the topological properties for systems with each of the 10 Altland-Zirnbauer (AZ) symmetry classes [78]. Each row correspond to distinct symmetry classes, identified by the first four columns: the first column shows the index of the class in the AZ classification, while the Greek letters Θ, Ξ, and Π in columns 2-4 indicate whether, respectively, time-reversal, particle-hole or chiral symmetry are present. For the two former, the sign indicates whether the symmetry operator squares to 1 or -1; these two cases correspond to physically distinct situations. Columns 5-12 show how many topologically distinct phases are supported, for each combination of symmetry class, and dimensionality d. The number 0 corresponds to all phases being topologically identical, $\mathbb{Z}_2$ indicates the existence of two distinct topological phases, and $\mathbb{Z}$ indicates that an infinite family of topological phases exists that can be labelled by integers. Note that chiral symmetry is automatically present when time-reversal and particle hole symmetry is present. The table was obtained in Refs. [18, 19].

deformation of the system that preserves the system's bulk gap and symmetry. In similar ways, any symmetry can potentially lead to the topological protection some property in a system. As described in Sec. 1.1, materials where nontrivial properties are topologically protected by the systems' band gaps and symmetries are collectively known as *topological insulators*. Topological insulators host a wide range of interesting, and potentially useful, physical phenomena characterized by their robustness, universality, and exotic nature [79]. In addition to the two cases discussed in Secs. 1.3, notable examples of topological insulators include topological insulators protected by time-reversal symmetry in two and three dimensions (see Fig. 1.1c). In this class of materials, time-reversal symmetry respectively leads to the topological protection of helical modes and Dirac nodes in the system's edge spectrum [9–11].

Any symmetry class can potentially support its own family of topological insulators by protecting topological features in the system. However, the most interesting symmetry classes from a physical perspective are the symmetries that are generically present in real-world systems – in particular, symmetries which are not broken by disorder. The most important among these are time-reversal symmetry, particle-hole symmetry, and chiral symmetry [78]. Dividing into cases where each of these four symmetries are present or not, one can verify that 10 distinct combinations of the symmetry classes are possible, including the trivial cases (See Fig. 1.4). These 10 symmetry classes are collectively described in the Altland-Zirnbauer (AZ) classification of symmetries [78].

After the discovery of topological insulators protected by time-reversal symmetry [9–11], extensive theoretical work sought to identify the topological phases that are supported by various symmetry classes[16]. An important result was the classification of all topological phases supported by each of the 10 AZ symmetry classes in any given dimension [18, 19]. The resulting "periodic table" of topological insulators is shown on Fig. 1.4 (see caption for explanation). Note that not all combinations of dimensionality and symmetry class can support a topological insulator – for example there exists no 1-dimensional version of the Chern insulator[17]. Note also that all combinations of symmetry class and dimensionality support a trivial topological phase: it is always possible for a system with of a given symmetry and dimensionality to be topologically trivial even though topological insulators are supported. For instance, not all 2-dimensional systems are Chern insulators.

The 10 AZ symmetry classes are not the only symmetries that can support topological insulators. Notably, crystal symmetries, such as inversion symmetry, can support new types of topological insulators, by topologically-protecting features in the bands of materials. Such crystal-symmetry protected topological insulators are a subject of current research [80].

1.5 Discussion

This chapter introduced a new class of materials – the topological insulators and superconductors. These materials are characterized by exotic, universal extremely robust properties. The theoretical description of topological insulators and superconductors have led to the the discovery of several

[16] See the beginning of this chapter for the definition of topological phase.

[17] In fact, in each dimension, only 5 of the 10 symmetry classes in the periodic table (Fig. 1.4) support a topological insulator.

materials with these novel properties, such as HgTe quantum wells, Bi_2Se_3, or proximity-coupled nanowires with strong spin-orbit coupling [11–13, 66, 76, 77]. While topological insulators and superconductors have been identified and studied experimentally, their novel properties have been challenging to realize as robust and useful effects [80, 81], except for the well-known (and remarkable) integer quantum Hall effect [14, 67]. Topological insulators and superconductors remain under intensive investigation, due to the exotic and potentially useful phenomena these materials may support.

Even while experimental signatures remain elusive, the theoretical discovery of topological insulators has had a profound impact. In particular, the theoretical advances described above have inspired the explorations of new topological effects far beyond the originally-imagined solid-state settings. Settings where topological effects are explored in this way include photonic crystals [59, 82–85], optical cavities [3, 57], mechanical systems [86–88], and adiabatic pumping effects [8, 65]. A solid-state field which has emerged after the discovery of topological insulators is the characterization of topological properties of non-gapped materials (Weyl semimetals) [89]. In several of the cases above, the theory of topological insulators played a crucial role in predicting new effects. The discoveries above open up the possibility for additional unexplored topological effects in non-solid-state settings.

A prominent direction of studies which originates from the discovery of topological insulators is the exploration of topological phases in periodically driven systems. This topic is the focus Chapters 2-7 in this thesis. Chapter 8 explores a novel, driving-induced topological effect that arises in a classical, non-solid-state setting [3].

Chapter 2

Topological Phases in Periodically Driven Systems

Secs. 2.1 and 2.2 of this chapter are partially based on Chapter 3 from the author's master's thesis (2015). The master's thesis is cited as Ref. [4].

The last chapter introduced a class of materials known as topological insulators and superconductors. Topological insulators and superconductors are characterized by universal, exotic, and extremely robust phenomena that have multiple potential applications. These effects can be seen as arising from the topological properties of the bulk materials. Here the term "topological" refers to the properties of materials which are invariant under gap-preserving deformations, as described in Sec. 1.1. Remarkably, as the discussion in Sec. 1.2 showed, materials *can* have such nontrivial topological features. The theoretical description and classification of topologically-invariant properties of materials has led to predictions and discovery of several materials and setups that act as topological insulators or superconductors [18, 19]. Examples which are now well-known include Bismuth Selenide, Mercury-Telluride quantum wells [11–13], and proximity-coupled nanowires with strong spin orbit coupling [66, 76, 77]. With the notable exception of the integer quantum Hall effect [14] however, signatures of topological insulators or superconductors have so far proven elusive to realize as roubst experimental effects [80, 81].

In recent years, periodic driving has been proposed as new a way of manipulating the properties of materials. Here periodic driving in practice means subjecting the system to an external oscillating force, such as the electromagnetic field from a laser. As we demonstrate in this chapter (Secs. 2.1-2.2), periodic driving can in certain respects be used to effectively modify the Hamiltonian of a system. Initial motivation for theoretical work in this field was to use this effect to drive an otherwise ordinary solid-state system into a nontrivial topological phase [21,23,24]. Currently, experimental realizations of such solid-state effects remain a challenge due to the high frequency and intensity required to significantly affect a material's properties. Still, subsequent theoretical work has led to multiple new discoveries and experiments beyond the originally-imagined solid-state setting [3, 37, 42, 49, 50, 52, 53, 57, 59–61, 63]. For instance, periodic driving has been used to realize the Haldane model[1] [90] in gasses of cold atoms in

[1]The Haldane model is an example of the Chern insulator that was discussed in Sec. 1.2.

optical lattice [41]. Other notable advances include the prediction of Floquet time crystals and its subsequent experimental discovery in systems of trapped ions [49, 50, 52], as well as novel topological effects in photonic crystals [59–61].

An important and surprising result has been the realization that periodically driven systems host a *richer* variety of topological phases than their nondriven counterparts [1,5,42]. In particular, it is possible to achieve entirely new topological phases in periodically driven systems, which have no equivalent in nondriven systems [1, 2, 5, 42, 46, 49, 50]. The topological properties of these new phases are not captured by an effective static Hamiltonian, but are encoded in the nontrivial dynamics of the system that takes place within each driving period. Such novel phases are of intrinsically nonequilibrium nature, and are known as *anomalous* topological phases. Anomalous topological phases include the Floquet time crystals [49, 50], as well as the anomalous Floquet-Anderson insulator, which can can support nonzero, quantized charge transport on its edges [2, 6, 91].

An important challenge to be overcome in the field is that large, interacting many-body systems almost always act as thermal baths. Systems with this property (known as *thermalizing* systems) irreversibly absorb energy from the periodic driving field, leading to an continuous and uncontrollable heating effect [92–94]. The fixed pint of this heating process is a trivial, infinite-temperature steady state which cannot support any nontrivial phase structure. There are currently several proposed strategies to counter the heating effect, such as coupling the system to external baths [95, 96], or realizing topological effects in the transient dynamics of the system, before heating becomes significant [62]. An important approach, which forms the basis of discussion in Chapters 5-6, is to prevent the system from acting as a thermal bath in the first place. Importantly, using disorder-induced many-body localization [97, 98]. The existence of nontrivial topological invariants of the micromotion (i.e., the dynamics of the system that take place within each driving period) allows driven many-body localized systems to support nontrivial topological phases [7, 45, 47, 49, 50, 99]. Chapters 5-6 will study the stability and topological features of such many-body localized topological phases.

This chapter introduces the subject of topological phases in periodically driven systems. The first part (Sec. 2.1) of this chapter reviews the theory of periodically driven quantum systems. The results of this section forms the basis for discussion in the rest of this chapter, and the remaining part of this thesis. Subsequently, Sec. 2.2 discusses the topological phases supported by noninteracting driven systems. In particular, Secs. 2.2.2-2.2.4 demonstrating that driven systems may host a richer topology than their nondriven counterparts. Following this, Sec. 2.3 discusses the qualitative differences between noninteracting and interacting driven systems, providing a more detailed description of the heating effect that was discussed above, as well as the possible strategies to counter this effect. The Chapter concludes with a brief review of experimental proposals in the field (Sec. 2.4) and a discussion (Sec. 2.5).

2.1 Theory of periodically driven systems

We begin the chapter by reviewing the theory of periodically driven systems in quantum mechanics. The results obtained here forms the basis for the description of topological phases in periodically driven systems. Moreover, this section common terminology, which will be used extensively in this thesis.

According to the laws of quantum mechanics, the state of a physical system associated with a vector $|\psi(t)\rangle$. The time-evolution is of the system is described by the Schrödinger equation

$$\partial_t|\psi(t)\rangle = -iH(t)|\psi(t)\rangle, \tag{2.1}$$

where $H(t)$ is the Hamiltonian operator of the system[2]. The above differential equation can be formally integrated, and its solution reads

$$|\psi(t)\rangle = U(t)|\psi(0)\rangle, \tag{2.2}$$

where the $U(t)$ denotes the *time-evolution operator* of the system. The time-evolution operator is unitary, and can be written as

$$U(t) \equiv \mathcal{T} e^{-i\int_0^t H(t')dt'}, \tag{2.3}$$

Here $\mathcal{T}$ denotes the time-ordering symbol[3]. This symbol orders the factors of $H(t')$ in the expansion of the exponential above according to the time t', such that operators associated with later times are placed left of operators associated with earlier times.

In the case where the Hamiltonian of the system is time-independent, $H(t) = H$, the time-evolution operator is given by $U(t) = e^{-iHt}$. In this case, the solution of the Schrödinger equation is simplified by the diagonalization of the Hamiltonian:

$$H|\Psi_n\rangle = E_n|\Psi_n\rangle. \tag{2.4}$$

The solutions $\{E_n, |\Psi_n\rangle\}$ to eigenvalue problem above allows one to compute the time-evolution of the system analytically, given any initial state. In this case, one can verify that $U(t) = \sum_n |\Psi_n\rangle\langle\Psi_n|e^{-iE_nt}$, and thus the solutions to the Schrödinger equation take the form

$$|\psi(t)\rangle = \sum_n c_n e^{-iE_nt}|\Psi_n\rangle. \tag{2.5}$$

The coefficients $\{c_n\}$ are constant in time, and are thus determined by the initial state: $c_n = \langle\Psi_n|\psi(0)\rangle$. In this way, Eq. (2.5) allows one to compute the time-evolution of any state, given the initial conditions. Systems where the Hamiltonian is time-independent are referred to as *nondriven* systems.

If the Hamiltonian $H(t)$ is not constant in time, it generally impossible to compute the system's time-evolution analytically as in Eq. (2.5). However, there is notable exception: if the Hamiltonian depends periodically on time, such that $H(t) = H(t+T)$ for some driving period T,

[2] In this chapter, we set $\hbar = 1$.

[3] In practice, the-time-evolution operator can by computed from the Suzuki-Trotter expansion: $U(t) \approx e^{-iH(t_N)\delta t}\dots e^{-iH(t_1)\delta t}$, where $t_n = n\delta t$, and $\delta t = t/N$. The approximation becomes an equality in the limit $N \to \infty$.

it is possible to analyze the time-evolution of the system in a similar fashion as for non-driven systems. Such systems are referred to as *periodically driven systems*.

In periodically driven systems, the time-evolution operator satisfies the relation

$$U(t+T) = U(t)U(T). \tag{2.6}$$

This result can for instance be verified using the Suzuki-Trotter expansion (see Footnote 3). In particular, $U(mT) = U(T)^m$ for each integer m. Hence, the time-evolution of a state $|\psi(t)\rangle$ at any integer multiple m of the driving period is given by

$$|\Psi(mT)\rangle = U(T)^m|\Psi(0)\rangle. \tag{2.7}$$

In the following, we will refer to the time evolution of the system at integer multiples of the driving period as the *stroboscopic* evolution of the system. Eq. (2.7) shows that the time-evolution operator $U(T)$ over one driving period fully describes the stroboscopic dynamics of periodically driven systems. This important operator is referred to as *Floquet operator*.

One of the most useful results in the theory of periodically driven systems is that the eigenvalues and eigenstates[4] of the Floquet operator describe the stroboscopic dynamics of the system in a similar way that the eigenstates and eigenvalues of the Hamiltonian describe the dynamics of nondriven systems. The central eigenvalue problem for periodically driven systems thus reads

$$U(T)|\Psi_n\rangle = e^{-i\varepsilon_n T}|\Psi_n\rangle, \tag{2.8}$$

where ε_n is real and has units of energy[5]. The numbers $\{\varepsilon_n\}$ are referred to as *quasienergies*, and the eigenstates $\{|\Psi_n\rangle\}$ are known as *Floquet eigenstates*. The Floquet eigenstates and quasienergies, allows one to analytically compute the stroboscopic evolution of any state $|\psi(t)\rangle$. Specifically, any integer multiple of the driving period m, the solutions to the time-dependent Schrödinger equation takes the form

$$|\psi(mT)\rangle = \sum_n c_n|\Psi_n\rangle e^{-i\varepsilon_n mT}, \tag{2.9}$$

where, as for non-driven systems, the coefficients $\{c_n\}$ are determined by the initial conditions: $c_n = \langle\Psi_n|\psi(0)\rangle$. Note that Eq. (2.8) only defines quasienergy ε_n up to an integer multiple of the driving frequency $\omega \equiv 2\pi/T$. Thus, in order to be represented by a real number, quasienergy requires a specification of an interval of width $2\pi/T$ in which it should take value, analogously to the choice of Brillouin zone for crystal momentum. Such a quasienergy interval is known as a *quasienergy Brillouin zone*.

From Eq. (2.9), we see that the stroboscopic evolution of the system are identical to the evolution generated by a static Hamiltonian, namely the Hamiltonian

$$H_{\text{eff}} = \sum_n |\Psi_n\rangle\langle\Psi_n|\varepsilon_n. \tag{2.10}$$

We refer to H_{eff} as the *effective Hamiltonian* of the system. Note that the effective Hamiltonian is not uniquely defined, but requires a specification of quasienergy Brillouin zone (see the discussion

[4]Note that the Floquet operator is unitary, and therefore diagonalizable.

[5]Since $U(T)$ is unitary, its eigenvalues are complex numbers of unit modulus. Thus ε_n must be real.

below Eq. (2.8)). Formally, the effective Hamiltonian is given by the logarithm of the Floquet operator, i.e., $H_{\text{eff}} = \frac{i}{T}\log U(T)$, where the choice of branch cut for the logarithm determines the quasienergy Brillouin zone for H_{eff}.

Comparing Eq. (2.9) to Eq. (2.5), we see that quasienergy plays a role analogous to energy for the time-evolution in periodically systems. Like energy, quasienergy is a conserved quantity in periodically driven systems[6]. Importantly, however quasienergy is only defined up to an integer multiple of $2\pi/T$, and is thus of periodic nature. The periodicity of quasi-energy constitutes one of the main qualitative differences in the analysis of non-driven and periodically driven systems. The distinction has important implications for the many-body dynamics and topological properties of periodically driven systems, as will be shown in the following sections.

Micromotion and Floquet states

The above discussion shows that the stroboscopic evolution of a periodically driven system is determined by the Floquet eigenstates and quasienergies of the system (Eq. (2.9)). However, in some cases, important properties of a system are not captured by its stroboscopic evolution, but depend on the dynamics of the system that takes place within a driving period [1, 100, 101]. This is in particular a defining feature for the new, intrinsically-nonequilibrium topological phases (the so-called anomalous Floquet phases) that can arise in periodically driven system, and will be a focus in the following. In this subsection, we therefore briefly discuss how the to analyze the motion of the system that takes place during the driving period. This part of a periodically system's dynamics is referred to as the *micromotion*.

The micromotion of a periodically driven system is conveniently expressed by a family of time-dependent states $\{|\Phi_n(t)\rangle\}$, known as the *Floquet states* (not to be confused with Floquet eigenstates). These states are defined from the Floquet eigenstates such that

$$|\Psi_n(t)\rangle = e^{-i\varepsilon_n t}|\Phi_n(t)\rangle, \tag{2.11}$$

where $|\Psi_n(t)\rangle \equiv U(t)|\Psi_n\rangle$. By construction, the Floquet states are periodic in time: $|\Phi_n(t)\rangle = |\Phi_n(t+T)\rangle$, as can be verified using Eqs. (2.6) and (2.8). The Floquet states can be used to express the *continuous* time-evolution of the system. Specifically, the solution to the time-dependent Schrödinger equation at *any* time takes the form

$$|\psi(t)\rangle = \sum_n c_n|\Phi_n(t)\rangle e^{-i\varepsilon_n t}, \tag{2.12}$$

where the amplitudes $\{c_n\}$ are determined from the initial conditions: $c_n = \langle\Psi_n|\psi(0)\rangle$. The existence of the solution in Eq. (2.11) was first established by Gaston Floquet in 1883 (although not in the context of quantum mechanics) and is known as the *Floquet theorem* [102].

The solutions Eq. (2.11) bear a clear resemblance to the Bloch wave functions of a periodic crystal. The Bloch theorem dictates that each eigenstate of a translationally-symmetric Hamiltonian can be expressed as a periodic function times a complex plane wave. The plane wave's wavenumber determines the crystal momentum of the state. Similarly to quasienergy, crystal

[6]This can be verified by explicitly computing the expectation value of the quasienergy $\langle\varepsilon\rangle = \sum_n\langle H_{\text{eff}}\rangle$ as a function of time.

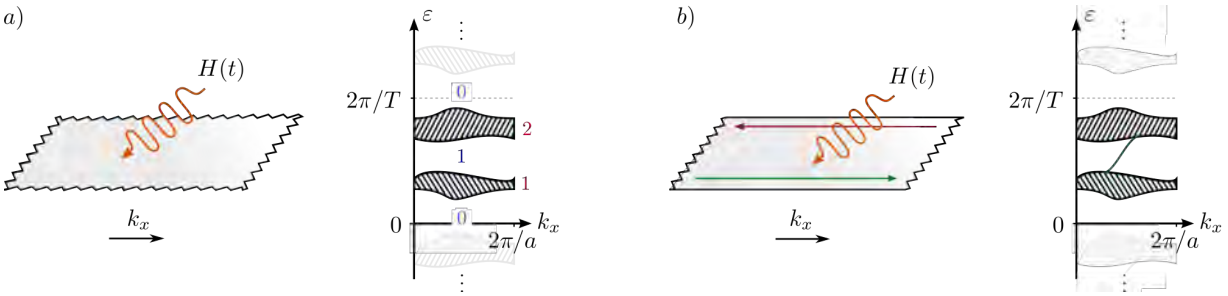

Figure 2.1: a) Schematic depiction and quasienergy spectrum of an infinite two-dimensional system subject to periodic driving. Red labels denote the indices of the bands, while blue labels denote the indices of the gaps, with the labelling scheme introduced in Sec. 2.2.1. Bright colors indicate copies of the quasienergy bands in the repeated-zone scheme. b) Schematic depiction and quasienergy spectrum of a topologically nontrivial system, confined to the geometry of a strip. In addition to the spectrum of bulk modes, only edge modes confined to the lower edge are displayed. Adapted from Ref. [4].

momentum is only defined up to an integer multiple of $2\pi/a$, where a is the lattice constant. Thus, quasienergy can be viewed as the temporal analogue of crystal momentum: while crystal momentum is conserved due to discrete spatial translation symmetry [103], the conservation of quasienergy results from the discrete time-translation symmetry which is present in periodically driven systems.

2.2 Topological phases in driven, noninteracting systems

Having reviewed the theory of periodically driven systems in quantum mechanics, we now explore their topological properties. Compared to nondriven systems, periodic driving leads to significant qualitative differences between noninteracting and interacting systems [92–94]. For this reason, this section will focus on noninteracting systems, while the case of interacting many-body systems in discussed in Sec. 2.3. The distinction between noninteracting and interacting driven systems is discussed in detail in Sec. 2.3.

Using the driven version of the two-dimensional system studied in Sec. 1.2 as an example, we demonstrate that periodically driven systems can support topologically-nontrivial band structures, as well as entirely new, intrinsically non-equilibrium phases of matter (Secs. 2.2.2-2.2.4). Subsequently, we briefly describe the role of symmetries in topologically-protecting nontrivial features in a driven systems (Sec. 2.2.5), and conclude by discussing the general topological classification of periodically driven systems (Sec. 2.2.6). The discussion in this section extensively uses the concepts and models that were introduced in Chapter 1.

2.2.1 Topological phases in a driven 2-dimensional system

We illustrate how topologically-nontrivial features can arise in a periodically driven system by considering a system of noninteracting fermions on a two-dimensional lattice. The system is

subject to periodic driving, meaning that the Hamiltonian depends on time in a periodic fashion: $H(t) = H(t+T)$. Here T denotes the driving period. While we note that the results discussed in this section can be obtained even for disordered systems, we assume for simplicity that the Hamiltonian has discrete spatial translation symmetry [2]. The discussion here will proceed analogously to Sec. 1.2, where the nondriven version of this system was studied in Sec. 1.2.

Due to the presence of spatial translation symmetry, crystal momentum $\mathbf{k}$ is a good quantum number in the system: Specifically, the Hamiltonian is block-diagonal in crystal momentum, such that the Hamiltonian is given by the Bloch space Hamiltonian $H(\mathbf{k}, t)$ within the subspace with crystal momentum $\mathbf{k}$. The time-evolution operator $U(t)$, which is obtained as an exponential of the Hamiltonian, inherits the block-diagonal structure of the Hamiltonian. In particular, time-evolution in the subspace with crystal momentum $\mathbf{k}$ is generated by the Bloch-space evolution operator

$$U(\mathbf{k}, t) = \mathcal{T} e^{-i \int_0^t dt' H(\mathbf{k}, t')}. \tag{2.13}$$

The locality and boundedness of the Hamiltonian implies that the time-evolution operator is continuous in crystal momentum and time, respectively [5]. The spectral decomposition of the Bloch-space Floquet operator $U(\mathbf{k}, T)$ defines the Floquet eigenstates $\{|\Psi_n(\mathbf{k})\rangle\}$ and quasienergy bands $\{\varepsilon_n(\mathbf{k}, t)\}$ of the system, analogously to the energy bands in the nondriven case (see Sec. 1.2):

$$U(\mathbf{k}, T) = \sum_n e^{-i\varepsilon_n(\mathbf{k})T} |\Psi_n(\mathbf{k})\rangle\langle\Psi_n(\mathbf{k})|, \tag{2.14}$$

The continuity of $U(\mathbf{k}, T)$ implies that the quasienergy bands $\{\varepsilon(\mathbf{k})\}$ are continuous in crystal momentum.

At this point, a qualitative difference between driven and nondriven systems arises: due to their periodic nature, there is no obvious way to label the quasienergy bands[7]. Specifically, the labelling of quasienergy bands requires a choice of quasienergy Brillouin zone (QBZ): we choose some arbitrary quasienergy ε_0 and label the quasienergy bands according to their values in the quasienergy Brillouin zone $[\varepsilon_0, \varepsilon_0 + 2\pi/T)$. With this labelling, we let gap n denote the quasienergy gap above band n, such that gap n separates band n and $n+1$ (for $n < N$), while gap 1 separates band N and 1. Fig. 2.1a, schematically depicts a possible quasienergy band structure for the two-dimensional system we study, as function of x-crystal momentum k_x, represented in a repeated zone scheme. Fig. 2.1 depicts the labelling of quasienergy bands (red) and gaps (blue) in the two-band system which results from a QBZ choice where $\varepsilon_0 = 0$.

To reveal the nontrivial topological features of the model, we confine the system to the geometry of a strip, in such a way that translational invariance is not broken along the x-axis (left panel in Fig. 2.1b). The strip has edges at $y = y_1$ and $y = y_2$, where $y_1 < y_2$, and we refer to these edges as 1 and edge 2, respectively. Due to the unbroken x-translation symmetry, k_x remains a good quantum number, and the quasienergies of the system are still given by smooth functions of k_x. As for the nondriven system discussed in Sec. 1.2, the quasienergy bands of the infinite system are unaffected by the presence of the edges and remain intact, when the strip is wide enough. These bands, indicated by (i) in Fig. 2.1b, are referred to as the bulk quasienergy bands of the system. In addition to the bulk quasienergy bands, the quasienergy spectrum can

[7]However, there *is* in fact a natural labelling of quasienergies, defined by continuation in t of the spectrum of $U(\mathbf{k}, t)$. See Sec. 3.2.2 for a discussion of this labelling scheme.

also contain edge modes, corresponding to states localized on either of the edges of the strip. In the same way as for the edge modes in the nondriven case (see Sec. 1.2), the quasienergies of these edge modes must lie within the gaps of the bulk bands.

As in the nondriven case (see Sec. 1.2), the quasienergy spectrum may hold chiral edge modes[8] that connect two bulk quasienergy bands across a gap. Such a situation is depicted in Fig. 2.1b: here, one of the the system's quasienergy gaps holds a single chiral edge mode (indicated by green), corresponding to a state located on the lower edge. As for the analogous nondriven case, this feature can only be eliminated under a smooth deformation of the system, if the bulk quasienergy gap closes. In this way, the single chiral edge mode is *topologically protected* by the finite width of the quasienergy gap. More generally, we identify the number z_n of chiral edge modes in quasienergy band n (confined to edge 1) as a topological invariant of the system[9]: As for the nondriven case, the existence of z_n rightmoving modes in gap n on the lower edge implies the existence of z_n leftmoving modes on the top edge. This is indicated by red in Fig. 2.1b.

As for the nondriven case in Sec. 1.2, the topologically nontrivial edge modes carry a topologically-protected chiral current. In particular, a wave packet constructed from a chiral edge mode will move unidirectionally along the edge, and is insensitive to any backscattering by impurities[10].

2.2.2 Anomalous topology and the micromotion invariant

For nondriven a system (Sec. 1.2), chiral edge modes are a manifestation of nontrivial topological properties of the bulk. This relationship is summarized by a *bulk-edge correspondence*, which links the Chern numbers $\{C_n\}$ of the bulk energy bands (see Eq. (1.2)) to the numbers $\{z_n\}$ of chiral edge modes in bulk energy each gap:

$$C_n = z_n - z_{n-1} \tag{2.15}$$

Since the number of rightmoving modes below the lowest energy band must be zero ($z_0 = 0$), the Chern numbers of the bulk energy bands $\{C_n\}$ fully determine the number of edge modes in any given gap.

For the periodically driven system discussed in this section, a result analogous to Eq. (2.15) holds for the chiral edge modes of quasienergy bands[11]. In this case, z_n refers to the number of chiral edge modes in quasienergy gap n, and C_n refers to the Chern number of the nth bulk quasienergy band[12]. Note that gap 0 is identical to gap N due to the periodic nature of the quasienergy bands. Crucially, due the periodic nature of quasienergy, chiral edge states may connect band N with band 1 across the edge of the quasienergy Brillouin zone, thus allowing z_0 to be nonzero; indeed, the location of gap 0 is matter of convention. Thus, the Chern numbers of

[8] See also Sec. 1.2 for definition of chiral edge modes.

[9] See Footnote 4 in Chapter 1 for a rigorous definition of z_n.

[10] This can for instance be shown using the fact that the stroboscopic dynamics of the driven system are replicated by a static "effective" Hamiltonian $H_{\text{eff}}(k_x)$ (see discussion in Sec. 2.1). The energy spectrum of $H_{\text{eff}}(k_x)$ is identical to the quasienergy spectrum $\{\varepsilon_n(k_x)\}$ of the system (including the chiral edge modes), and hence features a rightmoving edge mode at the bottom edge.

[11] The result in Eq. (2.15) can be established using similar spectral-flow arguments as for the nondriven case [65]

[12] The Chern number C_n is computed using the band projector $|\Psi_n(\mathbf{k})\rangle\langle\Psi_n(\mathbf{k})|$ in Eq. (1.2).

the quasienergy bands do not fully determine the numbers of chiral edge modes. For instance, the relationship in Eq. (2.15) implies that the Chern number of bands 1 and 2 in Fig. 2.1b are given by 1 and -1, respectively. This configuration of Chern numbers in Fig. 2.1b are also consistent with a situation where gap 0 and 1 hold 1 and 2 chiral edge modes, respectively. It is even possible for the system to have a nonzero number of chiral edge modes in each gap, while Chern numbers of all bulk bands are zero, as shown in Fig. 2.2 [1]. This situation is described in Sec. 2.2.3 below.

The discussion above shows that the periodically-driven, two-dimensional system has a *richer* topological structure than its nondriven counterpart [1]. Specifically, while the topological phase of nondriven system with N bands is characterized by $N-1$ independent integers, the topological phase of its driven counterpart is characterized by N integers. The integers characterizing nondriven systems are the numbers of chiral edge modes $z_1 \dots z_{N-1}$, or, equivalently, the Chern numbers[13] $C_1 \dots C_{N-1}$, while the N invariants characterizing periodically driven systems are the number of chiral modes $z_0 \dots z_{N-1}$. The existence of the additional invariant z_0 in driven systems results from the presence of an additional "quasienergy Brillouin zone edge gap" that can host chiral edge modes.

Importantly, even while the topological phase of a driven N-band system is characterized by N independent integers, the system's bulk quasienergy bands are only characterized by $N-1$ independent integers[14], namely the Chern numbers $C_1 \dots C_{N-1}$. Thus, as also described above, Eq. (2.15), the Chern numbers of the bulk bands do not capture *all* topological properties of the system: there exists exactly one additional integer-valued topological invariant of the bulk, ν, which is not associated with the quasienergy bands. As we show below, this invariant is associated with the bulk system's micromotion, and we refer to this invariant ν as the *micromotion invariant*.

The micromotion invariant will be play an important role in the discussion below, and throughout this thesis: the next chapter (Chapter 3) develops a general method for classifying the topological properties of the micromotion in periodically-driven systems (given any symmetry class), identifying ν with nodal points in the spectrum of the bulk evolution operator $U(\mathbf{k}, t)$. Following this, Chapter 4 explores the physical nature of the micromotion invariant, showing that ν characterizes the the orbital magnetization of the bulk: specifically, when disorder is present, the average orbital magnetization density of particles in the bulk takes the quantized value ν/T.

The existence of a micromotion invariant is a general feature in periodically driven systems [1, 2, 5, 42, 104]. Its existence implies that periodically driven systems support topological phases of matter which have no analogues in static systems [1, 2, 5, 42, 104]. These phases, which are characterized by a nontrivial value of the micromotion invariant, and of intrinsically non-equilibrium nature, are referred to as *anomalous (topological) phases*[15]. The following subsection explores the nature and manifestations of these anomalous topological phases in the two-dimensional system that was introduced in Sec. 2.2.1.

[13] The Chern number of band N is determined from the Chern numbers of the remaining bands: $C_N = -\sum_{n=1}^{N-1} C_n$ and is therefore not independent from the others [15]. Note that the bulk-edge correspondence in Eq. (2.15) ensures that the two sets of invariants ($\{z_n\}$ and $\{C_n\}$) are equivalent: distinct configurations of the invariants $z_1 \dots z_{N-1}$ correspond one-to-one to distinct configurations of the Chern numbers $C_1 \dots C_{N-1}$.

[14] The sum of all quasienergy bands' Chern numbers must be given by zero [15], and hence the Chern number of band N is determined from the Chern numbers of the previous $N-1$ bands, see footnote 13.

[15] More generally, *anomalous* refers to topological features, which have no analogue in nondriven systems. Anomalous topological features are typically associated with the driven system's micromotion.

Bulk-edge correspondence Even though the Chern numbers of the bulk quasienergy bands are not sufficient to determine the number of chiral edge modes in the quasienergy gaps, the bulk-edge correspondence for the two-dimensional system we study is well-established, and was first identified by Rudner *et al* in Ref. [1]. Here, it was shown that the number of chiral edge modes in quasienergy gap n is related to the full Bloch-space time-evolution operator $U(\mathbf{k},t)$ as follows:

$$z_n = -\frac{1}{8\pi^2}\int \mathrm{d}^2\mathbf{k}\mathrm{d}t\,\mathrm{Tr}\left(U_n^\dagger\partial_t U_n\left[U_n^\dagger\partial_{k_x}U_n, U_n^\dagger\partial_{k_y}U_n\right]\right) - x\leftrightarrow y, \tag{2.16}$$

where the time-periodic unitary operator $U_n(\mathbf{k},t)$ is given by $U_n(\mathbf{k},t) = U(\mathbf{k},t)e^{iH_{\mathrm{eff}}^{(n)}(\mathbf{k})t}$. Here $H_{\mathrm{eff}}^{(n)}$ is the effective Hamiltonian of the system, defined with a quasienergy Brillouin zone whose boundary lies in gap n (see Eq. (2.10)).

Eq. (2.16) demonstrates that the number of chiral edge modes depends on the entire micromotion of the system (i.e., the evolution that takes place within a driving period), which is encoded in the full time-evolution operator $U(\mathbf{k},t)$. This result is thus is in good agreement with the discussion above Eq. (2.15).

2.2.3 The AFAI phase

The discussion above shows that periodically driven systems are characterized by an additional micromotion invariant, compared to their nondriven counterparts. The existence of the micromotion invariant implies that driven systems support new, anomalous, topological phases, that have no equivalent in nondriven systems. This subsection studies the nature of such anomalous phases in the two-dimensional system that was introduced in Sec. 2.2.1.

To see how an anomalous topological phase can be realized in the system, note that quasienergy's periodic nature allows each gap in the quasienergy spectrum to hold a single chiral edge mode[16], in such a way that the edge modes "wrap" around the entire quasienergy Brillouin zone. This situation is depicted schematically in Fig. 2.2c. The relationship between edge modes and the Chern numbers in Eq. (2.15) implies that the Chern number of each quasienergy bulk band is zero. Thus the periodically driven system can host chiral edge modes, even though its bulk bands are topologically trivial. Note that chiral edge modes in nondriven systems implies the existence of topologically-nontrivial bulk bands. The configuration of chiral edge modes depicted in Fig. 2.2 is thus an *anomalous* topological feature: it cannot arise in any nondriven system.

The manifestations of the anomalous topology become apparent once disorder is introduced: as discussed in the end of Sec. 2.2.1, the chiral edge modes are unaffected by disorder, due to the absence of channels for backscattering by impurities [69]. However, even while the chiral edge modes persist, the presence of disorder can lead to localization of all Floquet eigenstates in the bulk, in a mechanism equivalent to Anderson localization [2]. In this way, a situation can arise where a fully localized bulk coexists with delocalized, topologically-protected chiral edge states, as depicted in Fig. 2.3a. Note that the coexistence of delocalized chiral edge states and a

[16] In this subsection (and in Fig. 2.2c) only we refer only to edge modes confined one edge, while we note that a chiral edge mode implies the existence of a counterpropagating mode localized at the other edge.

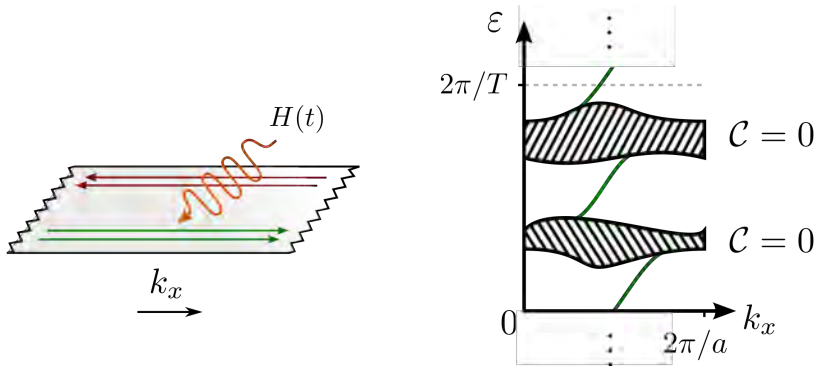

Figure 2.2: Schematic depiction of the configuration of edge modes that signifies the AFAI – an anomalous topological phase. The right panel shows the quasienergy spectrum of the system when confined to strip geometry. In addition to the bulk quasienergy bands, only quasienergies of edge modes confined to the lower edge are shown (green). Adapted from Ref. [4].

localized bulk states is a feature *unique* to periodically driven systems. In nondriven systems, the chiral edge modes implies the existence of bulk energy bands with nonzero Chern numbers. As originally explained by Laughlin (see Ref. [105]), bands with nonzero Chern numbers will always host delocalized states, even in the presence of disorder. The coexistence of chiral edge modes and localized bulk bands described above is the defining feature of an anomalous topological phase[17] known as the Anomalous-Floquet-Anderson Insulator (AFAI) [2]. The AFAI and its generalizations plays a major role in this thesis, and will be the focus of discussion in Chapters 4-7.

To explore the physical properties of the AFAI note that localization of all Floquet eigenstates in the bulk of the AFAI means that any particle initially located in the bulk remains confined near its initial position indefinitely[18]; in this sense, the bulk is fully insulating. At the same time, the persisting chiral edge modes cause particles at the edges move to unidirectionally along the system's edges, while the particles never penetrate into the bulk, due to the localization of Floquet eigenstates here. This situation is first described by Titum *et al* in Ref. [2], and is schematically depicted in Fig. 2.3a (taken from Ref. [2]). Interestingly, Ref. [2] showed that, when all states along one edge of the strip are filled, the chiral edge modes carry a quantized average current of ν/T. Here ν is the micromotion invariant identified in Sec. 2.2.2, which fully determines the topological phase of the system when all bulk Floquet eigenstates are localized[19]. Remarkably, this quantized effect is robust to perturbations, due to the stability of localization

[17] Formally, the AFAI denotes a *family* of topological phases, that are each characterized by a distinct (nonzero) number ν of chiral edge modes that appear in each gap while the bulk bands are trivial [2].

[18] To see this, note that a particle localized at position $\mathbf{r}$ in the bulk only overlaps significantly with nearby, localized Floquet eigenstates $\{|\psi_n\rangle\}$ whose centers are located near $\mathbf{r}$: $|\psi(0)\rangle = \sum_n c_n |\Psi_n\rangle$. Hence, at any integer multiple of the driving period, the state of the system must be a superposition of these localized Floquet eigenstates with the same weights (up to time-dependent phase factors), see Eq. (2.9). Thus, the particle remains confined near $\mathbf{r}$ after each multiple of the driving period. During the driving period, the particle must also remain confined near $\mathbf{r}$, due to the limited duration of the driving period, and the existence of a maximal velocity in the system (the Lieb-Robinson velocity) [106].

[19] See Footnote 17

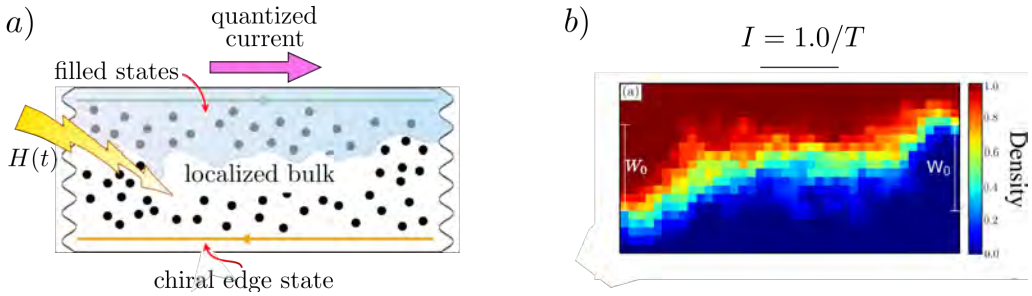

Figure 2.3: a) Schematic depiction of the AFAI phase, from Titum *et al*, Phys. Rev. X **6** 021013 (2016) [2]:. When chiral edge modes coexist with a trivial bulk (as in Fig. 2.2), disorder can localize all bulk Floquet eigenstates, while the chiral modes persist. In this case, a quantized current runs along the edge, once all states near the edge are filled [2]. b) Numerical simulations of possible detectable signatures of the AFAI, adapted from Kundu *et al*, arxiv:1708.05023 (2017) [91]. The figure shows time-averaged density in the system, when two leads are coupled to two opposite ends of the system (indicated by W_0 on the left and right edge), and a large bias is applied between the leads. In this case, a quantized current runs between the two leads [91].

of eigenstates in two dimensions [2].

Note that the effect described above only arises in periodically driven systems. Specifically, the effect relies on the presence of chiral edge modes in a system with a fully-localized bulk coexisting with a fully-localized bulk. If delocalized bulk states are present (as must be the case for a nondriven system with chiral edge modes), particles initially confined to the edges will eventually dissipate into the bulk. In this case, a quantized current will not run along the edges. Thus the novel signatures of the AFAI relies on the coexistence of chiral edge modes and topologically trivial bulk bands, which is only possible to achieve in periodically driven systems.

The novel signatures of the AFAI described above can lead to highly nontrivial experimental effects, such as quantized charge transport: in Ref. [91], it was shown by Kundu *et al* that the delocalized chiral edge modes of the AFAI conduct a quantized current, when two fermionic leads are coupled to opposite edges AFAI (in a rectangular geometry), and a large bias is applied between them. Fig. 2.3b is taken from Ref. [91], and depicts the time-averaged density in the system in such a setting, where $\nu = 1$. The behavior of the system in the simulation is in good agreement with the description of the AFAI phase above (see Fig. 2.4a). The current running between the two leads was found in Ref. [91] to be given by $1/T$, to exponential accuracy.

While the AFAI has so far not been realized in fermionic many-body systems, such as solid-state systems or gases of cold atoms, phenomena analogous to the AFAI have been detected in experiments with photonic crystals [59–61] (see Fig. 2.6). This experimental realization is discussed in more detail in Sec. 2.4.

2.2.4 Model of the AFAI phase

The above discussion established the AFAI as an anomalous topological phase In this subsection, we present a specific model that realizes the AFAI phase. The model was first introduced in Ref. [1],

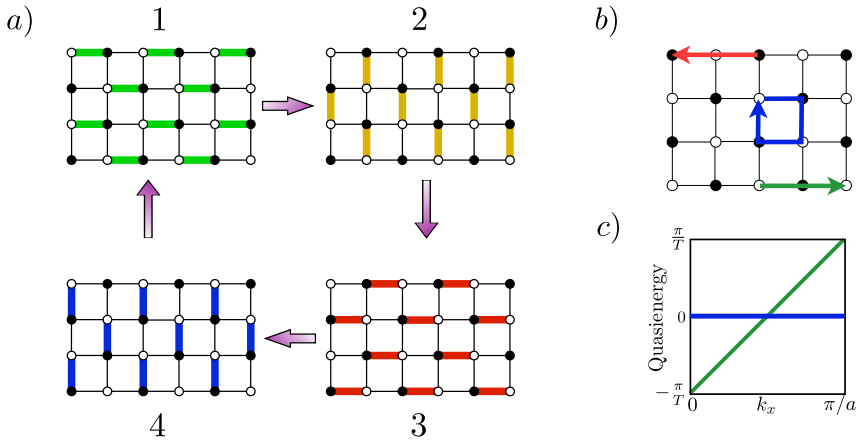

Figure 2.4: Tight-binding model that realizes AFAI phase, adapted from Rudner *et al*, Phys. Rev. X **3**, 031005 (2015) [1]. a) Depiction of the driving protocol introduced in Sec. 2.2.4. b) Depiction of the three qualitatively different trajectories of particles in the model: particles in the bulk (blue) traverse closed loops, while particles at the edge (red and green) are shifted by one unit cell along the edges of the system after one driving period. c) Quasienergy spectrum of the model, in a strip geometry (as a function of crystal momentum along the strip). Blue color indicates the bulk quasienergy bands, while red and green indicate the respective chiral edge modes.

and variants of the model have studied extensively in the literature, e.g., in Refs. [2, 6, 7, 46, 91]. The model we present below will also feature in multiple chapters of this thesis (Chapters 3-7).

The model consists of noninteracting fermions on a two-dimensional bipartite square lattice with lattice constant ℓ, subject to a time-dependent Hamiltonian $H(t)$. The system is periodically driven, implying that the Hamiltonian depends on time in a periodic fashion: $H(t) = H(t+T)$, where T denotes the driving period. The driving period is divided into four segments of equal length $T/4$, such that within the nth segment, $H(t) = H_n$, where

$$H_n = \frac{2\pi}{T} \sum_{\mathbf{r}\in A} (c^\dagger_{\mathbf{r}+\mathbf{a}_n} c_{\mathbf{r}} + c^\dagger_{\mathbf{r}} c_{\mathbf{r}+\mathbf{a}_n}). \tag{2.17}$$

Here $c_{\mathbf{r}}$ annihilates a fermion on the lattice site with coordinate $\mathbf{r}$, and the first sum runs over all sites $\mathbf{r}$ on sublattice A in the bipartite square lattice. Finally, the vectors $\{\mathbf{a}_n\}$ are given by $\mathbf{a}_1 = -\mathbf{a}_3 = (\ell, 0)$ and $\mathbf{a}_2 = -\mathbf{a}_4 = (0, \ell)$. The driving protocol described above thus turns on hopping on every other bond in the lattice, in a clockwise fashion, as depicted in Fig. 2.4a. The amplitude of the Hamiltonian H_n ensures that the time-evolution in the nth segment perfectly transfers a particle on site $\mathbf{r} \in A$ to site $\mathbf{r} + \mathbf{a}_n$, and vice versa. Letting $|\mathbf{r}\rangle$ denote the state $c^\dagger_{\mathbf{r}}|0\rangle$ with a particle on site $\mathbf{r}$ (here $|0\rangle$ denotes the vacuum), we have $e^{-iH_nT/4}|\mathbf{r}\rangle = -i|\mathbf{r} \pm \mathbf{a}_n\rangle$, where the sign depends on whether or not site $\mathbf{r}$ is in sublattice A.

In an infinite geometry, the driving protocol described above results in particles traversing perfect clockwise loops around a single plaquette during each driving period, as indicated by blue in Fig. 2.4b. After each of the four segments, each particle gains a phase factor of $-i$, resulting in

an overall phase factor of 1 after the driving period. We thus conclude that the Floquet operator of the infinite system is given by the identity: $U(T)|\mathbf{r}\rangle = |\mathbf{r}\rangle$. We conclude that any state is a Floquet eigenstate of the system with quasienergy zero; the bulk bands of the system are thus topologically trivial.

To study the topological properties of the model, we confine the system to the geometry of a strip, such that translational invariance along the x-direction is not broken. In this case, the dynamics of particles in the bulk of the strip are unaffected by the presence of the edges. The only case where the edges affects a particle's dynamics is when it initially located on a site in sublattice A on the bottom edge (we ignore the top edge in the following discussion); due to the presence of the edge, this particle will not be able to tunnel during the second or fourth segment (see Fig. 2.4a). In this way, one can verify that a particle initially located on site $\mathbf{r}$ in sublattice A will be shifted by one unit cell along the x-axis after each driving period, as indicated by green in Fig. 2.4b. Since $U(T)$ acts as the translation operator on A-sites on the edge, and acts trivially on all other states, one can verify that the system's quasienergy spectrum (shown in Fig. 2.4c) has a single, linearly dispersing edge mode (green) with fixed group velocity $\frac{\partial \varepsilon}{\partial k} = \frac{1}{T}$ as function of crystal momentum k along the x direction [1]. Sin nce the Floquet operator acts as the identity on all other states, all other quasienergy bands take value 0 (blue), and correspond to trivially localized eigenstawtes. The model thus features a single chiral edge mode, while its bulk bands are fully localized. We thus conclude that the model realizes the AFAI phase.

We note that the localization of the bulk bands for the specific model above arises from fine-tuning the model such that $U(T)$ takes value 1 in the bulk. However, the model above *is* a stable phase once disorder is introduced, e.g., in the form of a constant, random on-site potential. In this case, as was first shown in Ref. [2], the bulk Floquet eigenstates remain localized within a certain range of the disorder strength, while the chiral edge modes persist. The stability of the phase results from the robustness of localization of Floquet eigenstates in the bulk [2].

2.2.5 Symmetry-protected topological phases in driven systems

The discussion in this chapter has so far focused on the topological properties of a driven 2D system in the absence of any symmetries. However, as for nondriven systems (see Secs. 1.3-1.4), the presence of symmetries can lead to the topological protection of additional features in the system. In this section, we briefly discuss how symmetries may protect topological features in periodically driven system. As for the two-dimensional case in Sec. 2.2.3, symmetries may even lead to the topological protection of features which have no equivalent in nondriven systems.

These facts are illustrated by considering the case of a one-dimensional system with (Class D) particle-hole symmetry. The corresponding nondriven case is discussed in Sec. 1.3, and the discussion below proceeds analogously to Sec. 1.3. Particle-hole symmetry implies that the Hamiltonian is purely imaginary in some basis: $H(t) = -H^*(t)$ at any point in time [5, 42]. In this case, one can verify that the Floquet operator is real in the same basis: $U(T) = U(T)^*$. This in turn implies that the Floquet eigenstates of the system come in pairs: if $|\psi\rangle$ is a Floquet eigenstate with quasienergy ε, the complex conjugate[20] $|\psi^*\rangle$ is also a Floquet eigenstate of the system, with quasienergy $-\varepsilon$ (mod $2\pi/T$). Fig. 2.5a schematically depicts the bulk quasienergy

[20]Here, as in Sec. 1.3, the state $|\psi^*\rangle$ is obtained by complex-conjugating the elements of $|\psi\rangle$ in the basis where $H(t) = -H^*(t)$.

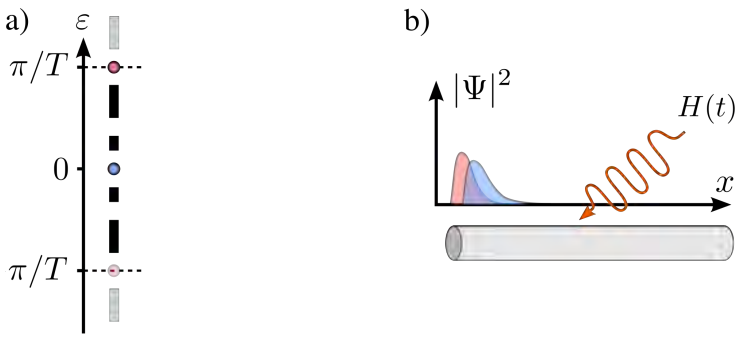

Figure 2.5: a) Quasienergy spectrum of a one-dimensional system of finite extent with particle hole symmetry. Red and blue colors indicates the particle-hole symmetric quasienergies that may support topologically-protected edge modes. Bright colors indicate copies of the quasienergy spectrum in the repeated-zone scheme, such that the quasienergy Brillouin zone is taken to be the interval $(-\pi/T, \pi/T]$. b) Schematic depiction of the system and the two distinct topologically-protected edge modes.

spectrum with this symmetry (black). Analogously to the nondriven case in Sec. 1.3, the Floquet operator of a finite one-dimensional system can have localized eigenstates at the two ends of the one-dimensional system, whose quasienergies lie within the system's bulk quasienergy (Fig. 2.5b). Moreover, it is possible for these localized end states to be their own particle-hole conjugates. In the same way as for nondriven case in Sec. 1.3, the parity of the number of self-conjugate end states in a given gap (on the same end of the system) is a topologically invariant feature of the system.

Importantly, since $-\pi/T \equiv \pi/T \pmod{2\pi/T}$, two distinct quasienergies can support self-conjugate Floquet eigenstates, namely 0, and π/T (indicated by blue red, respectively in Fig. 2.5a). Hence the system can support *two* distinct types of topologically protected edge states, in contrast to the nondriven case, which can only host a single protected edge mode [42]. The topologically-protected self-conjugate edge state at quasienergy π/T (known as a "π-Majorana") is an *anomalous* topological feature: it can only arise in periodically driven systems. The discussion above thus shows that driven particle-hole symmetric systems can support anomalous topological phases. In the same way as for the two-dimensional case in Sec. 2.2.1, π-Majoranas reflect nontrivial topological properties of the bulk system's micromotion [42].

2.2.6 Topological classification of noninteracting, driven systems

The above discussion demonstrates that symmetries can lead to the topological protection of features in driven systems. In the same way as for topological insulators and superconductors [18, 19], recent theoretical work has classified all the topological phases that may be protected by the 10 Altland-Zirnbauer (AZ) symmetry classes in periodically driven systems [78]. This includes particle-hole symmetry [42], the trivial class [1], time-reversal symmetry [107], and chiral symmetry [104]. In each of the cases mentioned above, the symmetry can support anomalous topological features that are associated with the system's micromotion. Ref. [5], introduced

a unified method for classifying the topological properties of a periodically driven system's micromotion. The approach, which is applicable in any symmetry class, gives an *exhaustive* classification of a periodically driven system's topological properties. This approach will be the focus of Chapter 3.

Symmetry classes of periodically driven systems We conclude with a brief discussion of the symmetry classes that may lead to the topological protection of features in periodically driven systems. For nondriven topological insulators, the discussion in Secs. 1.3-1.4 demonstrated that a symmetry S of the Hamiltonian can lead to the protection features of the system's edge spectrum. For analogous features to be topologically-protected in the edge spectrum of a driven system, its effective Hamiltonian H_{eff} must have the same symmetry S. Importantly, this condition is *not* equivalent to the instantaneous Hamiltonian of the system having the symmetry S.

This is illustrated in the case time-reversal symmetry. Time-reversal symmetry is present in a periodically driven system if $H_{\text{eff}} = VH_{\text{eff}}V^{-1}$, where V is some antiunitary operator[21]. One can show that this is achieved when the Hamiltonian $H(t)$ satisfies $H(t) = VH(T-t)V^{-1}$ [5, 107]. Hence, time-reversal symmetry relates the Hamiltonian at time t with its time-reversed conjugate at time $T - t$. More generally, the AZ symmetry classes can be divided into two groups for periodically driven systems [5]: the first group of symmetries are *time-local*, meaning they impose a condition on the instantaneous Hamiltonian, as in the particle-hole symmetric case discussed above. This group includes the particle-hole symmetric and trivial classes[22]. The other group of symmetries, which includes the remaining 7 symmetry classes of the AZ table of symmetries, are *time-nonlocal*: this group of symmetries relates the Hamiltonian at time t with the Hamiltonian at time $T - t$, as in the time-reversal symmetric case above. Importantly, this implies that time-nonlocal symmetry classes can be broken by imperfections of the driving field. Thus, in contrast to the nondriven case where all 10 AZ symmetry classes may remain unbroken in imperfect "real-world" systems, only particle hole-symmetry is generically robust in periodically driven systems.

2.3 Topological phases in driven many-body systems

The discussion in this chapter has so far focused on topological phases in periodically driven systems of noninteracting particles. Sec. 2.2 showed that it is possible to realize topologically nontrivial phases in periodically driven systems in the absence of interactions. The discussion in Sec. 2.2 relied on the many similarities between driven and nondriven systems. In particular, the evolution of periodically driven systems is determined by a conserved quantity (quasienergy) which plays a role analogously to energy in nondriven systems.

While driven and nondriven systems have many similarities in the noninteracting case, interacting driven systems exhibit fundamentally different behavior from their nondriven counterparts. Specifically, whereas isolated, nondriven many-body systems usually approach (nontrivial) thermal equilibrium steady-states, isolated, driven many-body systems almost always absorb energy from

[21] Antiunitary operators are operators on the form $U\mathcal{C}$, where U is a unitary operator and $\mathcal{C}$ is the complex conjugation operator with respect to some basis

[22] These three classes are classes C, D, and A in the Altland-Zirnbauer classification [78].

the driving field, resulting in a continuous and uncontrollable heating process whose fixed point is the trivial infinite-temperature state. Systems that experience this heating effect can therefore not support any phase structure. Importantly, however, there are cases where the heating effect is avoided, and nontrivial topological effects can be realized.

This section describes the above heating effect in detail, and in particular the conditions under which it does not arise. Crucially, Sec. 2.3.2 shows that many-body localized systems are not subject to the heating effect above, and moreover *can* support nontrivial topological phases.

2.3.1 Thermalization in many-body systems

This heating effect described above follows from one of the basic assumptions of statistical mechanics: namely, that large, interacting many-body systems act as thermal reservoirs. Systems with this very generic property are referred to as *thermal*. When a periodic driving field performs work locally on a thermal system, a portion of the energy inevitably dissipates into the surrounding system, which acts as a heat reservoir. In large many-body systems, which effectively follow the laws of thermodynamics, the absorption of energy is irreversible. As a result, thermal systems continuously heat up when subjected to periodic driving, and approach a trivial infinite temperature state [92–94].

To describe the effect in more concrete terms, we consider an observable q that only acts locally on a small subsystem A of a large complicated many-body system. Here q can for example be the local current, charge or spin density somewhere within subsystem A. Given an initial state $|\Psi(0)\rangle$, we are interested in the evolution $\langle q(t)\rangle$ of the observable q's expectation value. The fundamental laws of quantum mechanics imply that $\langle q(t)\rangle$ can be computed as

$$\langle q(t)\rangle = \mathrm{Tr}\Big(|\Psi(t)\rangle\langle\Psi(t)|q\Big), \tag{2.18}$$

where $|\Psi(t)\rangle \equiv U(t)|\Psi(0)\rangle$ denotes the time-evolved state of the system. As a first step, we we split the trace into the traces over degrees of freedom within subsystem A, and within the remaining part of the system, which we denote by B:

$$\mathrm{Tr}(\mathcal{O}) = \mathrm{Tr}_A\left[\mathrm{Tr}_B(\mathcal{O})\right]. \tag{2.19}$$

Here $\mathrm{Tr}_S(\mathcal{O})$ denotes the trace of the operator $\mathcal{O}$ over all degrees of freedom within subsystem S. Since q only acts on the degrees of freedom in subsystem A, we have that $\mathrm{Tr}_B(q\mathcal{O}) = q\mathrm{Tr}_B(\mathcal{O})$. Thus, we find that

$$\langle q(t)\rangle = \mathrm{Tr}_A(\rho_A(t)q), \quad \text{where} \quad \rho_A(t) = \mathrm{Tr}_B|\Psi(t)\rangle\langle\Psi(t)|. \tag{2.20}$$

The operator $\rho_A(t)$, referred to as the *reduced density matrix* within subsystem A, is a density matrix that describes the state of the system within subsystem A.

For subsystem B, which forms the main part of the system, is an extensive, interacting many-body systems. One of the basic assumptions of statistical mechanics is that large and complicated systems, like subsystem B, act as thermal reservoir. In the case where this assumption holds, the system is referred to as *thermal*. In this case, subsystem A can be analyzed as a small system coupled to a large thermal reservoir (subsystem B), with the density matrix ρ_A describing

the state of system A. In this case, the laws of thermodynamics dictate that the state ρ_A of subsystem A relaxes to a thermal equilibrium state ρ_0, after a transient relaxation period τ. The time-scale τ is determined from the parameters of the system, and is referred to as the thermal relaxation time here. The thermal-equilibrium state ρ_0 is the maximum-entropy state, given the conservation laws in the system[23] (a so-called *Gibbs-state*).

Thermalization in nondriven systems

In nondriven fermionic systems, where energy and particle number is conserved, the maximum-entropy state ρ_0 is described by the grand-canonical ensemble. Thus, for $t \gg \tau$, $\rho_A(t)$ takes the form

$$\rho_A(t \gg \tau) \approx \rho_0, \qquad \rho_0 = \lambda\, e^{-\beta H_A - \mu N_A}. \tag{2.21}$$

Here H_A is the Hamiltonian within subsystem A, N_A is the particle number operator within subsystem A, and $\lambda = \mathrm{Tr}_A(e^{-\beta H_A - \mu N_A})$ is a normalizing constant that ensures that $\mathrm{Tr}_A(\rho_A) = 1$. The temperature $1/\beta$ and chemical potential μ are determined from the energy E_0 and particle number N_0 of the system[24]. In this way, the thermal-equilibrium steady state ρ_0 only depends on the initial energy E_0 and particle number N_0 of the system, and thus takes the form

$$\rho_0 = \rho_A(E_0, N_0). \tag{2.22}$$

for some function $\rho_A(E_0, N_0)$ that takes value of a density matrix. Using this result, along with Eqs. (2.20) and (2.21), we thus find

$$\langle q(t \gg \tau)\rangle = f_q(E_0, N_0). \tag{2.23}$$

where the function $f_q(E_0, N_0)$ is given by $\mathrm{Tr}_A(q\,\rho_A(E_0, N_0))$.

Eq. (2.23) shows that the expectation value of the observable q settles to a constant value $f_q(E_0, N_0)$ after a transient relaxation period of duration τ. Importantly, the steady-state value $f_q(E_0, N_0)$ only depends on the initial energy E_0 and particle number N_0 in the system. In thermal systems, any information about the initial state that can be extracted from local observables is therefore lost over time, except for the values of quantities such as energy and particle number which are conserved due to the symmetries of the system. The mechanism described above, known as *thermalization*, is a generic feature of large, interacting many-body systems. Breakdown of thermalization is very rare, and only arises in systems where integrals of motion (i.e. conserved quantities) exist that can be expressed as local observables. A notable example of such a situation are many-body localized systems, which are subject of discussion in Sec. 2.3.2 below.

Thermalization in periodically driven systems

We now apply the above discussion to the case of a periodically driven system. When the system is thermal (i.e. the basic assumptions of statistical mechanics apply), the arguments

[23] Here the entropy S of a state is defined as $S = \mathrm{Tr}(\rho \log \rho)$.

[24] Specifically, β and μ are determined by requiring the expectation values of energy and particle number in the state $\rho(\beta, \mu) \equiv e^{-\beta H - \mu N}/\mathrm{Tr}(e^{-\beta H - \mu N})$ to be given by E_0 and N_0, respectively [108], where N denotes the particle number operator of the full system. Since energy and particle number are conserved quantities, E_0 and N_0 can be found from the initial state of the system $|\Psi(0)\rangle$.

below Eq. (2.20) show that the state of the system within subsystem A relaxes to a steady state ρ_0 which maximizes the entropy, given the conservation laws in the system. The breaking of continuous time-translation symmetry to discrete time-translation symmetry means that quasienergy ε, rather than energy E, is conserved. Thus, unless any other symmetry is present, the only conserved quantities in the system are quasienergy and particle number. Retracing the subsequent arguments that lead to Eq. (2.23) in the nondriven case, we find that the expectation value $\langle q(t)\rangle$ settles to a constant value $f_q(\varepsilon_0, N_0)$, which only depends on the initial quasienergy ε_0 and particle number N_0 of the system:

$$\langle q(t \gg \tau)\rangle = f_q(\varepsilon_0, N_0). \tag{2.24}$$

Here ε_0 and N_0 respectively denote the quasienergy and number of particles in the system in the state $|\Psi(0)\rangle$ (these are conserved quantities).

Due to the periodic nature of quasienergy, the function $f_q(\varepsilon, N)$ must be periodic in its first argument: $f_q(\varepsilon, N) = f_q(\varepsilon + 2\pi/T, N)$. At the same time, an initial small perturbation of the system somewhere far away from region A may change the initial quasienergy system by an amount comparable to $2\pi/T$[25]. In this way, any quasienergy in the interval $[0, 2\pi/T]$ can be reached by weakly perturbing the system far away from subsystem A. Since the steady-state value of $\langle q(t)\rangle$ should not be significantly affected by such perturbations, we conclude that $f_q(\varepsilon, N)$ must be constant as a function of ε: $f_q(\varepsilon, N) = f_q(N)$. Hence, steady-state value of $\langle q(t)\rangle$ only depends on the number of particles N_0:

$$\langle q(t \gg \tau)\rangle = f_q(N_0). \tag{2.25}$$

As a next step, consider the projector I_k into the sector with k particles. Since particle number is conserved, the time-evolution operator $U(t)$ commutes with I_k. This implies that the state $\rho_k \equiv I_k/\mathrm{Tr}(I_k)$ is always a steady state of the system. Specifically, $\rho_k(t) = \rho_k$, where $\rho_k(t) \equiv U(t)\rho_k U^\dagger(t)$ denotes the time-evolution of the (mixed) state described by ρ_k. The above discussion shows that the expectation value $\langle q(t)\rangle_k \equiv \mathrm{Tr}(\rho_k(t)q)$ remains constant in time when the system is initialized in the state ρ_k, and is given by

$$\langle q(t)\rangle_k = \mathrm{Tr}(\rho_k q). \tag{2.26}$$

Since Eq. (2.25) holds given *any* initial state of the system, it must in particular hold if the system is initialized in the state[26] ρ_k. We conclude that $f_q(N_0) = \mathrm{Tr}(\rho_{N_0} q)$. Noting that ρ_{N_0} projects into the subspace with N_0 particles (up to a normalization factor), we finally obtain

$$\langle q(t \gg \tau)\rangle = \mathrm{Tr}_{N_0}(q), \tag{2.27}$$

where $\mathrm{Tr}_{N_0}(\mathcal{O})$ denotes the trace of the operator $\mathcal{O}$ within the subspace with N_0 particles. Thus, for thermalizing, driven systems, any local observable q settles to the same fixed value $\mathrm{Tr}_{N_0}(q)$, regardless of the Hamiltonian or the initial state of the system. This situation is identical to the

[25]This can for instance be shown using the extended Hilbert space formalism, see, e.g., Ref. [1].

[26]The discussion in Sec. 2.3.1 assumed for clarity the system to be in a pure state, but it generalizes straightforwardly to the case where the system is in a mixed state.

infinite-temperature limit of nondriven equilibrium systems. Physically, the infinite-temperature steady-state results from the irreversible absorption of energy from the driving field which was described in the beginning of this section. The absorption of energy from the drive leads to a continuous heating process in the system, whose fixed point is the trivial infinite-temperature state.

The discussion above shows that, after a transient relaxation period τ, it is not possible to extract *any* information from local observables in a thermalizing, periodically driven system[27]. This in particular includes information about the Hamiltonian of the system: it is formally impossible to distinguish the Hamiltonians of thermalizing, periodically driven systems from each other, using physical (local) observables. Thus, thermalizing periodically driven systems cannot support any nontrivial phase structure. Physically, this fact results from the irreversible heating induced by the driving field that was described in the beginning of this section. This uncontrollable heating effect means that all thermal periodically driven systems have the same, trivial, infinite-temperature steady state.

2.3.2 Strategies to counter the heating problem

The above discussion shows that all thermal, periodically driven systems eventually reach a featureless, trivial, infinite-temperature steady-state, which cannot support any non-trivial phase structure; in fact, it is impossible to distinguish any feature of the system's Hamiltonian in the steady state. However, as mentioned in the beginning of this section, there *are* ways to prevent (or postpone) the heating effect described above, thus allowing for nontrivial topological effects to be realized in periodically driven many-body systems. This section discusses three of main approaches which are currently being studied.

Many-body localization The first approach, which forms the basis of Chapters 5-6 in this thesis, is to prevent the system from thermalizing, through many-body localization. The heating effect discussed in Sec. 2.3.1 was a consequence of thermalization, and a breakdown of thermalization allows the system to avoid the heating effect described in Sec. 2.3.1 [109]. Many-body localization arises when strong disorder localizes the many-body eigenstates of a system's Hamiltonian or Floquet operator, in mechanism analogous to Anderson localization of single-particle eigenstates [110, 111]. In this case, a complete set of local conserved quantities emerges, and the basic assumptions of statistical mechanics are violated [112], leading to a breakdown of thermalization. Physically, the breakdown of thermalization results from the vanishing heat conductance in many-body localized systems, which prevents the system from acting as a thermal reservoir. The breakdown of thermalization allows many-body localized periodically driven systems to avoid the heating effect described in Sec. 2.3.1.

While the bulk quasienergy bands of many-body localized systems are necessarily topologically trivial, periodically driven systems are characterized by an additional topological invariant that characterizes the dynamics of the system that take place within each driving period. The existence of the micromotion invariant thus allows driven, many-body localized systems to support nontrivial topological phases (see Sec. 2.2.2). There are several examples of nontrivial topological phases

[27] Other than the number of particles and other quantities conserved by the system's symmetries.

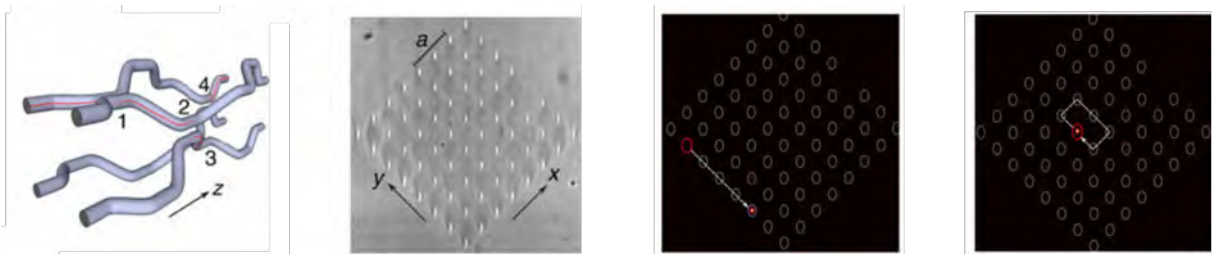

Figure 2.6: Realization of the AFAI phase in a photonic crystal. From Mukherjee *et al*, Nature Communications **8**, 13918 (2017) [60]. a) Schematic depiction of the photonic crystal's structure. b) White-light transmission micrograph of a xy facet of the photonic crystal. c) Emitted signal in the case where light enters the crystal on the edge (red circle). d) Emitted signal when in the case where light enters the crystal on the bulk (red circle). Note the similarity between panels c) and d) and Fig. 2.4b.

that arise in driven many-body localized systems [7, 45–47, 49, 50, 56]: notable examples include the Floquet time crystal [49, 50], and the Anomalous Floquet Insulator [7] (AFI), which can be seen as the interacting version of the AFAI phase discussed in Secs. 2.2.3-2.2.4. Verifying the picture above, these phases are all characterized by topologically nontrivial micromotion, and are thus of intrinsically non-equilibrium nature.

Stabilization of steady state with external baths Another approach to counter the heating from the driving field is to couple the system to an external bath, such as a phonon reservoir in a solid-state system. This approach has for instance been explored in Refs. [95, 96]. The presence of the external baths allows heat to escape from the system, thus preventing the system from heating to infinite temperature [95]. Appropriate couplings to external baths can stabilize steady states of driven systems which have topologically nontrivial features [96].

Prethermal phases A final approach to avoid the issue of heating in driven many-body systems is to realize topological effects in the transient (prethermal) dynamics of the system. Specifically, while a driven system may eventually heat up to a trivial infinite-temperature state, the thermal relaxation time τ, which sets the time-scale τ at which the heating becomes significant (see Eq. (2.27)), can be very long. For instance, in rapidly driven systems, the thermal relaxation time is exponentially large in driving frequency [113]. In strongly disordered systems, heating effects can be so slow that they can be ignored in any experimentally-relevant time scale [7]. Importantly, before the heating becomes significant, the system can reach prethermal (i.e., transient) steady which which for all purposes resemble a phase [114–116]. These prethermal steady states may have topologically non-trivial properties such as quantized average current [62].

2.4 Experimental realizations

We conclude this introductory chapter with a brief review of possible experimental realizations of topological phases in periodically driven systems that are currently proposed.

Solid state realizations Topological phases in periodically driven systems have originally been imagined in the setting of solid-state systems [21, 23, 24]. Notable proposals for realizing topological effects in these systems include inducing a topologically nontrivial quasienergy by irradiating graphene with circularly polarized light [21], or creating topological band inversion in a periodically driven semiconductor [24]. Current challenges with these experimental proposals arise from the high frequencies and intensities necessary to induce significant topological effects, while at the same time minimizing heat absorption.

In the setting of solid-state systems, the crystal-momentum dependent quasienergy bands that were the focus of discussion in Sec. 2.2.1 have been experimentally observed in Ref. [38]. Specifically, the experiment detected significant effects from periodic driving in the surface excitation spectrum of Bi_2Se_3, when irradiated by strong laser fields. The competing requirements of high intensity and low heat absorption were reconciled by irradiating the system with short (picosecond) intensive pulses of circularly polarized light. The excitation spectrum of the system were probed as a function of time, at a time-resolution finer than the pulses, using time- and angle resolved photoemission spectroscopy (TrARPES).

Cold atoms Gases of ultracold atoms in optical lattice is perhaps the most promising platform for realizing topological phases in periodically driven systems. The high degree of control in these systems allows for realization of many proposed models and driving protocols with current techniques. Periodic driving has for instance been used to realize the Haldane model (an example of a Chern insulator) in a gas of cold atoms [41]. In this experiment, periodic modulation of the optical lattice was used to generate an effective Hamiltonian H_{eff} with topologically nontrivial properties[28]. Concrete experimental protocols have also been proposed for realizing the AFAI phase in gases of cold atoms [53].

Photonic crystals Photonic crystals offer another platform for realizing topological phases in periodically driven systems. Photonic crystals are three-dimensional nanostructures engineered to control the motion of light that passes through the structure. While these systems cannot be characterized as many-body systems, they may support topological effects analogous to the topological phases discussed in this chapter.

Specifically, as light traverses these photonic crystals in the z direction, the evolution of electromagnetic waves in the xy plane is equivalent to that of fermionic wave functions in a two dimensional lattice model, such that slices of the photonic crystal at different values of z correspond to different points in time [59, 82, 83, 85]. Appropriate engineering the photonic crystals can result in dynamics of light analogous to static or time-dependent Hamiltonians. The effects of periodic driving are incorporated by making the properties of the crystal vary periodically along the z-direction.

[28] See Eq. (2.10) for a definition of the effective Hamiltonian.

Several experimental groups [60, 61] have constructed photonic crystals that "realize" the AFAI phase in the way described above. Figure 2.6 shows experimental data from Mukherjee *et al* published in Ref. [60]: Fig. 2.6a schematically depicts the structure of the waveguides in the photonic crystal, which "replicate" the AFAI model introduced in Sec. 2.2.4 (see Fig. 2.4). Fig. 2.6b shows a microscopic image (white-light transmission micrograph) of a xy facet of the photonic crystal. Fig. 2.6c,d show the initial location in the xy plane where light enters (red), analogous to the initial location of the fermionic wave function, along with the emitted signal (yellow), analogous to the final wave function of the fermions after one driving period. Fig. 2.6c shows these data in the case where the light enters the crystal at the xy-plane's edge, while Fig. 2.6c show the data in the case where light enters the crystal in the middle of the xy plane. The emitted signals in Fig. 2.6cd are consistent with the insulating bulk and chiral edge modes that are characteristic of the AFAI model in Sec. 2.2.4. Note the close similarity between the experimental data in Fig. 2.6cd and the predicted dynamics of the AFAI model in Fig. 2.6b. This photonic-crystal realization of the AFAI has been explored as a possible platform for loss-free or unidirectional propagation of light [85].

Optics A final experimental platform mentioned here is optical systems: for instance, Refs. [3,57] explore ideas where the degrees of freedom of light in an optical cavity, such as, e.g., orbital angular momentum, are be used as analogues for lattice degrees of freedom. Effects analogous to periodic driving can be realized with a succession of optical components that the light traverses in a cavity. In this way, experiments have detected topologically nontrivial signatures in the orbital angular moment of light, analogous to the chirally-symmetric topological phases driven systems [57].

2.5 Discussion

This chapter introduced the subject of topological phases in periodically driven systems. This Chapter, together with Chapter 1, serves as an introductory chapter, and hopefully gives the sufficient background for reading the rest of this thesis.

After reviewing the theory of periodically driven quantum systems, the discussion in Sec. 2.2 demonstrated that periodically driven systems may support topological phases of matter. In fact, as Secs. 2.2.2-2.2.5 showed, periodically driven systems support a richer variety of topological phases than their nondriven counterparts. The richer structure arises from the existence of a micromotion invariant which characterizes the dynamics of the system that take place within a driving period. The following two Chapters (Chapter 3-4) explore the nature of this micromotion invariant in further detail.

The existence of the micromotion invariant gives rise to new, so-called *anomalous* topological phases can arise in driven systems. These intrinsically non-equilibrium phases are characterized by nontrivial topological properties of the particles' motion, and have no equivalents in nondriven systems. An example of such an anomalous phase is the Anomalous Floquet-Anderson Insulator (AFAI) which arises in two-dimensional systems and supports quantized charge transport on its edges of a fully insulating bulk. Chapters 4-6 explores the nature of this phase, and its generalizations in further detail.

The discussion in Sec. 2.3 demonstrated that periodically driven many-systems typically heat up in an uncontrolled process, due to the absorption of heat from the driving field. However, as Sec. 2.3.2 discussed, there are several strategies to avoid this effect and realize nontrivial topological phases in driven many-body systems. Notably, many-body localized systems are not subject to the heating process described in Sec. 2.3.1. Crucially, and perhaps surprisingly, such many-body localized systems can support nontrivial topological phases. Notable examples of such phases include the Floquet time crystal [49, 50, 52], and the anomalous Floquet insulator [7], which is the interacting version of the AFAI introduced in Sec. 2.2.3. Chapters 5-6 explore the anomalous Floquet insulator in more detail.

Chapter 3

Topological Classification of Floquet-Bloch Systems

The contents of this chapter forms a part of an article published in New Journal of Physics **17**, *125014 (2015) by FN and Mark S. Rudner. The article is cited as Ref. [5] in this thesis.*

The discussion in Chapter 2 shows that periodically driven systems can have topologically-protected properties which have no equivalent in nondriven systems. These anomalous topological features, which include anomalous edge states (Sec. 2.2.1), and π-Majoranas (Sec. 2.2.5), may lead to effects with no equivalent in nondriven systems, such as quantized charge transport on edges of insulating systems [2]. The discussion in Sec. 2.2.2 shows that the new anomalous topological features are encoded in the bulk system's micromotion (i.e., the dynamics in the bulk that take place within a driving period). In particular, in addition to the Chern numbers that characterize of quasienergy bands of two-dimensional driven systems, an additional *micromotion invariant* ν characterizes the systems' micromotion. The existence of the micromotion invariant means that periodically driven systems have a richer topological structure than their nondriven counterparts.

This chapter introduces an an intuitive method for classifying the topological properties of micromotion in periodically-driven systems. A main result of the chapter is that micromotion invariants manifest themselves as topologically-protected nodal points in the bulk time-evolution operator's spectrum (see Fig. 3.1). The method developed in this chapter leads to an *exhaustive* classification of the topological phases in (noninteracting) periodically driven systems, given any symmetry class. While this chapter studies the case of a two-dimensional system in the absence of any symmetry, several other symmetry classes are considered in Ref. [5], which forms the basis of this chapter.

3.1 Introduction

After the discovery [14, 117] and explanation [15, 69, 70, 118, 119] of the quantized Hall effects, topology gained new importance as a mechanism for generating extremely robust quantum mechanical phenomena. The realization that the Bloch bands of solid state systems could

possess non-trivial topological characteristics led to the prediction [11, 17, 120] and experimental discovery [121, 122] of whole new classes of materials [123, 124] – the topological insulators and superconductors – which host a variety of remarkable and potentially useful phenomena. On a theoretical level, a complete topological classification [18, 19] of such systems has been developed, predicting a number of new phases. However, finding materials that realize these phases remains a very challenging task, with no known examples for many topological classes.

Motivated by the great successes and open challenges in the arena of topological matter, many authors have begun to explore the possibilities for realizing topological phenomena in *driven* quantum systems [20–32, 42, 95, 101, 104, 125–135]. Time-dependent driving offers the opportunity to control a material's properties in a variety of new ways, potentially opening new routes for studying topological phenomena in solid state [38], atomic [41, 42, 136], and optical systems [59, 137].

Intriguingly, driven systems may host an even richer array of topological phenomena than their non-driven counterparts. To date several examples of topological phenomena which can *only* be realized in driven systems have been found [1, 23, 42, 104, 107], such as the existence of robust chiral edge states in two dimensional systems whose Floquet bands have trivial Chern indices [1], and pairs of non-degenerate Majorana end modes with protected quasienergy splittings in one-dimensional systems [42]. This indicates that periodically driven systems feature additional topological structure beyond that found in non-driven systems. However, a unifying principle for understanding and classifying these new phenomena remains lacking.

In this work we answer the question: under what conditions does the evolution of a driven system become topologically distinct from that of a non-driven system? In doing so we develop a powerful and general framework that can be used to understand the topology of periodically driven systems.

In the analysis of periodically driven systems, the *Floquet operator*, denoted $U(T)$, plays a central role as the stroboscopic evolution operator that propagates the system forward in time through each complete driving period, T. The spectrum of the Floquet operator, given by $U(T)|\Psi_n\rangle = e^{-i\varepsilon_n T}|\Psi_n\rangle$, plays an analogous role to the spectrum of the Hamiltonian in a non-driven system, with real-valued energies replaced by periodically-defined *quasienergies*, $\epsilon_n + 2\pi N/T = \epsilon_n$ for any integer N. For a system on a lattice, the single particle spectrum forms bands, the so-called Floquet bands. Throughout this work we focus on systems defined on a lattice, with a finite number of bands. While knowledge of the Floquet bands is sufficient to understand many aspects of the dynamics of a driven system, it was recently shown that the topological properties of the evolution are in particular *not* described by $U(T)$ alone [1]. A proper description of the topology of driven systems must take into account the full evolution $U(t)$ for times t throughout the entire driving period, $0 \leq t \leq T$.

As a means of elucidating the nature of the evolution $U(t)$, we focus on the "phase bands" of the system, i.e., the time-dependent spectrum of the system's evolution operator throughout one driving period. As depicted in Fig. 3.1, for each time t in the interval $0 \leq t \leq T$, the eigenvalues $\{e^{i\phi(\mathbf{k},t)}\}$ of the Bloch evolution operator $U(\mathbf{k}, t)$ form bands as a function of the crystal momentum $\mathbf{k}$. For illustration we use a "repeated zone" representation for the phase bands, though the complete spectrum is contained within a single phase Brillouin zone of width 2π, as indicated by the shaded region in Fig. 3.1d. As a function of time, these phase bands form sheets which, along with the corresponding eigenvectors, contain full information about the

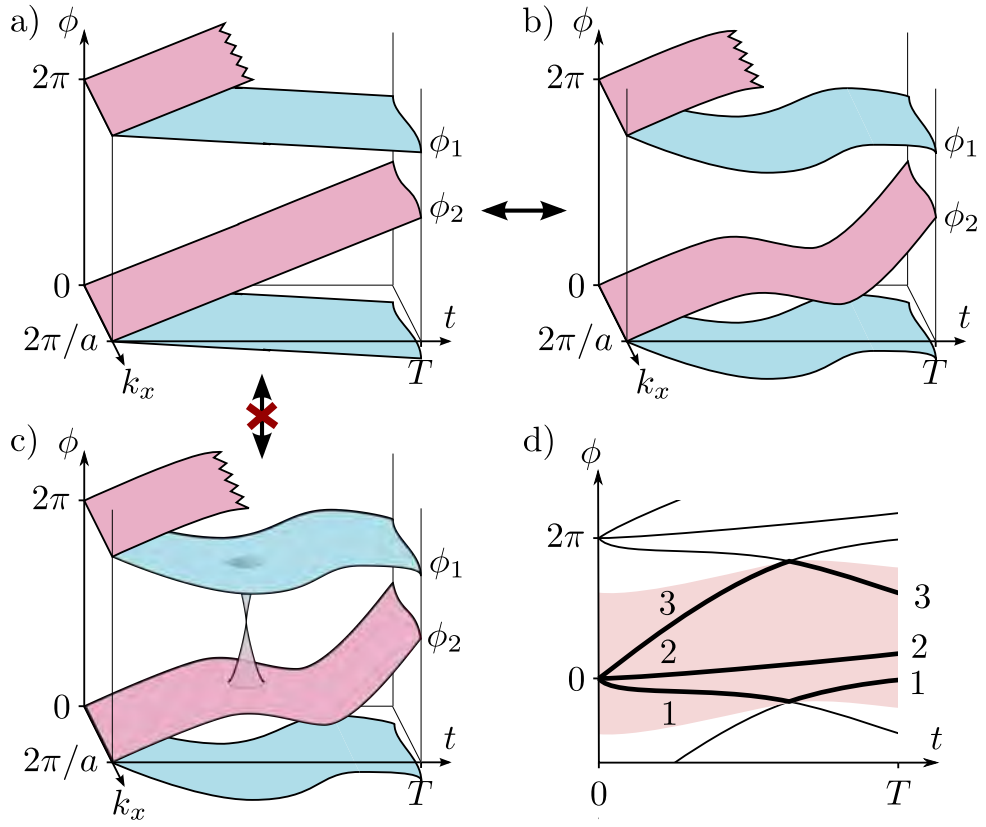

Figure 3.1: Phase band representation of the evolution operator $U(\mathbf{k}, t)$, Eq. (3.1). a) For a non-driven system, the phase eigenvalues grow linearly in time. b) Here we show phase bands of a periodically driven system which are non-degenerate for all $\mathbf{k}$ and t. The evolution can be smoothly deformed into one obtainable in a non-driven system without closing any quasienergy gaps. c) In this case the evolution operator features non-removable degeneracies which prevent such a deformation. The evolution is therefore topologically distinct from that of any non-driven system. d) Illustration of the phase band labeling scheme defined in Sec. 3.2. The shaded region indicates the "phase Brillouin zone."

evolution of the system.

Below we examine smooth deformations of the phase bands which, keeping the Floquet operator $U(T)$ fixed, determine when a given system's evolution can be smoothly deformed into one obtainable in a non-driven system. At time $t = 0$ the evolution is the identity. Therefore all phase bands must originate with phases ϕ which are integer multiples of 2π. For a non-driven system with Hamiltonian H, the evolution operator is given by $U(t) = e^{-iHt}$. In this case the phase bands diverge from one another *linearly* in time due to the linear phase winding $\phi = Et$ for each eigenstate of H with energy E (see Fig. 3.1a). For the case of a driven system as shown in Fig. 3.1b, the phase bands can be straightened through a continuous deformation, such that the evolution becomes indistinguishable from one generated by a time-independent Hamiltonian. Crucially, as we show below, phase bands may be connected via topologically-protected degeneracies, or "topological singularities" (Fig. 3.1c), which *prevent* the evolution from being deformed into the canonical form for a non-driven system. These singularities play a central role in defining the topology of periodically driven systems.

After establishing the existence of topological singularities in the bulk evolution, we study their ramifications for the edge mode spectrum of $U(T)$ for a two-dimensional system defined in a geometry with edges. If such a system may host genuine topologically-protected chiral edge modes, then by definition the net number of modes in each bulk gap may not change under smooth deformations of the evolution that keep the bulk gaps open. Focusing first on the bulk evolution, we then identify a complete set of independent topological quantities which are (by definition) invariant under any smooth deformation of the bulk evolution that preserves the Floquet operator $U(\mathbf{k}, T)$. Since we have identified above a *complete* set of quantities that are invariant under such deformations, we conclude that the net number of topologically-protected chiral edge modes in a given gap must be given by some function of these invariant bulk quantities. Standard spectral flow arguments that relate features of the bulk and edge spectra [119, 138, 139] let us determine the form of this function, thereby demonstrating the existence and form of the bulk-edge correspondence in terms of the bulk invariants that we found [see Eq. (3.10) below].

Ref. [5] (in which this chapter is included) shows how the method can be extended to systems in arbitrary dimensions, also including the role of symmetries, thus providing means for a complete topological classification of Floquet-Bloch systems. Ref. [5] that symmetries considered previously, e.g. in Refs. [42, 107], which generalize the Altland-Zirnbauer symmetry classes to the case of periodically driven systems, can be naturally incorporated into the phase-band picture. Importantly, Ref. [5] find that these symmetries can protect new types of topological singularities in the bulk.

In general we find that, for each bulk gap, the edge mode spectrum of a driven system in a given symmetry class has the same set of protected features as that of a non-driven system in the corresponding class. However, the *global* edge mode spectrum and the relation between edge modes and bulk bands can be quite different. Examples of such new or "anomalous" edge phenomena include Floquet-Majorana edge modes [42, 140] with quasi-energy π/T and chiral edge modes [1] in a 2D system with topologically trivial bulk Floquet bands. Here we also show that periodic driving, for example, allows *two-band* systems with time-reversal symmetry to have helical edge modes, while a minimum of four bands is required in the non-driven case.

Interestingly, we find that all the above phenomena are closely connected with the appearance of topological singularities in the bulk evolution. Due to the additional freedom presented by

time-dependence, we further speculate that there may be other new types of symmetry conditions (beyond those familiar from non-driven systems) which can protect new types of topological singularities and anomalous edge mode phenomena.

The remainder of the chapter is structured as follows. In Sec. 3.2 we formalize the description of phase bands, and characterize the singularities which may prevent them from being deformed into a trivial configuration. Then in Sec. 3.3 we cast the topological characterization of two-dimensional systems (without symmetries) in terms of the phase bands and their singularities, giving new insight into the winding number invariants found previously in Ref. [1]. Ref. [5] shows how additional symmetries (e.g., time reversal or particle-hole symmetry) can be naturally incorporated into this picture through their abilities to protect new types of singularities. Finally, in Sec. 3.4 we summarize our results and discuss the outlook for future work. Technical aspects of derivations are provided in appendices.

3.2 Phase bands of the evolution operator

We now study the question of when the evolution of a periodically-driven Floquet-Bloch system can be considered topologically distinct from that of a non-driven system. In order to do this, we begin by defining the phase band picture of Floquet-Bloch evolution. In this section we focus on "bulk" systems with discrete translation symmetry (with infinite extent or periodic boundary conditions). Here, the crystal momentum $\mathbf{k}$ is a good quantum number. For now we leave the number of spatial dimensions arbitrary.

The evolution of a periodically-driven quantum system may equivalently be prescribed in terms of either a Hamiltonian $H(t+T) = H(t)$, where T is the driving period, or by the corresponding evolution operator $U(t) = \mathcal{T} e^{-i\int_0^t H(t')dt'}$, where $\mathcal{T}$ denotes time ordering. In this chapter we primarily work directly with the evolution operator $U(t)$, which most clearly exposes the topological features of the evolution. Importantly, although the Hamiltonian satisfies $H(t+T) = H(t)$, the evolution operator $U(t)$ is generally *not* periodic in time.

For bulk systems, crystal momentum $\mathbf{k}$ and time t parametrize a family of Bloch evolution operators $U(\mathbf{k}, t)$, which act within the space of periodic Bloch functions. When the time-dependent Hamiltonian is local and bounded, $U(\mathbf{k}, t)$ is continuous in crystal momentum and time.

As an important first step in our analysis, we express $U(\mathbf{k}, t)$ in terms of its spectral decomposition

$$U(\mathbf{k}, t) = \sum_{n=1}^{N} P_n(\mathbf{k}, t) e^{-i\phi_n(\mathbf{k},t)}, \tag{3.1}$$

where $P_n(\mathbf{k}, t)$ is the projector onto the n-th eigenstate of $U(\mathbf{k}, t)$ and $e^{-i\phi_n(\mathbf{k},t)}$ is the corresponding eigenvalue. Here N is the number of bands in the system.

We refer to the functions $\{\phi_n(\mathbf{k}, t)\}$ as the *phase bands* of the system. In contrast to the quasienergy bands associated with a driven system's Floquet operator $U(\mathbf{k}, T)$, the phase bands depend on time, and are continuously defined *throughout an entire driving cycle*, $0 \leq t \leq T$. At time $t = T$, the phase bands coincide with the system's Floquet bands. An illustration of phase bands for a one-dimensional system with two bands is shown in Fig. 3.1.

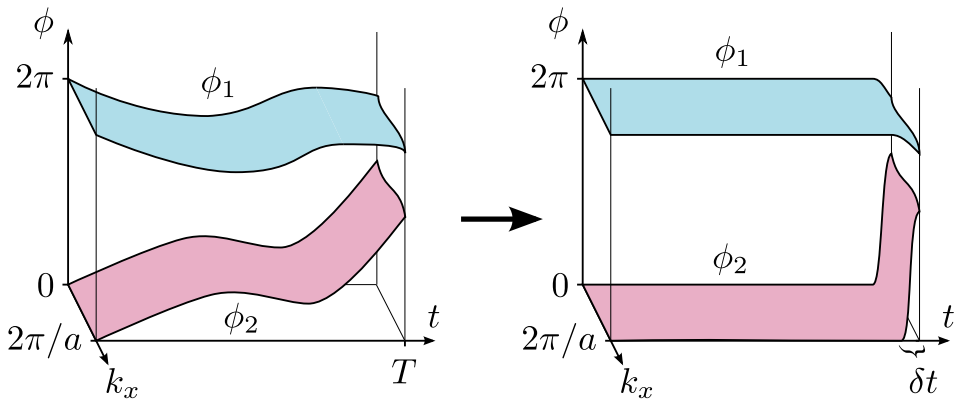

Figure 3.2: Graphical depiction of the deformation described in Sec. 3.2, where the time-evolution operator of a periodically driven system is deformed into the time-evolution operator of a non-driven system. This deformation is always possible if the time-evolution operator has no degeneracies. After flattening, the linear ramp region is expanded to the entire interval $0 < t < T$, and the bands are straightened into a form as in Fig. 3.1a.

To resolve the ambiguity of the labeling of eigenstates of $U(\mathbf{k}, t)$ we now define a prescription for assigning the values of the n indices. We focus on the phase bands $\{\phi_n(\mathbf{k}, t)\}$, and work in a repeated zone representation where the spectrum is copied and shifted through all integer multiples of 2π. Recalling that $U(\mathbf{k}, 0) = \mathbf{1}$, each phase eigenvalue must start from an integer multiple of 2π. However, as mentioned above, the full spectrum $\{e^{-i\phi_n(\mathbf{k},t)}\}$ of $U(\mathbf{k}, t)$ is contained within one "phase Brillouin zone."

While in principle we could choose $\phi_n(\mathbf{k}, 0)$ to be equal to any integer multiple of 2π, we choose to work in a fundamental phase Brillouin zone in which all phases originate from zero, i.e., $\phi_n(\mathbf{k}, 0) = 0$, for $n = 1 \dots N$ (see bold curves in Fig. 3.1d). Next, we demand that each $\phi_n(\mathbf{k}, t)$ is a real-valued continuous function[1] of both $\mathbf{k}$ and t. Finally, we impose an ordering condition: if $\phi_n(\mathbf{k}, t) \geq \phi_m(\mathbf{k}, t)$ for one point in $\mathbf{k}, t$-space, then this relation must hold for all $\mathbf{k}$, t. By ordering the indices such that $n > m$ implies $\phi_n \geq \phi_m$, this prescription defines a unique labeling of the phase bands.

The ordering condition above is constructed such that if two phase bands become degenerate at a particular value of $\mathbf{k}, t$, the bands do not "cross" (e.g., the index m stays with the lower branch everywhere, while the index n stays with the upper branch). This arrangement is in particular maintained when a band in the fundamental zone meets a band originating from a different zone, see for example band #3 in Fig. 3.1d. Such degeneracies between phase bands associated with different branches play an essential role in defining the topological characteristics that distinguish driven and non-driven systems.

We now use the phase band picture to demonstrate when it is possible to continuously deform the evolution of a Floquet-Bloch system into that of a non-driven system, while keeping $U(\mathbf{k}, T)$

[1]Since the "phases" ϕ_n are treated as real-valued continuous functions in the repeated zone scheme, their absolute values may exceed 2π. However, the labeling scheme guarantees that the full set of phase bands, in particular the Floquet bands $\epsilon_n = \phi(\mathbf{k}, T)/T$, are always grouped within a window of at most 2π.

fixed. Naively, the continuity of $U(\mathbf{k},t)$ and of the phase bands might lead one to expect that the projectors $P_n(\mathbf{k},t)$ are continuous as well. If this were true, any continuous deformation of the phase bands $\phi_n(\mathbf{k},t)$ would preserve the continuity of the evolution operator. It would then always be possible to deform the evolution into that of a non-driven system using a two-step "band-flattening" procedure (see Fig. 3.2). First, for every $n = 1 \dots N$, deform $\phi_n(\mathbf{k},t)$ to zero for all $0 \leq t \leq T - \delta t$ until a small time-interval δt before T, after which it grows linearly to its final value. If the interval δt is small enough, we can assume that the projectors are constant there, $P_n(\mathbf{k},t) = P_n(\mathbf{k},T)$. In the second step, let $\delta t \to T$, while keeping the projectors constant throughout the linear ramp of the phase. The deformed evolution is now identical to that of a non-driven system with the Hamiltonian

$$h(\mathbf{k}) = \frac{1}{T}\sum_n \phi_n(\mathbf{k},T)P_n(\mathbf{k},T). \tag{3.2}$$

The picture above seems to imply that all periodically-driven systems are topologically equivalent to non-driven systems (i.e., they can be related by smooth deformations that keep the Floquet operator fixed). However, the existence of phenomena such as anomalous edge modes [1, 23] shows that this *cannot* be the case.

Where could the argument break down? In the first step, we assumed that the phase bands could be continuously deformed to zero throughout the entire driving period, up to a short interval δt in which the projectors were assumed to be constant. However, in principle one may imagine that the evolution operator could host degeneracies around which the projectors are *discontinuous* (the degeneracy of the eigenvalues ensures that U stays continuous). In the presence of such a discontinuity, the degeneracy could not be lifted without breaking the continuity of U. In this way a phase band in the fundamental zone may become "glued" to another band from a neighboring branch of phases (see Fig. 3.1c).

In the absence of the discontinuities described above, the evolution of any driven system can be smoothly deformed to that of a non-driven system, as in Fig. 3.2, and anomalous edge states would be impossible. Thus we are led to the unavoidable conclusion that the evolution operators of periodically driven systems must support topologically-protected degeneracies. In the next subsection we show explicitly that such degeneracies can exist in two-dimensional (2D) systems. Ref. [5] generalizes these ideas to other dimensions and symmetry classes. Below we refer to these topologically-protected degeneracies as "topological singularities."

3.2.1 Topological singularities in two-dimensional systems

In this subsection we explicitly demonstrate the existence and nature of topological singularities in the evolution operators of two-dimensional systems. We furthermore show that in a region in $\mathbf{k},t$-space where $U(\mathbf{k},t)$ is degenerate, the degeneracy can either be lifted everywhere or reduced to a cluster of isolated singularities.

Let $U(\mathbf{k},t)$ be the bulk time evolution operator of a two-dimensional system with no symmetries other than the discrete translational symmetry of the lattice. Consider now a point $\mathbf{s}_0 = (\mathbf{k}_0, t_0)$ in $\mathbf{k},t$-space where two adjacent phase bands, m and m', are degenerate (mod 2π). At $\mathbf{s}_0$, the degenerate subspace is spanned by the Bloch states $|\psi_m\rangle$ and $|\psi_{m'}\rangle$. Due to the continuity of $U(\mathbf{k},t)$ and the existence of gaps to other phase bands, we can assume that the subspace spanned

by the two intersecting bands is constant within some finite sized neighborhood around $\mathbf{s}_0$ in $\mathbf{k}, t$-space. The remaining non-degenerate bands $\{|\chi_n\rangle\}$ and their associated phases $\{\phi_n\}$ can also be assumed to be constant within this neighborhood. Close to $\mathbf{s}_0$, the time evolution operator thus takes the form

$$U(\mathbf{s}) = \sum_{n \neq m,m'} |\chi_n\rangle\langle\chi_n| e^{-i\phi_n} + \sum_{a,b=m,m'} |\psi_a\rangle\langle\psi_b| M_{ab}(\mathbf{s}), \tag{3.3}$$

where M is a 2×2 unitary matrix and we parametrize the three-dimensional $(\mathbf{k}, t)$ space by a single variable $\mathbf{s}$.

The unitarity of M means that we can write it as

$$M(\mathbf{s}) = \exp\left[-i\phi_d(\mathbf{s}) - if_j(\mathbf{s})\sigma_j\right], \tag{3.4}$$

where summation over repeated indices is used. Here $\phi_d(\mathbf{s})$ is a real-valued function, whose value at $\mathbf{s}_0$ gives the common eigenvalue of the two degenerate bands, $\{\sigma_j\}$ are the Pauli matrices, and $\{f_j(\mathbf{s})\}$ are real continuous functions that satisfy $f_i(\mathbf{s}_0) = 0$.

We assume that U, and thereby f, is differentiable in a neighborhood around $\mathbf{s}_0$, and expand f_j to linear order in $(\mathbf{s} - \mathbf{s}_0)$ around $\mathbf{s}_0$. Noting that $f_j(\mathbf{s}_0) = 0$, we write

$$M(\mathbf{s}) \approx \exp\left[-i\phi_d(\mathbf{s}) - i(\mathbf{s} - \mathbf{s}_0)_j S_{jk}\sigma_k\right], \tag{3.5}$$

where $S_{jk} = \partial_j f_k(\mathbf{s}_0)$ is a real 3×3 matrix. The case where the linear term in $(\mathbf{s} - \mathbf{s}_0)$ also vanishes will be covered shortly.

We first consider the case where the matrix S has rank three, such that the coefficients of all three Pauli matrices vary independently as $\mathbf{s}$ explores the neighborhood around $\mathbf{s}_0$. In this case, the degeneracy is topologically protected, similar to the case of a Weyl node [141]: an infinitesimal change of the time evolution operator can never lift the degeneracy, but rather can only infinitesimally shift the location where it appears. A single such degeneracy can thus not be lifted with a continuous deformation of the system, and is therefore topologically protected. We thus define a topological singularity of a two-dimensional system to be an isolated degeneracy of the time evolution operator where the matrix S describing the linearization of U in its neighborhood [Eq. (3.5)] is invertible.

In addition to the isolated singularities described above, we may also find cases where S is not invertible. This occurs when two phase bands are degenerate along a line, surface, or three-dimensional region in $\mathbf{k}, t$-space, such that $\mathbf{s}_0$ is one point on this manifold. In such cases, the rank of S is equal to $3 - D$, where D is the dimension of the degenerate manifold. These extended degeneracies are not topologically protected: the degeneracy can generically be lifted in a neighborhood of $\mathbf{s}_0$ with a local perturbation, letting $f_i(\mathbf{s}) \to f_i(\mathbf{s}) + \delta g(\mathbf{s}) v_i$ in Eq. (3.4). Here δ controls the strength of the perturbation, $\mathbf{v}$ is a 3-dimensional vector satisfying $v_i S_{ij} = 0$, and $g(\mathbf{s})$ is a real continuous function that vanishes outside a neighborhood around $\mathbf{s}_0$, within which $|\psi_{m,m'}\rangle$ can be taken to be constant.

Importantly, the local perturbations described above only lift the degeneracy patch-wise, in one small region at a time. If one tries to lift the degeneracy over the entire manifold, two cases are possible: either the degeneracy can be lifted everywhere, or there will be a discrete set of points where topological singularities remain. Hence we conclude that, if the time evolution

operator is degenerate throughout a finite-dimensional manifold, it is always possible to apply an infinitesimal perturbation that either completely lifts the degeneracy, or reduces it to a cluster of topological singularities.

With the existence of topological singularities established, we now further characterize their properties. Each singularity can be assigned a charge (or vorticity) q:

$$q = \mathrm{sgn}\,[\det S], \tag{3.6}$$

where S is the linearization of $f_k(\mathbf{s})$ around $\mathbf{s}_0$, see Eqs. (3.4) and (3.5).

In two-dimensional systems, the charges of topological singularities have direct connections with the Chern numbers of the phase bands. Consider the "instantaneous" Chern number of phase band n, $C_n(t) = \frac{1}{4\pi}\int d^2k\,\mathrm{Tr}\{P_n[\partial_{k_x}P_n, \partial_{k_y}P_n]\}$. As long as no singularities are encountered, the Chern number $C_n(t)$ cannot change due to the continuity of $P_n(t)$. However, when two phase bands meet at a singularity with vorticity q, the Chern number for the "upper" phase band changes by q as the singularity is traversed in time, while the Chern number of the other band changes by $-q$. Here, the "upper" band is band $m+1$ if the singularity connects bands m and $m+1$, and band 1, if the singularity connects band 1 and N through the phase Brillouin zone edge. As a consequence of the argument above, any driving protocol that yields Floquet bands with different Chern numbers from those of the initial Hamiltonian $H(0)$ *must* induce one or more topological singularities in $U(\mathbf{k}, t)$.

In this section we showed that the evolution operator of a periodically-driven system may host topologically-protected degeneracies, or "topological singularities." As we concluded in the beginning of the section, topological singularities can obstruct the smooth deformation of the evolution of the driven system into that of a non-driven system. Specifically, in the case where the "bottom" and "top" phase bands, 1 and N, are connected by a singularity through the phase Brillouin zone-edge, their respective phase values at the singularity must differ by 2π. In this situation it is impossible to simultaneously flatten both of the bands to zero (compare Figs. 3.1c, d with Fig. 3.2). In contrast, for singularities that *do not* pass through the phase zone edge (i.e., those connecting bands m and $m+1$, with $m < N$), the two corresponding phase eigenvalues coincide at the singularity. In this case nothing prevents deforming the two phase bands simultaneously to zero, thereby removing the singularity. Hence singularities of the first type, i.e., "zone-edge singularities," are special: it is precisely these singularities that cannot be eliminated by smooth phase-band deformations, thus distinguishing driven from non-driven evolution. In Sec. 3.3 below we formulate the topological classification for two-dimensional periodically driven systems in terms of the phase bands and zone-edge topological singularities, and derive the corresponding bulk-edge correspondence.

3.2.2 Natural quasienergy zone

Before moving on to classification, we briefly introduce some further labeling notation that will be useful for referring to specific Floquet bands and gaps in the discussion below. In particular, we apply the phase band labeling prescribed in the beginning of this section to the Floquet bands themselves. We define a convention where we label Floquet band n such that $\varepsilon_n(\mathbf{k}) = \phi_n(\mathbf{k}, T)/T$, with $\phi_n(\mathbf{k}, t)$ determined by the labeling convention explained below Eq. (3.1), see Fig. 3.1d. This uniquely determines "natural" quasienergy band indices for a system, and the bands $\{\varepsilon_n\}$

for $n = 1 \dots N$ define a natural choice of the quasienergy (or Floquet) Brillouin zone within the repeated zone scheme.

Below we will also apply the labeling scheme to the quasienergy *gaps*. For the following discussion, we refer to the quasienergy gap *above* band m as gap m. Due to the periodicity of quasienergy, a driven system with N bands has an additional gap (as compared to a non-driven system), which separates band N from band 1, across the quasienergy zone edge. We thus refer to gap N as the "zone-edge gap" of the Floquet spectrum. In the non-driven limit $T \to 0$, the zone-edge gap becomes infinitely wide, while the other gaps remain finite.

We note that the natural quasienergy zone identified above has physical meaning, as the quasienergy bands within the zone are directly related to the spectrum of the time-averaged Hamiltonian. In particular, within the convention above, the quasienergy bands in the natural zone satisfy

$$\begin{aligned}\sum_n \varepsilon_n(\mathbf{k}) &= \frac{1}{T}\sum_n \phi_n(\mathbf{k}, T) \\ &= \frac{1}{T}\int_0^T dt\, \mathrm{Tr}\left[U^\dagger(\mathbf{k},t) i\partial_t U(\mathbf{k},t)\right].\end{aligned}$$

The last equality follows from the spectral decomposition (3.1), after using the relations $P_n \partial_t P_n = \partial_t P_n - (\partial_t P_n) P_n$, and $\sum_n P_n = 1$ to eliminate the derivatives of the projectors. Finally, substituting $i\partial_t U(\mathbf{k},t) = H(\mathbf{k},t)U(\mathbf{k},t)$ we find the following non-trivial relation

$$\sum_n \varepsilon_n(\mathbf{k}) = \frac{1}{T}\int_0^T dt\, \mathrm{Tr}\left[H(\mathbf{k},t)\right]. \tag{3.7}$$

Within the repeated zone scheme, this relation is uniquely satisfied for the quasienergy bands within the natural zone.

3.3 Topological classification of Floquet-Bloch systems in two dimensions

Having introduced the concept of phase bands and demonstrated the existence of topological singularities, we now consider the implications of these results for the topological properties of a two-dimensional Floquet-Bloch system with no symmetries. By "topological" we mean those properties that are invariant under any continuous deformation of the bulk time-evolution operator that preserves its continuity in crystal momentum and time, and keeps the bulk gaps open in the quasienergy spectrum of the Floquet operator $U(T)$. Any such quantity is a topological invariant of the system. Importantly, this definition means that topological invariants must be independent of the choice of time origin[2]

Analogous to a Chern insulator, a two-dimensional Floquet-Bloch system defined in a geometry with edges may host protected chiral edge modes within its bulk quasienergy gaps. The chiral

[2]To see this, note that a continuous change of time origin from 0 to t' gives rise to a smooth deformation of the evolution operator from $U(t)$ to $U(t+t')U^\dagger(t')$. Given that the quasienergy spectrum is invariant under changes of time origin, the topological invariants must remain the same for any choice of time origin as well.

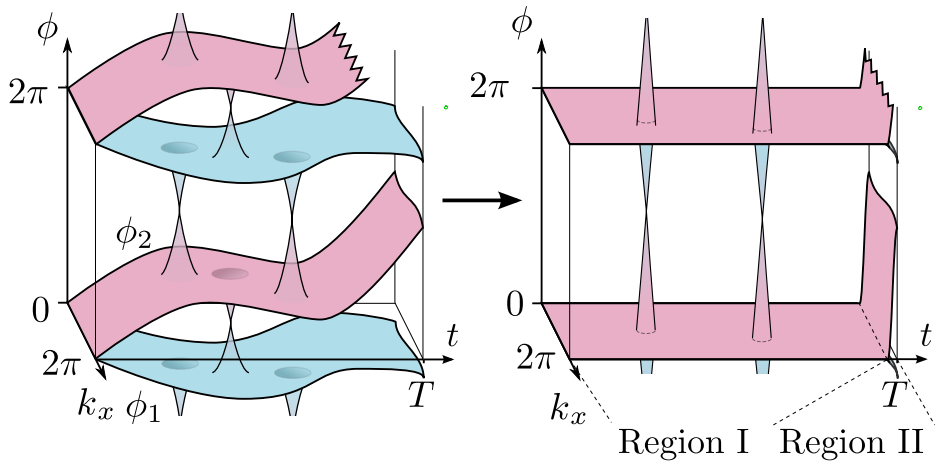

Figure 3.3: Continuous deformation of a generic time evolution operator which only preserves information about the topological singularities spanning the zone-edge gap (region I), and the Floquet bands (region II). These features cannot be removed, since the Chern indices of the Floquet bands and the total charge of the zone-edge singularities can only be changed by closing at least one quasienergy gap. Any topological invariant should be expressible in terms of only these non-removable features. Note that the singularity in the gap around phase $\phi = 0$ is eliminated under the deformation.

edge modes are topologically protected, meaning that the net number $n_{\text{edge}}(m)$ of chiral edge modes in bulk quasienergy gap m is invariant under continuous deformations of the bulk evolution operator $U(\mathbf{k}, t)$, or equivalently of the Hamiltonian $H(t)$, that keep quasienergy gap m open. Thus we recognize $n_{\text{edge}}(m)$ as a topological invariant of the system.

In this section we demonstrate that considerations about the bulk phase bands allow us to identify all independent topological invariants of a two-dimensional Floquet-Bloch system. Subsequently, we use these invariants to construct the bulk-edge correspondence, providing a direct link between the edge mode spectrum and the bulk phase band properties of two-dimensional Floquet-Bloch systems.

3.3.1 Topological invariants of 2D systems

In this subsection we identify the properties of a two-dimensional Floquet-Bloch system that are invariant under smooth deformations of the phase bands. In Sec. 3.2.1 we found that the phase bands of a 2D system can safely be deformed anywhere in $\mathbf{k}, t$-space except at isolated topological singularities. Therefore we may expect that the singularities play an important role in the topological classification of periodically driven systems.

To elucidate the importance of topological singularities we consider the following deformation of a time-evolution operator $U(\mathbf{k}, t)$, shown schematically in Fig. 3.3. Without changing the eigenstate projectors $P_n(\mathbf{k}, t)$, deform the phase bands $\phi_n(\mathbf{k}, t)$ to zero everywhere except for within small isolated regions that surround each zone-edge singularity and within a small time-

interval δt before T, where the phase bands wind linearly to their final values. These final values, which define the Floquet bands, are kept fixed under the deformation. We refer to the region $t < T - \delta t$ in $\mathbf{k}, t$ space as region I, and to the final region $t > T - \delta t$ as region II (see Fig. 3.3). Any time-evolution operator can be deformed in this way such that continuity is preserved and no quasienergy gap is closed. Without changing any topological invariant, the deformation effectively discards all information about the time-evolution operator except for the phase bands at time $t = T$ (i.e., the Floquet bands themselves), and the zone-edge singularities.

Consider now the remaining features of the phase band structure that could not be smoothly deformed away. We found in Sec. 3.2.1 that it was possible to change the location $\mathbf{k}, t$ of each singularity through a continuous deformation. Through such a deformation, it is furthermore possible to create and annihilate pairs of zone-edge singularities with opposite charges. Hence the only invariant quantity we can associate with region I is the sum of the charges $\{q_i^{(\mathrm{ZES})}\}$ of all zone-edge singularities, $\sum_i q_i^{(\mathrm{ZES})}$. For region II, we note that at $t = T$ any two projectors $P(\mathbf{k}, T)$ and $P'(\mathbf{k}, T)$ can be continuously deformed into each other if and only if their Chern numbers are the same [70]. Hence the only independent invariants we can associate with region II are the Chern numbers of the individual phase bands at $t = T$.

The arguments above show that a two-dimensional Floquet-Bloch system with N bands has exactly N independent topological invariants characterizing it. These invariants are the integers

$$\left(C_1, \ldots C_{N-1}, \sum_i q_i^{(\mathrm{ZES})} \right), \tag{3.8}$$

where C_n is the Chern number of Floquet band n (see Sec. 3.2.2 for definition of the quasienergy band indices). The index i in the sum runs over all topological singularities in the zone-edge gap. The Chern number of the last band C_N is not included since $\sum_n C_n = 0$. We see that while an N-band non-driven system is characterized by $N - 1$ independent integer-valued ($\mathbb{Z}$) invariants (the Chern numbers of each of the $N - 1$ lowest bands), Floquet-Bloch systems are characterized by N integer ($\mathbb{Z}$) topological invariants. The additional invariant is the net charge of the topological singularities in the zone-edge gap.

Bulk-edge correspondence for two-dimensional Floquet-Bloch systems

We now seek to derive a bulk-edge correspondence that gives the net number of chiral edge states that will appear within a given gap m of the bulk Floquet spectrum when the system is defined in a geometry with an edge. To this end we identify which nontrivial combinations of the N numbers in Eq. (3.8) remain invariant when all gaps except for gap m are allowed to close (see Sec. 3.2.2 for the labeling convention for the quasienergy gaps). Later we will use this feature to relate the invariant combination to the number $n_{\mathrm{edge}}(m)$ of edge modes in gap m, which also shares this property.

In order to find the combinations of the above quantities which have this invariance, we note that the Chern numbers of the individual bands 1 to m can be changed by closing the quasienergy gaps between them. Only their sum $S_m = \sum_{n=1}^{m} C_n$ remains constant under such operations [70]. Furthermore, if $m \neq N$, all zone-edge singularities can be removed through the plane $t = T$ by closing the zone-edge quasienergy gap (i.e., the gap between band N and band 1). Importantly,

however, the Chern number of band 1, and thereby S_m, changes by q each time a singularity of charge q is removed in this way (see the discussion at the end of Sec. 3.2.1 on the relationship between Chern numbers and singularities). Hence there only exists *one* independent combination of the invariants in Eq. (3.8) which remains invariant under all of these operations, i.e., when only gap m is required to stay open:

$$w_m[U] = \sum_{n=1}^{m} C_n - \sum_i q_i^{(\mathrm{ZES})}. \tag{3.9}$$

Any two evolutions characterized by the same value of the invariant w_m can be smoothly deformed into one another without closing quasienergy gap m. Crucially, this tells us that if topologically-protected chiral edge modes are possible, the number $n_{\mathrm{edge}}(m)$ of them in gap m should be some function of w_m, and possibly m itself. Standard spectral flow arguments show that chiral edge modes must exist in certain cases, and that $n_{\mathrm{edge}}(m) - n_{\mathrm{edge}}(m-1) = C_m$, see e.g., Refs. [119, 138, 139]. The only way this can be realized is if $n_{\mathrm{edge}}(m) = w_m + K$ for some universal constant K. Considering the trivial special case $H(t) = 0$, where both w_N and $n_{\mathrm{edge}}(N)$ are zero, we find that K must be zero. We thus arrive at the following new result for the net number of chiral edge modes in a two-dimensional system:

$$n_{\mathrm{edge}}(m) = \sum_{n=1}^{m} C_n - \sum_i q_i^{(\mathrm{ZES})}. \tag{3.10}$$

The simple expression above provides a direct way of evaluating the edge mode count given by the winding number formula found in Ref. [1]. The first term is the result one obtains simply when analyzing a non-driven system with the phase band framework, taking T to be so small that the phase bands do not cross. The second term has no equivalent in non-driven systems, and accounts for the anomalous edge modes that were discussed in Refs. [1, 23]. Additionally, Eq. (3.10) shows that the number of edge modes in the zone-edge gap is given by the net charge of all zone-edge topological singularities.

In Appendix B.1 we provide an explicit derivation showing that Eq. (3.10) is equivalent to the winding number formula of Ref. [1]. Below we refer to $w_m[U]$ as the winding number of U in gap m.

3.3.2 Topological singularities in a specific 2-band model

To make our discussion more concrete, in this subsection we demonstrate the results above on a variation of the explicit model considered in Ref. [1]. Consider a tight-binding model on a 2D bipartite square lattice, described by the time-dependent Bloch Hamiltonian

$$H(\mathbf{k}, t) = \sum_{n=1}^{4} J_n(t) \left(\sigma^+ e^{i\mathbf{b}_n \cdot \mathbf{k}} + \sigma^- e^{-i\mathbf{b}_n \cdot \mathbf{k}} \right) + V\sigma_z, \tag{3.11}$$

where σ_z and $\sigma^\pm = (\sigma_x \pm i\sigma_y)/2$ are the Pauli matrices acting in the sublattice space, and the vectors $\{\mathbf{b}_n\}$ are given by $\mathbf{b}_1 = -\mathbf{b}_3 = (a, 0)$, and $\mathbf{b}_2 = -\mathbf{b}_4 = (0, a)$, with a being the lattice constant. In real-space, Hamiltonian (3.11) consists of hopping terms between nearest neighbor

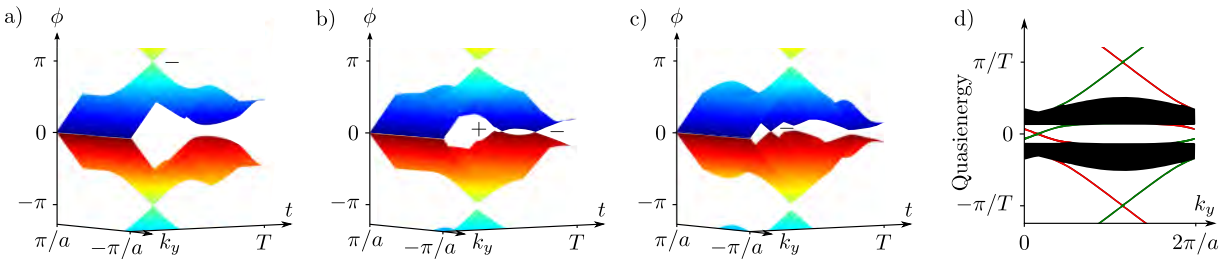

Figure 3.4: Explicit demonstration of topological singularities and anomalous edge states. a-c) Phase band structures for the model in Eq. (3.11) for fixed values of k_x, with singularity charges (all ± 1) indicated. The k_x values are a) $0.245/a$, b) $1.533/a$, c) $2.084/a$. d) Quasienergy band structure of the model in a strip geometry. Both bands have Chern number zero, and we find one chiral mode on each edge, in each quasienergy gap. Edge modes on opposite edges are indicated by different colors.

sites on the bipartite lattice. The Hamiltonian is T-periodic in time. Each driving cycle consists of five time intervals of length $T/5$, with $J_n(t) = \lambda_n$ during the n-th interval, while all the other hopping amplitudes are set to zero. In the fifth interval, all hopping amplitudes are zero while the sublattice potential V remains on.

In Ref. [1], anomalous edge modes were observed in the case where $\lambda_n = J$, for certain ranges of the parameters J and V. According to the discussion in the subsections above, this implies that topological singularities are present. Indeed, when in a nontrivial phase, the two phase bands touch through the zone-edge along the line $k_x = k_y$, at a specific time that depends on parameter values. To demonstrate that this degenerate region contains topological singularities, we add a small time-dependent perturbation to break the extended degeneracy into isolated singular points (see section 3.2.1). We implement the perturbation by reducing the hopping in the y-direction slightly compared to the x-direction, such that $\lambda_1 = \lambda_3 = J$ and $\lambda_2 = \lambda_4 = (1-\alpha)J$, where α is a small parameter. We then numerically calculate the time-evolution operator at a representative set of points in $(\mathbf{k}, t)$-space for the parameter choice $J = -2.5\pi/T$, $V = 0.8\pi/T$, and $\alpha = 0.2$. From diagonalization of the time-evolution operator we obtain the phase band structure of the model, and find four topological singularities (see Fig. 3.4). One singularity has charge -1 and connects the two bands through the zone edge, while the other three have charges $1, -1$, and -1, but do not cross the zone-edge. The charges are found numerically.

In Figs. 3.4a-c, the phase band structure is plotted for three values of fixed k_x. The k_x values are chosen where the four topological singularities appear (two of the singularities appear at the same k_x). The Chern numbers of the Floquet bands are zero.

Next we confine the model to a strip geometry with edges parallel to the y-direction, by truncating the real-space Hamiltonian of the model in the x-direction. We numerically calculate the Floquet operator of this truncated tight-binding Hamiltonian and obtain the quasienergy band structure shown in Fig. 3.4d. On each edge we find the net number of chiral edge modes to be 1, in both bulk quasienergy gaps. This behavior is fully consistent with result (3.10) above.

3.4 Discussion

In this chapter we found that the "phase-band structures" of time evolution operators provide a powerful basis for visualizing and understanding the topology of Floquet-Bloch systems. By considering smooth deformations of the phase bands, we showed that topologically protected degeneracies, or topological singularities, play a crucial role in distinguishing the topology of driven and non-driven systems. In particular, the presence of phase Brillouin zone edge topological singularities can present an obstruction to smoothly deforming the evolution of a driven system into one obtainable in a non-driven system.

In this chapter, we studied the case of a two-dimensional system in the absence of any symmetries. However, the approach we introduced here can also be applied to the classify systems with symmetries, such as particle-hole, time-reversal or chiral symmetries. Ref. [5], which forms the basis for this chapter, demonstrates that the method can be used to *exhaustively* classify the topological properties of a Floquet-Bloch system, given any symmetry class.

Our work thus demonstrates a general method for topological classification of Floquet-Bloch systems, based on identifying all features of the phase band structure of a given system that cannot be removed by smooth deformations [5]. This approach appears to offer means to exhaustively classify Floquet-Bloch systems and to straightforwardly derive the corresponding bulk-edge correspondences.

In the case we considered, we found that the edge spectra associated with individual bulk gaps of the Floquet operator have the same features as those of the corresponding non-driven system. However, we found that periodic driving could induce *global* edge spectra that are impossible to obtain in non-driven systems. This same is the case, when symmetries are present [5]. For instance, with periodic driving, topologically protected helical edge states can be produced in time-reversal invariant systems with only two-bands, while a minimum of four bands is needed without driving. In each of these cases, these new "anomalous" features are closely related with the appearance of zone-edge singularities in the time-bulk [5]. These phenomena further demonstrate that the relation between the topological properties of the bulk evolution and the appearance of protected edge modes is fundamentally changed in the driven context: the topology of a periodically driven system cannot be fully characterized by the stroboscopic Floquet operator $U(\mathbf{k}, T)$ or the corresponding effective Hamiltonian alone.

Finally, our results provide new intuition about the topology of Floquet-Bloch systems. While time-domain invariants such as the winding number found in Ref. [1] offer a mathematically well-defined prescription for characterizing topology in driven systems, often a clear physical picture is missing. Here, one of our central results is that non-trivial topological phenomena in periodically driven systems appear when topological singularities are introduced into the phase bands of the bulk time-evolution operator. In particular, in any driven system where the Floquet bands have different topology from that of the initial instantaneous Hamiltonian (i.e., at $t = 0$), at least one topological singularity must be encountered during the evolution. We expect that this insight may help provide guidance for the construction of new driving protocols to realize non-trivial topological phases in periodically driven systems.

Part II

Anomalous Floquet Insulators

Chapter 4

Quantized Magnetization Density in Periodically Driven Systems

This chapter has been published in Physical Review Letters **119***, 186801 (2017) by the author, Mark S. Rudner, Netanel H. Lindner, Erez Berg, and Gil Refael. The article is cited as Ref. [6] in this thesis.*

Chapters 2-3 demonstrated that periodically driven systems in two dimensions are characterized by one additional topological invariant compared to their nondriven counterparts. The additional, so-called micromotion invariant, ν is associated with the the dynamics of the system that take place within a driving period, and is unique feature of periodically driven systems. Nonzero values of ν result in phenomena with no equivalent in nondriven systems, such as quantized charge transport at the edges of fully insulating systems [2]. Chapter 3 explored the nature of the micromotion invariant ν in more detail, demonstrating its relation with nodal points in the bulk evolution operator's spectrum. This chapter studies the physical significance of the micromotion invariant.

The physical meaning of the micromotion invariant is revealed when disorder is introduced in the two-dimensional system. In this case, disorder can fully localize all bulk quasienergy bands, even while the micromotion invariant ν remains nonzero [2]. In this case, the system is in a stable topological phase protected by disorder, known as the Anomalous Floquet-Anderson Insulator (See Sec. 2.2.3). As a main result, this chapter demonstrates that nontrivial topology of the system, characterized by a nonzero (integer) value of the micromotion invariant ν, results in a nonzero, quantized orbital magnetization density. Specifically, this chapter finds that the orbital magnetization density within regions where all sites are occupied (Fig. 6.1) is given by ν/T. This result establishes the physical significance of the micromotion invariant ν which was introduced in Sec. 2.2.2. Interestingly, the results of this chapter demonstrate that, while nontrivial topology in nondriven systems lead to quantized response functions, topological features in driven systems can lead to the quantization of *observables*.

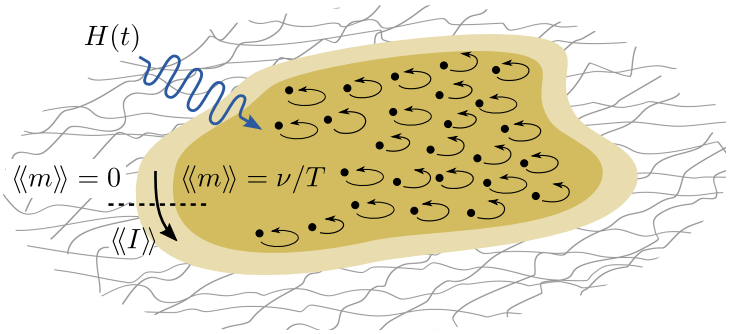

Figure 4.1: Quantized magnetization density in a two-dimensional periodically driven system where all Floquet eigenstates are localized. In a region where all sites are initially occupied (shaded area), the time-averaged orbital magnetization density $\langle\langle m\rangle\rangle$ is quantized as ν/T, where ν is an integer and T is the driving period. A quantized average current $\langle\langle I\rangle\rangle = \nu/T$ runs along the edge of the filled region.

4.1 Introduction

Periodic driving was recently introduced as a means for achieving topological phenomena in a wide variety of quantum systems. Beyond providing new ways to obtain topologically nontrivial band structures [20–31, 125–129, 131], periodic driving can give rise to wholly new types of topological phenomena without analogues in equilibrium [1, 2, 5, 23, 42, 44–50, 52, 99, 104, 107, 142].

In a periodically driven system, the unitary Floquet operator acts as a generator of discrete time evolution over each full driving period. As in non-driven systems, the spectrum and eigenstates of the Floquet operator can be classified according to topology [21–24]. However, in addition to the stroboscopic evolution of the system, the *micromotion* that takes place within each driving period is crucial for the topological classification of periodically driven systems [1,5,42,44–48,104,107,142].

Here we uncover a new type of topological quantization phenomenon associated with the micromotion of periodically driven quantum systems. We focus on periodically driven two-dimensional (2D) lattice systems in which *all* bulk Floquet eigenstates are localized by disorder (see Fig. 6.1). We show that, within a region where all states are occupied, the time-averaged orbital magnetization density $\langle\langle m\rangle\rangle$ is *quantized*: $\langle\langle m\rangle\rangle = \nu/T$, where ν is an integer and T is the driving period. The bulk observable $\langle\langle m\rangle\rangle$ thus serves as a topological order parameter, characterizing the topologically distinct fully-localized phases found in Ref. [2]. We propose a bulk interference measurement to probe this invariant in cold atom systems.

Topological invariants are often associated with quantized response functions. Famously, the Hall *conductivity* of an insulator is proportional to the TKNN invariant, or Chern number [15]. Interestingly, topology in driven systems may directly give rise to quantization of time-averaged observables, such as the pumped *current* in the Thouless pump [65]. Similarly, the response of magnetization density to changes of chemical potential in a quantum Hall system is quantized

when the chemical potential lies in an energy gap[1]. In contrast, here we find quantization of the *magnetization density* itself.

4.2 Setup

For concreteness, we consider a periodically-driven two-dimensional lattice model with one orbital per site. The dynamics in the system are governed by a time-periodic Hamiltonian $H(t) = H(t+T)$, where T is the driving period. The periodic driving gives rise to a unitary evolution $U(t) = \mathcal{T} e^{-i\int_0^t dt'\, H(t')}$, where $\mathcal{T}$ denotes time ordering. The spectrum of the Floquet operator $U(T)$, given by $U(T)|\psi_n(0)\rangle = e^{-i\epsilon_n T}|\psi_n(0)\rangle$, defines the Floquet eigenstates $\{|\psi_n(t)\rangle\}$ and their quasienergies $\{\epsilon_n\}$.

We characterize micromotion in this system via the orbital magnetization[2]

$$M(t) = \frac{1}{2}\left(\mathbf{r} \times \dot{\mathbf{r}}(t)\right) \cdot \hat{\mathbf{z}}, \tag{4.1}$$

where $\dot{\mathbf{r}}(t) = -i[\mathbf{r}, H(t)]$. The magnetization operator (4.1) is equivalently expressed as the response of the Hamiltonian to an applied uniform magnetic field B: $M(t) = -\frac{\partial H(t)}{\partial B}$ (see Appendix). In non-driven systems, the magnetization of a state hence determines the response of its energy to the field: $\Delta E \sim -\mathbf{M}\cdot\mathbf{B}$. In periodically driven systems, a similar relation holds between a Floquet eigenstate's time-averaged magnetization and the response of its quasienergy to an applied magnetic field. We define $\langle \mathcal{O} \rangle_\tau \equiv \frac{1}{\tau}\int_0^\tau dt\, \langle\psi(t)|\mathcal{O}(t)|\psi(t)\rangle$ as the time-averaged expectation value of an operator $\mathcal{O}(t)$ in the state $|\psi(t)\rangle$. The single-period averaged magnetization of a (localized) Floquet eigenstate $|\psi_n(t)\rangle$ is given by[3] (see Appendix):

$$\langle M \rangle_T^{(n)} \equiv \frac{1}{T}\int_0^T dt\, \langle\psi_n(t)|M(t)|\psi_n(t)\rangle = -\frac{\partial \varepsilon_n}{\partial B}. \tag{4.2}$$

Using Eqs. (4.1) and (4.2), we may associate a net magnetization with a single particle in a localized Floquet eigenstate. It is useful to define a local time-averaged *magnetization density*, associated with each plaquette p of the lattice, that characterizes the response of quasienergy to a magnetic flux ϕ_p applied locally through plaquette p. We define the magnetization density operator as[4]

$$m_p(t) = -\frac{\partial H(t)}{\partial \phi_p}, \quad \phi_p = \int_p d^2 r\, B(\mathbf{r}), \tag{4.3}$$

where the integral is taken over the area of plaquette p. The total time-averaged magnetization, $\langle M \rangle_\tau$, is given by the sum of magnetization densities over all plaquettes: $\langle M \rangle_\tau = \sum_p \langle m_p \rangle_\tau a^2$, where a is the lattice constant.

[1] This follows from the Streda formula [143–145].

[2] The orbital magnetization, Eq. (1), is independent of shifts of origin $\mathbf{r} \to (\mathbf{r} - \mathbf{r}_0)$ when evaluated in stationary states with $\langle \dot{\mathbf{r}} \rangle = 0$. In a fully localized system, this implies that the magnetization of a Floquet eigenstate averaged over an integer number of driving periods is origin-independent.

[3] We measure magnetic field in units of [1/Area], such that the Aharonov-Bohm phase of a closed trajectory is equal to the flux enclosed by the path.

[4] Although the particle density is not strictly stationary, localization implies $\lim_{\tau\to\infty} \langle \dot{\rho} \rangle_\tau = 0$. Therefore the long time average $\langle\langle m_p \rangle\rangle$ is gauge invariant (see Footnote 2) and obeys Ampere's law, Eq. (4.4)

The definition of magnetization density in Eq. (4.3) applies for both single particle and many-body systems. In particular, for a (single or many particle) Floquet eigenstate $|\psi(t)\rangle$ with quasienergy ε, the time-averaged magnetization density is given by $\langle m_p \rangle_T = -\frac{\partial \varepsilon}{\partial \phi_p}$.

In the continuum, equilibrium magnetization density is related to the current density $\mathbf{j}$ through Ampere's law, $\mathbf{j} = \nabla \times \mathbf{m}$. For a (stationary) system on the lattice, Ampere's law relates the time-averaged magnetization densities on adjacent plaquettes p and q to the time-averaged current $\langle I_{pq} \rangle_\tau$ on the bond between them (see Appendix):

$$\langle I_{pq} \rangle_\tau = \langle m_p \rangle_\tau - \langle m_q \rangle_\tau. \tag{4.4}$$

Here we take positive current to be counterclockwise with respect to plaquette p.

4.3 Magnetization in finite droplets.

We now discuss the consequences of the quantized magnetization density for the experimentally relevant case of a finite droplet We now show that the time-averaged magnetization density is quantized in a finite "droplet," where all states in a region of linear dimension R are initially occupied while the surrounding region is completely empty (Fig. 6.1). Specifically, we consider the long-time average of the magnetization density for a plaquette p deep inside the droplet, $\langle\langle m_p \rangle\rangle$, where $\langle\langle \mathcal{O} \rangle\rangle \equiv \lim_{\tau\to\infty} \langle \mathcal{O} \rangle_\tau$. Below we show that $\langle\langle m_p \rangle\rangle$ takes a constant value $\bar{m}_\infty$, up to exponentially small corrections (see Footnote 4). We then show that $\bar{m}_\infty$ is quantized.

Since all Floquet eigenstates are localized, the particle density will only evolve significantly in a strip of width ξ around the boundary of the filled region, where ξ is the single-particle localization length of the Floquet eigenstates. Hence, the droplet retains its shape up to a smearing of its boundary. At a distance $d \gg \xi$ from this boundary, the density change remains exponentially small in d/ξ at any time. Within the droplet, all (time-averaged) bond currents therefore vanish: $\langle I_{pq} \rangle_\tau = 0$ for all τ. The magnetization density $\langle\langle m_p \rangle\rangle$ must therefore be the same for all plaquettes deep within the droplet.

The uniform value of the magnetization density deep within the droplet may depend on the droplet's size. We note that $\langle\langle m_p \rangle\rangle$ is given by the sum of magnetization contributions from all occupied states that overlap with plaquette p. Therefore, if the droplet size is increased by adding a section of new (filled) sites in a region far away from plaquette p, $\langle\langle m_p \rangle\rangle$ can only change by an exponentially small amount due to the contributions of the tails of the newly added localized states. Thus, for a plaquette located a distance d from the boundary, we obtain $\langle\langle m_p \rangle\rangle = \bar{m}_\infty + \mathcal{O}(e^{-d/\xi})$, where $\bar{m}_\infty$ is the value in the thermodynamic limit. As we show below, $\bar{m}_\infty$ is quantized.

Interestingly, a nonzero value of $\bar{m}_\infty$ implies that a current circulates around the boundary of the droplet. The magnetization density drops from the value $\bar{m}_\infty$ to zero over a distance of order ξ across the droplet's boundary. Using Amperes law (4.4), the total time-averaged current $\langle\langle I \rangle\rangle$ passing through a cut through this strip (see Fig. 6.1) is $\langle\langle I \rangle\rangle = \bar{m}_\infty + \mathcal{O}(e^{-R/\xi})$.

4.4 Quantization of magnetization density.

To prove the quantization of $\bar{m}_\infty$, we consider the total magnetization $\langle\langle M\rangle\rangle$ of a droplet of N particles. On one hand we have $\langle\langle M\rangle\rangle = \sum_n{}' \langle M\rangle_T^{(n)} + \mathcal{O}(N^{1/2})$, where the sum runs over single particle Floquet eigenstates $|\psi_n\rangle$ with centers localized within the perimeter of the droplet. The $\mathcal{O}(N^{1/2})$ correction accounts for the partially-occupied Floquet eigenstates near the droplet's boundary. On the other hand, since the magnetization density deep inside the droplet is constant and given by $\bar{m}_\infty$, we have $\langle\langle M\rangle\rangle = Na^2\bar{m}_\infty + \mathcal{O}(N^{1/2})$. Here Na^2 is the total area of the droplet, with the $\mathcal{O}(N^{1/2})$ correction capturing the uncertainty of the area due to its fuzzy boundary. By equating the expressions for $\langle\langle M\rangle\rangle$ and taking the $N \to \infty$ limit, we identify

$$\bar{m}_\infty = \lim_{N\to\infty} \frac{1}{Na^2} \sum_n{}' \langle M\rangle_T^{(n)}. \tag{4.5}$$

The quantity $\frac{1}{N}\sum_n{}' \langle M\rangle_T^{(n)}$ is simply the average magnetization of Floquet eigenstates in the droplet; below, we show that this average is quantized in large, fully-localized systems. To do this, we explicitly compute the average magnetization over all Floquet eigenstates for a fully-localized system on a large torus of area $A = L^2a^2$, where L^2 is the number of sites.

For the system on a torus, we compute the time-averaged magnetization $\langle M\rangle_T^{(n)}$ of each Floquet eigenstate $|\psi_n(t)\rangle$ using Eq. (4.2). To use the form $\langle M\rangle_T^{(n)} = -\frac{\partial\epsilon_n}{\partial B}$, we must specify how the field B is introduced. Crucially, on a torus, the net magnetic flux must be an integer multiple of Φ_0 (the flux quantum)[5]; consequently, the strength of a *uniform* field cannot be varied continuously. However, for $\xi/L \ll 1$, we may use $\langle M\rangle_T^{(n)} = -\frac{\partial\epsilon_n}{\partial B} + \mathcal{O}(e^{-L/\xi})$, where $\epsilon_n(B)$ is the quasienergy of state $|\psi_n\rangle$ in the presence of a *locally* uniform magnetic field, of strength B within the support region of $|\psi_n\rangle$, but zero net flux through the torus. The $\mathcal{O}(e^{-L/\xi})$ correction arises from the non-uniformity of the field, which is concentrated where the wave function is exponentially small.

To evaluate the average magnetization of localized Floquet eigenstates, $\frac{1}{L^2}\sum_n \langle M\rangle_T^{(n)} = -\frac{1}{L^2}\sum_n \frac{\partial\epsilon_n}{\partial B}$, we examine the Floquet operator $U(T)$ in the presence of a global uniform magnetic field of strength $B_0 = 2\pi/A$, corresponding to precisely one flux quantum piercing the torus. For large A, the quasienergy in the uniform field B_0 is equal to that in the locally uniform field described above (with $B = B_0$), up to an exponentially small correction in L/ξ. Moreover, for small field strengths, $\frac{\partial\epsilon_n}{\partial B}$ is well approximated by a finite difference, such that[6]:

$$\langle M\rangle_T^{(n)} = -[\varepsilon_n(B_0) - \varepsilon_n(0)]/B_0 + \mathcal{O}(1/A). \tag{4.6}$$

The $\mathcal{O}(1/A)$ correction accounts for the error in discretizing the derivative.

Using Eq. (4.6), we can access $\sum_n \langle M\rangle_T^{(n)}$ directly via the determinant of the system's Floquet operator [5], $|U(T)|$. Writing $\log|U(T)| = \int_0^T dt\, \partial_t \log|U(t)|$, we use the identity $\partial_t \log|U(t)| =$

[5]This follows from the Dirac quantization condition: the torus can enclose an integer number of magnetic monopoles, each with a quantized charge of Φ_0.

[6]The labeling of Floquet eigenstates in the presence of the uniform field B_0 is defined such that $\langle\psi_n(t, B_0)|\psi_m(t, 0)\rangle = \delta_{nm} + \mathcal{O}(1/A)$. For large systems, this prescription holds for all but an exponentially small subset of disorder realizations.

$\mathrm{Tr}\left[U^\dagger(t)\partial_t U(t)\right]$, together with $\partial_t U(t) = -iH(t)U(t)$, and find[7]

$$\log|U(T)| = -i\int_0^T dt\,\mathrm{Tr}\left[H(t)\right]. \tag{4.7}$$

When a magnetic field is introduced, the hopping amplitudes between sites of the lattice acquire additional Peierl's phases: $H_{ab} \to H_{ab}e^{i\theta_{ab}}$. In the position basis, the magnetic field thus only affects the *off-diagonal* elements of the Hamiltonian, and we conclude that $\mathrm{Tr}[H(t)]$ and hence $|U(T)|$ are independent of magnetic field. Using $|U(T)| = e^{-i\sum_n \varepsilon_n T}$, we find

$$\sum_n \varepsilon_n(B_0) = \sum_n \varepsilon_n(0) - \frac{2\pi\nu}{T}, \tag{4.8}$$

where ν is an integer.

We now recall that $\bar{m}_\infty$ (the magnetization density in a filled droplet) is obtained from the average magnetization of the Floquet eigenstates in the droplet, see Eq. (4.5). The torus geometry discussed above allows us to compute this average in the thermodynamic limit. Using Eqs. (4.6) and (4.8) we obtain $\frac{1}{L^2}\sum_n \langle M\rangle_T^{(n)} = \frac{2\pi\nu}{L^2 B_0 T}$[8].Comparing to Eq. (4.5), we find:

$$\bar{m}_\infty = \frac{\nu}{T}. \tag{4.9}$$

Remarkably, this quantization has a topological origin. As we show in the Appendix, the integer ν is equal to the winding number invariant characterizing the Anomalous Floquet-Anderson Insulator (AFAI) phase, introduced in Ref. [2]. The magnetization density thus serves as a bulk topological order parameter that characterizes distinct fully-localized Floquet phases. Note that the emergence of a non-zero, quantized magnetization density is a unique dynamical phenomenon, with no counterpart in non-driven systems: for static systems, Eq. (4.9) must hold for all values of T, which requires $\nu = 0$.

4.5 Interferometric probe of quantized magnetization.

We now outline an interferometric scheme for measuring the spatially averaged magnetization density $\langle\langle\overline{m}\rangle\rangle = \langle\langle M\rangle\rangle/A_{\text{filled}}$ of a cloud of fermionic cold atoms in an optical lattice (see Fig. 4.2), where A_{filled} is the area of the initially filled region. We thus offer a direct probe to measure the bulk topological invariant of the AFAI.

Consider an atom traversing a closed trajectory in the presence of a weak magnetic field B. Semiclassically, the wave-function picks up an additional phase shift $\Delta\phi = BA_{\text{orb}}$ due to the field, where A_{orb} is the area enclosed by the orbit[9]. Correspondingly, a simple quantum mechanical calculation (see Appendix) shows that the phase shift acquired by an atom in Floquet eigenstate $|\psi_n(t)\rangle$ over a full driving period is proportional to the state's magnetization, $\Delta\phi_n = \langle M\rangle_T^{(n)} BT$.

[7]Here we choose $\log|U(t)|$ to be continuous in time, with $\log|U(0)| = 0$.

[8]On the torus, $\sum_n \langle M\rangle_T^{(n)}$ is used mathematically to find the average magnetization of Floquet eigenstates. It does *not* represent the magnetization of a fully filled torus, which is unmeasurable.

[9]More precisely, the overlap between the wave functions evolved with and without the magnetic field given by $1 - i\Delta\phi$ to first order in B.

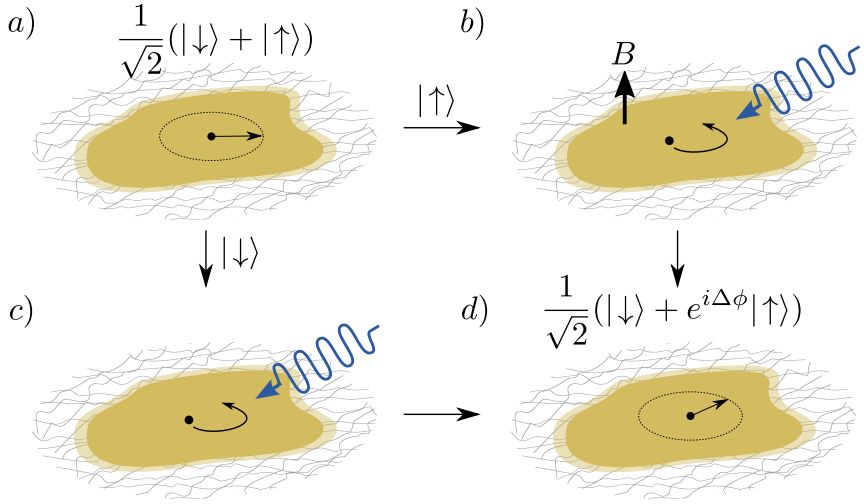

Figure 4.2: Interferometric measurement of quantized orbital magnetization density in a cold-atom system. a) The system is prepared by filling a region of an optical lattice with spin-1/2 atoms fully polarized along x. b,c) The system is evolved with a spin-independent periodic driving Hamiltonian, plus a weak spin-dependent uniform synthetic magnetic field. d) The spin-dependent field gives rise to a phase-difference $\Delta\phi$ between the $|\uparrow\rangle$ and $|\downarrow\rangle$ components of each atom's wave function. The phase shift yields a net y-polarization of total spin, proportional to the system's time-averaged magnetization.

Using this phase shift, the magnetization of a cloud of atoms can be measured in a Ramsey-type interference experiment in a situation where the atoms have two internal ("spin") states $|\uparrow\rangle$ and $|\downarrow\rangle$. First, the system should be prepared by completely filling a region of known area, A_{filled}, with atoms fully spin-polarized along the "x"-direction, $|\psi(0)\rangle \propto (|\uparrow\rangle + |\downarrow\rangle)/\sqrt{2}$, (Fig. 4.2a). The system should then be evolved with the driving Hamiltonian to allow the particle density to reach a steady profile[10], as in Fig. 4.3a. To perform the measurement, the cloud of atoms is then evolved through N driving periods in the presence of a weak spin-dependent orbital effective magnetic field B (Figs. 4.2bc), which, e.g., acts only on the $|\uparrow\rangle$ species. Through the evolution, the $|\uparrow\rangle$ component of each atom's wave function gains a phase shift relative to the $|\downarrow\rangle$ component, yielding a nonzero average y-spin per particle, $\langle\overline{\sigma}_y\rangle$, (Fig. 4.2d). For small precession angles, the average y-spin after N periods is given by $\langle\overline{\sigma}_y(NT)\rangle \equiv \Omega_{NT} B a^2 NT$, with (see Appendix)

$$\Omega_{NT} = \langle\langle\overline{m}\rangle\rangle + \frac{1}{NT}\mathcal{O}\left(\frac{\xi^{3/2}}{aR^{1/2}}\right) + \mathcal{O}(B). \tag{4.10}$$

Importantly, the second term vanishes in the long time limit (and scales to zero at finite times for large systems), thus revealing the quantized magnetization density (see Appendix).

[10]This initial evolution step minimizes systematic transients due to the sharp boundary, see SOM.

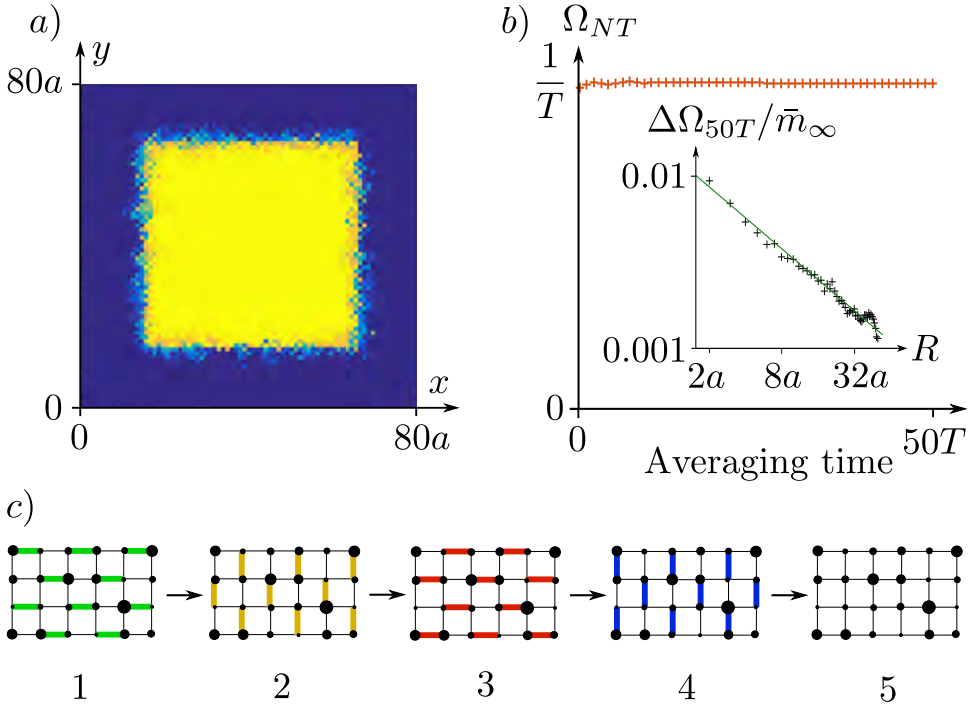

Figure 4.3: a) Particle density in the system after 20 driving periods, for an initially filled 50×50 square of sites. b) Normalized growth rate Ω_{NT} of the average y-spin per atom [see text above Eq. (4.10)]. The long-time-averaged magnetization density $\langle\langle \overline{m} \rangle\rangle$ is extracted from the saturation value at long times. *Inset*: Deviation $\Delta\Omega_{50T}$ of Ω_{50T} from the quantized value $\bar{m}_\infty$ *vs.* droplet size R. The value of $\Delta\Omega_{50T}$ is obtained as an RMS average of $\Omega_{50T} - \bar{m}_\infty$ over 100 disorder realizations. c) Depiction of the tight-binding model.

4.6 Numerical results

We simulated the experimental protocol outlined above using a tight-binding model on a two-dimensional bipartite square lattice, with Hamiltonian $H(t) = H_{\text{clean}}(t) + V_{\text{disorder}}$. The Hamiltonian $H_{\text{clean}}(t)$ was considered in Ref. [1], and is of the form

$$H_{\text{clean}}(t) = \sum_{\mathbf{r}\in A}\sum_{n=1}^{4} J_n(t)(c^\dagger_{\mathbf{r}+\mathbf{b}_n}c_{\mathbf{r}} + h.c.), \tag{4.11}$$

where $c_{\mathbf{r}}$ is the fermionic annihilation operator on the lattice site with coordinate $\mathbf{r}$, and the first sum runs over sites $\mathbf{r}$ on sublattice A. The vectors $\{\mathbf{b}_n\}$ are given by $\mathbf{b}_1 = -\mathbf{b}_3 = (a, 0)$ and $\mathbf{b}_2 = -\mathbf{b}_4 = (0, a)$, where a is the lattice constant. The driving period is divided into five segments of equal length $T/5$. In the nth segment ($n \leq 4$), $J_n(t) = J$, while all other hopping amplitudes are set to zero; in the 5th segment all hopping amplitudes are set to zero (see Fig. 4.3c). We introduce disorder through a time-independent potential $V_{\text{disorder}} = \sum_{\mathbf{r}} w_{\mathbf{r}} c^\dagger_{\mathbf{r}} c_{\mathbf{r}}$, where the sum runs over all sites, and the on-site energies $\{w_{\mathbf{r}}\}$ are randomly drawn from a uniform distribution in the interval $[-W, W]$. The model has hopping amplitude J and disorder strength W both set to $2.5\pi/T$. This brings the system well into the AFAI phase, for which we expect $\bar{m}_\infty = 1/T$ [146].

To find the magnetization density of the system, we consider a single disorder realization on a lattice of 80×80 sites and open boundary conditions. We initially fill a region of 50×50 sites (i.e., $R = 50$) centered in the middle of the lattice, and prepare the state by evolving it for 20 driving periods at zero magnetic field (see Fig. 4.3a). For further times ranging from 0 to $50T$ we evolve the system in the presence of a spin-dependent magnetic field of strength $Ba^2 = 2\pi \cdot 10^{-4}$. We extract the spatially averaged magnetization density $\langle\langle \overline{m} \rangle\rangle$ from the long-time limit of the normalized growth rate Ω_{NT} of average y-spin per atom, $\langle \overline{\sigma}_y(NT) \rangle$. Ω_{NT} rapidly converges (up to a finite-size correction) to the quantized value of the magnetization density, $1/T$, reaching 0.9998 after 100 periods (see Fig. 4.3b and SOM). The inset in Fig. 4.3b shows the deviation of Ω_{50T} from the quantized value $\bar{m}_\infty = 1/T$ for various sizes of the droplet, taken as a root-mean-square average over 100 disorder realizations at each system size. We find a power law decay of the fluctuations with system size, $\Delta\Omega_{50T} \sim R^{-0.55}$.

4.7 Discussion

In this chapter we showed that the orbital magnetization density is quantized in fully-filled regions of localized Floquet systems. We then proposed an experimental scheme for measuring the quantized magnetization density in cold atomic systems.

We derived the quantization of magnetization density within a tight-binding model with one (s-type) orbital per site. This means that each on-site orbital does not carry any intrinsic magnetization. In the continuum, small non-quantized contributions to the magnetization density may arise due to mixing with higher bands. Such contributions are strongly suppressed when the driving is adiabatic with respect to the gap to higher bands, and the lattice is very deep such that the gap is large compared to the bandwidth [146].

It is natural to expect that our results will hold also in the presence of interactions, given that the system is strongly disordered and hence may be many-body localized. Recently, progress

has been made in constructing interacting analogues of the AFAI [56, 147]. The fate of the magnetization in the presence of interactions will be studied in the following chapters.

Chapter 5

Anomalous Floquet Insulators

This chapter has been submitted for publication, and can be found as an arxiv preprint on arxiv:1712.02789 (2017) by FN, Mark S. Rudner, Dmitry Abanin, Netanel H. Lindner, and Erez Berg. The article is cited as Ref. [7] in this thesis.

Chapter 2 introduced the Anomalous Floquet-Anderson Insulator (AFAI) as a stable phase in periodically driven systems of noninteracting fermions[1]. Chapter 4 subsequently showed that the AFAI phase is characterized by a quantized, nonzero orbital magnetization density. The quantized value of magnetization, which serves as an order parameter for the AFAI, is topologically protected from changing whenever all Floquet eigenstates in the systems remain localized. The robustness of the AFAI, and its signature of quantized magnetization, thus arises from the stability of eigenstate localization in noninteracting systems [2].

This chapter studies the stability of the AFAI in the presence of interactions. As explained in Sec. 2.3.1, thermalizing periodically driven many-body systems cannot support any nontrivial phase structure, due to the uncontrolled heating induced by the driving [92,93,98]. However, many-body localization (MBL), induced by strong disorder, may prevent thermalization [109]. With MBL, periodically driven systems may therefore in principle support nontrivial topological phases. The potential for realizing the AFAI in many-body localized systems raises a highly nontrivial question: are the requirements for the AFAI phase compatible with many-body localization?

At first sight, a positive answer to the question above seems unlikely: the AFAI phase is characterized by nontrivial motion of particles within a driving period, while MBL is characterized by particles remaining "frozen" in the system. However, using a rotating frame transformation, we find that the AFAI phase can be realized in a model that meet the expected requirements for MBL (although this chapter does not prove the existence of MBL). This supports the existence of a stable, many-body localized topological phase in two-dimensional periodically driven systems: the so-called anomalous Floquet insulator (AFI). This chapter focuses on the stability of the AFI, while the following chapter (Chapter 6) explores the topological properties of this phase.

[1] This result was originally obtained Ref. [2].

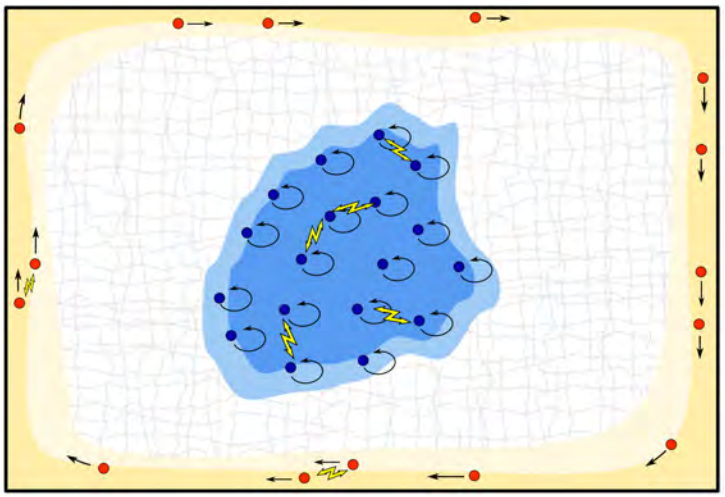

Figure 5.1: Schematic illustration of the anomalous Floquet insulator (AFI) – an interacting phase of matter only possible out-of-equilibrium. The bulk states are many-body localized in the presence of disorder and interactions, under conditions discussed in the main text. The nontrivial topology of the AFI is manifested in chiral edge states that exhibit protected thermalization.

5.1 Introduction

At or near equilibrium, the emergence of universal phenomena enables us to organize our description of physical systems in terms of distinct phases of matter. Intriguingly, a similar phase structure can emerge far from equilibrium, in *periodically-driven* quantum many-body systems. While some of the corresponding "Floquet phases" are analogous to phases that occur in equilibrium [20–41, 59], others, such as discrete time crystals [44–52] or the anomalous Floquet-Anderson insulator (AFAI) [1,2,53] and its generalizations [42,43,54–56], display unique dynamical and topological features that cannot occur in equilibrium. We label such phases "anomalous Floquet phases."

The fact that stable phases of matter can exist at all in isolated periodically-driven systems is itself a non-trivial statement: in the absence of a heat bath that can extract energy and entropy, such systems are generally expected to continually absorb energy from the driving field and heat towards a featureless infinite-temperature state at long times [93, 148, 149]. Crucially, in the presence of strong disorder, many-body localization (MBL) may prevent such heating [98,109,150]. Despite their localization, MBL systems support a rich variety of symmetry-breaking and topological phases [151, 152].

Previous works [98, 109] have shown that MBL may persist in periodically-driven systems when the driving field has a *high frequency* and *low amplitude*. However, the genuinely new phases of Floquet systems (anomalous Floquet phases), *cannot* be realized in the high-frequency regime. Specifically, anomalous Floquet phases are characterized by nontrivial evolution over the course of a single driving period, which requires the drive frequency to be at most comparable to other energy scales of the system. In order to realize the full potential of many-body Floquet systems,

we thus must understand the conditions under which anomalous Floquet phases may be realized.

In this work we investigate the stability of the two-dimensional (2D) anomalous Floquet insulator (AFI) phase, an interacting version of the AFAI [2] (see Fig. 5.1). The AFAI is a topologically nontrivial single-particle anomalous Floquet phase, characterized by a quantized bulk magnetization density [6] and protected chiral edge states. Here we show that the AFI bulk may be many-body localized in the presence of interactions.

To demonstrate MBL, we find conditions under which the original problem can be mapped onto an effective high-frequency driving problem in an appropriately constructed rotating frame. The same arguments that support MBL in the high-frequency limit [109] then imply MBL of the AFI in the corresponding regime. This approach can also be applied to establish the stability of other anomalous Floquet phases, such as discrete time crystals [49, 50] (see Appendix), and other generalizations of the AFAI [55, 56]. We support our conclusions with numerical simulations of the long-time dynamics and level statistics of the AFI.

The crucial differences between the AFI and the AFAI, and some of the AFI's most intriguing properties, are revealed in a geometry with edges. First, due to interactions, we expect the topologically protected edge states to give rise to "protected thermalization" at the AFI edge, with the particle distribution on the edge rapidly approaching an infinite-temperature-like state. Second, interactions couple thermalizing edge states and localized bulk states, resulting in a non-trivial competition. We explore this competition numerically and conclude that, in finite-size samples, the edge and bulk may effectively remain decoupled. This opens prospects for realizing quantized edge transport [2, 91] in AFIs at high temperature.

5.2 Existence of the anomalous Floquet insulator.

We first show the existence of the AFI phase for sufficiently weak interactions between particles. We consider a system of spinless fermions on a square lattice with two sublattices, A and B, described by the following time-periodic Hamiltonian (with driving period T):

$$H(t) = H_{\text{id}}(t) + H_{\text{dis}}(t) + H_{\text{int}}, \;\; H(t+T) = H(t). \tag{5.1}$$

Here $H_{\text{id}}(t)$ is the translationally invariant, single-particle Hamiltonian, which realizes the ideal limit of the AFAI (see Ref. [1] and below). H_{dis} describes a random on-site disorder potential, which stabilizes the AFAI in the absence of interactions [2]. The new ingredient is the two-particle interaction described by H_{int}.

For concreteness, we consider the following driving protocol, illustrated in Fig. 6.2a. More general driving schemes will be discussed below. Each period T is divided into five segments: the first four segments each have duration $\alpha T/4$, and the last segment has duration $(1-\alpha)T$. H_{id} acts during the first four segments, while disorder is applied during the last segment; interactions are always present. Importantly, the parameter $0 < \alpha \leq 1$ tunes the effective strength of the disorder. Below we define how $H(t)$ acts within a single driving period, $0 \leq t < T$; its form at later times is obtained from time-periodicity, $H(nT+t) = H(t)$, for any integer n.

The Hamiltonian H_{id} consists of hopping terms, which are cyclically applied as illustrated in

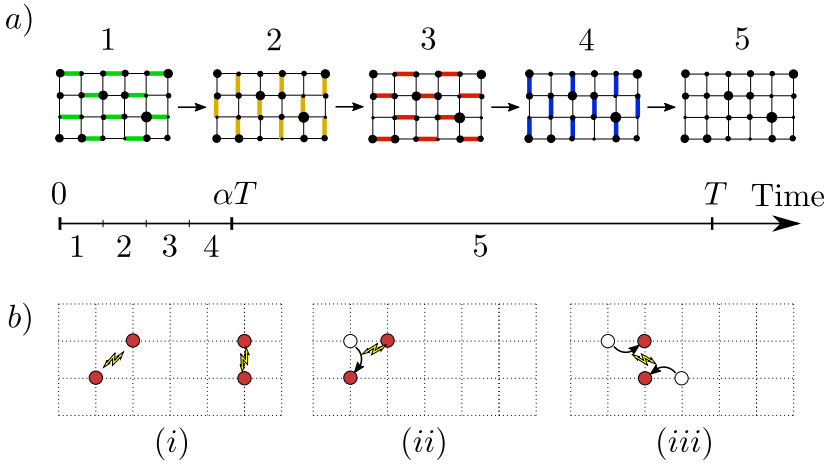

Figure 5.2: a) Each driving period consists of five segments. During the first four segments, time-dependent hopping $H_{\rm id}(t)$ [Eq. (6.20)] transfers particles between A and B sublattices, cyclically around plaquettes of the lattice. Disorder, $H_{\rm dis}$ [Eq. (E.66)], is applied during the fifth segment, while interactions, $H_{\rm int}$ [Eq. (5.5)], are always present. b) Schematic depiction of the terms contained in the transformed interaction Hamiltonian, see Eq. (5.7). Three kinds of terms are illustrated: (i) density-density interaction; (ii) hopping with an amplitude dependent on the density of a nearby site; (iii) correlated hopping of pairs of particles.

Fig. 6.2a:

$$H_{\rm id}(t) = J \sum_{\mathbf{r}\in A} \sum_{n=1}^{4} f_n(t)(c^\dagger_{\mathbf{r}+\mathbf{b}_n} c_{\mathbf{r}} + \text{h.c.}), \tag{5.2}$$

where the first sum runs over sites $\mathbf{r}$ on sublattice A, and $f_n(t) = 1$ for $(n-1)\alpha T/4 \le t < n\alpha T/4$, and $f_n(t) = 0$ otherwise. The vectors $\{\mathbf{b}_n\}$ are given by $\mathbf{b}_1 = -\mathbf{b}_3 = (a, 0)$ and $\mathbf{b}_2 = -\mathbf{b}_4 = (0, a)$, where a is the lattice constant. The amplitude J is chosen such that the nth "pulse" perfectly transfers a particle on site $\mathbf{r} \in A$ to site $\mathbf{r} + \mathbf{b}_n$, and vice versa:

$$J\alpha T/4 = \pi/2. \tag{5.3}$$

Here and throughout we set $\hbar = 1$. We write the disorder Hamiltonian as:

$$H_{\rm dis}(t) = H_{\rm dis} f_5(t), \quad H_{\rm dis} = \sum_{\mathbf{r}} W_{\mathbf{r}} c^\dagger_{\mathbf{r}} c_{\mathbf{r}}, \tag{5.4}$$

where $W_{\mathbf{r}} \in [-W, W]$ is a random on-site potential, and $f_5(t) = 1$ for $\alpha T \le t < T$, and 0 otherwise. Finally, we choose $H_{\rm int}$ to consist of nearest-neighbor interactions:

$$H_{\rm int} = \lambda \sum_{\langle \mathbf{r}\mathbf{r}'\rangle} n_{\mathbf{r}} n_{\mathbf{r}'}. \tag{5.5}$$

In the non-interacting limit, $\lambda = 0$, this model is exactly solvable and describes an ideal AFAI with topological edge states and zero localization length in the bulk.

5.2.1 Rotating frame transformation.

Our goal is to find the conditions when the AFI can be many-body localized. Importantly, the driving described above is manifestly *not* in the high-frequency limit: condition (5.3) implies that the hopping amplitude J is of the same order as the driving frequency, $\omega = 2\pi/T$. Therefore, *a priori*, the analysis of Ref. [109] cannot be directly applied.

We now perform a time-dependent unitary transformation to map our problem onto an equivalent one, which lies in the high-frequency regime as long as $W \ll \omega, J$. To avoid complications arising from delocalized edge states, we first consider a system on a torus. We transform to a rotating frame in which the fast motion associated with $H_{\rm id}$ is removed:

$$|\Phi(t)\rangle = Q^\dagger(t)|\Psi(t)\rangle,\ Q(t) = \mathcal{T}e^{-i\int_0^t ds H_{\rm id}(s)}, \tag{5.6}$$

where $|\Psi(t)\rangle$ ($|\Phi(t)\rangle$) is the state in the original (rotating) frame. We note that $Q(T) = I$ is the identity operator: over one full period, evolution with $H_{\rm id}(t)$ alone returns every particle to its initial position. It follows that $Q(t)$ is time-periodic: $Q(t) = Q(t+T)$.

The time evolution of $|\Phi(t)\rangle$ is generated by a transformed Hamiltonian $\tilde{H}(t)$, given by $\tilde{H}(t) = Q^\dagger(t)H(t)Q(t) - iQ^\dagger(t)\partial_t Q(t)$. By construction, Eq. (5.6) gives $Q^\dagger H_{\rm id}(t)Q - iQ^\dagger\partial_t Q = 0$. Thus we obtain:

$$\tilde{H}(t) = Q^\dagger(t)(H_{\rm dis}(t) + H_{\rm int})Q(t). \tag{5.7}$$

Since $Q(t)$ and $H_{\rm dis}(t)$ are both T-periodic, $\tilde{H}(t)$ is also time-periodic with period T. The periodicity of $Q(t)$ further implies that the Hamiltonian $\tilde{H}(t)$ generates the same Floquet operator as $H(t)$, and therefore the same stroboscopic evolution, $|\Psi(nT)\rangle = |\Phi(nT)\rangle$. It follows that if the system described by $\tilde{H}(t)$ is many-body localized, so is the system described by $H(t)$.

With the help of the unitary transformation Q, we have eliminated the large-amplitude term $H_{\rm id}(t)$ from the Hamiltonian. The resulting Hamiltonian $\tilde{H}(t)$ has terms of order W, λ, which can be much smaller than the driving frequency ω. In this limit, the system in the rotating frame is in the high-frequency regime, where MBL can be stable with respect to driving.

5.2.2 Conditions for many-body localization.

To establish the conditions for MBL more precisely, we examine the transformed Hamiltonian (5.7), see also Eqs. (E.66) and (5.5). Due to the fact that $H_{\rm id}(t)$ acts only during the first four segments of the driving cycle, $Q(t) = I$ for all $t \in [\alpha T, T]$. Since $H_{\rm dis}(t)$ acts only during the *fifth* segment, the disorder Hamiltonian [Eq. (E.66)] is unchanged by the transformation $Q(t)$. The disorder term can be decomposed into a time-averaged component $(1-\alpha)H_{\rm dis}$, and a time-dependent component, which changes step-wise at times $t = \alpha T$ and T. In the absence of interactions, $H_{\rm dis}(t)$ gives (single-particle) eigenstates that are trivially localized on each site of the lattice.

The transformed interaction Hamiltonian, $\tilde{H}_{\rm int}(t) = Q^\dagger(t)H_{\rm int}Q(t)$, has a clear structure including three kinds of terms of extended but finite range (see Fig. 6.2b): (i) density-density interactions between nearby sites, (ii) hopping between nearby sites with an amplitude that depends on the density on one of the nearby sites, and (iii) correlated hopping of pairs of particles. Explicit expressions for these terms and the ranges over which they act are discussed in the appendix.

Crucially, the transformed interactions remain short-ranged. All of the terms described above have time-averaged (constant) parts with strengths $\sim \mathcal{O}(\alpha\lambda)$, as well as oscillating parts at frequency ω and higher harmonics, see the appendix.

We proceed in two steps, first analyzing the dynamics generated by the static, time-averaged part of $\tilde{H}(t)$, then investigating the role of the remaining (small) time-dependent terms. The time-averaged part of $\tilde{H}(t)$ contains on-site potential disorder with characteristic scale $W(1-\alpha)$, and one- and two-particle hopping terms induced by interactions, with strength $\sim \lambda\alpha$. In the limit $\lambda\alpha \ll W(1-\alpha)$ the delocalizing processes induced by interactions are typically off-resonant, and the (static) system is in the MBL phase [110]. At a critical interaction strength λ_c, the system undergoes a transition into a thermal, delocalized phase. Thus stability requires:

$$\frac{\lambda\alpha}{W(1-\alpha)} \leq \kappa_c, \tag{5.8}$$

where κ_c is the critical ratio at which the MBL-delocalization transition occurs.

As we explain in the appendix, the time-dependent terms of $\tilde{H}(t)$ have Fourier components with amplitudes of the order $\alpha\lambda, \alpha W$. In the "high-frequency" limit, $\omega \gg \alpha W, \alpha\lambda$, the analysis of Ref. [109] shows that such time-dependent terms do not lead to delocalization.

The above arguments show that our system exhibits MBL for $\lambda, W \ll \frac{1}{\alpha}\omega$, $\lambda < \frac{1-\alpha}{\alpha} W\kappa_c$. The AFI thus constitutes a stable anomalous Floquet phase of matter.

5.3 Numerics: existence of AFI phase.

We support the above analytical arguments with numerical simulations. To investigate the stability of the phase, we compare two driving protocols: (i) the model defined by Eqs. (5.1)-(5.5), with disorder applied only during the fifth segment, and (ii) the same as (i), but with (constant) disorder applied throughout the driving cycle.

As an indicator of MBL, we study the quasienergy level statistics of the Floquet operator $U(T) = \mathcal{T}\exp\left(-i\int_0^T H(s)\,ds\right)$, obtained via exact evolution [93, 98, 150, 153]. The level spacing ratio around many-body Floquet state n is defined as $r_n = \min\{\delta_n/\delta_{n+1}, \delta_{n+1}/\delta_n\}$, where $\delta_n = \varepsilon_n - \varepsilon_{n-1}$ is the quasienergy gap below level n. For a Poisson distribution of levels, this ratio is ~ 0.4; for the Circular Unitary Ensemble, it is ~ 0.6 [93].

We computed the average level spacing ratio by exact diagonalization of the Floquet operator for multiple realizations of the model with 8 particles on a 4×4 square lattice with periodic boundary conditions. For model (i) we take $W = 0.1\omega$, and for model (ii) we take $W = \omega$.

Figure 5.3 shows the resulting data as a function of λ/W. Each curve shows the mean value of the average level spacing ratio obtained from an ensemble of 100 disorder realizations per point [2], for a fixed value of α. The peaks visible near the transition for $\alpha = \frac{1}{16}$ and $\alpha = \frac{1}{64}$ in model (i) arise due to resonances where the periodic driving breaks up clusters of 2, 3 and 4 particles that are otherwise bound by the interactions [3].

[2] For a given value of α, the realizations are different for each value of λ.

[3] In the rotating frame, interactions may bind small droplets of particles together. However, when $\lambda = \frac{z\omega}{n}$ for integers z, n, the residual periodic driving in the rotating frame can lead to resonances where these clusters break up. Due to the breaking up of clusters at these values of λ, the system becomes more delocalized.

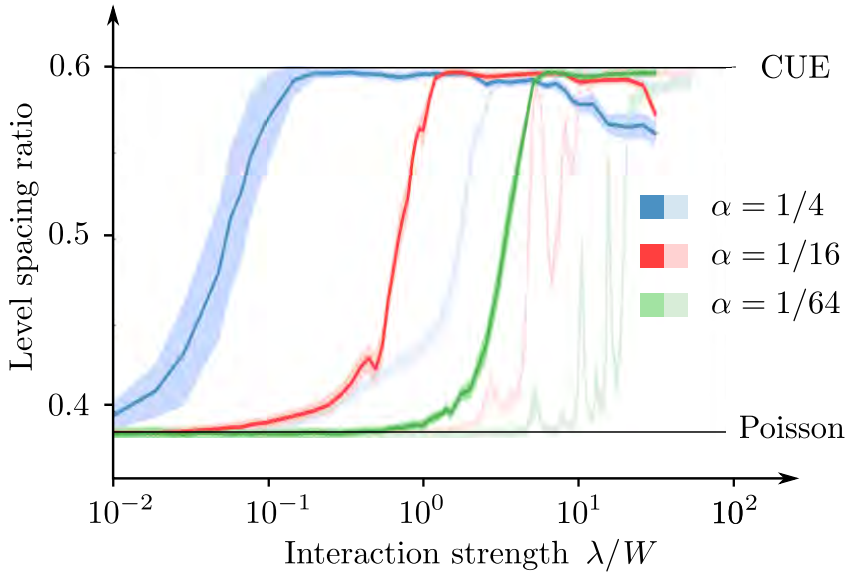

Figure 5.3: Average level spacing ratio as function of interaction strength, in a half-filled system of 4×4 sites. Each point on each curve results from averaging over 100 disorder realizations. Light curves correspond to model (i), with $W = 0.1\omega$, while dark curves correspond to model (ii) with $W = \omega$. In all cases, Poisson level statistics, indicating MBL, are observed at low enough interaction strength.

The data in Fig. 5.3 show that, for all the values of α we examined, the level spacing ratio converges to 0.38 for sufficiently small values of λ, indicative of Poisson level statistics and MBL. Additionally, the critical value $\lambda_{\text{critical}}/W$ at which the localization-delocalization transition occurs shifts upwards for smaller values of α, as anticipated above. When $\alpha = 1/64$, the system is localized even when the interaction strength is an order of magnitude larger than W. Smaller values of α will likely push up the transition further.

For a given α, the value of $\lambda_{\text{critical}}$ in model (ii), where $W = \omega$, is shifted to lower values than in model (i). However, $\lambda_{\text{critical}}$ remains finite and controllable by α. The AFI phase thus appears to extend beyond the regime of the sufficient condition $W \ll \omega$ discussed above.

5.3.1 Dynamics of an AFI with edges.

So far, we have established the stability of the AFI in a closed geometry without an edge. In the non-interacting AFAI in an open geometry (i.e., a geometry with edges), the system's nontrivial topology gives rise to propagating chiral edge states and novel quantized transport phenomena [2, 91]. Due to the topological and *chiral* nature of the edge states, we expect that interactions will lead to thermalizing behavior at the edge. The competition between thermalization on the one-dimensional edge and MBL of the two-dimensional bulk is a subtle and important issue to explore, in particular, as bulk localization is required to observe quantized edge transport.

To gain insight into the dynamics at the edge, we numerically investigated the AFI in an

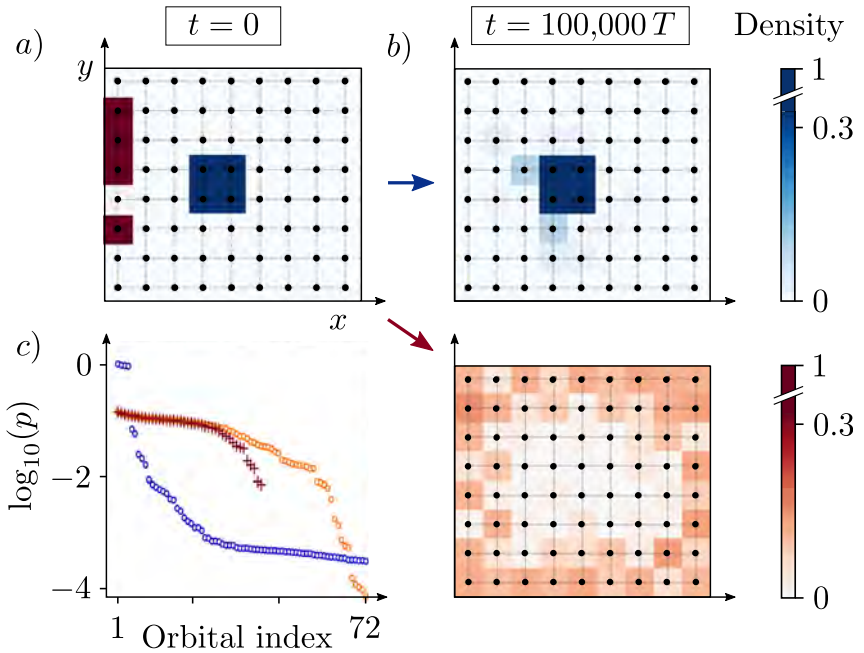

Figure 5.4: Time evolution of 4 particles on a square lattice of 8×9 sites (black dots) with open boundary conditions. We simulate model (ii), with time-independent disorder, and parameter values $W = \omega$, $\lambda = 0.1W$, and $\alpha = \frac{1}{16}$. a) The two different initial site occupations considered, indicated by red and blue squares. b) The cluster initialized in the bulk (blue, upper panel) remains stable over 10^5 periods. For the edge initialization (red, lower panel), the particle density is homogenized around the perimeter, with negligible leakage into the bulk. c) Eigenvalues of the one-body reduced density matrix, $\rho_R^{(1)}$. For the bulk initialization (blue), we take R to be the full lattice; a clear gap between near-unity and smaller eigenvalues indicates localization. For the edge initialization, we consider R as the full lattice (orange), or only the sites along its edge (red). The nearly identical plateaus of eigenvalues in the two cases indicate thermalization confined to the edge.

open geometry. We simulated model (ii) discussed above, for 4 particles moving in a rectangle of 9×8 sites with open boundary conditions [4]. We initialized the particles either in a droplet of 2×2 sites in the center of the system, or in sites along the edge (Fig. 5.4a). In Fig. 5.4b, we show the corresponding particle densities after time-evolution for $100,000$ driving periods. Even after this very long evolution the droplet profile has only slightly broadened, indicating that the bulk acts localized on this time scale (and likely indefinitely). For the edge initialization, the particle distribution has homogenized around the perimeter [5], and broadened in a narrow strip near the edge. We have further confirmed that, at long times, the system carries a nonvanishing

[4] For real time dynamics we are able to simulate larger systems than for level statistics due to the smaller number of particles and because full diagonalization is not needed.

[5] In the non-interacting, clean limit, the chiral edge mode resides on alternating sites on the edge. The observed distribution is homogeneous on these sites, with remaining fluctuations on other sites due to finite-size effects.

circulating current around its perimeter (see appendix).

To further investigate thermalization, we first define a region R to be "thermalized" if the reduced density matrix on R takes an infinite temperature form, $\rho_R \sim \exp(-\eta \hat{N})$, where $\hat{N}$ is the number operator on R and η is a constant that fixes the particle density. This definition implies, in particular, that on a thermalized region the eigenvalues p_i of the one-body reduced density matrix $[\rho_R^{(1)}]_{\mathbf{r}\mathbf{r}'} \equiv \langle \Psi(t)| c_{\mathbf{r}}^\dagger c_{\mathbf{r}'} |\Psi(t)\rangle$, with $\mathbf{r}, \mathbf{r}'$ in R, are all equal within each particle number sector [154]: $p_i = N/\mathcal{N}_R$, where N is the number of particles, and $\mathcal{N}_R$ is the number of sites in R.

In Fig. 5.4c, we show the eigenvalues of $\rho_R^{(1)}$ after a long time evolution, for both the droplet and edge initializations. The initial states in both cases are four-particle Slater determinants. The corresponding one-body density matrices on regions containing all particles would have four unit eigenvalues, with the rest being equal to zero. For the droplet initialization we choose the region R to be the entire 9×8 lattice; we see that four eigenvalues remain close to one, with only weak correlations among other "natural orbitals." This is a signature of localization [154]. For the edge initialization we show the spectra of $\rho_R^{(1)}$ evaluated on a one-site-wide strip running around the perimeter of the system, and on the whole lattice. For both we find a long plateau of nearly equal eigenvalues signifying thermalization on the edge.

5.4 Discussion.

Our study establishes the AFI as a stable anomalous Floquet phase protected by MBL and opens up several directions for future investigations. First, our results strongly suggest that for finite strengths of disorder and interactions, the bulk remains localized for, at least, time scales that are exponentially long time in the system size, even while the edge thermalizes. This gives promise that the AFI may support quantized transport on all practical/experimental time-scales. We leave a detailed analytical study of the edge-bulk competition in the thermodynamic limit for a future study.

Second, we found that the chiral AFI's edge hosts *protected thermalization*. The competition between thermalizing and MBL regions is a subject of ongoing debate [155], and the AFI may provide an interesting platform for systematically investigating this interplay. For example, consider an AFI punched with holes of circumference $\sim \ell$, typically separated by a distance L. The system can then be viewed as an array of thermalizing regions, each comprised of $\sim \ell$ sites, embedded in a localized background. Tuning ℓ, L allows one to change the volume fraction of thermalizing regions in the system. Thus, the *geometry* of an AFI sample may be used to control and study thermalization.

Chapter 6

Quantized Properties of the Anomalous Floquet Insulator

This chapter is written in collaboration with Mark S. Rudner, Dmitry Abanin, Netanel H. Lindner, and Erez Berg and is being prepared for submission to a journal.

The results of the last chapter strongly suggest that the anomalous Floquet insulator (AFI) is a stable phase in periodically driven systems. The AFI can be seen as the interacting version of the Anomalous Floquet-Anderson Insulator (AFAI) [2], which was introduced in Sec. 2.2.3, and discussed in Chapter 4. Chapter 5 found that the topological properties of the AFAI are captured in a quantized, nonzero magnetization density within regions where all sites are occupied.

This chapter explores the topological properties of the AFI. The results obtained here generalize the results from Chapter 4 to systems of interacting particles. In contrast to the noninteracting special case (the AFAI phase), which is characterized by a single integer-valued invariant, the AFI is characterized by a *family* of invariants, that are encoded in the system's time-averaged magnetization operator. Specifically, the kth topological invariant is associated with k-particle correlations of the system's time-averaged magnetization.

Interestingly, the topological properties of the AFI do no rely on full many-body localization, but rather on *partial* localization, where all Floquet eigenstates with up to k particles (for some finite k) are localized. In this case, the system is characterized by k topological invariants, where the kth invariant is protected by the localization of Floquet eigenstates in the k-particle subspace. This opens up the potential for detecting nontrivial topological signatures in periodically driven systems that are not fully many-body localized.

6.1 Introduction

In recent years, a wide range of new, intrinsically non-equilibrium phases of matter have been found in periodically driven systems [1, 2, 6, 8, 44, 46–52]. These "anomalous" phases are characterized by novel, topologically robust properties of their micromotion (the dynamics of the system that takes place within a driving period), such as frequency-locked oscillations in Floquet time crystals [49, 50], or quantized orbital magnetization density in the two-dimensional Anomalous

Floquet-Anderson Insulator (AFAI) [1, 2, 6].

Disorder plays a crucial role for stabilizing Floquet phases. In particular, in the presence of interactions, disorder-induced many-body localization (MBL) may play a crucial role in stabilizing Floquet phases by providing a mechanism for the system to avoid absorbing energy uncontrollably from the driving field [97]. Importantly, the requirement of many-body localization does not forbid topologically-nontrivial micromotion from taking place during the driving period [7, 49, 50].

In this chapter, we study the topological properties of time-evolution in localized, two dimensional interacting fermionic systems subject to periodic driving (see Fig. 6.1). Starting from the assumption that the system is many-body localized (see Ref. [7]), we show that the system's evolution is characterized by a family of (bulk) topological invariants, $\{\mu_k\}$. The values of these invariants are encoded in the long-time-averaged magnetization density operator in the Fock space of the system. Interestingly, in the absence of interactions, only a single one of these invariants (μ_1) can be nonzero; this is the topologically-quantized orbital magnetization found in Ref. [6]. With interactions, higher invariants can become nonzero. Generalizing the orbital magnetization captured by μ_1, these higher invariants can be associated with correlated circulating orbits of two or more particles. The topological protection of each invariant μ_k relies not on full many-body localization in the thermodynamic limit, but rather on *partial* localization (i.e. localization of all states consisting of up to k particles).

The invariants $\{\mu_k\}$ characterize the Fock space evolution operator of the system as a whole, independent of any particular state. Once a specific number of particles is present, and a state specified, the nontrivial topology encoded in the $\{\mu_k\}$ is manifested as a quantized magnetization density in any filled region of the lattice, as schematically depicted in Fig. 6.1.

When one or more of the higher invariants are nonzero, the system is in a new, intrinsically many-body phase which has no equivalent in noninteracting systems. It is not presently clear if nonzero values of the new invariants can be realized together with MBL. However, since the invariants do not rely on full MBL for their protection, it may be possible to see signatures of the new invariants in large, but finite systems. We demonstrate that nonzero values of the higher invariants may be realized in models with correlated hoppings.

The rest of the chapter is organized as follows. In Sec. 6.2, we first briefly review the structure of the Floquet operator in many-body localized systems, and of the orbital magnetization operator (Sec. 6.2 below). Following this, we identify from the time-averaged magnetization operator a set of topological invariants $\{\mu_k\}$ that characterize the AFI phase (Sec. 6.3). After establishing the the topological invariance of the invariants $\{\mu_k\}$, we show that they must be quantized as integers (Sec. 6.3.1), and that nonzero values of the invariants gives rise to quantized bulk magnetization density (Sec. 6.3.2). We support our discussion with numerical simulations (Sec. 6.4), and conclude with a discussion (Sec. 6.5).

6.2 Structure of the Floquet operator

In this chapter we study the dynamics of interacting fermions in a two-dimensional lattice with disorder. The system is subject to periodic driving, described by the time-periodic Hamiltonian $H(t) = H(t+T)$. In the following we assume that the system is fully many-body localized (MBL), due to strong disorder (see Ref. [7]). In this case, the system has a complete emergent set of

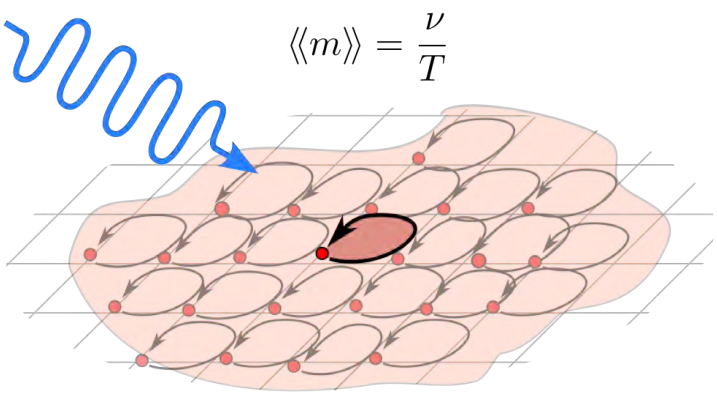

Figure 6.1: Schematic depiction of the two-dimensional anomalous Floquet insulator. This interacting phase is characterized by driving-induced circular motion of bulk particles, and is described by a family of integer-valued topological invariants $\{\mu_k\}$ that are protected by localization. Nontrivial topology reveals itself in a quantized, nonzero magnetization density within regions where all states are filled, given by $\langle m \rangle = \frac{1}{T}\sum_k \mu_k$.

quasilocal integrals of motion [97,112] (LIOMs), $\{\hat{n}_a\}$. The Floquet operator $U(T) = \mathcal{T}e^{-i\int_0^T dt H(t)}$ can be written as $U(T) = e^{-iH_{\text{eff}}T}$ (here and throughout we set $\hbar = 1$), where H_{eff} takes the simple form in terms of the LIOMs $\{\hat{n}_a\}$:

$$H_{\text{eff}} = \sum_{a_1} \hat{n}_{a_1}\varepsilon_{a_1} + \sum_{a_1,a_2} \hat{n}_{a_1}\hat{n}_{a_2}\varepsilon_{a_1 a_2} + \dots . \tag{6.1}$$

Here the coefficients $\varepsilon_{a_1 \dots a_k}$ (referred to as quasienergy coefficients in the following) are real numbers with units of energy. The operators $\{\hat{n}_a\}$ mutually commute and form a complete set of integrals of motion. Finally, the sum $\sum_{a_1 \dots a_k}$ runs over all $\binom{D}{k}$ distinct configurations of the indices $a_1 \dots a_k$, where $\binom{a}{b}$ denotes the binomial coefficient, and D denotes the number of distinct LIOMs in the system (or, equivalently, the dimension of the system's single-particle Hilbert space). For a system on a square lattice with one orbital per unit cell, D is given by A/ℓ^2, where A is the area of the system, and ℓ is the lattice constant. The above form of the Floquet operator implies that each of the LIOMs $\{\hat{n}_a\}$ is preserved by the stroboscopic evolution of the system, and thus the operators $\{\hat{n}_a\}$ can manifestly be seen to be integrals of motion.

Each of the integrals of motion can be written in the form $\hat{n}_a = \hat{f}_a^\dagger \hat{f}_a$, where $\hat{f}_a$ is a (dressed) localized fermionic annihilation operator. The fermionic annihilation operator $\hat{f}_\alpha$ can be constructed from the original lattice annihilation and creation operators as $\hat{f}_a = \sum_\alpha f_a^\alpha \hat{c}_\alpha + \sum_{\alpha\dots\gamma} f_a^{\alpha\beta\gamma}\hat{c}_\alpha^\dagger \hat{c}_\beta \hat{c}_\gamma + \sum_{\alpha\dots\epsilon} f_\alpha^{\alpha\beta\gamma\delta\epsilon}\hat{c}_\alpha^\dagger \hat{c}_\beta^\dagger \hat{c}_\gamma \hat{c}_\delta \hat{c}_\epsilon + \dots$, where $\hat{c}_\alpha$ annihilates a fermion on site α in the lattice. In this way, the LIOM operators $\{\hat{n}_a\}$ count the number of fermions such that $\sum_a \hat{n}_a$ gives the total number of fermions in the system. Moreover, each integral of motion $\hat{n}_a$ is localized around a particular location $\mathbf{r}_a$ in the system[1]. Specifically, the magnitude of the

[1]The point $\mathbf{r}_a$ may for instance be defined as $\mathbf{r}_a = \frac{\sum_k \sum_{\alpha_1\dots\alpha_k} |f_a^{\alpha_1\dots\alpha_k}|^2 (\mathbf{r}_{\alpha_1}+\dots\mathbf{r}_{\alpha_k})}{\sum_k \sum_{\alpha_1\dots\alpha_k} |f_a^{\alpha_1\dots\alpha_k}|^2}$.

coefficient $f_a^{\alpha_1\ldots\alpha_k}$ decreases exponentially with the distance δ from any of the sites $\alpha_1\ldots\alpha_k$ to $\mathbf{r}_a$: $f_a^{\alpha_1\ldots\alpha_k} \sim e^{-\delta/\xi}$, where ξ is the localization length in the system. We refer to the operators $\{\hat{n}_a\}$ as localized integrals of motion (LIOMs) in the following. In addition to the operators $\{\hat{n}_a\}$ being localized, the quasienergy coefficients $\{\varepsilon_{a_1\ldots a_k}\}$ also exhibit similar localized behavior. Specifically, $\varepsilon_{a_1\ldots a_k}$ decays as $e^{-d/\xi}$, where d is the distance between any two of the LIOMs $a_1\ldots a_k$.

The LIOM decomposition above defines a labelling for the Floquet eigenstates, which we make use of in the following. Specifically, we let $|\Psi_{a_1\ldots a_k}\rangle$ denote the k-particle Floquet eigenstate which satisfies $\hat{n}_a|\Psi_{a_1\ldots a_k}\rangle = |\Psi_{a_1\ldots a_k}\rangle$ if $a \in \{a_1\ldots a_k\}$, while $\hat{n}_a|\Psi_{a_1\ldots a_k}\rangle = 0$ if $a \notin \{a_1\ldots a_k\}$. In the same way, we let $E_{a_1\ldots a_k}$ denote the quasienergy associated with the Floquet eigenstate $|\Psi_{a_1\ldots a_k}\rangle$. The quasienergy $E_{a_1\ldots a_k}$ can be found from the quasienergy coefficients as

$$E_{a_1\ldots a_k} = \sum_{n_1=1}^{k} \varepsilon_{a_{n_1}} + \sum_{n_1,n_2=1}^{k} \varepsilon_{a_{n_1}a_{n_2}} + \ldots. \tag{6.2}$$

In the following, we use the LIOM structure of the Floquet operator to identify the invariants $\{\mu_k\}$ that characterize the AFI phase. As mentioned in the introduction of this section, these invariants are encoded in the time-averaged magnetization density operator of the system. Before we identify the invariants we therefore briefly review the properties of orbital magnetization in two-dimensional systems.

6.2.1 Characterization of micromotion

As mentioned in the introduction, the topological properties of the system are encoded in the system's micromotion, specifically in circulating currents within the system. Circulating currents are reflected in the system's magnetization density. In this section, we therefore discuss the magnetization density operator and its properties.

In two-dimensional systems, magnetization density m_p in a given plaquette p measures the total current that encircles the plaquette. It can be defined from the response of the Hamiltonian to the insertion a magnetic flux in the plaquette p[2]:

$$m_p(t) = -\frac{\partial H(t)}{\partial \phi_p}, \quad \phi_p = \int_p d^2r\, B(\mathbf{r}), \tag{6.3}$$

where the integral is taken over the area of plaquette p.

As defined above, the magnetization density operator depends on the gauge used to implement the magnetic flux ϕ_p. However, expectation values of M are *gauge-independent* when evaluated in states where the particle density $\rho_\alpha \equiv \hat{c}_\alpha^\dagger \hat{c}_\alpha$ is stationary. More generally, we define $\langle\mathcal{O}\rangle_\tau \equiv \frac{1}{\tau}\int_0^\tau dt\, \langle\psi(t)|\mathcal{O}(t)|\psi(t)\rangle$ as the time-averaged expectation value of an operator $\mathcal{O}(t)$ in the state $|\psi(t)\rangle$. The time-averaged magnetization $\langle m_p\rangle_\tau$ is then gauge-independent if $\langle\dot{\rho}_a\rangle_\tau = 0$ (see Appendix **??** for proof). Importantly, in an MBL system, *any* state is stationary in the long-time limit since $\lim_{\tau\to\infty}\langle\dot{\rho}\rangle_\tau = 0$. Hence the long-time average $\langle\!\langle m_p\rangle\!\rangle \equiv \lim_{\tau\to\infty}\langle m_p\rangle_\tau$ is always gauge-independent.

[2]In this work, magnetic field has dimensions of [1/Area], such that the Aharonov-Bohm phase acquired by following a closed path equals the enclosed magnetic flux.

The magnetization density is related to the current through Ampere's law. Letting $I_{pq}(t)$ denote the bond current operator on the bond between two adjacent plaquettes p and q (such that positive current is counterclockwise with respect to plaquette p), we have, in any stationary state [6]:

$$\langle I_{pq}\rangle_\tau = \langle m_p\rangle_\tau - \langle m_q\rangle_\tau. \tag{6.4}$$

The above result is the lattice version of Ampere's law in the continuum[3]: $\mathbf{j} = \nabla \times \mathbf{m}$.

Below, we show that the topological invariants characterizing the AFI phase are encoded in the long-time average of the magnetization density operator. For any given initial state $|\Psi\rangle$, the long-time averaged magnetization can be computed as $\langle\langle m_p\rangle\rangle = \langle\Psi|\bar{m}_p|\Psi\rangle$, where

$$\bar{m}_p = \lim_{\tau\to\infty}\frac{1}{\tau}\int_0^\tau dt\ U^\dagger(t) m_p(t) U(t). \tag{6.5}$$

Note that the magnetization density operator is explicitly time-dependent in the Schrodinger picture due to the time-dependence of the Hamiltonian [see Eq. (6.3)]. The magnetization density operator in the Heisenberg picture that enters in the integral above is thus obtained by transforming the time-dependent operator $m_p(t)$ with the time-dependent unitary $U(t)$.

Since the long-time average of any Heisenberg picture operator is diagonal in the basis of Floquet eigenstates[4], $\bar{m}_p$ must be an integral of motion [156]. Thus, it can be written in terms of the of the LIOMs $\{\hat{n}_a\}$ introduced in Eq. (6.1) as

$$\bar{m}_p = \frac{1}{T}\left(\sum_{a_1}\mu^p_{a_1}\hat{n}_{a_1} + \sum_{a_1 a_2}\mu^p_{a_1 a_2}\hat{n}_{a_1}\hat{n}_{a_2} + \dots\right). \tag{6.6}$$

Here, for each term involving a product of k LIOMs, the sum $\sum_{a_1\dots a_k}$ runs over the $\binom{D}{k}$ distinct choices of $a_1\dots a_k$. Noting that $\bar{m}_p$ has units of energy, the magnetization coefficients $\{\mu^p_{a_1\dots a_k}\}$ are dimensionless.

As we now argue, Ampere's law implies that these coefficients vanish as $e^{-d/\xi}$, where d is the distance from the plaquette p to any of the LIOMs $a_1\dots a_k$. To see this, note that the operators $\hat{f}_a$ and $\hat{f}_a^\dagger$ that "flip" the LIOM $\hat{n}_a$ only act on the system locally, in the vicinity of $\mathbf{r}_a$, or hence by the value of $\hat{n}_a$. If $\mathbf{r}_a$ is sufficiently far away from plaquette p, the total current that circulates around plaquette p is not significantly affected when acting on the system with $\hat{f}_a$ or $\hat{f}_a^\dagger$. In this way, $\bar{m}_p$ can only depend significantly on the values of the LIOMs that are located within a localization length of the plaquette. Thus $\mu^p_{a_1\dots a_k}$ decays exponentially as $e^{-d/\xi}$ with the distance d from any of the LIOMs $a_1\dots a_k$ to the plaquette p (due to the exponentially decaying tails of the LIOMs)[5].

[3]This relation implies that magnetization is only well-defined when particle density is stationary: $\nabla\cdot\mathbf{j} = 0$.

[4]In case of degeneracies, one can always pick a basis of eigenstates where $\bar{m}_p$ is diagonal

[5] Specifically, note that the magnetization density in a plaquette can be computed from Ampere's law as $\langle\langle m_p\rangle\rangle = -\Sigma_n\langle\langle I_{p_{n+1}p_n}\rangle\rangle$, where $(p_1, p_2, \dots)$ can be any sequence of neighboring plaquettes that goes from infinity to p. Flipping an l-bit a_0 at some point $\mathbf{r}_0$ away from plaquette p does not affect the value of $\langle\langle m_p\rangle\rangle$since we can always compute this number with a sequence $(p_1, \dots)$ that never approaches the flipped LIOM. The change of the bond currents $\langle\langle I_{p_{n+1}p_n}\rangle\rangle$ along this path is exponentially suppressed in the distance from the flipped LIOM to the path. Thus $\mu^p_{a_1\dots a_k}$must be exponentially suppressed in d/ξ, where d is the distance of any of the LIOMs $a_1\dots a_k$ to plaquette p.

6.3 Topological invariants of the time evolution

We now show that, for each order of the product of LIOMs (i.e., for each value of k), the sum of the magnetization coefficients $\sum_{a_1 \ldots a_k} \mu^p_{a_1 \ldots a_k}$ remarkably does not depend on the location of the plaquette p, and is insensitive to (locality-preserving) perturbations of the system. The sum is given by a universal constant μ_k, which we identify as a topological invariant of the system.

To show that each sum $\sum_{a_1 \ldots a_k} \mu^p_{a_1 \ldots a_k}$ is a topological invariant (for different values of k), we consider the case where the system is confined to a closed geometry, such as, a torus[6] of dimensions $L \times L$. As a first step, we compare the traces of $\bar{m}_p$ and $\bar{m}_q$, in the k-particle subspace, for two neighboring plaquettes p and q. To compute the traces we note that Ampere's law [Eq. (6.4)] dictates that

$$\langle \Psi | \bar{m}_p | \Psi \rangle - \langle \Psi | \bar{m}_q | \Psi \rangle = \langle \Psi | \bar{I}_{pq} | \Psi \rangle, \tag{6.7}$$

where $\bar{I}_{pq} \equiv \lim_{\tau \to \infty} \frac{1}{\tau} \int_0^\tau dt \; U^\dagger(t) I_{pq}(t) U(t)$, Thus, $\langle\!\langle I_{pq} \rangle\!\rangle = \langle \Psi | \bar{I}_{pq} | \Psi \rangle$. The above result holds for any given state $|\Psi\rangle$. Letting $\mathrm{Tr}_k(A)$ indicate the trace of the operator A in the k-particle subspace, we thus have that

$$\mathrm{Tr}_k \bar{m}_p - \mathrm{Tr}_k \bar{m}_q = \mathrm{Tr}_k \bar{I}_{pq}, \tag{6.8}$$

Using the cyclic property of the trace, we note that $\mathrm{Tr}_k \bar{I}_{pq} = \lim_{\tau \to \infty} \frac{1}{\tau} \int_0^\tau dt \, \mathrm{Tr}_k I_{pq}(t)$. Since the current operator is traceless, we find that $\mathrm{Tr}_k \bar{I}_{pq} = 0$, and hence

$$\mathrm{Tr}_k \bar{m}_p = \mathrm{Tr}_k \bar{m}_q. \tag{6.9}$$

Since this relation holds for any two neighboring plaquettes, it must hold for *any* two plaquettes in the lattice.

We now insert the expansion (6.6) of $\bar{m}_p$ into Eq. (6.9). One can verify from combinatorial arguments that $\mathrm{Tr}_k(\hat{n}_{a_1} \ldots \hat{n}_{a_n}) = \binom{D-n}{k-n}$. Using this fact,

$$\mathrm{Tr}_k \bar{m}_p = \sum_{n=1}^{k} \binom{D-n}{k-n} \sum_{a_1 \ldots a_n} \mu^p_{a_1 \ldots a_n}. \tag{6.10}$$

Comparing the traces $\mathrm{Tr}_k \bar{m}_p$ and $\mathrm{Tr}_k \bar{m}_q$ for each value of k, an inductive argument[7] can be used to show that, for each value of k,

$$\sum_{a_1 \ldots a_k} \mu^p_{a_1 \ldots a_k} = \sum_{a_1 \ldots a_k} \mu^q_{a_1 \ldots a_k}. \tag{6.11}$$

[6] In the case of a closed geometry, the definition of $m_p(t)$ from the response of the Hamiltonian to a magnetic flux in Eq. (6.3) technically requires the specification of a compensating magnetic field somewhere else on the torus, since the total magnetic flux through the surface cannot be varied continuously (See Ref. [6]). As we show in Appendix E.1, this fact does not affect any of the conclusions above. Furthermore, the dependence of m_p on the exact implementation of the compensating field is of order $e^{-L/\xi}$, and thus vanishes in the thermodynamic limit.

[7] To see why Eq. (6.11) holds, we note first that Eq. (6.11) trivially follows from Eqs. (6.9) and (6.10) in the case $k = 1$. Additionally, using the same two results, one can show that Eq. (6.11) holds in the case $k = k_0$ if it holds for all values of k smaller than k_0. Hence Eq. (6.11) must hold for all k.

The above result holds for any two plaquettes p and q in the lattice, and hence $\sum_{a_1\ldots a_k}\mu^p_{a_1\ldots a_k}$ must be given by the same value for *all* plaquettes in the lattice[8]:

$$\sum_{a_1\ldots a_k}\mu^p_{a_1\ldots a_k}=\mu_k. \tag{6.12}$$

We now argue that the constant μ_k is a topological invariant of the system in the thermodynamic limit ($L\to\infty$)[9].

To show this, consider smoothly changing the parameters of the system in some region R of the system, in such a way that MBL is not broken. We recall that the coefficient $\mu^p_{a_1\ldots a_k}$ only depends on the details of the system around the plaquette p, up to an exponentially small correction (due to the exponentially decaying tails of the LIOMs). Hence, for a plaquette p_0 located a distance $d\approx L/2$ from the region R, the coefficient $\mu^{p_0}_{a_1\ldots a_k}$ may only change by an amount of order $e^{-L/2\xi}$ during the deformation. These considerations imply that the sum $\sum_{a_1\ldots a_k}\mu^{p_0}_{a_1\ldots a_k}$ remains constant during the deformation in the thermodynamic limit. Noting that the result in Eq. (6.12) holds for any plaquette in the system (including p_0) we conclude that μ_k does not change during the deformation. Since the global parameters of the system can be changed by a sequence of local perturbations of the type above, μ_k must remain invariant under any smooth change of the system that preserves MBL. We thus conclude that μ_k is a topological invariant of the system which can only change its value at a phase transition where the system delocalizes. In the following subsection, we show that μ_k is *quantized*, and must take the value of an integer.

6.3.1 Values of the invariants $\{\mu_k\}$

Here we show that the topological invariants $\{\mu_k\}$ are integers. The approach we use here is analogous to the noninteracting case (see Ref. [6]). We give here an outline of the arguments, while technical details of the proof can be found in Appendix E.2. We find the value of μ_k by computing the trace of $\bar{m}_p$ in the k-particle subspace, $M_k\equiv \mathrm{Tr}_k\bar{m}_p$. Specifically, Eq. (6.10) implies that that $M_k=\sum_n\binom{D-n}{k-n}\mu_n$. Having found the value of M_k for all k, we may infer the values of the invariants $\{\mu_k\}$.

Using Eq. (6.9), i.e., that the value of $\mathrm{Tr}_k\bar{m}_p$ is the same for every plaquette on the lattice, we compute M_k by taking the average value of $\mathrm{Tr}_k\bar{m}_p$ over all plaquettes in the lattice. Noting that there are (L^2/ℓ^2) plaquettes in total, where ℓ is the lattice constant, we thus have $M_k=\frac{\ell^2}{L^2}\sum_p\mathrm{Tr}_k\bar{m}_p$. Explicitly writing out the trace $\mathrm{Tr}_k\bar{m}_p$ in terms of the k-particle Floquet eigenstates, we thus find

$$M_k=\frac{\ell^2}{L^2}\sum_p\sum_{a_1\ldots a_k}\langle\Psi_{a_1\ldots a_k}|\bar{m}_p|\Psi_{a_1\ldots a_k}\rangle. \tag{6.13}$$

[8]Technically, the magnetization operator $\bar{m}_p$ is only defined up to a correction of order $e^{-L/\xi}$ (see Footnote 6) and thus, the above result holds up to a correction of order $e^{-L/\xi}$ for systems of finite size. At the same time, an increase the system size can only change the sum $\Sigma_{a_1\ldots a_k}\mu^p_{a_1\ldots a_k}$ by an amount of order $e^{-L/\xi}$, due to the exponentially decaying tails of the LIOMs. Thus, for systems of finite size, the sum $\Sigma_{a_1\ldots a_k}\mu^p_{a_1\ldots a_k}$. is given by μ_k, where μ_k is the value of the sum in thermodynamic limit.

[9]For a finite system, the fact that $\mu^p_{a_1\ldots a_k}$ is exponentially insensitive to the details of the system far away from the plaquette p means that it may only change by an amount of order $e^{-L/\xi}$ when the system size is increased. This implies that the sum $\Sigma_{a_1\ldots a_k}\mu^p_{a_1\ldots a_k}$ is given by its value in the thermodynamic limit, up to a correction of order $e^{-L/\xi}$.

Recall that $\langle \Psi_{a_1 \ldots a_k} | \bar{m}_p | \Psi_{a_1 \ldots a_k} \rangle$ gives the time-averaged magnetization density $\langle\!\langle m_p \rangle\!\rangle$ of the Floquet eigenstate $|\Psi_{a_1 \ldots a_k}\rangle$ in plaquette p. Thus the sum $\ell^2 \sum_p \langle \Psi_{a_1 \ldots a_k} | \bar{m}_p | \Psi_{a_1 \ldots a_k} \rangle$ gives the total time-averaged magnetization $\langle\!\langle M \rangle\!\rangle \equiv \int d^2\mathbf{r} \, \langle\!\langle m(\mathbf{r}) \rangle\!\rangle$ of the Floquet eigenstate $|\Psi_{a_1 \ldots a_k}\rangle$. In analogy to non-driven systems, where the magnetization of a state gives the response of its energy to a uniform perpendicular magnetic field, the time-averaged magnetization of a Floquet eigenstate gives the response of its *quasienergy* $E_{a_1 \ldots a_k}$ to the application of a uniform perpendicular magnetic field B in the region of support of the state $|\Psi_{a_1 \ldots a_k}\rangle$ (see Appendix E.2):

$$\sum_p \ell^2 \langle \Psi_{a_1 \ldots a_k} | \bar{m}_p | \Psi_{a_1 \ldots a_k} \rangle = -\frac{\partial E_{a_1 \ldots a_k}}{\partial B}. \tag{6.14}$$

As we show in Appendix E.2, the derivative $\frac{\partial E_{a_1 \ldots a_k}}{\partial B}$ can be approximated from the response of the system's quasienergy spectrum to the insertion of a (weak) uniform field $B_0 = \frac{2\pi}{L^2}$ corresponding to precisely one flux quantum piercing the torus. In particular, we show that, even though the system's quasienergy spectrum of undergoes exponentially many avoided crossings under a continuous perturbation, the eigenstates and quasienergies in the presence of the field B_0 are approximately identical to those of the the system in the absence of the field B_0 (for all but a measure zero set of disorder realizations). Specifically, with a probability that goes to 1 in the thermodynamic limit (and for any finite value of k), we may label the Floquet eigenstates $\{|\tilde{\Psi}_{a_1 \ldots a_k}\rangle\}$ of the one-flux system such that, for *each* choice of the LIOM indices $a_1 \ldots a_k$, $|\tilde{\Psi}_{a_1 \ldots a_k}\rangle = |\Psi_{a_1 \ldots a_k}\rangle + \mathcal{O}(\ell/L)$, up to a gauge transformation. With this labelling, the associated quasienergy $\tilde{E}_{a_1 \ldots a_k}$ of the one-flux system satisfies

$$\tilde{E}_{a_1 \ldots a_k} = E_{a_1 \ldots a_k} + B_0 \frac{\partial E_{a_1 \ldots a_k}}{\partial B} + \mathcal{O}(A_S B_0 \sqrt{\ell/L}), \tag{6.15}$$

where A_S is the area of the region where the Floquet eigenstate $|\Psi_{a_1 \ldots a_k}\rangle$ has its support. The correction above is subleading in L, and can be neglected in the thermodynamic limit where $L \to \infty$ while k remains constant. We may thus use Eq. (6.15) to approximate the value of the derivative $-\frac{\partial E_{a_1 \ldots a_k}}{\partial B}$.

Making this substitution in Eq. (6.14), and using Eq. (6.13), along with $B_0 = 2\pi/L^2$, we find

$$M_k = \frac{1}{2\pi} \sum_{a_1 \ldots a_k} (\tilde{E}_{a_1 \ldots a_k} - E_{a_1 \ldots a_k}). \tag{6.16}$$

As our next step, we relate the sum on the right hand side above to the determinants of the Floquet operators $U_1(T)$ and $U(T)$ of the one- and zero-flux systems, respectively. Letting $|A|_k$ denote the determinant of the operator A within the k-particle subspace, we find that

$$\frac{|U_1(T)|_k}{|U(T)|_k} = e^{-i \sum_{a_1 \ldots a_k} (\tilde{E}_{a_1 \ldots a_k} - E_{a_1 \ldots a_k}) T}. \tag{6.17}$$

Crucially, the determinants $|U_1|_k$ and $|U|_k$ must be identical. To see this, note that the determinant of any time-evolution operator can be found from the time-averaged trace of the Hamiltonian: $|U(T)|_k = \exp(-i \int_0^T dt' \, \mathrm{Tr}_k H(t))$ (for proof, see e.g., Ref. [5]). Since the insertion of a magnetic flux only modifies off-diagonal elements of the Hamiltonian (in position space), the trace of the

Hamiltonian is unaffected by the magnetic field B_0. We thus find $|U_1(T)|_k = |U(T)|_k$. The expression in Eq. (6.17) must therefore be equal to 1. By comparing with Eq. (6.16), we conclude that M_k must be an integer multiple of $1/T$.

We now use this result to infer the values of the invariants $\{\mu_k\}$. According to Eq. (6.10), $M_k = \frac{1}{T}\sum_{n=1}^{k} \binom{D-n}{k-n}\mu_k$. From this fact, along with the result that M_k is an integer multiple of $1/T$ for any value of k, it follows that each μ_k must be an integer[10].

6.3.2 Quantized magnetization density in fully occupied regions

Here we show that the values of the invariants $\{\mu_k\}$ can be measured directly from the magnetization density within a region of the system where all sites are occupied.

We consider preparing the system in a state $|\Psi\rangle$ by filling all sites in some finite region of the lattice, of linear dimension d, with all sites outside remaining empty. For a plaquette p located deep within the fully occupied region, we find the time-averaged magnetization density as $\langle\!\langle m_p \rangle\!\rangle = \langle \bar{m}_p \rangle$, where we introduced the shorthand $\langle \mathcal{O} \rangle \equiv \langle \Psi | \mathcal{O} | \Psi \rangle$. Using the expansion of $\bar{m}_p$ in Eq. (6.6), we thus find:

$$\langle\!\langle m_p \rangle\!\rangle = \sum_{a_1} \frac{\mu^p_{a_1}}{T} \langle \hat{n}_{a_1} \rangle + \sum_{a_1 a_2} \frac{\mu^p_{a_1 a_2}}{T} \langle \hat{n}_{a_1} \hat{n}_{a_2} \rangle + \ldots . \tag{6.18}$$

To analyze the sum, we note that, for a LIOM $\hat{n}_a$ whose center $\mathbf{r}_a$ is located deep within the filled region, all sites where $\hat{n}_a$ has its support are occupied. Thus[11] $\hat{n}_a|\Psi\rangle = |\Psi\rangle + \mathcal{O}(e^{-d/\xi})$. Here the correction arises from the exponentially decaying tail of $\hat{n}_a$ outside the filled region. For terms in the above equation where the centers of all the LIOMs $a_1 \ldots a_k$ are located near the plaquette p, the above result implies that $\langle \hat{n}_{a_1} \ldots \hat{n}_{a_k} \rangle = 1 + \mathcal{O}(e^{-d/\xi})$, since all of the LIOMs $\hat{n}_{a_1} \ldots \hat{n}_{a_k}$ are located deep within the initially occupied region. For all remaining terms in Eq. (6.18), one or more LIOMs $a_1 \ldots a_k$ are located outside the filled region, and thus at least a distance $\sim d$ from the plaquette p. In this case, the magnetization coefficient $\mu^p_{a_1 \ldots a_k}$ is exponentially small in d/ξ [see the discussion below Eq. (6.6)]. For both categories of terms, we thus find that we can set $\langle \Psi | \mu^p_{a_1 \ldots a_k} \hat{n}_{a_1} \ldots \hat{n}_{a_k} | \Psi \rangle = \mu^p_{a_1 \ldots a_k}$, at the cost of a correction which is exponentially small in d/ξ. Doing this, we obtain

$$\langle\!\langle \bar{m}_p \rangle\!\rangle = \frac{1}{T} \left(\sum_{a_1} \mu^p_{a_1} + \sum_{a_1 a_2} \mu^p_{a_1 a_2} + \ldots \right) + \mathcal{O}(e^{-d/\xi}).$$

Using Eq. (6.12), we identify the kth sum above as the invariant μ_k. Thus, since $\langle \Psi | \bar{m}_p | \Psi \rangle = \langle\!\langle m_p \rangle\!\rangle$, we find

$$\langle\!\langle m_p \rangle\!\rangle = \sum_k \mu_k + \mathcal{O}(e^{-d/\xi}). \tag{6.19}$$

[10] Specifically, setting $k = 1$, we find $\mu_1 = M_1 T$, which implies that μ_1 is an integer. Next, setting $k = 2$, we find $M_2 T = \mu_2 + (D-1)\mu_1$. Since both μ_1 and $M_2 T$ are integers, it follows that μ_2 must itself be an integer . By repeating this argument for higher values of k, we conclude that μ_k is an integer for each value of k.

[11] To see this, note that $\hat{n}_a|\Psi\rangle = (1 - f_a f_a^\dagger)|\Psi\rangle$. The operator $f_a^\dagger$ is a polynomial in $\{c_\alpha\}$ and $\{c_\alpha^\dagger\}$, where each term has the net effect of creating one fermion in the region around LIOM a. Since all sites near the LIOM a are occupied for the state $|\Psi\rangle$, $f_a^\dagger|\Psi\rangle = 0$, and thus $\hat{n}_a|\Psi\rangle = |\Psi\rangle$.

Hence the magnetization density deep within the filled region is given by the sum of the invariants $\{\mu_k\}$[12]

6.3.3 Nature of higher-order invariants

Above, we found that the AFI phase is characterized by a family of topological invariants $\{\mu_k\}$. In this subsection, we briefly discuss the nature of this family of invariants.

The invariant μ_k is computed from the terms in the expansion (6.6) that involve products of k LIOMs (i.e. k fermions). Thus μ_k encodes information about the k-body correlations of the system. In the absence of interactions, where the evolution of the system is described by a slater-determinant of time-evolved single particle states, correlations between two or more particles are absent, and we must have $\mu^p_{a_1 \dots a_k} = 0$ when $k \geq 2$. Therefore, only the invariant μ_1 may be nonzero when interactions are absent. In this case, the system is in the AFAI phase [1,2,6], and we identify μ_1 as the "winding number" invariant that characterizes this phase.

The arguments in the end of Sec. 6.3 show that the invariant μ_k cannot change under smooth deformations that keep the Floquet eigenstates with k particles or less localized. Hence, the "higher" invariants $\mu_2, \mu_3, \dots$ must all take value zero for an AFI that can be smoothly connected to the noninteracting AFAI without breaking MBL (for instance if the Hamiltonian of the AFI is constructed by adding weak interactions to an AFAI). However, it is in principle possible for the higher invariants to be nonzero. Systems characterized by nonzero values of one or more of the invariants $\mu_2, \mu_3 \dots$ will be in a new, intrinsically interacting phase that cannot exist in the absence of interactions. In Appendix E.3, we demonstrate that a nonzero value of the invariant ν_2 can be realized in a model with correlated hopping. A more detailed study of the nature of these additional invariants is beyond the scope of this work, but may be an interesting direction for future studies.

We note that the topological protection of the invariant μ_k does not require full many-body localization. While the discussion above for simplicity assumed the system to be MBL, the arguments proving the topological invariance and quantization of μ_k only rely on Floquet eigenstates with k particles or less being localized[13]. In this way, the topological robustness of the system relies on *partial localization* (i.e., localization of the system when constricted to sectors with up to k particles, where k is finite). In particular, if all Floquet eigenstates with k_0 particles or less are localized, the system is characterized by the k_0 topological invariants $\mu_1 \dots \mu_{k_0}$. The invariant μ_k can only change its value at phase transitions where the Floquet eigenstates with k particles or fewer become delocalized. From this perspective, the 2D AFI can exhibit non-trivial topological properties in the presence of interactions, regardless of whether or not it is MBL in the thermodynamic limit.

[12] To see that the sum in Eq. (6.19) converges, note that the coefficient $\mu^p_{a_1 \dots a_k}$ vanishes when the distance from the LIOM centers $\mathbf{r}_{a_1} \dots \mathbf{r}_{a_k}$ to the plaquette p is much larger than ξ. When k is much larger than the number of LIOMs whose centers are located within a radius $\sim \xi$ from the plaquette p, the coefficient $\mu^p_{a_1 \dots a_k}$ therefore vanishes, and we conclude that μ_k must equal zero.

[13] When restricted to the the subspace with n particles or less, the Floquet operator can in this case be represented in terms of LIOMs $\{\hat{n}_a\}$ as in Eq. (6.1). Here the LIOM operators $\{\hat{n}_a\}$ have all of the properties described in Sec. 6.2 when restricted to the subspace with k particles or less. The arguments proving the topological invariance of the invariant μ_{k_0} only relies on the existence of LIOMs in the subspaces with k particles or less, and hence μ_{k_0} will be a topologically-protected integer for all k_0 smaller than k.

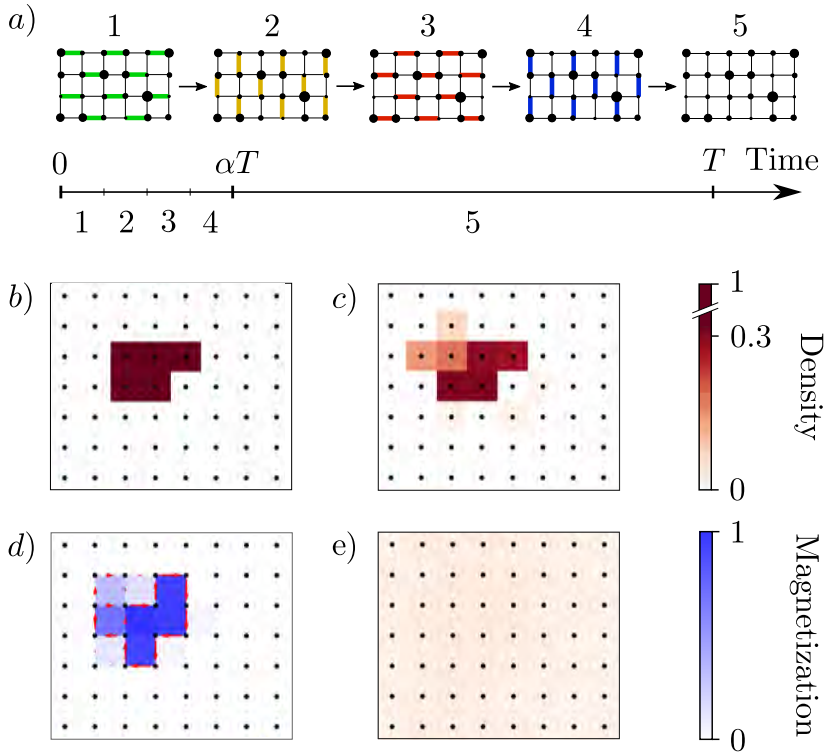

Figure 6.2: a) Schematic depiction of the model studied in Sec. 6.4. Each driving period consists of five segments. During the first four segments, time-dependent hopping $H_{\mathrm{id}}(t)$ [Eq. (6.20)] transfers particles between A and B sublattices, cyclically around plaquettes of the lattice, while disorder H_{dis} and interactions H_{int} [Eq. (E.66)] are always present. b-e): Particle density and magnetization density in a system with 5 particles on a square lattice of 7×8 sites. The sites are indicated by black dots. b) Initial density in the system, c) Density after 14400 periods for a realization with parameters $\alpha = 1/16$, $W = 2\pi/T$, $V = 0.5W$. d) Time-averaged magnetization density over 14400 periods for the same system. e) Particle density after 14400 periods, for a realization with parameters for $\alpha = 1/16$, $W = 2\pi/T$, $V = 2W$.

6.4 Numerical simulations

To support our conclusions above, we numerically investigate the magnetization density of a droplet of particles for the model also studied in Ref. [7]. We study a system on a two-dimensional bipartite square lattice with periodic boundary conditions. The Hamiltonian of the system is given by $H(t) = H_{\mathrm{dr}}(t) + H_{\mathrm{dis}} + H_{\mathrm{int}}$, where $H_{\mathrm{dr}}(t)$ consists of piecewise-constant, time-dependent hopping, while H_{dis} and H_{int} are time-independent disorder and interaction potentials. The driving protocol is divided into five segments, and is schematically depicted in Fig. 6.2. The first four of the segments each have duration $\alpha T/4$, while the fifth segment has duration $(1-\alpha)T$, where the parameter α is a number between 0 and 1. In the fifth segment, $H_{\mathrm{dr}}(t) = 0$. In the remaining four segments, $H_{\mathrm{dr}}(t)$ turns hopping on for the four different bond types in a

counterclockwise fashion, as indicated in Fig. 6.2, such that, in the nth segment (where $n \leq 4$),

$$H_{\rm dr}(t) = J \sum_{\mathbf{r}\in A} (\hat{c}^\dagger_{\mathbf{r}+\mathbf{b}_n} \hat{c}_{\mathbf{r}} + \text{h.c.}). \tag{6.20}$$

Here $\hat{c}_{\mathbf{r}}$ annihilates a fermion on the site with location $\hat{r}$, and the sum runs over sites $\mathbf{r}$ in sublattice A. The vectors $\{\mathbf{b}_n\}$ are given by $\mathbf{b}_1 = -\mathbf{b}_3 = (\ell, 0)$ and $\mathbf{b}_2 = -\mathbf{b}_4 = (0, \ell)$, where ℓ is the lattice constant. The tunneling strength J is given by $\frac{2\pi}{T}$, such that $H_{\rm dr}$ generates a perfect transfer of particles across the active bonds in each of the first four segments. The terms $H_{\rm int}$ and $H_{\rm dis}$ that contain disorder and interactions are given by

$$H_{\rm dis} = \sum_{\mathbf{r}} w_{\mathbf{r}} \hat{\rho}_{\mathbf{r}}, \quad H_{\rm int} = V \sum_{\langle \mathbf{r}\mathbf{r}'\rangle} \hat{\rho}_{\mathbf{r}} \hat{\rho}_{\mathbf{r}'}. \tag{6.21}$$

For each site, $w_{\mathbf{r}}$ is a random number in the interval $[-W, W]$, and $\hat{\rho}_{\mathbf{r}} \equiv \hat{c}^\dagger_{\mathbf{r}} \hat{c}_{\mathbf{r}}$ denotes the occupancy on site $\mathbf{r}$. The parameter V has units of energy and denotes the strength of the interactions.

The model above was studied in Ref. [7], and was found to remain stable on all numerically accessible time-scales in the regime where $1/\alpha T \gg W \gg V$. Here the parameter α controls how rapidly the "hopping pi-pulses" are applied, and was found to control the localization properties of the model. In this section, we study the model in the same regime, and compute the magnetization of a droplet of particles. We consider a single realization of the model, with 6 particles on a lattice of 7×6 sites with periodic boundary conditions. In the simulation, we set $W = 2\pi/T$, $V = 0.5\,W$, and $\alpha = 1/16$, which, following the results in Ref. [7] appears to bring the model into the localized regime.

Since the model is obtained by adding weak interactions to a model of the AFAI with winding number 1 (see Refs. [2, 6]), we that expect $\mu_1 = 1$, while $\mu_k = 0$ for all other values of k (see the discussion in Sec 6.3.3). When the system is completely filled with particles, the average magnetization density in the system $m_{\rm av} \equiv \frac{1}{D}\sum_p \langle\!\langle m_p \rangle\!\rangle$ is given by $1/T$. Here $D = L^2/\ell^2$ is the number of plaquettes in the system. Noting that the completely filled system contains D particles, we expect that that average magnetization density in the system with a finite number of particles n is given by n/DT. Following these considerations, we use the normalized average magnetization density $\bar{m}_{\rm av} \equiv m_{\rm av} D/n$ to probe the topological properties of the model, with $\bar{m}_{\rm av} = 1/T$ indicating nontrivial topology.

We initialized the system by filling a small region of the lattice with particles (the particle density of the initial system is shown in Fig. 6.2a). We then evolved this state through 14400 driving periods. The resulting final particle density is shown in Fig. 6.2b. From the time-average bond-currents, we calculated the time-averaged magnetization density. We show in Fig. 6.2c the local bond-current and magnetization density in the system, averaged over the first 14000 periods. With the 5 particles present, the normalized average magnetization density in the system was found to be $\bar{m}_{\rm av} = -1.0001/T$, in good agreement with the predicted quantized value.

6.5 Discussion

In this chapter, we studied the topological properties of the two-dimensional anomalous Floquet insulator. We identified a family of topological invariants that are encoded in the time-averaged

magnetization operator, and characterize the phase. Importantly, the nontrivial topological properties of the system does not rely on full many-body localization, but rather on *partial localization*, where the system remains localized up to a finite number of particles.

Interestingly, we find that the AFI is not characterized by a single invariant, but rather a *family* of invariants. The nature of these invariants is not clear at this point, and a characterization of their properties will be an interesting direction of future studies. In particular, since their existence does not rely on full many-body localization, the additional topological invariants may lead to experimental signatures in the prethermal dynamics of the system (regardless of whether or not the system is fully MBL).

Part III

Topological Pumping Effects in Periodically Driven Systems

Chapter 7

Topological Floquet-Thouless Energy Pump

This chapter is published in Physical Review Letters **120***, 150601, 2018 (Ref. [8]) by Michael H. Kolodrubetz, FN, Takahiro Morimoto, Snir Gazit, and Joel E. More. MHK, who is first author in Ref. [8], is the primary contributor to this chapter. The author of this thesis, who is second author in Ref. [8], contributed by connecting the studied phenomenon studied with the quantized magnetization of the AFAI. This allowed for identification of the pumped quantity in the model, and contributed to identifying disorder as a factor that stabilizes the effect. The author of this thesis moreover took part in the writing and editing of the manuscript.*

Parts 1 and 2 of this thesis has focused on topological phases of matter in periodically driven systems. Importantly, however, topological phenomena can arise in many other ways than as phases of matter[1]. There are multiple examples of physical effects which are not manifestly of solid-state nature, but still exhibit the universality and robustness characteristic of topological phenomena. Notable examples of such topological phenomena include quantized adiabatic pumping effects [9, 65], or topologically-protected modes in photonic crystals [59, 82–85] and mechanical metamaterials [86–88].

In the same way that topological phenomena arise outside the world of solid-state physics, the topological classification of phases of matter (in nondriven or driven systems) can be applied far beyond the originally-imagined solid-state setting: many of the novel topological effects described in the paragraph above have been theoretically predicted by "mapping" the Hamiltonian of a topological insulator to a non-solid state setting. For instance, Thouless' charge pump is constructed by by letting a tunable parameter replace crystal momentum of a Chern insulator (see Sec. 1.2) [65]. Similarly the nontrivial photonic effects described in Sec. 2.4 arise when wavefunctions in a topologically-nontrivial lattice model are replaced with the electromagnetic field in an analogous photonic crystal [82].

[1]Here "topological" means that the effects are a topologically-protected by some well-motivated constraint on the system. For instance, the quantized charge transport in Thouless' adiabatic charge pump (discussed below) is topologically-protected by the adiabaticity of the cycling protocol: the quantized transport resulting from a full tuning cycle Q_{cycle} is not affected by any perturbation of the system, as long as the cycling protocol remains adiabatic (relative to the instantaneous energy gap of the model).

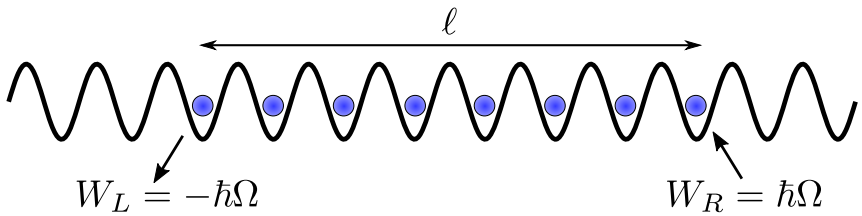

Figure 7.1: Illustration of the topological energy pump. Upon ramping the pump adiabatically around a cycle, the filled region of length $\ell \gg 1$ remains localized, but nevertheless quantized work is performed at the edges of the filled region in quanta of the drive energy $\hbar\Omega$.

Using a similar approach as the one discussed above, Chapters 7-8 explores analogous novel effects in periodically driven systems, exploiting the theoretical results that were described in Chapters 1-6. The phenomena described in Chapters 7-8 are of topological nature, but arise in different systems than the solid-state settings considered in Chapters 1-6. Below, Chapter 7 explores the dimensional reduction of the AFI to an adiabatic pump, analogously to Thouless' charge pump [65]. As the following discussion shows, the adiabatic pumping parameter, together with the periodic driving field, can lead to a topologically-robust energy pumping effect.

7.1 Introduction

The Thouless charge pump serves as a simple yet fundamental example of topology in quantum systems [65]. The hallmark of this effect is the transport of a precisely quantized amount of charge during an adiabatic cycle in parameter space. This remarkable phenomenon has been demonstrated experimentally in various physical systems such as few-body semiconductor quantum dots [157–160] and more recently in a one-dimensional chains of ultra-cold atoms trapped in an optical lattice [161–163].

Recently, the classification of topological phases of matter has been extended to periodically driven (Floquet) systems far from equilibrium [1, 5, 23, 42, 44]. In particular, periodic driving can lead to new topological phases that have no analogy in undriven systems [2, 44–50, 55, 56, 142, 164–169], an idea which has been confirmed experimentally [54, 60]. A natural question to ask is whether these far-from equilibrium systems can also exhibit new topological pumping effects?

In this chapter, we answer this question in the affirmative by explicitly constructing a generalized adiabatic pump in a Floquet system. We find a novel phase in which energy, rather than charge, undergoes quantized pumping. Specifically, upon adiabatic cycling of a particular parameter, partially filled systems in this phase transport energy from one side of the filled region to the other, as illustrated in Fig. 7.1. The energy transported per cycle is quantized in units of the drive frequency $\hbar\Omega$.

Using numerical and analytical arguments, we show that this phenomenon is stabilized by disorder and, via many-body localization, remains robust in the presence of interactions. In this way, we demonstrate the existence of a stable topological pump that can only be realized in the presence of periodic driving.

7.2 Model

Let us begin by introducing a simple model that exhibits topological energy pumping, which we will later demonstrate is topologically robust to perturbations. The model consists of a five-step driving protocol, with Hamiltonians $H_j = h_j + h.c.$, where

$$h_1 = -J\sum_{x=1}^{L/2} c^\dagger_{A,x}c_{B,x}, \qquad h_2 = -J\sum_{x=1}^{L/2} e^{i\lambda}c^\dagger_{B,x}c_{A,x+1}$$
$$h_3 = -J\sum_{x=1}^{L/2} c^\dagger_{B,x}c_{A,x+1}, \quad h_4 = -J\sum_{x=1}^{L/2} e^{i\lambda}c^\dagger_{A,x}c_{B,x},$$
$$h_5 = \frac{\Delta}{2}\sum_{x=1}^{L/2}\left(c^\dagger_{A,x}c_{A,x} - c^\dagger_{B,x}c_{B,x}\right) \tag{7.1}$$

acting on L sites with open boundary conditions. The protocol is chosen to be time periodic with $H(t) = H(t+T)$ such that $H(0 < t < T/5) = H_1$, $H(T/5 < t < 2T/5) = H_2$, etc. This model is particularly simple if the tunneling strength J takes the value $J_{\text{tuned}} \equiv 5\hbar\Omega/4$, where $\Omega = 2\pi/T$. At this fine-tuned point, the fermions hop exactly one site at each step, such that a fermion initialized at any site returns to the same site after one driving cycle, as illustrated in Fig. 7.2a.

Using the Floquet formalism, we write the single-particle time evolution U in the form $U(t) = \mathcal{P}(t)e^{-iH_F t}$, where the micromotion $\mathcal{P}(t) = \mathcal{P}(t+T)$ describes the dynamics within each cycle and H_F is the effective Hamiltonian that describes stroboscopic behavior at multiples of the period T [101]. For $J = J_{\text{tuned}}$, the Floquet eigenstates are localized states $|x,\alpha\rangle \equiv c^\dagger_{\alpha,x}|\text{vac}\rangle$. The eigenvalues of H_F, known as quasienergies, are only well-defined modulo $\hbar\Omega$. For a particle initially located on a site in the bulk, the phase $e^{i\lambda}$ acquired during step 2 is cancelled by the phase $e^{-i\lambda}$ during step 4, yielding flat quasienergy bands at $\epsilon^F_{\text{bulk}} = \pm\Delta/5$. However, a particle initially located at site $|1,B\rangle$ or $|L,A\rangle$ is unable to hop during steps 2 and 3, causing it pick up a λ-dependent phase during the driving cycle, which translates into a λ-dependence of these edge state quasienergies (Fig. 7.2b). While the bulk bands are trivial and can be shown to have vanishing Chern number with respect to λ and quasimomentum k [2], the edge states (red and blue) clearly exhibit topologically nontrivial winding. The question, then, is how to characterize and measure the topological properties of this model?

7.3 Topology and measurement.

The main insight for understanding our model comes from noting that the band structure in Fig. 7.2b is identical to that found in the two-dimensional anomalous Floquet insulator (cf. Fig. 1 in Ref. [1]) with the the pump parameter λ playing the role of momentum k_y. In this way, our model is a dimensionally reduced version of the anomalous Floquet insulator [1, 2], in the same way that the Thouless pump may be thought of as the dimensional reduction of a Chern insulator.

[2]Explicitly, if $|u^\alpha_F(k,\lambda)\rangle$ is a single-particle Floquet eigenstate in band α with quasienergy $\epsilon^\alpha_F(k,\lambda)$, then the Floquet Chern number $C_1^{F,\alpha} \equiv \frac{i}{2\pi}\int d\lambda dk\,(\langle\partial_k u^\alpha_F|\partial_\lambda u^\alpha_F\rangle - h.c.)$ vanishes. Note that C_1^F is independent of the choice of origin t_0 used to define $H_F = i\log(U[t_0 \to t_0+T)]/T$.

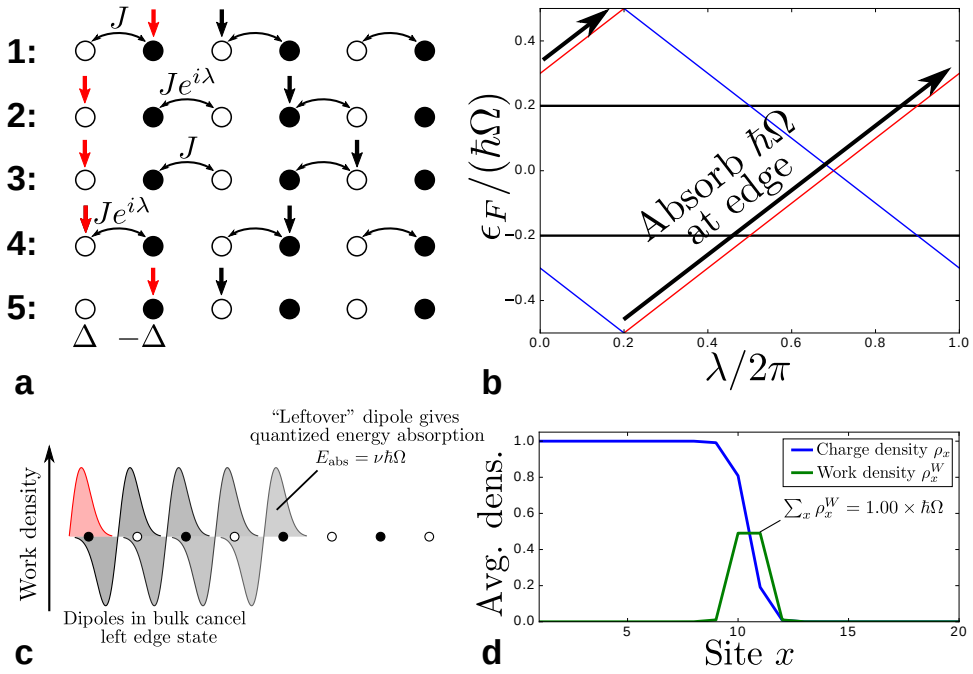

Figure 7.2: (a) Illustration of the anomalous Floquet pump (Eq. 7.1), which involves five steps of period $T/5$ with fined-tuned hopping $J_{\rm tuned} = 5\hbar\Omega/4$. Red and black arrows trace the positions of edge and bulk states respectively. (b) Quasienergy spectrum as a function of the tuning parameter λ show bulk bands (black), left edge state (red), and right edge state (blue). (c) Illustration of response measured in numerics, for which only the left half of the system is filled. (d) Numerical results for the local work and charge density for the model in Eq. 7.1 averaged over a single ramp from $\lambda = 0$ to 2π with $L = 20$, $N_c = 12$, and $N_\lambda = 1$. Data for ρ_x^W is in units of $\hbar\Omega$.

This immediately implies the existence of a topological invariant characterizing our pump, namely the winding number of the micromotion,

$$\nu = \frac{1}{8\pi^2}\int dt d\lambda dk \mathrm{Tr}\left(\left[\mathcal{P}^\dagger\partial_\lambda\mathcal{P}, \mathcal{P}^\dagger\partial_t\mathcal{P}\right]\mathcal{P}^\dagger\partial_k\mathcal{P}\right), \tag{7.2}$$

defined on the compact three-dimensional parameter space (t, λ, k). While the micromotion and thus the winding number in principle depend on the branch cut defining H_F, the fact that Chern numbers of the bulk bands vanish implies that the winding number is independent of this choice [1]. In particular, the winding number for a branch cut at quasienergy ϵ_{cut} in some gap gives precisely the number of edge states crossing that gap. For the model we consider here, $\nu = 1$.

One hint for the observable consequences of this topological index comes from examining the quasienergy spectrum in the presence of open boundary conditions (Fig. 7.2b). Upon adiabatically ramping λ from 0 to 2π, the bulk remains unchanged while the left (right) edge state wraps around the Floquet Brillouin zone, absorbing (emitting) a quantum of energy. Upon completing the cycle, the system returns to its initial electronic state. Therefore the nontrivial topology does not lead to any direct pumping of the fermions. Instead, as we will show, ramping λ performs quantized work on the external driving fields.

Specifically, we now show that the quantized observable is the λ-averaged "force polarization" $P_F \equiv \sum_x x\rho_x^F$, where

$$\rho_x^F = \frac{1}{2}\left\langle\left\{\sum_\alpha c_{\alpha,x}^\dagger c_{\alpha,x}, \partial_\lambda H\right\}\right\rangle \tag{7.3}$$

is the local generalized force required to change λ by a small amount. Here curly braces denote the anti-commutator, $\alpha = \{A, B\}$ sums over sublattices, and the expectation value is taken with respect to an arbitrary quantum state [3]. Changing λ by a finite amount thus requires a local work

$$\rho_x^W = \int \rho_x^F\left[\lambda(t), t\right]\dot{\lambda}(t)dt.$$

While the above expressions hold for arbitrary non-equilibrium situations, the work becomes independent of speed in the limit of slow ramps, for which the wave function is given by (Floquet) adiabatic transport. Thus a finite work polarization $P_W = \int P_F d\lambda = \sum_x x\rho_x^W$ implies that work is done on one half of the system and done by the other half. We will see that quantization of P_W thus implies that this differential work is quantized, as illustrated in Fig. 7.1.

Quantization of P_W follows immediately from dimensionally reducing the anomalous Floquet insulator, as the topologically quantized magnetization [6] immediately reduces to P_W. In practice, the work polarization may be directly measured by filling part of the system and measuring the time-dependence local force ρ_x^F near the edges of the filled region, as illustrated in Fig. 7.1. Within the fully filled or fully empty regions nothing is able to move, hence no work is done: $\rho_x^W = 0$. Furthermore, as the net work on the entire system vanishes, the work done near the left edge of the filled region, W_L, must exactly cancel that done near the right edge: $W_R = -W_L$.

[3] One may readily see this by analogy: if $H(x)$ is a complicated potential acting on a point particle due to the fermions in the lattice, then $-\langle\psi|\partial_x H|\psi\rangle$ is the force acting on x. Note that this is true for arbitrary state ψ, whether or not in equilibrium.

For a filled region of length ℓ lattice sites which is much larger than the localization length ξ, the total work polarization is then given by $P_W^{\text{tot}} \approx (W_R - W_L)\ell/2$. As the average work polarization per filled unit cell is quantized to be $\overline{P}_W = \nu\hbar\Omega$, we also have $P_W^{\text{tot}} = \nu\hbar\Omega\ell$. Equating these expressions, we find that

$$W_R = -W_L = \nu\hbar\Omega. \tag{7.4}$$

Further details on this derivation may be found in the Appendix.

To confirm these predictions, we consider a slightly different setup in which we fill only the left half of the system, i.e., sites 1 through $L/2$. Then the only contribution to the force comes from the density step at $L/2$, such that the entire system absorbs/emits an integer number of photon quanta. Fig. 7.2c illustrates how this emerges from adding the quantized polarization in each localized state. Numerically, we start from this initial state and ramp λ from 0 to $2\pi N_\lambda$ at a constant rate $\dot{\lambda} = 2\pi/(N_c T)$. While slow time-dependence of λ formally breaks the T-periodicity, it has been shown than an appropriate extension of adiabaticity may be defined [64, 170, 171], which is nevertheless subtle due to the presence of resonances which must be crossed diabatically. In practice, we find that an appropriate adiabatic limit is reached for $N_c \gg 1$ and ramping over many adiabatic cycles ($N_\lambda \gg 1$) to remove initial transients [4]. We then expect the total energy absorbed by the system,

$$E_{\text{abs}} \equiv \int \langle \partial_\lambda H \rangle \dot{\lambda} dt, \tag{7.5}$$

to be quantized in units of $\hbar\Omega$. In the Appendix, we show this analytically for our simple model, and we verify this numerically in Fig. 7.2d.

7.4 Disorder and interactions.

Having determined the basic properties of our topological energy pump in an analytically tractable limit, we now demonstrate its robustness to disorder and interactions. One might naively expect this robustness to be trivial, as topological states are often argued to be protected against weak perturbations. However, in the presence of disorder, the ability to adiabatically track a given localized eigenstate is known to be ill-defined, as the eigenstate will undergo weakly avoided crossings on arbitrary length scales [172]. We will address this issue analytically in a follow up work [173], but for now we provide numerical support regarding its stability.

Specifically, we add static chemical potential disorder to our Floquet system,

$$H_{\text{dis}} = \sum_{\alpha,x} w_{\alpha,x} c^\dagger_{\alpha,x} c_{\alpha,x} \ , \tag{7.6}$$

where the disorder is drawn from a box distribution $w_{\alpha,x}/\Omega \in [-W, W]$. We also consider deviating from the fine-tuned limit by a "detuning" α [5]. such that

$$\Delta = \alpha\Omega \ , \ J = J_{\text{tuned}}(1-\alpha). \tag{7.7}$$

[4] In follow up work, we will prove many of our claims in the extreme adiabatic limit $\left|\dot{\lambda}\partial_\lambda \epsilon_F\right| \ll \Delta^2_{\text{miniband}}$, where $\Delta_{\text{minibands}} \sim e^{-L/\xi}$ is the exponentially-small gap between disorder minibands. In the numerics, we are nowhere near this limit, but nevertheless find surprising robustness of our results. We postulate therefore that adiabaticity should be in reference to other characteristic energy scales of the system, such as the hopping amplitude J and the drive frequency Ω. This is equivalent to the statement that $N_c \gg 1$.

[5] This choice of detuning Δ and J simultaneously is not unique. Other choices will give similar results.

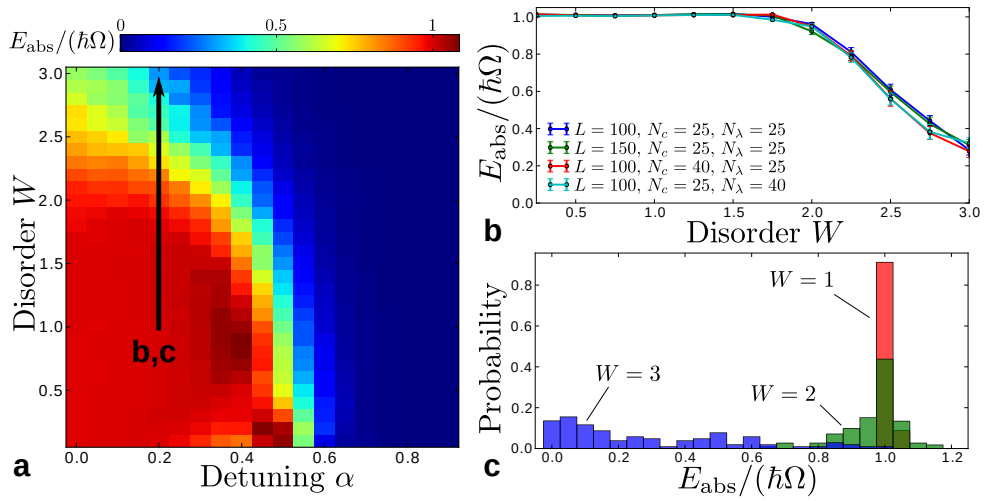

Figure 7.3: (a) Phase diagram of energy pump as a function of disorder W and detuning α (see Eq. 7.7) at fixed $L = 100$ and $N_c = N_\lambda = 25$. In the absence of disorder a phase transition occurs at $\alpha = 1/2$. In the presence of disorder, the topological plateau appears stable over a wide region. Note that some data, particularly at small W, is not fully converged to the $L, N_c, N_\lambda \to \infty$ limit due to large localization length. We analyze this limit further in the Appendix. (b) Cut at fixed $\alpha = 0.2$ showing a slow crossover to topologically trivial independent of L, N_c, and N_λ. (c) Histogram over disorder configurations of $E_{\rm abs}$ at three points along the crossover showing the breakdown of topological quantization.

We then carry out the same procedure as in Fig. 7.2c to measure topological energy absorption.

The disorder-averaged phase diagram for a wide range of disorder strengths and detunings is shown in Fig. 7.3a. There is clearly a wide region with well-quantized energy pumping (red), up to disorder strengths and detuning of order $\hbar\Omega$. In fact, for the majority of the phase diagram, disorder is actually necessary to see quantization of the energy transport. The simplest reason for this is that, in the absence of disorder, any generic model will not be localized and our measurement of $E_{\rm abs}$ at the localized density edge is not meaningful. This is seen in our phase diagram for $\alpha \neq 0$, where a small amount of disorder clearly improves the quantization for the system size shown. Furthermore, we will show in a follow up work [173] that even the appropriately defined clean limit of P_F has a non-topological contribution which is suppressed by localization. In either case, the phase diagram clearly shows a large nearly quantized plateau at weak disorder below the topological transition at $\alpha = 1/2$. For instance, the data in Fig. 7.3b is quantized to within 0.4% and 0.8% at $W = 1$ and $3/2$ respectively for $L = 150$, $N_c = N_\lambda = 40$. We also note that the quantized work polarization is robust to choice of initial conditions, as demonstrated numerically in the Appendix.

At large disorder strengths, we expect a topological transition to a trivial state while maintaining Anderson localization throughout [6]. Surprisingly, we instead find a slow crossover for

[6] Anderson localization should always exist, even in the presence of driving, for this one-dimensional model [174–176].

which energy is still pumped, but not quantized. This is unlike the sharp transition found in the anomalous Floquet Anderson insulator [2], and illustrates a fundamental difference regarding the role of disorder in one dimensional pumps compared to their higher-dimensional counterparts. For the energy pump, one of the tuning parameters, λ, couples strongly to the quasienergies, even when the system is localized. For the anomalous Floquet Anderson insulator, the winding number is defined as in Eq. (7.2) with angles θ_x and θ_y defining twisted boundary conditions in place of the parameters λ and k. For that model, the localization of Floquet eigenstates implies that the change of quasienergy due to either twist angles is exponentially suppressed. In contrast, the "dimensional extension" of the energy pump features Floquet states that are delocalized in the y-direction. Hence the quasienergy spectrum is sensitive to changes of θ_y, i.e., λ.

The breakdown of topological energy pumping may be traced to this increased sensitivity to λ. As the disorder strength W is increased, the L individual quasienergy mini-bands $\varepsilon_n(\theta_x, \lambda)$ may undergo topological gap closings and reopenings, potentially introducing non-trivial Chern numbers. This yields a Floquet branch cut dependence of the winding number $\nu(\epsilon^F_{\text{gap}})$ [1], where in the disordered case the winding number is defined as in Eq. (7.2) with θ_x in place of k_x. As our measurement populates quasienergy states at random (the "infinite temperature" ensemble), we stochastically sample over these winding numbers. Thus the non-quantized energy pump may be thought of as an average of the topological winding number over both gaps and disorder realizations [173].

This argument is consistent with the histogram of E_{abs} in this crossover region (Fig. 7.3c), which shows broadening from a perfectly quantized δ-function peak at $E_{\text{abs}} = \hbar\Omega$ towards statistical ensemble that will eventually be non-topological ($\overline{E}_{\text{abs}} = 0$). Importantly, this breakdown by a proliferation of Berry monopoles is precisely the mechanism that leads to the loss of charge pump quantization in disordered systems [177, 178]. Thus the crossover behavior in our system likely falls into the same class as this undriven case.

Many-body localization. Finally, let us see that our results hold in the presence of many-body localization. We test this by adding nearest neighbor interactions

$$H_{\text{int}} = U \sum_j \left(n_j - \frac{1}{2}\right)\left(n_{j+1} - \frac{1}{2}\right) \tag{7.8}$$

throughout the cycle and simulate the dynamics via exact diagonalization [7]. In Fig. 7.4a, we map out the phase diagram as a function of interaction and disorder strengths. The data confirm that the energy absorption remains beautifully quantized in the topological phase (Fig. 7.4b). We note that, in the absence of disorder, the system is expected to heat to infinite temperature, and thus approach $E_{\text{abs}} = 0$ for $N_\lambda \to \infty$. The remarkable quantization we see is likely a prethermal phenomenon. Interestingly, the data indicate that weak interactions also stabilize the topological phase. While this may be due to a trivial microscopic effect such as shortening of the localization length due to interactions, it leaves open the tantalizing possibility that interactions stabilize the phase and lead to an energy pump that is again topologically protected.

[7] Here we mean nearest neighbors independent of sublattice, i.e., $|1B\rangle$ neighbors $|1A\rangle$ and $|2A\rangle$.

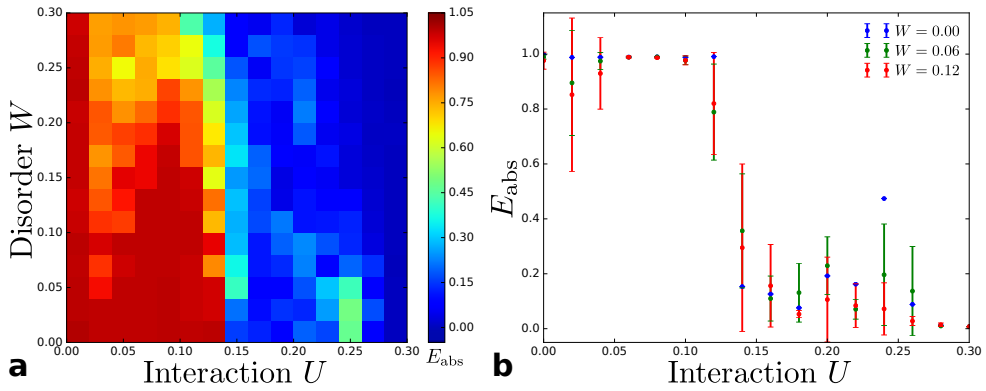

Figure 7.4: Phase diagram of energy pumping in an interacting many-body localized (MBL) system for $\alpha = 0$, $L = 16$, $N_\lambda = 64$, and $N_c = 256$. Error bars in (b) show standard error over a fixed number of disorder configurations. Interestingly, the error bars become smaller – indicating increased stability of the MBL energy pump – in the presence of weak nonzero interactions. E_{abs} is in units of $\hbar\Omega$, while W and U are in units of hopping amplitude J.

7.5 Experiments

The topological energy pump is directly amenable to being realized experimentally, requiring hopping models in one dimension similar to those recently realized in optical lattice charge pumps [161–163]. Instead of measuring local charge, these experiments would simply have to measure local force, ρ_x^F. This should be readily realized by combining adiabatic pump protocols with systems that enable site-resolved measurement, such as optical lattice microscopes [179, 180], trapped ion arrays [181], and other engineered platforms [182–184], where ρ_x^F is simply the measurable local current operator during steps 2 and 4 [185]. In addition to the pulsed multi-step protocols discussed in this work, which are quite natural in such engineered systems, we will show elsewhere that the topological pumping may also occur in monochromatically driven models, such as a driven version of the Rice-Mele model [173, 186]. This opens the intriguing possibility to directly measure the back-action on the drive lasers. For instance, if the periodic driving is realized by a pair of Raman lasers with frequency difference Ω, adiabatic cycling of the pump parameter λ would result in quantized transfer of ν photons from one Raman beam to the other. If one further quantizes the Floquet drive photons, for instance by use of a high-Q cavity, then each adiabatic cycle would directly back-act on the cavity photons. This can, for example, lead to either quantized absorption/emission of cavity photons, whose behavior at low photon number represents an interesting quantum limit of our problem.

7.6 Conclusion

We have introduced a novel topological energy pump which exhibits a new type of topologically protected response with no equivalent in undriven systems. The pump is inspired by a dimensional reduction scheme from the anomalous Floquet insulator, but features fundamentally different

topological protection and transport properties. We note that other topological energy pumps recently introduced in the driven qubit systems derive instead from reducing the Thouless charge pump to zero dimensions, replacing momentum with a magnetic field angle [64] or the phase of a second incommensurate drive [3]. This suggests a number of fascinating future directions from dimensional reduction of other entries in the Floquet periodic table [5, 44], such as the Floquet generalization of the $\mathbb{Z}_2$ pump [9, 187] or fractionalized systems [188]. Furthermore, studying the back-action of our topological pump on a classical or a quantum drive represents an interesting quantum adiabatic limit on statistical mechanics, where pumping of bosonic objects such as the drive photons is a long sought-after goal [189, 190].

Chapter 8

Robustness of Topological Frequency Conversion with a Magnetic Particle

This chapter is written in collaboration with Ivar Martin and Gil Refael, and is being prepared for submission to a journal.

Chapter 7 introduced the topological Floquet-Thouless energy pump. This adiabatic pump can be seen the dimensional reduction of the Anomalous Floquet insulator that was explored in Chapters 4-6. In the system, the combination of a periodic driving field, and an adiabatically-tuned parameter can result in a novel, topologically-robust energy pumping effect.

This chapter explores a different topological energy pumping effect which can also arise in periodically driven systems. Specifically, this chapter studies an implementation of Thouless' adiabatic charge pump with photons in an optical cavity. The model consists of a magnetic (spin-1/2) particle, coupled to a single, circularly polarized cavity mode. The combined state of the particle and the cavity mode describes a spin-1/2 particle in a one-dimensional lattice, where the number of photons in the cavity mode plays the role of the lattice index. When an appropriate, slowly oscillating driving field is applied to the magnetic particle, the analogous lattice model can act as a Thouless pump. This quantized charge transfer in the analogous lattice model implies a topologically-robust transfer of photons to the cavity.

The chapter explores the robustness of the mechanism in further detail, and finds that that the topological energy transfer persists in the presence of dissipation. Interestingly, this chapter finds that the "photon-space Thouless pump" described above can be understood purely as a purely classical effect.

Some of the results in this chapter are obtained using a novel, Floquet-Lindblad master equation, which is derived in Appendix A. This master equation may have applications beyond the system discussed here.

8.1 Introduction

In recent years, theoretical developments have predicted the existence an extensive family of new phases of matter – the topological insulators – that exhibit exotic, but robust phenomena with

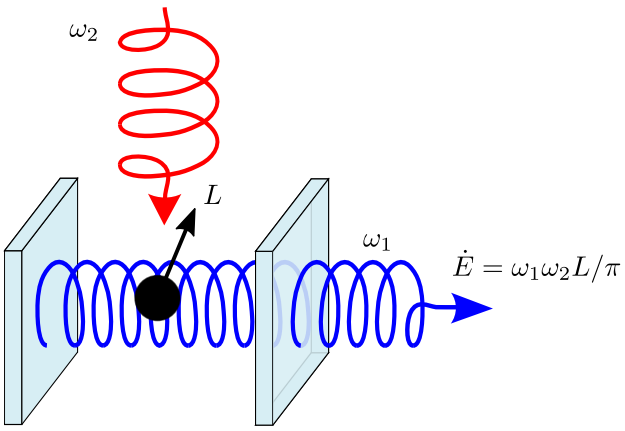

Figure 8.1: Schematic depiction of the setup discussed in this chapter (see main text for details). The model consists of a single magnetic particle (black), with angular moment L, coupled to two circularly polarized electromagnetic modes, where one (red) is externally driven, while the other (blue) is a cavity mode. When dissipative effects of a semitransparent mirror is included in the system's dynamics, the model supports a "lasing" steady state, where the cavity emits photons at the topologically-quantized rate of $\dot{E} = \omega_1\omega_2 L/\pi$.

useful applications [9, 11, 15, 17–19]. More recently, it has been shown that analogous [20–41], or entirely new [1, 2, 5, 42–56] topological phases of matter may be realized in periodically driven systems.

In addition to these advances, other setups that can not necessarily be characterized as phases of matter have been explored for utilizing the novel topological effects that were predicted by the theoretical work above. These systems are analogous to topological insulators, in the sense that the electronic degrees of freedom (or some of them) have been substituted with other degrees of freedom. The most well-known example is perhaps Thouless' adiabatic charge pump [65], which can be seen as a two-dimensional Chern insulator, where one of the spatial dimensions is replaced with a tunable parameter; more recent examples of this idea include Refs. [8, 9, 63, 64], where, for instance, novel, energy pumping effects arise when the tunable parameter is assisted by one or more external driving fields.

The approach which is the focus of this chapter is to use the numbers of photons in electromagnetic modes as an analogy to lattice degrees of freedom, with which nontrivial topology can be realized [3, 63, 191–193]. Specifically, this chapter focuses on the setup discussed in Ref. [3] by Martin, Refael, and Halperin, where a spin is coupled to two circularly polarized electromagnetic modes. Interpreting the photon numbers of the two modes as lattice degrees of freedom, and the spin as an orbital degree of freedom, this setup is equivalent to a two-dimensional, two-band lattice model. In topologically-nontrivial parameter regimes, where the analogous lattice model is a Chern insulator, it was shown in Ref. [3] that the spin effectuates a transfer of energy between the two modes (1 and 2), at the topologically-quantized rate of one photon of mode 1 per cycle of mode 2. This topological effect can be used for amplification of frequency conversion

of electromagnetic radiation.

In this work, we study the setup of Ref. [3] in further detail, in particular focusing on the robustness of the effect. We investigate the experimentally relevant case where one of the modes is an external driving field (such as an externally applied laser) while the other is a degree of freedom in the system (such as a cavity mode), as schematically depicted in Fig.8.1.

We first study the model as a quantum mechanical system. Analyzing the dynamics of the system in detail, we find, among other things, that the energy transfer effect can arise even if the cavity mode is initially empty.

The robustness of the effect becomes clear when dissipation is included. We couple the cavity mode to the external electromagnetic environment, and include the effects extrinsic spin fluctuations to the model, exploring its dynamics using a novel Floquet-Lindblad master-equation approach (Appendix A). With these sources of dissipation and (quantum) noise included, we find that the pumping effect persists, and the system settles to a steady state, where a single photon of the cavity mode is on average emitted per driving period (see Fig. 8.1).

The dissipation makes the cavity field more classical, which hints that the topological energy transfer is not an intrinsically quantum-mechanical effect. We verify this intuition, demonstrating that the topological energy transfer can be understood fully as a classical effect. Specifically, we consider a classical version of the model, where a macroscopic a magnetic particle with angular moment L is coupled to two classical, circularly-polarized modes, with one mode being an external driving force, while the other is a dynamical variable. We show that, for this fully classical model, there exists a topologically nontrivial regime, in which energy is transferred between the two modes at the quantized rate $\dot{E} = \omega_1\omega_2 L/\pi$, where ω_1 and ω_2 are the angular frequencies of the two modes. This demonstrates that the quantized, topological frequency conversion [3] is not of quantum mechanical nature, but can arise in purely classical systems.

To further explore the robustness of the effects, we investigate the dynamics of the system when multiple cavity modes are included in the model. In realistic settings, the magnetic particle is coupled to multiple electromagnetic modes, such as the higher harmonics of the fundamental cavity mode, as well as their time-reversed partners. Exploring the effects of these additional modes on the classical system, we find that the energy transfer effect is stable in certain parameter regimes, and with suitable, experimentally achievable engineering of the cavity.

The results of this work thus indicate that the topological energy transfer is a stable effect, and opens up the possibility for realizing the effect in realistic, macroscopic settings, such as, e.g., with Weyl-semimetals, Yttrium-Iron Garnet (YIG) spheres, or mechanical gyroscopes.

The rest of the chapter is organized as follows: in Sec. 8.2, we present the model we will study in this chapter. Subsequently, we study in Sec. 8.3 the dynamics of the model , treating it as a quantum mechanical system. We consider both the case where dissipation is absent (Sec. 8.3.3) and the case where dissipation is present (Sec. 8.3.4), demonstrating the stability of the effect. Following this, we show in Sec. 8.4 that the effect can be understood as a purely classical phenomenon, by analyzing the analogous classical model. In Sec. 8.5, we investigate the stability of the energy transfer in the classical model when cavity multiple modes are present. We conclude with discussing the results of this chapter, as well as possible experimental realizations (Sec. 8.6).

8.2 Model system

Here we present the model that we will study in this chapter.

8.2.1 Hamiltonian

The setup we consider is an electromagnetic cavity, containing a magnetic particle with angular momentum $\mathbf{L}$. The moment is subjected to two perpendicular, circularly polarized electromagnetic modes $\mathbf{B}_1$, $\mathbf{B}_2$ in the x and y-direction, with angular frequencies ω_1, ω_2. There is also a static magnetic field B_0 in the z-direction that can be used to tune the direction of energy pumping between the modes. The Hamiltonian of the magnetic moment reads

$$H_{\text{mag}} = -gB_0L_z - g(\mathbf{B}_1 + \mathbf{B}_2) \cdot \mathbf{L}. \tag{8.1}$$

Here g is the moment's gyromagnetic ratio, and the circularly polarized modes can be written in terms of their phases $\{\phi_i\}$ and amplitudes $\{B_i\}$ as

$$\mathbf{B}_1 = B_1(0, \sin\phi_1, -\cos\phi_1), \tag{8.2}$$
$$\mathbf{B}_2 = B_2(\sin\phi_2, 0, -\cos\phi_2). \tag{8.3}$$

While in Ref. [3] the amplitudes B_i and phases ϕ_i were considered as externally imposed, here we will make them dynamical variables. The Hamiltonian of the two modes $H_{\text{field}} = \frac{V}{\mu_0}(|\mathbf{B}_1|^2 + |\mathbf{B}_2|^2)$, where μ_0 is the vacuum permeability, and V is the volume of the cavity (assumed the same for both modes). For the circularly polarized modes, the conjugate momentum to the phase ϕ_i is $\frac{V}{\mu_0\omega_i}B_i^2$. Thus, the complete Hamiltonian of the spin-field system reads

$$H = \frac{V}{\mu_0}\left(|\mathbf{B}_1|^2 + |\mathbf{B}_2|^2\right) + H_{\text{mag}}. \tag{8.4}$$

This Hamiltonian describes coupled dynamics of two cavity modes and the magnetic particle. In this chapter, however, we will focus on the case where the energy of the mode mode 1 is provided externally, e.g. by a coherent laser field, while the second mode is free. Later in the chapter we will also allow for damping of the cavity and spin relaxation. Thus, we set $B_1 = B_d$, and $\phi_1 \to \Omega t$, where Ω and B_d are constants (here Ω is the driving frequency). This makes the Hamiltonian explicitly time-dependent, describing a system driven with the period $T = \frac{2\pi}{\Omega}$. In the following, we suppress the subscript 2 from the variables and parameters associated with the second mode.

8.2.2 Rescaling of parameters

In order to simplify the discussion below, we rescale the remaining variables and parameters, to make the dynamical variables dimensionless. Specifically, we introduce an arbitrary scale of action L_0 [1], and define the coefficient $\beta_0 \equiv \sqrt{\omega\mu_0 L_0/V}$ which has the units of magnetic field, (for ω in the THz range, $V \sim 10^{-9}\text{m}^3$, and with $L_0 = \hbar$, this field is of order 10^{-10}T.) From

[1] the value of L_0 does not affect the dynamics of the dimensionless quantities A, ϕ (see below), but only the overall energy scale

this coefficient, we introduce the new parameters $\eta = g\beta_0$, which has units of frequency, and the dimensionless fields $M = B_0/\beta_0$, $A_d = B_d/\beta_0$, $A = B_2/\beta_0$. In terms of these new quantities, the conjugate momentum to ϕ is L_0A^2. We reexpress the system's Hamiltonian in terms of these new quantities, suppressing the constant shift due to the driving field's energy, obtaining

$$H(t) = L_0\omega A^2 + \eta \mathbf{h}\cdot\mathbf{L}. \tag{8.5}$$

Here the dimensionless field $\mathbf{h}$ is given by

$$\mathbf{h}(A,\phi,t) = \begin{pmatrix} A_c\sin(\omega_d t) \\ A\sin(\phi) \\ M - A\cos(\phi) - A_d\cos(\omega_d t)) \end{pmatrix} \tag{8.6}$$

8.3 Quantum treatment

We first perform a quantum mechanical analysis of the problem, where both the magnetic moment and the cavity mode are treated as quantum objects. We first confirm that the the external driving indeed produces pumping, consistent with the result obtained previously in Ref. [3] under the assumption that both electromagnetic modes are classical variables. The full treatment reveals, however, that the dynamical quantum state is highly non-classical, with spin and field states entangled, including the possibility of macroscopic "cat" states. The pumping itself finds a natural interpretation in terms of the one-dimensional Thouless pump. We also include the effects to decoherence and dissipation of cavity mode and spin, and see that it leads to reduced entanglement, collapse of the "cat" states and leads to *stabilization of pumping*, thus foreshadowing the classical interpretation and description of the pumping phenomenon, that is the subject of Section 8.4.

8.3.1 Quantum Hamiltonian

To quantize the model, we treat the observables $\mathbf{L}$, A and ϕ as operators whose pairwise commutators are given by the respective Poisson brackets, with an additional factor of $-i\hbar$. In this way, $\mathbf{L}$ describes a quantum mechanical angular momentum. The quantization of angular momentum implies that its magnitude must be a half-integer $z/2$ multiple of $\hbar$. In order to quantize the cavity field, we introduce the classical variables $Z = Ae^{i\phi}$ and $Z^* = Ae^{-i\phi}$. From the Poission bracket $\{A,\phi\} = \frac{1}{2AL_0}$, it follows that Z and Z^* have the poisson bracket $\frac{i}{L_0}$, where L_0 was an arbitrary scale of action we introduced in Sec. 8.2. With canonical quantization means the associated operators $\hat{Z}$ and $\hat{Z}^\dagger$ have commutator $\frac{\hbar}{L_0}$. With the choice $L_0 = \hbar$, we thus have $[\hat{Z},\hat{Z}^\dagger] = 1$. We identify $\hat{Z}$ as the operator a that annihilates a photon in the cavity mode. Thus, expressing the classical Hamiltonian in terms of Z and Z^*, and using the canonical quantization prescription $Z \to a$, we obtain the following quantum mechanical Hamiltonian describing the system:;

$$H(t) = \hbar\omega\left(\frac{1}{2} + a^\dagger a\right) - \eta\,\mathbf{h}(\mathbf{t})\cdot\mathbf{L} \tag{8.7}$$

where

$$h_x(t) = \frac{a - a^\dagger}{2i}, \tag{8.8}$$
$$h_y(t) = A_d \sin(\omega_d t), \tag{8.9}$$
$$h_z(t) = M - \frac{a + a^\dagger}{2} - A_d \cos(\omega_d t). \tag{8.10}$$

Below, we neglect the constant shift $\hbar\omega/2$ to $H(t)$, due to the cavity's vacuum energy.

8.3.2 Frequency conversion as a photon Thouless pump

Here we demonstrate that, in the frequency conversion regime of the classical model, the quantum Hamiltonian $H(t)$ acts locally in photon space as an adiabatic Thouless pump.

The quantized energy transfer arises when $\eta h \gg \Omega$, and the cavity field energy is in the interval $[E_0, E_1]$, where $E_{0,1} = L_0\omega(M \pm A_d)^2$. The first requirement implies that the scale of M and A_d is large compared to $\frac{\Omega}{\eta}$. In the quantum case where we set L_0 to $\hbar$, the second condition is equivalent to requiring the number of cavity photons to be in the interval $(M - A_d)^2$, $(M + A_d)^2$. Thus the number of cavity photons must also be large compared to $\frac{\Omega}{\eta}$.

To simplify the discussion, we restrict ourself to looking at states where the number of photons is in the interval $[n_0 - \Delta n, n_0 + \Delta n]$ for some large n_0, and $\Delta n \ll n_0$. We may locally write the photon annihilation operator as

$$a = A_0 \sum_n |n-1\rangle\langle n| \left(1 + \mathcal{O}\left(\Delta n/n_0\right)\right), \tag{8.11}$$

where $A_0 \equiv \sqrt{n_0}$ is the dimensionless amplitude of the cavity field around this number of photons.

With this approximation, the Hamiltonian of the system then reads

$$\begin{aligned} H(t) = &-\frac{\eta A_0}{2i}(T - T^\dagger)L_x - \eta A_d \sin(\omega_c t) L_y \\ &- \eta\left(M - \frac{A_0}{2}(T + T^\dagger) - A_d\cos(\omega_d t)\right) L_z \\ &+ \hbar\omega\hat{n} + \mathcal{O}\left(\frac{\eta L \Delta n}{A_0}\right). \end{aligned}$$

Here, $T = \sum_n |n-1\rangle\langle n|$ is the "translation operator" in photon space, and $\hat{n} \equiv a^\dagger a = \sum_n n|n\rangle\langle n|$ is the photon counting operator. Since $A_0 = \sqrt{n_0}$, we see that the last term is supressed by $\frac{\Delta n}{n_0}$ compared to the other terms, and we ignore it below. Apart from the last term, we see that the above Hamiltonian is translationally invariant in photon space, and hence diagonal in the basis of "crystal momentum states" $|k\rangle \equiv \frac{1}{\sqrt{\Lambda}} \sum_{n=0}^{\Lambda} e^{-ikn}|n\rangle$, where Λ is some arbitrary cutoff number of photons. The term $\hbar\omega\hat{n}$ can be eliminated by a rotating frame transformation $|k\rangle \to |k - \omega t\rangle$, and $H(t)$ is then purely diagonal in k. After this transformation, the Bloch Hamiltonian associated to this Hamiltonian is given by

$$H(k, t) = H_0(k - \omega t, t), \tag{8.12}$$

where

$$H_0(k,t) = -\eta \begin{pmatrix} A_d \sin(\Omega t) \\ A_0 \sin(k) \\ M - A_0 \cos(k) - A_d \cos(\Omega t)) \end{pmatrix} \cdot \mathbf{L} \tag{8.13}$$

As a function of k and t, the Hamiltonian $H_0(k,t)$ has $2k$ energy bands, corresponding to different (quantized) value of the projection of the spin onto the field $\mathbf{h}(k-\omega t, t)$. The typical gap ΔE between each band is of the order of $\hbar\eta A_{\min}$, where $A_{\min} = \min|M \pm A_0 \pm A_d|$. As long as $A_{\min} \gg \frac{\Omega}{\eta}$, the change of $H(k,t)$ is therefore slow enough for the system to be considered adiabatic. In this case, if the system is initialized in a particular band (a particular projection fo $\mathbf{L}$ along the field), it will remain there at all times.

The Hamiltonian $H_0(k,t)$ has previously intensively studied in the context of two-dimensional topological insulators, with t replaced by crystal momentum in the y-direction. It is well-established, that, if $A_0 < A_c < A_1$, where $A_0 = |M - A_d|$, $A_1 = |M + A_d|$, the mth lowest band of $H_0(k,t)$ has Chern number $C_m = (2q + 1 - m)$ with respect to k and t [65]. The Hamiltonian $H(t)$ thus describes an adiabatic Thouless pump locally in photon space, with a weak electric field of strength ω applied longitudinally. As long as the system remains in the mth band, the photon number $\langle \hat{n} \rangle$ will on average change by C_m each driving period. Thus, if the spin is aligned with the field (lowest band), the energy of the cavity field changes at the rate

$$\langle \dot{E}_c \rangle = \frac{z\hbar\omega}{T}. \tag{8.14}$$

Here z indicated the magnitude of the angular momentum in units of $\hbar/2$.

8.3.3 Dynamics with no dissipation

Above, we concluded that the frequency conversion took place if the spin is aligned with the field, and the dimensionless amplitude of the cavity mode is initialized between A_0 and A_1. This corresponding to the number N of photons being between N_0 and N_1, where $N_{0,1} = (M \pm A_d)^2$. If $N \in [N_0, N_1]$, the number of photons will on average increase at the quantized rate $\frac{2q}{T}$, where q is the spin of the magnetic moment.

To test this picture, we simulated a realization of the setup, with a spin-$\frac{1}{2}$ magnetic moment, using direct time-evolution from some given initial state, with the first 800 photon states included in the Hilbert space (Fig. 8.2a-d). In the simulation, we picked the parameters $\eta = \frac{5}{2}\Omega$, $\omega = \Omega/\varphi$, $M = 8$, $A_d = 17$.

The system was first initialized at time 0 in a direct product of a coherent cavity state and a spin state. The cavity state was centered at 289 photons, corresponding to an initial amplitude of $\sqrt{289} = 17$, at phase zero. The spin was initially in the state $|\downarrow\rangle$, aligned with the field. This choice of initial state clearly brings the system in the topological regime, which is between $N_0 = 81$ and $N_1 = 625$ photons. Fig. 8.2a shows the absolute square of the system's wave function in photon space, as function of time for the subsequent evolution, for the first 200 driving periods. As can be seen in the figure, the photon number increases with the quantized rate $\frac{1}{T}$ (indicated by blue line), as expected.

The energy transfer rate depends on the way spin is aligned with respect to the instantaneous direction of the field. If the spin initially *anti-aligned* with the field (i.e. in the state $|\uparrow\rangle$), as can

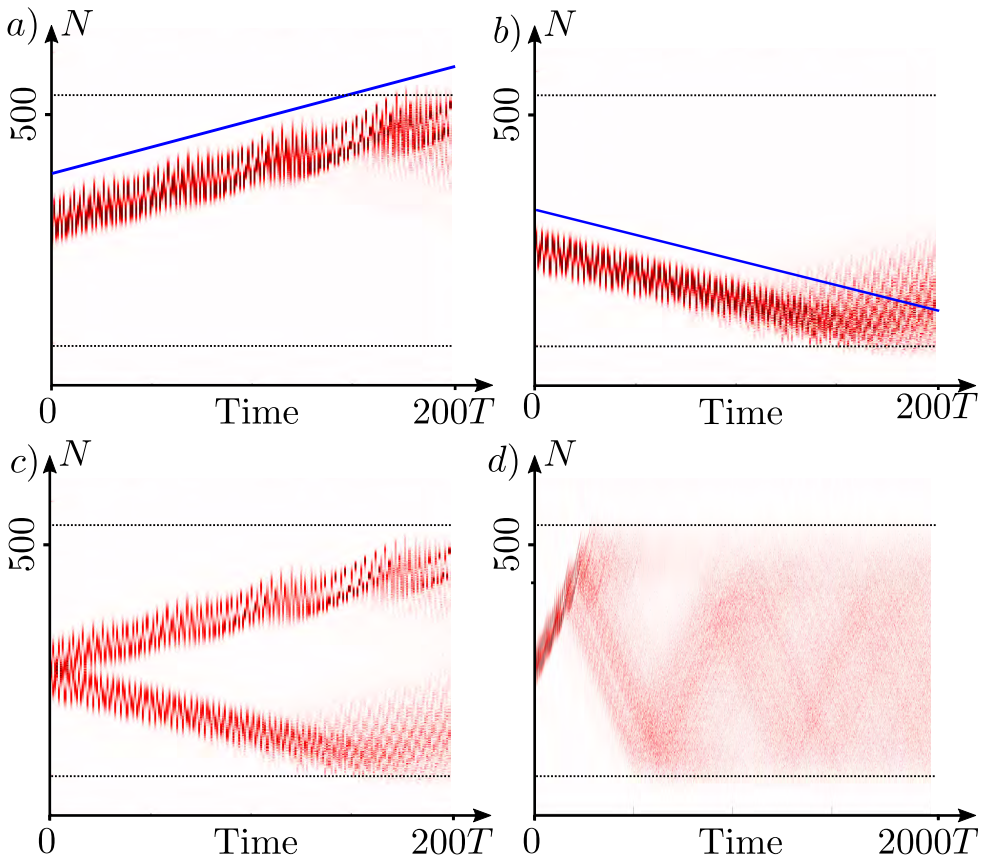

Figure 8.2: Wave function (Absolute square) of the driven cavity-spin system in various setups. Vertical axis shows number of photons. a-c) Evolution of the wave function, when the cavity field is initialized in a coherent state with amplitude 17 and phase 0, and the spin is initially a) aligned along the z-axis (the direction of the initial field), b) anti-aligned with the z-axis. c) aligned along the x axis. Dashed lines indicate the topological phase boundaries $N_0 = 81$, and $N_1 = 625$. d) Evolution of the wave function for the same system as in panel a, at longer times.

be seen in Fig. 8.2b, the number of photons decreases at the rate $\frac{1}{T}$ (indicated by blue line). This behavior continues until the photon number reaches the phase boundary $N_0 = 81$, indicated by the lower dashed line. In the subsection below, we discuss what happens at this point.

The quantization of angular momentum implies a quantization of the energy transfer rate – the number of photons can only change at rates which are integer multiples of $\frac{1}{T}$. If the system is not in a unique "band" of $H_0(k,t)$, the different components of the wave function will be subject to different energy pumping rates. This is demonstrated in Fig. 8.2c. Here we show the evolution of a system, with cavity initialized in the same way as in Figs. 8.2a-b, but with the spin initially *perpendicular* to the field (in the state $\frac{1}{\sqrt{2}}(|\uparrow\rangle + |\downarrow\rangle)$). The subsequent evolution shows that the aligned and anti-aligned components of the system's wave function evolve separately. For this system, the number of cavity state is highly entangled with the spin of the magnetic moment.

Boundary effects

If there is no dissipation, the system will eventually reach one of phase boundaries $N = N_0$ or $N = N_1$. At this point, the gap between the bands of $H_0(k,t)$ will become so small that the driving can no longer be considered adiabatic: specifically, the spin will have a significant probability of Landau-Zener tunneling between bands (corresponding to different projections of the angular momentum onto the direction of the instantaneous field). Thus, the wave function will gradually be modified, until the energy transfer rate is reversed for the entire wave function. The full reversal process occurs over many driving periods, and the wave function of the system therefore gets smeared out in time. If the evolution of the system goes on undisturbed over long periods, one should be able to see multiple such "Landau Zener reflections" – at each reflection, the wave function gets increasingly smeared out in time.

This picture is indeed born out numerically in Fig. 8.2d. Here we plot the evolution of the same system as in panel a, but over a longer time-window. The phase boundaries at N_0 and N_1 are indicated by the dashed lines in the figure. In the figure, the wave function gets reflected around 5 times during the time period from 0 to $2000T$. Over time, the wave function gets increasingly smeared out. The wave function clearly remains confined to the topological regime $[N_0, N_1]$, as expected.

The behavior described above is only possible in the absence of dissipation. If even slight dissipation is introduced to the dynamics of the spin, the spin will tend to align itself with the field, and the Landau-Zener tunneling described above will be suppressed. In this case, the state of the cavity will be "stuck" at the upper phase boundary.

8.3.4 Dynamics with dissipation

We now discuss the behavior of the driven cavity-spin system when dissipation is introduced. We consider two sources of dissipation: dissipation of cavity mode and spin relaxation. The cavity dissipation can for example result from a partially-transparent mirror in the cavity that results in emission of photons to the outside electromagnetic environment. The spin relaxation is introduced to model a more realistic setting, where the magnetic energy of the spin can dissipate into the surrounding environment.

As we will see, both sources of dissipation lead to a stabilization of the energy pumping. With

no dissipation, the quantization of energy transfer depends on the degree of alignment of the spin with the field, which is sustained by adiabaticity condition $\eta h \gg \Omega$. Spin dissipation increases the tendency of the spin to align with the field, and thus stabilizes the quantized energy transfer beyond the frequency ranges allowed by the adiabaticity condition.

Moreover, since cavity dissipation is proportional to the mode energy, while the pumping rate is constant, we find that the introduction of cavity dissipation allows the system to reach a "lasing" steady state, where all the energy transferred to the cavity mode by the driving (at the rate $\frac{2q\hbar\omega}{T}$) is exactly compensated by the cavity emission losses.

To model the effects of cavity and spin dissipation, we use a master equation approach. In quantum mechanics, dissipation arises when a degree of freedom in the system is coupled to an external bath. When the bath is so large that its degrees of freedom form a continuum, the resulting exchange of energy and entropy with the bath is effectively irreversible, and this leads to dissipation in the system.

In our case, we model cavity dissipation by connecting the cavity field $\frac{1}{2}(a + a^\dagger)$ to an external bath in the way described above, with coupling strength γ_c, which determines the reflection coefficient of the partially-transparent mirror. Spin dissipation is modeled by coupling each of the spin's components L_x, L_y, L_z to individual external baths, with the same coupling strength γ_s. For both the cavity and spin degrees of freedom, we take the associated baths to be Ohmic, meaning that the spectral functions $S(\omega)$ are linear in ω [194]: $S_{c,s}(\omega) = S(\omega) \equiv \frac{\omega}{\omega_0}$, where ω_0 is some fixed energy scale. Absorbing all variable parameters into the coupling strength γ, we set $\omega_0 = 1/T$.

The dynamics of the system can in principle be obtained by computing the time-evolution generated by the full system-bath Hamiltonian H_{SB}. Having obtained the time-evolution of the full system-bath state $|\Psi(t)\rangle$ we can compute the evolution of any system observable from the reduced density matrix $\rho(t) \equiv \mathrm{Tr}_B|\Psi(t)\rangle\langle\Psi(t)|$, where Tr_B traces out all the bath degrees of freedom.

Often, the physical baths are found to be nearly Markovian (short time correlated, compared to the relevant time scale of the system), meaning that the density matrix of the system at time $t + dt$ depends only on the density matrix at time t. This implies that the evolution of $\rho(t)$ can be described by a linear first order differential equation, referred to as a master equation. In Appendix A we derive a master equation for periodically driven system, making this assumption. Doing so, one finds that the evolution of ρ obeys the following differential equation:

$$\dot{\rho} = -i[H, \rho] + \sum_k 2\pi\gamma_k \left(L_k \rho L_k^\dagger - \frac{1}{2}\{L_k^\dagger L_k, \rho\} \right). \tag{8.15}$$

Here the sum runs over the four different channels of dissipation. The so-called jump operators $L_k(t)$ are time-dependent with the same periodicity as the Hamiltonian, and are defined from the quasienergies $\{\varepsilon_a\}$ and the time-periodic Floquet states $|\phi_a(t)\rangle$ [2] of $H_S(t)$ as follows:

$$L_k(t) = \sum_{a,b,n} |\phi_a(t)\rangle\langle\phi_b(t)| e^{-in\Omega t} L_k^{ab}[n], \tag{8.16}$$

[2] Here the Floquet states are the unique sets of states whose evolution is given by a linearly increasing phase times a time-periodic state: $U(t)|\ \phi_a(0)\rangle = e^{-i\varepsilon_a t}|\ \phi_a(t)\rangle$, where $|\ \phi_a(t)\rangle = |\ \phi_a(t+T)\rangle$. The Floquet theorem dictates that a complete orthonormal basis of states with this property always exist for periodically driven systems.

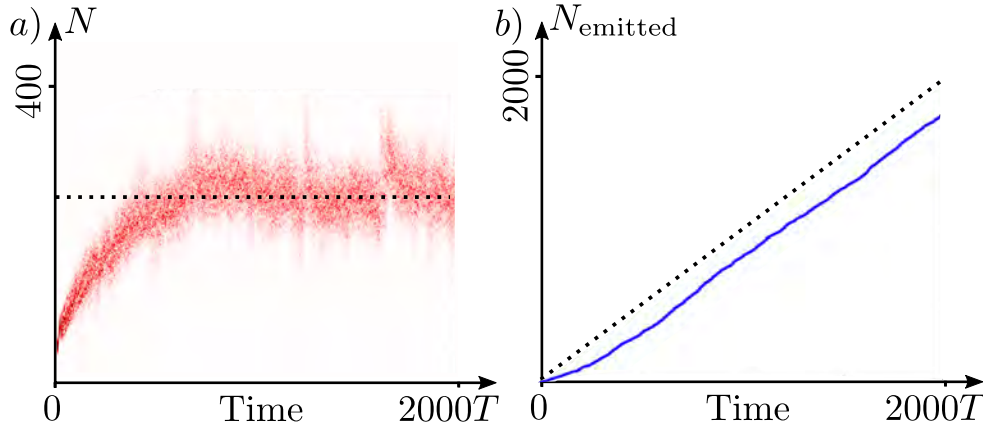

Figure 8.3: a) Evolution of the wave function (Absolute square) of the driven cavity-spin system, in the presence of spin- and cavity dissipation, for a randomly picked SSE realization (see Sec. 8.3.4 for details. Vertical axis shows number of photons. The dashed line indicates the predicted number of photons (250) in the steady state consistent with the emission of one photon per driving period. b) cumulative number of photons emitted, as function of time for the SSE realization depicted in panel a (blue). The black dashed line indicates the slope consistent with emission of one photon per driving period.

where $L_k^{ab}[n] = \sqrt{2\pi\gamma_k J_k(\varepsilon_b - \varepsilon_a + n\Omega)}A_k^{ab}[n]$, and

$$A_k^{ab}[n] = \frac{1}{T}\int dt \langle\phi_a(t)|A_k|\phi_b(t)\rangle e^{-i\Omega nt}. \tag{8.17}$$

In the above, A_k is the operator connected to bath k (i.e. either $\frac{1}{2}(a + a^\dagger)$, or $S_{x,y,z}$), and the function $J_k(\omega)$ is given by $J_k(\omega) = S_k(|\omega|)(\theta(\omega) + n_k(|\omega|))$, where $S_k(\omega)$ is the spectral function that enters in the kth system-bath coupling in Eq. (**??**), and $n_k(\omega)$ is the thermal expectation value of the photon number at frequency ω in bath k. In our case, we set the bath temperatures to zero, so $J_k(\omega) = \theta(\omega)\omega/\omega_0$.

Numerical results

To learn about the behavior of the system when subject to dissipation, we simulate the evolution of the system using the above master equation. The Master equation is integrated stochastically, using the Stochastic Schrödinger Equation (SSE) method [195]. Doing this, we obtain trajectories of the system that can be seen representative for the actual time evolution with the above master equation.

The parameters we use are $\eta = \frac{5}{2}\pi$, $L = \frac{\hbar}{2}$, $M = A_d = 10$.The latter brings the system to the special point, where $N_0 = 0$. We include 400 photon states in the Hilbert space we simulate. We set $S(\omega) = \omega T$, $\gamma_s = \frac{0.001}{T}$, $\gamma_c = \frac{0.0006366}{T}$ – the latter leads to a steady state with 250 photons. In Fig. 8.3a, we show the evolution of a single, randomly picked realization of the SSE evolution for the first 2000 periods, after the cavity is initialized in a coherent state centered around 50 photons, and the spin is initially aligned perpendicularly initial field. The predicted steady state

of 250 photons is indicated by the dashed line. As can be seen, the system quickly reaches a steady state, number of photons in the cavity mode fluctuates around the predicted value of 250.

As another indicator for the robustness of the energy transfer to the cavity mode, we compute the cumulative number of photons emitted from the cavity, N_{emitted}, as a function of time [195], for the realization depicted in Fig. 8.3a. The results are shown Fig. 8.3b. Here the dashed line, indicates the predicted slope of N_{emitted} consistent with the quantized rate of one photon per driving period. As can be seen, the N_{emitted} quickly reaches a slope consistent with emission of one photon per driving period, thus confirming the picture discussed in the beginning of this subsection.

Note that the spin dissipation leads to an alignment of the spin with the field, and there is no reversed pumping in the system, unlike in the non-dissipative case.

8.4 Classical treatment

We will now consider the classical limit of the system in Hamiltonian (8.5) and show that the topological frequency conversion can be understood as a purely classical effect. Qualitatively, the pumping occurs when the classical magnetic moment nearly follows the instantaneous direction of the magnetic field. Because the instantaneous magnetic field direction rotates, the center of moment precession becomes slightly offset from the field direction. This retardation is the root of the energy pumping phenomenon. Just like in the classical case, spin relaxation improves pumping stability, as it suppresses spin unlocking from the field direction that inevitably occurs due to non-adiabaticity.

8.4.1 Equations of motion

In classical mechanics, the equations of motion for an observable X can be written in terms of the Hamiltonian H as

$$\dot{X} = \{X, H\}, \tag{8.18}$$

where $\{a, b\} = -\{b, a\}$ denotes the Poisson bracket between the variables a and b. Poisson brackets obey the chain rule $\{a, bc\} = \{a, b\}c + b\{a, c\}$, and the equations of motion can thus be constructed from the Poisson brackets between the independent variables $\mathbf{L}, \phi, A$. Going back to the Hamiltonian in Sec. 8.2, we recall from the discussion there that the phase ϕ of the cavity field was canonically conjugate to the variable $A^2 L_0$, where A was the dimensionless amplitude of the field – *i.e.*, $\{\phi, L_0 A^2\} = 1$. Using this, along with the usual Poisson bracket relations for the angular moment $\mathbf{L}$, we find that variables $A, \phi, \mathbf{L}$ obey the following Poisson bracket relations

$$\{\phi, A\} = \frac{1}{2AL_0}, \quad \{L_i, L_j\} = \epsilon_{ijk} L_k, \tag{8.19}$$

while all other possible Poisson brackets between the variables are zero. In the above, ϵ_{ijk} denotes the Levi-Civita symbol, and L_0 was the arbitrary scale of action introduced in Sec. 8.2 to make A dimensionless.

The chain rule property of the Poisson brackets imply that the ϕ-Poisson bracket for any quantity $F(\mathbf{L}, A, \phi)$ in the system can be written as $\{\phi, F\} = \{\phi, A\}\frac{\partial F}{\partial A}$, while $\{A, F\} = \{A, \phi\}\frac{\partial F}{\partial \phi}$.

Using this in Eq. (8.18), together with the definition of the Hamiltonian in Eq. (8.6), the equations of motion for A, ϕ and $\mathbf{L}$ become

$$\dot{\phi} = \omega + \frac{\eta}{2AL_0}\partial_A \mathbf{h}\cdot\mathbf{L}. \tag{8.20}$$

$$\dot{A} = -\frac{\eta}{2AL_0}\partial_\phi \mathbf{h}\cdot\mathbf{L}. \tag{8.21}$$

$$\dot{\mathbf{L}} = \eta\,\mathbf{h}\times\mathbf{L}. \tag{8.22}$$

Below, we analyze these equations of motion, showing they give rise to a quantized, topologically-protected frequency conversion in certain parameter regimes.

8.4.2 Classical pumping conditions

We find that, the energy transfer between the two modes is quantized (and may be nonzero) when the following two requirements are met: 1) the moment should precesses much faster than the field oscillates: $\eta h \gg \Omega_0$, where denotes the magnitude of $\mathbf{h}$ on the time scale of the two modes' oscillations, and $\Omega_0 = \max(\omega, \Omega)$ denotes the typical frequency scale of the field's oscillations. 2) the field amplitude should be large enough that the presence of the angular moment only weakly perturbs the motion of the cavity field on the time-scale of the two modes' oscillations.These conditions parallel those discussed in the quantum treatment of Section 8.5, and can be quantified by introducing the dimensionless parameter $\alpha \equiv \frac{\Omega_0}{\eta h}$ and dimensionfull $\kappa \equiv \frac{\eta L}{AL_0}$, which has the units of frequency. The parameter α measures the ratio between the field's oscillations and the moment's precession frequency, and condition 1) is equivalent the requiring $\alpha \ll 1$. The parameter κ^{-1} sets the time scale over which the magnetic moment $\mathbf{L}$ significantly affects the cavity field, and for condition 2) to hold, κ must be much smaller than the modes' frequencies ω and Ω. Specifically, since $\partial_A \mathbf{h}$ is of order unity, Eq. (8.20) implies $\dot{\phi} = \omega + \mathcal{O}(\kappa)$. At the same time, since $\partial_\phi \mathbf{h} = \mathcal{O}(A)$, Eq. (8.21) implies that $\dot{A} = \mathcal{O}(\kappa A)$. Thus, when $\kappa \ll \omega, \Omega$, the relative change in the cavity field amplitude is negligible on the time-scales ω^{-1}, Ω^{-1} of the two modes' oscillations.

8.4.3 Trajectory of L

We now focus on the equations of motion for $\mathbf{L}$, expressing the in terms of the magnitude h hand direction $\hat{\mathbf{n}}$ of the field $\mathbf{h}$. If the field $\mathbf{h}$ was stationary, Eq. (8.22) implies that $\mathbf{L}$ would precess around $\hat{\mathbf{n}}$ with precession frequency ηh. For the setup we discuss here, however, the field $\mathbf{h}$ depends on time, and oscillates with typical frequency Ω_0, which is much smaller than the precession frequency ηh,

$$|\dot{\mathbf{h}}| \sim \mathcal{O}(\Omega_0 h). \tag{8.23}$$

To analyze the equations of motion in the limit $\alpha \to 0$, we exploit the separation of time scales between the precession and the field's oscillations in the limit.

Specifically, we write $\mathbf{L}(t) = \mathbf{L}_{\text{slow}}(t) + \mathbf{L}_{\text{fast}}(t)$, where $\mathbf{L}_{\text{fast}}(t)$ contains the fast, precessing component of $\mathbf{L}(t)$ that oscillates with typical frequency ηh, while the remaining, slow component

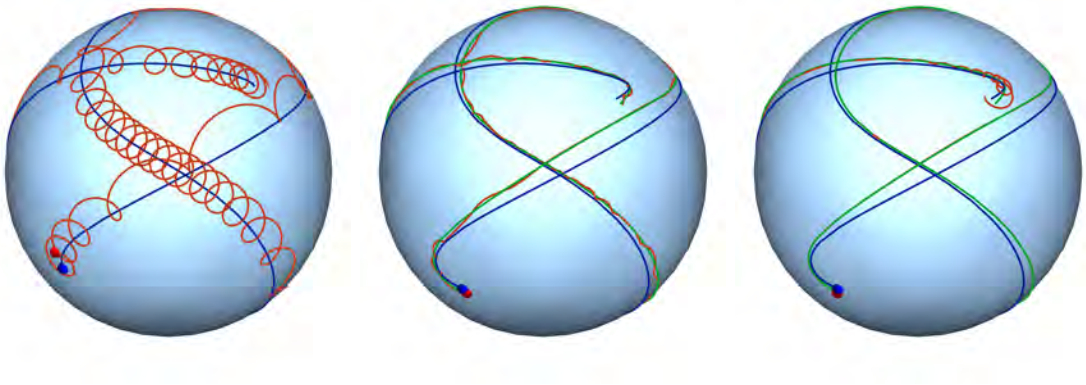

Figure 8.4: Trajectories for the classical model discussed in Sec. 8.4.3. a) Trajectory of $\mathbf{L}$ (red) and $\mathbf{h}$ (blue) for the model in the absence of dissipation. b) Trajectories of the estimated center of precession $\mathbf{L}_{\text{slow}}$ (red), along with $\hat{\mathbf{n}}$ (blue) and $\mathbf{S}_0$ (green) for the same system. c) Trajectories of $\hat{\mathbf{n}}$ (blue), $\mathbf{L}$ (red), and $\mathbf{S}_0$ (green) for the system, when weak spin-dissipation is included in the equations of motion.

$\mathbf{L}_{\text{slow}}$ contains the component of the spin's motion that changes on the time-scale $\frac{1}{\Omega_0}$ [3]. Writing $\mathbf{h} = h\hat{\mathbf{n}}$, the equation of motion for $\mathbf{L}$ becomes

$$\dot{\mathbf{L}}_{\text{slow}} + \dot{\mathbf{L}}_{\text{fast}} = \eta h \hat{\mathbf{n}} \times (\mathbf{L}_{\text{slow}} + \mathbf{L}_{\text{fast}}). \tag{8.24}$$

Using the separation of time-scales, we find

$$\dot{\mathbf{L}}_{\text{fast}} = \eta h \hat{\mathbf{n}} \times \mathbf{L}_{\text{fast}} \tag{8.25}$$

$$\dot{\mathbf{L}}_{\text{slow}} = \eta h \hat{\mathbf{n}} \times \mathbf{L}_{\text{slow}}. \tag{8.26}$$

These equations imply that the magnitudes of $\mathbf{L}_{\text{slow}}$ and $\mathbf{L}_{\text{fast}}$, respectively, are constants of motion. We denote these by λ_0 and λ_1.

Analyzing the above equations of motion (see Appendix G.1 for details), we find that $\mathbf{L}_{\text{slow}}$ is given by

$$\mathbf{L}_{\text{slow}} = \lambda_0 \mathbf{S}_0 + \mathcal{O}(\alpha^2 \lambda_0), \tag{8.27}$$

where

$$\mathbf{S}_0 = \hat{\mathbf{n}} - \frac{1}{\eta h} \hat{\mathbf{n}} \times \dot{\hat{\mathbf{n}}} \tag{8.28}$$

Additionally, we find that $\mathbf{L}_{\text{fast}}$ precesses around $\mathbf{S}_0$ with frequency $\sim \eta h$, and with a fixed radius of precession given by λ_1. Note that the instantaneous axis of precession is *not* given by the field's direction $\hat{\mathbf{n}}$, but has a finite offset from this given by $\hat{\mathbf{n}} \times \dot{\hat{\mathbf{n}}}/\eta h$. As we will show, this finite offset is responsible for the topological frequency conversion.

[3] the distinction between $\mathbf{L}_{\text{slow}}$ and $\mathbf{L}_{\text{fast}}$ can be made rigorous by letting $\mathbf{L}_{\text{fast}}(t)$ consist of the Fourier components of $\mathbf{L}(t)$ with frequency above some cutoff $\Omega_0 \ll \Lambda \ll \eta h$.

To support the conclusion that $\mathbf{L}$ precesses around $\mathbf{S}_0(t)$ rather than $\hat{\mathbf{n}}(t)$, we plot in Fig. 8.4b the time-averaged trajectory of $\mathbf{L}(t)$ on the unit sphere (red) for the same model studied in Fig. 8.4a. Specifically, we plot the trajectory of $\mathbf{V}(t)$ on the unit sphere, where $\mathbf{V}(t) \equiv \frac{1}{\Delta t}\int_{t-\Delta t/2}^{t+\Delta t/2} \mathbf{L}(t)dt$, and $\Delta t = 0.1$, in units where $\Omega = 2\pi$. Within time-windows of this width, $\mathbf{L}_{\text{fast}}$ approximately averages out to zero, while $\mathbf{L}_{\text{slow}}$ remains constant, and we thus expect $\hat{\mathbf{V}}$ to be a good estimate for the instantaneous axis of precession, $\mathbf{L}_{\text{slow}}$. In addition to showing the trajectory of $\mathbf{V}(t)$, we plot the trajectory of the field $\hat{\mathbf{n}}$ (blue), and the predicted axis of precession $\mathbf{S}_0$ (green). The data shows that $\mathbf{V}$ tracks $\mathbf{S}_0(t)$ closely, which further supports our conclusion above that $\mathbf{L}$ precesses around $\mathbf{S}_0$ rather than $\hat{\mathbf{n}}$.

Effects of dissipation

We now consider the case where the motion of the spin is a subject to dissipative forces. If the field $\mathbf{h}$ were static, the dissipation would cause the spin to aligning with the direction $\hat{\mathbf{n}}$ of the field. Now we will show that if $\mathbf{h}$ is time-dependent, dissipation of will lead to relaxation to the direction $\mathbf{S}_0(t)$ (rather than $\hat{\mathbf{n}}$) for a wide range of dissipation strengths, leading to an increased stability of the frequency conversion, as we will show in the following section. In particular, the frequency conversion will not depend as much on a separation of time-scales as was necessary for the dissipationless case.

The equations of motion for $\mathbf{L}$ can be expressed as a first-order differential equation, which implies that the dissipation depends on $\mathbf{L}$ and $\dot{\mathbf{L}}$. With dissipation, the equation of motion for $\mathbf{L}$ thus takes the form $\dot{\mathbf{L}} = \{L, H(t)\} + \mathbf{F}_{\text{dis}}(\mathbf{L}, \dot{\mathbf{L}})$ for some function $\mathbf{F}_{\text{dis}}$. We consider the case where the dissipative forces conserve the magnitude of $\mathbf{L}$. In this case, the equation of motion for $\mathbf{L}$ in the frequency conversion setup takes the form

$$\dot{\mathbf{L}} = -\left(\eta\mathbf{h}(t) + \mathbf{v}_{\text{dis}}(\mathbf{L}, \dot{\mathbf{L}})\right) \times \mathbf{L}. \tag{8.29}$$

The dissipation potential $\mathbf{v}_{\text{dis}}(\mathbf{L}, \dot{\mathbf{L}})$ has units of angular velocity and can in principle take any form. For simplicity, we consider here the case where the dissipative forces enter as a Gilbert-type term above [196]. Specifically, $\mathbf{v}_{\text{dis}}(\mathbf{L}, \dot{\mathbf{L}}) = -\frac{\gamma}{L}\dot{\mathbf{L}}$, where γ denotes the dimensionless dissipation strength.

In Appendix G.2, analyze this equation of motion in detail. By going to the rotating frame where $\mathbf{h}$ is aligned with the $\hat{\mathbf{z}}$ axis, we find that $\mathbf{L}(t)$ aligns itself with $L\mathbf{S}_0(t)$ when γ is in the regime

$$\alpha^2 \ll \gamma \ll 1. \tag{8.30}$$

Trajectory of L from numerical simulations

These analytical results above are in good agreement with numerical simulations. We numerically solved the equations of motion for the model, with the parameters $\eta = 0.1\Omega$, $\omega_c = \omega_c/\varphi$, where $\varphi = (1+\sqrt{5})/2$, while $L = \frac{L_0}{2}$, and $A_d = M = 100$. We initialized the cavity field in the state $A = 100$, $\phi = \pi$, while the spin was initially aligned along the z-direction (which was also the initial direction of the field), first without dissipation. In this case, the field amplitude is typically of order 100, so the precession frequency ηh is of order 10 times faster than the oscillation

frequency Ω, ω_c of the field. Fig. 8.4a shows the computed trajectory of $\mathbf{L}$ on the unit sphere over first three driving periods (red), and the direction of the field (blue), while the blue and the red points indicate the final values of $\mathbf{L}$ and $\hat{\mathbf{n}}$. The data clearly show that $\mathbf{L}$ precesses with with the center of precession approximately following $\hat{\mathbf{n}}$, and the radius of precession approximately constant. We then computed the trajectory of $\mathbf{L}$ for the same parameters, but with a weak dissipative force acting on the spin. The dissipation is included in the equations of motion in the form of a Gilbert-type term with strength $\gamma = 0.05$, which brings the system well within the regime $\alpha^2 \ll \gamma \ll 1$ (since $\alpha = 0.1$). In Fig. 8.4c we plot the resulting trajectory of $\mathbf{L}$ over the first three driving periods (red), along with the trajectory of the field $\hat{\mathbf{n}}$ (blue), and the predicted "relaxed" direction $\mathbf{S}_0(t)$ (green). The data clearly shows that $\mathbf{L}(t) = L\mathbf{S}_0(t)$.

8.4.4 Emergence of energy transfer

Having found the trajectory of $\mathbf{L}$ both in the presence and the absence of dissipation, we now consider the consequences for the dynamics of the cavity field. Here we show that the deviation of $\mathbf{L}_{\text{slow}}$ (or $\mathbf{L}$ in the dissipative case) from the cavity field direction gives rise to a quantized energy transfer between the driving field and the cavity mode.

As a first step, we note from Eqs. (8.20) and (8.21) that the time-scale on which the amplitude A and phase ϕ change significantly is of order $\frac{1}{\Omega_0}$, and therefore the contribution from $\mathbf{L}_{\text{fast}}$ to Eq. (8.20) and (8.21) on average cancels out. We may therefore replace $\mathbf{L}$ with $\mathbf{L}_{\text{slow}} = \lambda_0 \mathbf{S}_0$ in these equations, where λ_0 was a constant of motion, up to bounded, time-dependent fluctuations. In the case where the moment $\mathbf{L}$ is subject to dissipation, we found above that $\mathbf{L} = L\mathbf{S}_0$ after a transient relaxation period of duration $\sim \frac{1}{\eta h \gamma}$. In either case, in the equations of motion for the cavity field, we may substitute $\mathbf{L}$ with $\lambda_0 \mathbf{S}_0$, where λ_0 was a constant of motion (specifically, in the dissipative case, $\lambda_0 = L$). Making this substitution in Eqs. (8.20) and (8.21), we obtain

$$\dot{\phi} = \omega + \frac{\eta \lambda_0}{2AL_0} \partial_A \mathbf{h} \cdot \mathbf{S}_0 \tag{8.31}$$

$$\dot{A} = -\frac{\eta \lambda_0}{2AL_0} \partial_\phi \mathbf{h} \cdot \mathbf{S}_0 \tag{8.32}$$

We first consider the equation of motion for the field's amplitude A. Writing $\mathbf{h} = \hat{\mathbf{n}} h$, and inserting the expression (G.7) for $\mathbf{S}_0$ in Eq. (8.31), we find [4]

$$\dot{A} = -\frac{\eta \lambda_0}{2AL_0} \partial_\phi h - \frac{\lambda_0}{2AL_0} \partial_\phi \hat{\mathbf{n}} \cdot (\hat{\mathbf{n}} \times \dot{\hat{\mathbf{n}}}), \tag{8.33}$$

where we, used $\partial_\phi \hat{\mathbf{n}} \cdot \hat{\mathbf{n}} = \frac{1}{2} \partial_\phi (\hat{\mathbf{n}} \cdot \hat{\mathbf{n}}) = 0$, and $\hat{\mathbf{n}} \cdot (\hat{\mathbf{n}} \times \dot{\hat{\mathbf{n}}}) = 0$.

We now consider the evolution of the energy $E_c = L_0 \omega A^2$ stored in the cavity mode. The field energy obeys the equation of motion $\dot{E}_c = 2AL_0 \omega \dot{A}$. Inserting this in the expression for $\dot{E}_c$, and using $\mathbf{a} \cdot (\mathbf{b} \times \mathbf{c}) = \mathbf{b} \cdot (\mathbf{c} \times \mathbf{a})$, we find

$$\dot{E}_c = -\eta \omega \lambda_0 \partial_\phi h + \omega \lambda_0 \, \hat{\mathbf{n}} \cdot (\dot{\hat{\mathbf{n}}} \times \partial_\phi \hat{\mathbf{n}}). \tag{8.34}$$

[4] recall that the definition $\hat{\mathbf{n}} = \mathbf{h}/|\mathbf{h}|$ implies that $\hat{\mathbf{n}}$ is a function of A, ϕ, t.

We now make use of the assumption that $\kappa \ll \omega, \Omega$ – i.e., that the angular moment only weakly perturbs the motion of the cavity field on the time scales of the two modes' oscillations. On these time scales, we may set $\dot{\hat{\mathbf{n}}} \approx \partial_t \hat{\mathbf{n}} + \omega \partial_\phi \hat{\mathbf{n}}$, and we find

$$\dot{E}_c = -\eta\omega\lambda_0 \partial_\phi h + \omega\lambda_0 \, \hat{\mathbf{n}} \cdot (\partial_t \hat{\mathbf{n}} \times \partial_\phi \hat{\mathbf{n}}) + \Delta\dot{E}. \tag{8.35}$$

Where $\Delta\dot{E}$ is an insignificant correction due to the approximation made above. As show in Appendix G.3, the time-averaged value of $\Delta\dot{E}$ goes to zero as $\lambda_0\omega/\tau$, where τ denotes the averaging time.

We now recall that $\kappa \ll 1$ implies that the amplitude A of the cavity field stays effectively constant on the time scales Ω^{-1}, ω^{-1}, while ϕ increases linearly at the rate ω, up to a small correction of order κ. If ω/Ω is a sufficiently irrational number, the trajectory of $(\phi(t), t)$ will then effectively cover the entire 2D manifold $t \in [0, T]$, $\phi \in [0, 2\pi]$ within a finite time-window, within which $A(t)$ can be assumed constant. In this case, the time-averaged value of $\dot{E}_c$ is given by

$$\langle \dot{E}_c \rangle = \frac{\omega\lambda_0}{2\pi T} \int_0^T dt \int_0^{2\pi} d\phi \, \left(\eta \partial_\phi h + \hat{\mathbf{n}} \cdot (\partial_t \hat{\mathbf{n}} \times \partial_\phi \hat{\mathbf{n}})\right), \tag{8.36}$$

where $T = \frac{2\pi}{\Omega}$ is the driving period.

In the above expression, the first term is zero, since h is periodic in ϕ. We identify the second term as the solid angle on the unit sphere S_2 covered by the image of the torus $T_2 = [0, T] \times [0, 2\pi]$ with respect to the mapping $\hat{\mathbf{n}} : T_2 \to S_2$. The image of the torus is a closed manifold, and must hence cover the sphere an integer number of times, which implies that the solid angle is an integer multiple ν of 4π. Thus $\langle \dot{E} \rangle = \nu \cdot \frac{2\lambda_0\omega}{T}$. In the case where dissipation is present (or the spin is initially aligned with the field), $\lambda_0 = L$, and we obtain

$$\langle \dot{E}_c \rangle = \nu \cdot \frac{2L\omega}{T}, \tag{8.37}$$

where ν must be an integer. For the model we consider, it has previously been established that the index ν takes the value 1 when $A_0 < A < A_1$, where $A_0 = |M - A_d|$, and $A_1 = M + A_d$ [11] (assuming, wihtout loss of generality, that $M, A_d > 0$). In other words, the invariant ν takes value 1 if the energy E_c of the cavity is in the interval $[E_0, E_1]$, where $E_{0,1} = \omega L_0 (M \pm A_d)^2$. This implies that the energy of the cavity field will continually incrase at the quantized average rate $\frac{2L\omega}{T}$ as long as E_c is in the interval between E_0 and E_1. When E_c is outside this interval, $\nu = 0$, and the energy in the cavity field on stays constant on average.

Notably, by naive interpolation, this purely classical analysis predicts that the smallest possible energy pumping rate is exactly one cavity photon per driving period; this is achieved when the angular momentum L along $\mathbf{S}_0$ takes the minimal nontrivial value possible: $\frac{\hbar}{2}$ (a single spin-1/2 degree of freedom). In this case, $\langle \dot{E}_c \rangle = \nu \cdot \hbar\omega/T$. Thus, the pumping rate is quantized in units of one cavity photon per driving period. This is the exact same result that was arrived at in the quantum problem.

In the case when there is no dissipation, while the field energy $E_c = L_0 \omega A^2$ is in the "topological regime" $[E_0, E_1]$, energy is transferred from the driving field to the cavity mode. The energy transfer rate is given by $2\lambda_0\omega/T$, where λ_0 is approximately given by the projection of $\mathbf{L}$ onto the field. As shown in the above subsections, λ_0 is a constant of motion when $\alpha \ll 1$, which is ensured when $E_0 < E_c < E_1$ (since $h \sim \mathcal{O}(A, A_d)$ in this range).

Classical boundary effects

The increase of the cavity field energy E_c will go on until it reaches the upper phase boundary at E_1. In the "ideal" case $\alpha \to 0$, the energy of the cavity will keep increasing exactly until it reaches E_1. In practice, however, the energy transfer rate will begin deviate from the quantized value before this point. To see why, note that the energy transfer rate is only quantized as long as the dimensionless field strength $|\mathbf{h}|$ is much larger than the ratio ω/η.For a fixed amplitude of the cavity field, the minimal value of h is given by $h_{\min} = \min|M \pm A_d \pm A|$ (this is achieved when ϕ or Ω take values 0 or π). When $h_{\min}$ becomes comparable to ω/η, the field magnitude will be too weak for the moment's axis of precession to keep up with the motion of the field's direction, and the derivation made in Sec. 8.4.3 breaks down. At this point, the energy transfer rate may deviate from the quantized value, and $\mathbf{L} \cdot \mathbf{S}_0$ is no longer conserved.

8.4.5 Classical numerical simulations of pumping

No dissipation

To test the above derivations, we numerically simulate the model, first without dissipation, for the coupling strength η is set to $\frac{5}{2}\Omega$, while $A_d = 17$, $M = 8$, which leads to $\alpha \sim 25$ in the topological regime (where $h \sim \mathcal{O}(A_d, A)$). The parameters of the model were chosen to be identical to the parameters used in the quantum mechanical model case (see Fig. **??**): The resonance frequency ω of the cavity is set to Ω/φ, where $\varphi = (1+\sqrt{5})/2$. Setting $L_0 = L$, the driving frequency Ω and angular moment L fix the energy and time scales of the system. The results above imply that the field energy E_c should grow at a constant rate $2\omega\lambda_0 f_d$ as long as E_c is between $162\omega L$ and $1250\omega L$.

We initialize the cavity field in the state with $A = 17$, and $\phi = 0$, while the spin is initialized with a small deviation angle of 0.01 radians from the direction of the field, such that $\lambda_0 \approx L$ (specifically, $\mathbf{L}(0) = \frac{L}{\sqrt{1.0014}}(0.01, 0.01, -1)$. The spin is thus initially nearly aligned with the field, whose initial value is given by $\mathbf{h}(0) = (0, 0, -26)$. In Fig. 8.5a, we show the energy of the cavity mode $E_{\text{cav}} = \omega A^2$ as function of time (red curve) for the subsequent motion of the system. Note that the time-scale in the figure is linear from 0 to $400T$, and from $400T$ to $3000T$.

As can be seen in the figure, the energy initially increases at the quantized rate $L\omega/T$, indicated by the slope of the light blue line in the figure, as predicted in the previous subsection. The energy keeps increasing until $t \approx 250T$, where E_c is too close to the upper phase boundary at $E_1 = 1250L\omega_1$ for the energy pumping rate to remain quantized. From this point, the energy of the cavity field remains at the upper phase boundary until $t \approx 2000T$, where E_c suddenly starts decreasing at a constant rate.

This behavior can be explained by the system's moving chaotically at the upper phase boundary (it cannot cross the phase boundary, since above the phase boundary $\dot{E} = 0$, due to the results from the previous section). Hence the projection $\lambda(t) = \mathbf{L}(t) \cdot \mathbf{S}_0(t)$ changes chaotically in time. At some point, the system may be at the lower end of the phase boundary, where the quantized energy transfer will begin to have significant effect. If λ is negative at this instant, the quantized energy transfer will begin to drive the field energy further down into the regime where λ is conserved. This gives a mechanism for the system to escape the upper phase boundary,

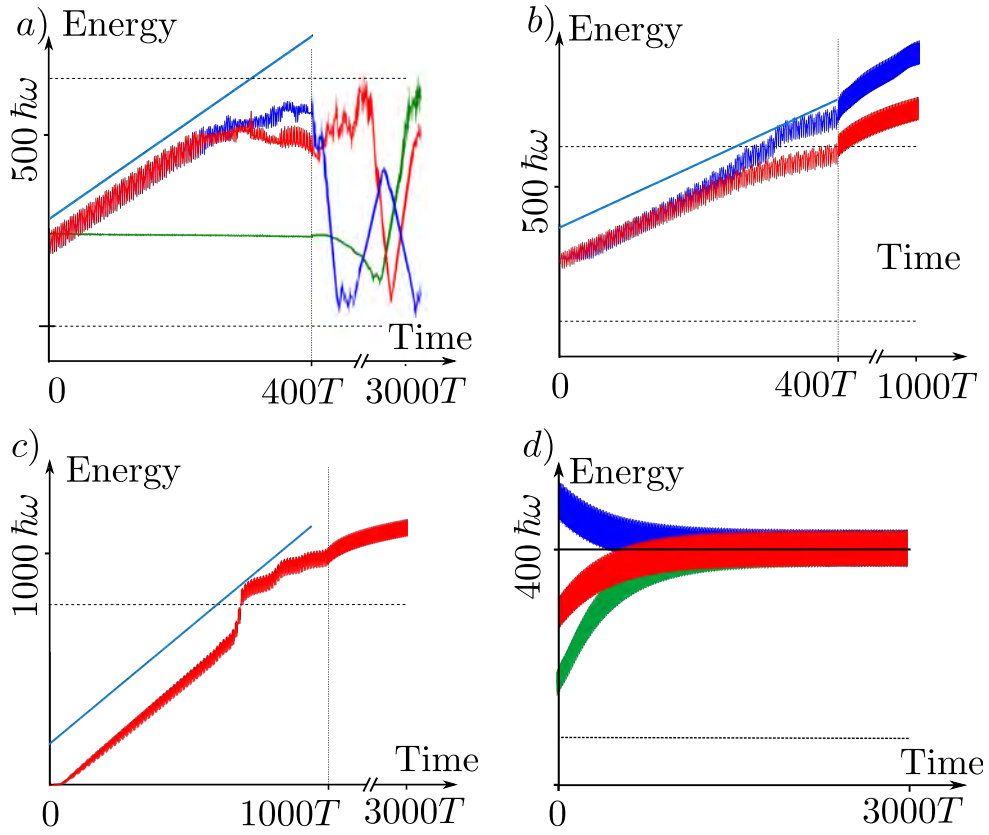

Figure 8.5: Dynamics of the classical system (see main text for details). The time-scale in panels a-c is piecewise linear, with the vertical dashed line indicating the shift of time-scale. Horizontal dashed lines indicate the boundaries E_0, E_1 of the pumping regime. a) Energy of the cavity field as function of time for three different initializations of the system when there is no dissipation.b) Energy of the cavity field for the same system as in panel a, with the addition of spin dissipation. c) Energy of the cavity field, at the special point $M = A_d$ in the phase diagram, where the cavity field is initially zero, and the spin is subject to dissipation. d) Energy of the cavity field when cavity dissipation is included in addition to spin dissipation.

and in this case, the E_c begin to decrease at a constant rate, given by the value at which λ gets "frozen".

This behavior will continue until the system reaches the lower phase boundary, where a similar process can happen. On long time scales, the energy of the system will thus "zig-zag" between the two phase boundaries, as in the right end of Fig. 8.5a. The time it takes for the system to perform a "bounce" is essentially random, due to the chaotic nature of the system's motion near the phase boundaries. In addition, the value of λ after a bounce may not exactly be $\pm L$, but can take any value in the interval $[0, \pm L]$.

To verify the chaotic nature of the bounces, we investigated the motion of the system with a slightly different initial state than discussed above, namely $A(0) = 17$, $\phi(0) = 0$, but $\mathbf{L}(0) = \frac{L}{\sqrt{1.0026}}(0.01, 0.05, -1)$. The motion is plotted in the blue curve in Fig. 8.5a. As can be seen the motion of the red and the blue curve is approximately identical until the first bounce at $t = 250T$. Here, the trajectories of the two systems begin to deviate, and the first "bounce" of the second system takes place much earlier than for the first system. Note also that the slope of E_c is not as large after the second and third bounces, indicating that $|\lambda|$ in these parts of the system's motion has acquired a value smaller than L.

To demonstrate that the projection λ indeed decides the energy pumping rate, we also initialized the system in the state $A = 17, \phi = 0$, $\mathbf{L} = L(1, 0, 0)$, such that $\mathbf{L}$ is approximately orthogonal to $\mathbf{S}_0$ (since $\mathbf{S}_0 \approx \hat{\mathbf{n}}$ and the field initially points along the z axis). In this case, $\lambda = 0$, which should lead to no energy transfer. We plot the motion in the green curve of Fig. 8.5a. As can be seen, the energy remains constant for the first 1000 driving periods – the energy transfer is thus indeed absent with this initialization. Eventually, the energy of the cavity does begin to change. This deviation may be due to fact that the separation of time scales in Eqs. (8.26) and (8.25) is only valid on finite (although long) time scales.

Stabilization of energy transfer with dissipation

As discussed in the previous section, spin dissipation is expected to stabilize the energy pumping, since it will cause $\mathbf{L}$ to relax to $L\mathbf{S}_0$, (i.e., always cause λ_0 to relax to L), which in turn should lead to quantized energy transfer at the rate $\frac{2\omega L}{T}$.

To test this expectation, we simulated the same model as described in the above subsection, but adding a Gilbert-type dissipation of the form $\gamma_s \mathbf{L} \times \dot{\mathbf{L}}$ in the right hand side of the equations of motion for $\mathbf{L}$ (8.22). In our simulation, we set $\gamma_s = 0.001 L^{-1}$. We initialize the system in the state $A = 17, \phi = 0$, with the $\mathbf{L}$ initially orthogonal to the field – i.e. the same initialization as for the green curve in Fig. 8.5a.

In Fig. 8.5b, we plot the evolution of E_c as a function of time (red curve). As can be seen, the system immediately enters the frequency conversion regime, and E_c grows at the quantized rate $\frac{2L\omega}{T}$ (indicated by the slope of the light blue line). This is in contrast to the dissipationless case, where the energy transfer rate depended on the initial alignment of $\mathbf{L}$ with the field – in the case where $\mathbf{L}$ was initially orthogonal to the field, the cavity field energy E_c would remain constant for the first ≈ 1000 driving periods. At the upper phase boundary E_1, we do not see chaotic behavior as in the dissipationless case, since the dissipation keeps $\mathbf{L}$ pointing along $\mathbf{S}_0$. In

this case, we find that the energy keeps increasing, although at a slower rate[5]

To further demonstrate the stability of the energy transfer with spin dissipation, we repeat the same simulation, but with dissipation strength two orders of magnitude higher, $\gamma_s = 0.1/L$. The data are shown in the blue curve in Fig. 8.5b. We see that the trajectory of E_c is nearly qualitatively identical to the previous case, which demonstrates that the energy transfer rate remains quantized over several orders of magnitude of the dissipation strength.

If we set $A_d = M$, there is no lower phase boundary ($E_0 = 0$), and the cavity can in principle absorb energy from the drive at the quantized rate, even when the cavity amplitude is zero. Without dissipation, the field amplitude would be too weak for $\mathbf{L}$ to track the motion of the field, and there will be no pumping (at least not immediately). But sufficient dissipation, can make $\mathbf{L}$ track $\mathbf{S}_0$ even for small field amplitudes. This is demonstrated in Fig. 8.5c, where we plot the trajectory of E_c for a system where $A_d = M = 14$. We set $\gamma_s = 0.02/L$, and initialize the system in the empty cavity state, with $\mathbf{L}(0) = L(1, 0, 0)$. As can be seen, the energy starts to increase at the constant rate $\frac{2\omega L}{T}$ (light blue curve) after a few periods.

"Lasing" steady state with cavity dissipation

As the final step, we include dissipation of the cavity field in the equations of motion, to simulate the effect of a partially-transparent mirror. This is included as a term $-\frac{1}{2}\gamma_c A$ on the right hand side of the equation of motion for the cavity field amplitude (8.21). This type of dissipation leads to the cavity emitting energy at the rate $-\gamma_c E_c$, where E_c was the energy of the cavity field. In our simulation, we consider the same system as in panels a-b in Fig. 8.5, with the spin dissipation rate set to $\gamma_s = \frac{0.01}{L}$, and a cavity dissipation rate $\gamma_c = 0.0025/T$.

With this type of dissipation included, we expect the system to reach a steady state E_s where the energy absorption rate from the drive $\frac{2L\omega}{T}$ exactly matches the energy loss due to cavity dissipation $\gamma_c E_s$, provided $E_0 < E_s < E_1$ (provided that the energy of the cavity field is initially in the same "topological" range). The parameters we use result in $E_s = 400L\omega$, which is well within this regime. In Fig. 8.5d, we plot the motion of E_c for three different initializations of the cavity field, namely $\mathbf{L}(0) = (L, 0, 0)$, $\phi(0) = 0$, $A(0) = 13$ (green), 17 (red), or 22 (blue). The black horizontal line indicates the predicted steady state energy $E_s = 400L\omega$. As can be seen, the cavity reaches the steady state for all three initializations. The steady state thus appears to be very robust. Once the steady state is reached, the cavity emits energy at the quantized rate $\frac{2L\omega}{T}$.

8.5 Multiple cavity modes

So far, the discussion in this chapter has focused on the case where there a single circularly-polarized cavity mode is connected to the magnetic particle. However, in an actual cavity, the magnetic particle will generally be coupled to several electromagnetic modes. In this section, we discuss how these additional modes affect the topological frequency conversion. Based on analytic arguments, we identify below conditions in which topological frequency conversion may be possible. Subsequently, we support our conclusions with numerical simulations (see Fig. 8.6)

[5]Even though the arguments leading to Eq. (8.37) break down in this regime, the system may still absorb energy from the driving, although not necessarily at the quantized rate.

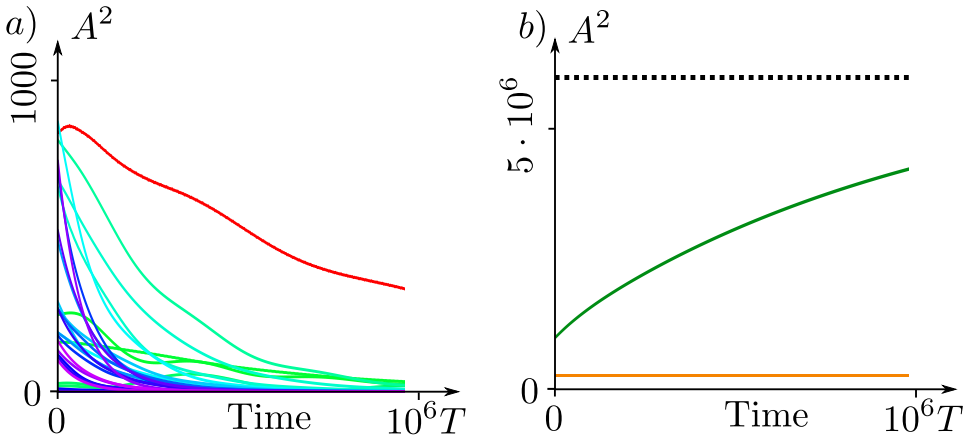

Figure 8.6: Evolution of squared amplitudes of the cavity modes in a setting where the first harmonic is in the topological regime, while the remaining modes are only weakly excited initially. See discussion in Sec. 8.5.2 for details. a) squared amplitudes of modes $\pm 2 \ldots \pm 15$ (green-purple curves) and mode -1 (red curve). b) squared amplitude of mode 1 (green curve).

that firmly demonstrate that topological frequency conversion can persist, even though the cavity holds multiple modes.

To include the additional modes in our model, we assume that the cavity is effectively one-dimensional. In this case, it will support an infinite number of circularly polarized modes with frequencies $n\omega$ for all positive integers n, along with their time-reversed partners (i.e. modes with the same frequency, but reversed polarization). The cavity field is thus described by the variables $(B_{\pm 1}, \phi_{\pm 1}); (B_{\pm 2}, \phi_{\pm 2}); \ldots$ where the variables B_n and ϕ_n describe the amplitude and phase of mode n, and the modes are labelled such that mode $-n$ is the time-reversed partner of mode n. The variables B_n and ϕ_n have the poisson bracket $\{B_n^2, \phi_n\} = \frac{\omega_n \mu_0}{V}$, where $\omega_n = n\omega$, and ω is the fundamental frequency of the cavity.

The full Hamiltonian of the system is given by

$$H(t) = \sum_n \left(\frac{V}{\mu_0} \mathbf{B}_n^2 + g_n \mathbf{B}_n \cdot \mathbf{L} \right) + g_d \mathbf{B}_d(t) \cdot \mathbf{L}, \tag{8.38}$$

where $\mathbf{B}_d(t) = (B_d \sin \Omega t, 0, M - B_d \cos \Omega t)$ denotes the driving field, and $\mathbf{B}_n = B_n(0, \sin \phi_n, -\cos \phi_n)$ denotes contribution to the field from mode n. Note that we allow the coupling g_n to depend on the frequency on the mode.

The above Hamiltonian can be written in terms of dimensionless variables $\{A_n, \phi_n\}$, similar to the ones introduced in Sec. 8.2.2, by substituting $\frac{V}{\mu_0} B_n^2 \to L_0 |\omega_n| A_n^2$, and $g_n \mathbf{B}_n \to \eta_n \mathbf{h}_n$. Here $\eta_n = g_n \beta_n$, where $\beta_n \equiv \sqrt{|\omega_n| \mu_0 L_0 / V}$, and $\mathbf{h}_n = A_n(0, \sin \phi_n, -\cos \phi_n)$. Finally, L_0 denoted an arbitrary scale of action that was introduced in Sec. 8.2. Below, we will work with these variables.

8.5.1 Qualitative discussion

We now consider how the additional cavity modes may affect the frequency conversion. In Sec. 8.4, we found that topological frequency conversion arises in the regime where the magnetic moment's instantaneous precession frequency $\eta|\mathbf{h}|$ is much larger than the field's oscillation frequencies. However, if more than one cavity mode has significant amplitude, the "effective" field $\mathbf{h}_{\text{eff}} = \sum_n \eta_n \mathbf{h}_n + \eta_d \mathbf{h}_d(t)$ that acts on $\mathbf{L}$ will in general become zero for some values of the phases [6]. This will cause the spectral gap to close at some times during the evolution, thus making the derivation of quantized frequency conversion in Sec. 8.4 break down.

The problem above can be avoided if only a single mode is significantly excited, while the amplitudes of all the other modes are kept small. This is achieved if the undesirable modes dissipate energy sufficiently quickly. To study how dissipation affects the system, we include cavity dissipation in the model n the same way as in Sec. 8.4.5. Specifically, we modify the equations of motion for the field amplitudes A_n such that $\dot{A}_n = \{H(t), A_n\} - \frac{\gamma_n}{2} A_n$ (here we allow the dissipation rate γ_n to depend on the index of the mode).

Having included cavity dissipation in our model, we now consider the energy flows in and out of a mode n during time evolution. The motion of the magnetic particle's moment $\mathbf{L}$ pumps energy into mode n at a rate which is controlled by η_n, and the energy is dissipated away at the rate controlled by γ_n. Since the mode n oscillates at frequency ω_n, it is moreover driven by the Fourier component of $\mathbf{L}(t)$ around the frequency ω_n. In Appendix **??** we study this problem in further detail, and find that the rms-averaged amplitude of mode n is given by

$$\overline{|A_n|} = q_n |\Phi_n|, \quad \text{where} \quad q_n \equiv \sqrt{\pi} \frac{\eta_n L}{\sqrt{\gamma_n} L_0}. \tag{8.39}$$

Here $|\Phi_n|$ is the rms averaged value of $\Phi(\omega)$ in a window of width γ_n around ω_n[7], where $\Phi(\omega)$ is the Fourier transform[8] of the complex-valued function $\Phi(t) \equiv \frac{1}{L}(L_x(t) + iL_y(t))$. The above considerations show that we need to keep Φ_n and $\{q_n\}$ as small as possible in order to avoid the spurious modes obstructing the energy transfer.

Note, that Eq. (8.39) applies not only to the spurious modes, but also to the selected mode that we are trying to pump. Let n_0 be the index of the excited mode; then Eq. (8.39) implies conditions on η_{n_0} and γ_{n_0}. Using that $\Phi_{n_0} \leq 1$[9], the coefficient q_{n_0} must be larger than A_0, where A_0 is the amplitude of the excited mode in the steady state predicted in Sec. 8.4.5, i.e., $A_0^2 = \omega_{n_0} \Omega L / \gamma_{n_0}$.

There is a variety of strategies to minimize Φ_n and $\{q_n\}$ for the spurious modes. To minimize the former, we can utilize the fact that in the frequency-conversion regime, the Fourier transform of $\Phi(\omega)$ will contain sharp peaks at integer-multiple combinations of ω_{n_0} and Ω. Thus, the energy pumped into the undesirable modes can be dramatically decreased if the frequencies $\{\omega_n\}$ are

[6] In this case $\mathbf{h}_{\text{eff}}$ will depend on more than two independent variables, namely on time t, and the phases of the excited modes. Since $\mathbf{h}_{\text{eff}}$ lives in a three-dimensional space, there will generically be points where $\mathbf{h}_{\text{eff}}$ is tuned to zero, similar to Weyl points in case of 3 parameter space, and higher dimensional $\mathbf{h}_{\text{eff}} = 0$ in case of more independent variables.

[7] Specifically, it is weighted with a Lorentzian around ω_n, of width $\gamma_n/2$ (see Eq. (**??**) in Appendix **??** for the exact expression).

[8] Note that $\Phi(\omega)$ is a Wiener measure, and has dimensions of $\omega^{-1/2}$

[9] This follows from the fact that $|\Phi(t)| \leq 1$, and that $\int d\omega |\Phi(\omega)|^2$ is the rms average of $\Phi(t)$.

even slightly detuned from those peaks, e.g., if $\omega_n = n\omega_0 + \delta\omega$. Such detuning can be realized by inserting phase-shifting mirror in the cavity [197, 198].

The coefficients $\{q_n\}$ can be minimized independently of q_{n_0} if the physical coupling g_n and dissipation strengths γ_n depend on the frequencies of the modes. The coupling g_n can for example be made frequency dependent if the magnetic particles are distributed over an extended spatial region in the cavity. In this case, the effective coupling g_n to modes with higher frequency (shorter wavelength) decreases as $|n|^{-1}$. Frequency dependence of the dissipation parameter γ_n can be realized if the mirrors in the cavity have frequency-dependent reflection coefficients. This can for instance be realized with Fabry-Pérot devices, which may effectively suppress all undesirable harmonics [199–201].

8.5.2 Numerical study

Making use of the above discussion, we now demonstrate in numerical simulations that the system can indeed be in a regime where mode 1 undergoes topological energy transfer, while the rest of the modes remain only weakly excited.

We include the first 15 harmonics in the simulation, along with their time-reversed partners. Following the discussion above, we consider the case where the frequencies of the modes are slightly detuned from the integer multiples of the fundamental frequency, and where the couplings and dissipation strengths are frequency dependent. Specifically, we set $\omega_n = n\omega_0 + \delta\omega$, with $\delta\omega = 0.05\omega_0$, where the value ω_0 is given below. In addition to this, we let the coupling strengths $\{g_n\}$ decrease as $|n|^{-1}$. Thus, since $\eta_n \propto |\omega_n|^{1/2}$, and $|\omega_n| \approx n\omega_1$, we set $\eta_n = \eta_1|n|^{-1/2}$. Finally, we let the absorption coefficients of the mirror be proportional to the frequency of the mode such that $\gamma_n = |n|\gamma_1$.

Working in units where $\Omega = 2\pi$, we set $\omega_0 = 2\pi/\varphi$ with $\varphi = (1+\sqrt{5})/2$. The dissipation strength of the spin is set to $\gamma_s = 0.01$, and γ_1 is set to 10^{-6}. Finally, we set $\eta_d = \eta_1 = 0.03$, while $M = 2{,}000$, $A_d = 1{,}400$ and $L/L_0 = 3$. Mode 1 is thus in the frequency conversion regime if its amplitude lies in the interval $[600, 3400]$. In this case, it should go to a steady state with squared amplitude $A_0^2 = \frac{L\Omega}{\pi L_0 \gamma_1} = 6 \cdot 10^6$.

We initialize mode 1 in a state with amplitude 1000, while the initial amplitudes of the remaining 29 modes are randomly distributed in the interval $[0, 32]$. The phases of all modes are initially set to zero. From this initial state, we numerically solve the classical equations of motion, and plot in Fig. 8.6ab the resulting evolution of the modes's squared amplitudes over the first 10^6 driving periods. The red curve in panel a) indicates the squared amplitude of mode -1, while the dark green curve on panel *b*) indicates that of mode 1. The remaining curves in panel a) indicate the squared amplitudes of the other modes, with green colors indicating lower harmonics, while blue/purple colors indicate higher harmonics. In panel b), the lower topological phase boundary is indicated by the orange horizontal line, while the predicted steady state $A_0^2 = 10^6$ is indicated by the horizontal dashed line.

As can be seen in panel a), the amplitudes of all modes other than mode 1 decay to near zero[10], over a few hundred thousand driving periods, with the higher-frequency modes decaying

[10] The slower decay of mode -1 is due to the fact that this mode's time-reversed partner, mode 1, is excited. Thus $\mathbf{L}(t)$ thus has a major Fourier component at frequency $\pm\omega_1$. Since $\omega_{-1} \approx -\omega_1$, the coefficient Φ_{-1} should take a relatively large value.

more rapidly. If more harmonics were included in the simulation, we expect them to decay even faster. The fact that their amplitudes remain small means that these modes do not obstruct the topological energy transfer to mode 1. As can be seen in panel b), the squared amplitude of mode 1 does indeed approaches the steady state value of $A_0^2 = 10^6$, consistent with topological frequency conversion[11].

8.6 Discussion

In this work, we demonstrated the robustness of the topological energy transfer between two circularly polarized modes that was studied in Ref. [3]. We studied the setup under the experimentally relevant settings where one of the modes is externally driven, while the other is a dynamical cavity mode. Using a novel Floquet-Lindblad master equation approach (see Appendix **??**), we established that the quantum mechanical version of the effect is stable in the presence of dissipation. In particular, cavity dissipation, in the form of a semitransparent mirror, can stabilize a steady state where cavity photons are emitted at the quantized rate of one per driving period. The dissipation due to the magnetic particle's motion may even add to the robustness of the effect, by keeping the magnetic moment aligned with the instantaneous field. Finally, we find that the effect can be realized even if the cavity is initially empty.

The robustness of the topological energy transfer is further reflected in the fact that the effect can be understood purely as a *classical* phenomenon. Hence, it does not rely on coherence of wave functions for its stability, and can be realized in noisy, macroscopic systems. Interestingly, this work thus demonstrates that classical systems can also exhibit quantized, topologically-robust behavior.

The fact that the topological energy transfer is a classical phenomenon furthermore implies that the effect can be effectively simulated by classical equations of motion. This allows for simulation of the effect under much more complex settings than if it were a purely quantum mechanical effect. We used the latter fact to show that the effect can persist even if multiple modes are present in the cavity. These facts together opens up the possibility for realistic experimental realizations.

Experimental realization and future work — To realize the topological energy transfer experimentally, one can exploit the fact that the effect is classical. Hence the effect may be demonstrated in macroscopic, mechanical systems. We speculate that the model discussed in this work for example can be realized with a gyroscope coupled to mechanical harmonic oscillators (rather than electromagnetic modes), such as pendulums or springs.

Alternatively, the model can be realized with an actual magnetic moment coupled to electromagnetic modes. As discussed in Ref. [3], large values of the coupling g can for example be achieved with an Yttrium-Iron garnet (YIG) sphere [202], or electronic or NMR spin resonance systems [203].

We note that the coupling g between the electromagnetic modes and the angular moment $\mathbf{L}$ (See Eq. (8.1)) sets the range of available frequencies. Specifically, the discussion in Secs. 8.3 and **??**

[11] The amplitude might eventually settle at a value slightly below the steady state value, due to the energy loss to the other modes.

shows that the effect arises when the moment's instantaneous precession frequency $g|\mathbf{B}|$ is larger than the frequency of the modes. For a magnetic moment with the largest possible gyromagnetic ratio (namely that of the electron), i.e. $g \sim 10^{10}\,\mathrm{Hz\,T^{-1}}$, and for strong radiation intensities of $1\,\mathrm{W/mm^2}$, equivalent to magnetic field amplitudes $|\mathbf{B}| \sim 10^{-4}\,\mathrm{T}$, the precession frequency of the moment is in the MHz range. Thus the setup may work in the radio-frequency range with magnetic particles.

The above discussion show that the electromagnetic modes need to be coupled to an *electric* degree of freedom (where much stronger couplings can be achieved), in order to realize the effect with higher frequencies. . The question of how this can be implemented is an interesting direction of future studies. For instance, it may be possible to substitute the moment $\mathbf{L}$ with the orbital (pseudospin) degree of freedom in a Weyl semimetal [204–207], as is also dicussed in Ref. [3], thus allowing for topological energy transfer at higher frequencies. Note that the quadratic dependence of the energy transfer rate on the frequencies ($\dot{E} = \omega_1\omega_2 L/\pi$) mean that a tiny net angular moment can result in macroscopic energy transfer rates, for sufficiently large frequencies.

Finally, the discussion in Sec. 8.5 shows that the effectiveness of the topological frequency conversion is highly dependent on the properties of the electromagnetic cavity. In particular, the effect depends strongly on the spectrum of modes in the cavity, and their dissipation rates. A detailed discussion of how a cavity with suitable properties can be implemented is beyond the scope of this work, and is left for future work.

Concluding remarks and outlook

As discussed in the beginning of this thesis, periodically driven systems may host topological phases with no equivalent in nondriven systems. These anomalous phases are defined by a nonzero value of a so-called micromotion invariant ν, which characterizes the topological properties of the driven system's micromotion (i.e. the dynamics of the system that take place within a driving period). The results of this thesis elucidate the nature of the micromotion invariant, and the anomalous topological phases it defines.

Chapter 3 introduced a method for classifying the topological properties of noninteracting periodically driven systems, in two dimensions. The method showed that the micromotion invariant ν is associated with nodal points in the bulk-evolution operator's spectrum. Ref. [5], in which Chapter 3 is published, shows that the method is applicable to any combination of symmetry class and dimensionality, and thus leads to an *exhaustive* classification of noninteracting, periodically-driven systems.

The physical meaning of the micromotion invariant was revealed when disorder was introduced. Chapter 4-6 studied the anomalous Floquet insulator (AFI), which is the anomalous topological phase that arises when the micromotion invariant ν is nonzero, and disorder is present. These chapters found that the AFI is characterized by quantized, nonzero bulk magnetization density, given by ν/T. The further study of the nature of this micromotion invariant, as well as its analogues in different symmetry classes could lead to new insights about the role of topology in condensed matter physics.

In addition to studying the nature of the micromotion invariant, Chapters 5-6 explored the stability of the AFI. The discussion in Chapter 5 strongly suggests that the AFI can be realized as a stable many-body localized phase in periodically-driven systems. Importantly, a nonzero value of the micromotion invariant is compatible with many-body localization, even though the bulk quasienergy bands necessarily are topologically trivial in this case. A conclusive proof of the stability of the AFI is beyond the scope of this work, due to the challenges in proving the existence of many-body localization in more than one dimension. However, the results of Chapters 5-6 strongly suggest that the AFI can at least support nontrivial topological effects in extremely long time-scales.

Interestingly, with interactions present, the AFI is characterized by a *family* of integer-valued topological invariants, rather than a single invariant as in the noninteracting special case. The nature of this family of invariants is not fully clear, and could be an interesting subject for future studies. The discussion in Chapter 6 reveals several remarkable properties of the family of invariants. Firstly, the topological invariants of the AFI do not rely on full many-body localization for their protection. Secondly, the invariants of the AFI are properties of the system's evolution operator, and do not rely on the particular state of the system.

Chapters 7-8 explored novel topological pumping effects that can arise in periodically driven systems. Chapter 7 demonstrated that the dimensional reduction of the AFI leads to a novel, topological energy pumping effect, analogously to the charge pumping effect that arises from the dimensional reduction of the Chern insulator [65]. Chapter 8 demonstrated a different energy pumping effect, which arises in a strongly driven magnetic particle, and can be seen as a Thouless pump of photons. As Chapter 8 further demonstrated, the latter phenomenon can be understood

as a purely classical effect. Remarkably, the discussion in Chapter 8 thus demonstrates that a seemingly simple *classical* system can exhibit highly nontrivial topological effects, when subject to periodic driving. Possible realizations of the effects described in Chapters 7,8 (see also Ref. [3]), such as in Weyl semimetals, could also be an interesting direction of future studies.

The discussion in the last chapters of this thesis show that surprising and potentially useful topological effects can arise when a topological insulator is mapped to a seemingly unrelated system. Such unconventional realizations of topological insulators have resulted in the discovery of novel topological effects in systems photonic crystals, mechanical metamaterials, and (as Chapter 8 showed) even in the classical dynamics of driven harmonic oscillators. The recent discoveries of these novel effects in otherwise well-understood systems opens up the possibility for additional unexplored topological phenomena beyond solid-state systems.

Appendices

Appendix A

Master Equation for Periodically Driven Systems

In this appendix we derive the Master equation in Eqs. (8.15)-(8.17), which used in the main text to describe the behaviour of the system when subject to dissipation. We derive this master equation, using only a single approximation in our derivation, namely that the bath is Markovian. The master equation derived in this appendix in principle describes any periodically driven system which is coupled to external baths, as long as the baths are effectively Markovian.

In this appendix, we consider the case where only a single variable is connected to a bath. The case of multiple baths follows the same lines.

Absorbing all prefactors into the system operator A, the Hamiltonian describing the full system-bath setup of a non-driven system is of the form

$$H_{SB} = H_S(t) + H_B + A\int d\omega\, \sqrt{S(\omega)}(b^\dagger(\omega) + b(\omega)). \tag{A.1}$$

where $H_B = \int d\omega\, \omega b^\dagger(\omega)b(\omega)$, and A_S and H_S only act on the system degrees of freeedom. As our starting point, we perform a rotating frame transformation generated by $H_B + H_S(t)$, thus going to the interaction picture. In this case, the full time-evolution operator of the system $\mathcal{U}(t)$ is given by $\mathcal{U}(t) = U_S(t)U_B(t)U(t)$, where $U_{S,B}(t) = \mathcal{T}e^{-i\int_0^t H_{S,B}(t')dt'}$, with $\mathcal{T}$ denoting the time-ordering symbol. The interaction picture evolution operator $U(t)$ is generated by the Hamiltonian

$$H(t) = A(t)B(t). \tag{A.2}$$

With

$$B(t) = \int d\omega (b(\omega)e^{-i\omega t} + b^\dagger(\omega)e^{i\omega t})\sqrt{S(\omega)}, \tag{A.3}$$

and $A(t) = U_S^\dagger(t)AU_S(t)$. At this point, we are interested in finding the time-evolution of full density matrix in the system, $\rho_F(t) = |\Psi(t)\rangle\langle\Psi(t)|$, where $|\Psi(t)\rangle$ is the time-evolution of the combined system-bath state from some initial state $|\Psi_0\rangle$. Later, we will trace out the bath degress of freedom, obtaining the time-evoluton of the reduced density matrix of the system.

A.1 Time evolution in the superoperator picture

To achieve this, it turns out to be convenient to make use of superoperator notation. With this formalism, we exploit the fact that linear operators on the Hilbert space are themselves as vectors, whose (Heisenberg picture) time-evolution obeys a Schrodinger-type equation. To make the vector nature of the operators explicit, we use double brackets $|\cdot\rangle\!\rangle$ to indicate operators in the following. These vectors live in the "operator Hilbert space" $\mathcal{H}_2$, whose inner product refers the Hilbert-Schmidt inner product, i.e. $\langle\!\langle X|Y\rangle\!\rangle \equiv \mathrm{Tr}(X^\dagger Y)$.

Using the notation above, the time-evolution of the combined system-bath state ρ_F is given by

$$\partial_t|\rho_F\rangle\!\rangle = -i\hat{H}(t)|\rho_F\rangle\!\rangle. \tag{A.4}$$

where $\hat{H}$ is a superoperator (i.e. a linear operator that acts on vectors in $\mathcal{H}_2$), and is defined from the Hamiltonian H of the system as follows:

$$\hat{H}|M\rangle\!\rangle = |HM - MH\rangle\!\rangle. \tag{A.5}$$

The above linear differential equation has the solution

$$|\rho_F(t)\rangle\!\rangle = U(t)|\rho_F(0)\rangle\!\rangle. \tag{A.6}$$

Here $U(t)$ is the full time-evolution (super)operator, given by

$$U(t) = \mathcal{T}e^{-i\int_0^t dt'\hat{H}(t')}. \tag{A.7}$$

The time-evolution operator $U(t)$ can formally be written

$$U(t) = \sum_{n=0}^{\infty}(-i)^n \int_0^t dt_1 \dots dt_n \prod_{k=1}^{n} \theta(t_k - t_{k-1})\hat{H}(t_n). \tag{A.8}$$

In the following, it will be useful to rewrite, inserting $\hat{H}(t) = A(t)_l B(t)_l - A(t)_r B(t)_r$, where the superoperators X_l, X_r are defined from the operator X as

$$X_l|M\rangle\!\rangle = |XM\rangle\!\rangle, \quad X_r|M\rangle\!\rangle = |MX\rangle\!\rangle. \tag{A.9}$$

Note that, by this definition, $A_r B_r = (BA)_r$. Using these definitions,

$$\begin{aligned} U(t) = \sum_{n=0}^{\infty}\sum_{d}(-i)^n \int_0^t dt_1 \dots dt_n \\ \prod_{k=1}^{n} \theta(t_k - t_{k-1}) s_{d_k} A(t_k)_{d_k} B(t_k)_{d_k}. \end{aligned} \tag{A.10}$$

where $t_0 = 0$, and we introduced the symbol s_d, defined by $s_l = 1$, $s_r = -1$. Finally, the sum $\sum_d$ is used as shorthand for $\sum_{d_1\in\{l,r\}} \dots \sum_{d_n\in\{l,r\}}$, and hence sums over 2^n tems.

A.2 Reduced time evolution operator for the system

We consider now the case, where the system is initially in some state $\rho(0)$, and the bath is in a thermal state ρ_B at some fixed temperature. The combined system-bath initial state can then be written $\rho_F(0) = \rho(0) \otimes \rho_B$. The goal of this appendix is to find the evolution of the reduced density matrix of the system $\rho(t) = \mathrm{Tr}_B(\rho_F(t))$. In this subsection, we show from Eq. (A.10) that $\rho(t)$ in the form $|\rho(t)\rangle\!\rangle = U_R(t)|\rho(0)\rangle\!\rangle$ for some linear superoperator $U_R(t)$, which we will find below.

As our first step, we note that partial trace Tr_B over the bath degree of freedom can be expresed as the dual vector (i.e. a bra) of the bath identity operator $|I_B\rangle\!\rangle$[1]. Specifically, $|\mathrm{Tr}_B(M)\rangle\!\rangle_S = \langle\!\langle I_B| \circ |M_{SB}\rangle\!\rangle$. Thus, the reduced density matrix can be found as

$$|\rho(t)\rangle\!\rangle = \langle\!\langle I_B|U(t)\Big(|\rho(0)\rangle\!\rangle \otimes |\rho_B\rangle\!\rangle\Big). \tag{A.11}$$

We can express this as

$$|\rho(t)\rangle\!\rangle = U_R(t)|\rho(0)\rangle\!\rangle, \tag{A.12}$$

where the reduced time-evolution operator $U_R(t)$ acts on the operator space of $\mathcal{H}_S$, and is given by

$$U_R(t) = \langle\!\langle I_B|U(t)|\rho_B\rangle\!\rangle. \tag{A.13}$$

Inserting the expression (A.10) for $U(t)$ in the above, and using the fact that only the operators $\{B(t)_{l,r}\}$ act on the bath degrees of freedom, we obatin

$$\begin{aligned} U_R(t) = \sum_{n=0}^{\infty} \sum_{d} (-i)^n \int_0^t \prod_{k=1}^{n} \theta(t_k - t_{k-1}) dt_k \\ \prod_{k=1}^{n} s_{d_k} A(t_k)_{d_k} \cdot K_d(t_1 \dots t_n) \end{aligned} \tag{A.14}$$

where $K_d(t_1 \dots t_k)$ is a scalar function, and is given by

$$K_d(t_1, \dots t_n) \equiv \langle\!\langle I_B| \prod_{k=1}^{n} B(t_k)_{d_k} |\rho_B\rangle\!\rangle. \tag{A.15}$$

Using the explicit form of $B(t)$ in Eq. (A.3), we can write $K_d(t_1 \dots t_k)$ as

$$\begin{aligned} K_d(t_1, \dots t_n) = \int_0^{\infty} d^{2l}\omega \, \langle\!\langle I_B| \prod_{k=1}^{n} \sqrt{S(\omega_k)} \\ \Big[e^{-i\omega_k t_k} b(\omega_k)_{d_k} + e^{i\omega_k t_k} b^\dagger(\omega_k)_{d_k}\Big] |\rho_B\rangle\!\rangle. \end{aligned} \tag{A.16}$$

The thermal state $|\rho_B\rangle\!\rangle$ is diagonalized by the eigenstates of the photon number operators $\{b^\dagger(\omega)b(\omega)\}$. Expanding the product above, the integrand above can then only be nonzero when

[1] Since the Hilbert space has a direct product structure (i.e. it is spanned by a basis of the form $|a\rangle_S \otimes |b\rangle_B$), the operator Hilbet space inherits the same structure, and is spanned by the basis vectors $\{|a_1 a_2\rangle\!\rangle_S \otimes |b_1 b_2\rangle\!\rangle_B\}$, where $|ab\rangle\!\rangle_i \equiv |a\rangle_i \langle b|_i$. The bath identity operator can be written as $|I_B\rangle\!\rangle = \Sigma_b |bb\rangle\!\rangle_B$.

n is even, and for the values of $(\omega_1, \ldots \omega_n)$, for which each distinct freuqency appears an even number of times. Summing together all possible pairings of the frequencies, we can rewrite the above as

$$K_d(t_1, \ldots t_{2l}) = \int_0^\infty d^l\omega \, \langle\!\langle I_B| \sum_{\sigma \in \mathcal{S}_{2l}} \prod_{k=1}^{l} S(\omega_k) \Big[e^{-i\omega_k (t_{\sigma_{2k+1}} - t_{\sigma_{2k}})} b(\omega_k)_{d_{\sigma_{2k+1}}} b^\dagger(\omega_k)_{d_{\sigma_{2k}}} + e^{i\omega_k (t_{\sigma_{2k+1}} - t_{\sigma_{2k}})} b^\dagger(\omega_k)_{d_{\sigma_{2k+1}}} b(\omega_k)_{d_{\sigma_{2k}}} \Big] |\rho_B\rangle\!\rangle.$$

where $\mathcal{S}_{2z}$ is the set of all permutations σ of the integers $1 \ldots 2z$ such that $\sigma_{2i+1} > \sigma_{2i}$ for all i. The sum over permutations count all distinct sequences of emissions that result in the same configuration of emitted photons.

Next, we use that both $|\rho_B\rangle\!\rangle$ and $|I_B\rangle\!\rangle$ can be written as direct products of operators that live in the operator Hilbert spaces of the individual modes: $|\rho_B\rangle\!\rangle = \prod_\omega |\rho_\omega\rangle\!\rangle$, $|I_B\rangle\!\rangle = \prod_\omega |I_\omega\rangle\!\rangle$. Here $|\rho_\omega\rangle\!\rangle$ denotes the density matrix for the mode at frequency ω, and $|I_\omega\rangle\!\rangle$ is the identity operator on the Hilbert space of the mode with frequency ω.

Doing this, we obtain

$$K_d(t_1, \ldots t_n) = \int_0^\infty d^l\omega \sum_{\sigma \in \mathcal{S}_{2l}} \prod_{k=1}^{l} S(\omega_k) \, f_{d_{\sigma_{2k+1}}, d_{\sigma_{2k}}}(\omega_k; t_{\sigma_{2k+1}} - t_{\sigma_{2k}}). \tag{A.17}$$

where

$$f_{\mu,\nu}(\omega; t) \equiv \langle\!\langle I_\omega | b(\omega)_\mu b^\dagger(\omega)_\nu | \rho_\omega \rangle\!\rangle e^{-i\omega t} + \langle\!\langle I_\omega | b^\dagger(\omega)_\mu b(\omega)_\nu | \rho_\omega \rangle\!\rangle e^{i\omega t}.$$

We recall that $\langle\!\langle I_\omega | X | \rho_\omega \rangle\!\rangle$ is different notation for $\mathrm{Tr}_{B_\omega}[X \circ \rho_\omega]$, where Tr_{B_ω} traces out the degree of freedom in the mode with frequency ω. Using the definitions (A.9), and considering all four possible configurations of μ and ν, one can verify that

$$\begin{aligned} \langle\!\langle I_\omega | b(\omega)_\mu b(\omega)^\dagger_\nu | \rho_\omega \rangle\!\rangle &= n(\omega) + \delta_{\nu l}. \\ \langle\!\langle I_\omega | b(\omega)^\dagger_\mu b(\omega)_\nu | \rho_\omega \rangle\!\rangle &= n(\omega) + \delta_{\nu r}. \end{aligned}$$

Here $\langle n(\omega) \rangle = \mathrm{Tr}(\rho_\omega b^\dagger(\omega) b(\omega))$ is the thermal expectation value of the photon number in the bath mode with frequency ω. This is given by the Bose-Einstein distribution. The symbol $\delta_{\nu l}$ takes value 1 if $\nu = l$, and value 0 if $\nu = r$, and $\delta_{\nu r}$ is defined in a similar fashion.

Inserting this into the expression for $f_{\mu,\nu}(\omega, t)$, we find

$$f_{\mu,\nu}(\omega; t) = n(\omega)(e^{i\omega t} + e^{-i\omega t}) + e^{-i s_\nu \omega t} \tag{A.18}$$

We now consider the ω_k integral in the above expression, and find that

$$\int_0^\infty d\omega_k S(\omega_k) f_{\mu,\nu}(\omega_k; t) = g_\nu(t). \tag{A.19}$$

Here the bath correlation function $g_\nu(t)$ is given by

$$g_\nu(t) \equiv \int_{-\infty}^{\infty} d\omega J(s_\nu \omega) e^{-i\omega t}, \tag{A.20}$$

where the spectral function of the bath $J(\omega)$ given by

$$J(\omega) = S(|\omega|)(\theta(\omega) + n(|\omega|)) \tag{A.21}$$

The bath correlation function describes how fast information is lost in the bath, and generally decays rapidly to zero.

Inserting the result Eq. (A.19) into Eq. (A.17), we write $K_d(t_1, \dots t_n)$ in terms of the bath correlation function as[2]:

$$K_d(t_1, \dots t_n) = \sum_{\sigma \in \mathcal{S}_{2l}} \prod_{k=1}^{l} g_{d_{\sigma_{2k}}}(t_{\sigma_{2k+1}} - t_{\sigma_{2k}}) \tag{A.22}$$

Inserting this result into the expression (A.14) for $U_R(t)$, and using $K_d(t_1 \dots t_n) = 0$ for odd n, we find

$$\begin{aligned} U_R(t) = &\sum_{l=0}^{\infty} (-1)^l \sum_d \int_0^t \prod_{k=1}^{2l} dt_k \theta(t_{k+1} - t_k) s_{d_k} A(t_k)_{d_k} \\ &\sum_{\sigma \in \mathcal{S}_{2l}} \prod_{k=1}^{l} g_{d_{\sigma_{2k}}}(t_{\sigma_{2k+1}} - t_{\sigma_{2k}}) \end{aligned}$$

As our next step, we write $A(t)$ in terms of its fourier transform: $A(t) = \int dq A(q) e^{-iqt}$ in the above, obtaining

$$\begin{aligned} U_R(t) = &\sum_{l=0}^{\infty} (-1)^l \sum_d \int d^{2l}\mathbf{q} \int_0^t \prod_{k=1}^{2l} dt_k \theta(t_{k+1} - t_k) s_{d_k} \\ &\prod_{k=1}^{2l} A(q_k)_{d_k} e^{-iq_k t_k} \sum_{\sigma \in \mathcal{S}_{2l}} \prod_{k=1}^{l} g_{d_{\sigma_{2k}}}(t_{\sigma_{2k+1}} - t_{\sigma_{2k}}). \end{aligned}$$

Here we introduced the notation $\mathbf{q} = (q_1 \dots q_{2l})$, and $d^{2l}\mathbf{q} = dq_1 \dots dq_{2l}$. As our next step, we collect the time integrals in one factor, obtaining

$$U_R(t) = \sum_{l=0}^{\infty} (-1)^l \sum_d \int d^{2l}\mathbf{q} \prod_{k=1}^{2l} s_{d_k} A(q_k)_{d_k} M_d(\mathbf{q}, t), \tag{A.23}$$

where d is shorthand for $(d_1 \dots d_{2l})$, and

$$\begin{aligned} M_d(\mathbf{q}, t) = &\sum_{\sigma \in \mathcal{S}_{2l}} \int_0^t \prod_{k=1}^{2l} dt_k \theta(t_{k+1} - t_k) e^{-iq_k t_k} \\ &\prod_{k=1}^{l} g_{d_{\sigma_{2k}}}(t_{\sigma_{2k+1}} - t_{\sigma_{2k}}). \end{aligned} \tag{A.24}$$

[2]Even though it is not necessary for the following, it turns out that the "correlation kernel" can be written as $K_d(t_1, \dots t_n) = n! \Pi_{k=1}^{2l} \theta(t_k - t_{k-1}) \mathrm{Hf}(G_d[\{t_n\}])$ where Hf(M) is the so-called Hafnian of the matrix M, and the matrix G_d is defined as $G_d(ab) = g(s_{d_a}|t_a - t_b|)$.

Inserting the expression (A.20) for the bath correlation function $g_\nu(t)$,

$$M_d(\mathbf{q},t) = \sum_{\sigma\in\mathcal{S}_{2l}} \int_0^t \prod_{k=1}^{2l} dt_k \theta(t_{k+1}-t_k) \int_{-\infty}^{\infty} d\omega_k J(s_{d_{\sigma_{2k}}}\omega_k) \prod_{k=1}^{l} e^{-i(\omega_k+q_{\sigma_{2k+1}})t_{\sigma_{2k+1}}} e^{-i(-\omega_k+q_{\sigma_{2k}})t_{\sigma_{2k}}}$$

A.3 Markov Approximation

Up to this point, our analysis has been exact. To move on from here we make our first and only approximation, namly the approximation of the bath as Markovian. This approximation is necessary to arrive at a linear, first-order differential equation for ρ, which we will do in the following.

To motivate our approximation, we consider the integral above for a given permutation σ in $\mathcal{S}_{2l}$. We note that the integral above can be seen as a sum of paths, where t_k indicates the time of the k th photon emission or absorption from the bath. This time is typically integrated over time-windows of length $\frac{1}{\Gamma}$, where Γ indicates the average rate of photon emission. The $t_{\sigma_{2k}}$ integral is only nonvanishing if the integrand is non-oscillatory on this time-scale – i.e. if $\omega_k \sim q_{\sigma_{2k}} \pm \Gamma$. The same arguments show that the $t_{\sigma_{2k+1}}$ integral is nonzero if $\omega_k \sim -q_{\sigma_{2k+1}} \pm \Gamma$. Taken together, this means that we must have $q_{\sigma_{2k}} \sim -q_{\sigma_{2k+1}} \pm \Gamma$ for the $t_{\sigma_{2k}}$ integral to be nonvanishing.

We now assume that $J(\omega)$ is a smooth, slowly changing function that can be assumed constant over intervals of width Γ. In this case, since the integral is only nonvanishing when $\omega \sim q_{\sigma_{2k}} \pm \Gamma$, we may replace $J(s_{d_{\sigma_{2k}}}\omega_k)$ with $J(s_{d_{\sigma_{2k}}}q_{\sigma_{2k}})$ in the above. Equivalently, we can replace it with $J(-s_{d_{\sigma_{2k}}}q_{\sigma_{2k+1}})$, since the difference between $q_{\sigma_{2k}}$ and $-q\sigma_{2k+1}$ must be of order Γ, for the t_{2k} and t_{2k+1} integrals to be nonzero. In this way, there are several ways of approximating $J(\omega_k)$ in the above that result in the same value of the integral, given our assumption about J holds. In fact, the above arguments show that any approximation of $J(\omega)$ is valid if it equals $J(q_{\sigma_{2k}})$ or $J(-q_{\sigma_{2k+1}})$ up to a correction of order Γ. In the following, we choose to make the following approximation, which is also valid from the above arguments:

$$J(s_{d_{\sigma_{2k}}}\omega_k) \approx \sqrt{J(-s_{d_{\sigma_{2k}}}q_{\sigma_{2k+1}})J(s_{d_{\sigma_{2k}}}q_{\sigma_{2k}})}. \tag{A.25}$$

Making the abpve approximation in the expression for $M_d(\mathbf{q},t)$, and subsequently integrating out $\omega_1 \ldots \omega_k$, we obtain

$$M_d(\mathbf{q},t) \approx \sum_{\sigma\in\mathcal{S}_{2l}} \int_0^t \prod_{k=1}^{2l} dt_k \theta(t_{k+1}-t_k)(2\pi)^l \prod_{k=1}^{l} \sqrt{J(-s_{d_{\sigma_{2k}}}q_{\sigma_{2k+1}})J(s_{d_{\sigma_{2k}}}q_{\sigma_{2k}})} e^{-i(q_{\sigma_{2k+1}}+q_{\sigma_{2k}})t_{\sigma_{2k}}} \delta(t_{\sigma_{2k+1}}-t_{\sigma_{2k}})$$

By comparing with Eq. (A.24), we see that the our approximation assumes the bath correlation function $g_\nu(t)$ to be proportional to the Dirac delta function. Thus, our approximation assumes the bath to be Markovian (i.e. to have no memory of the system at any time). Note that it would not be possible to obtain a linear first-order differential equation for ρ below if we did not assume g to be proportional to the δ function.

As our next step, we now note that the time integral in the above is only nonzero for a single permutation in $\mathcal{S}_{2l}$ – namely the identity permutation $\sigma_k = k$. For all other permutations in $\mathcal{S}_{2l}$, the δ functions require $t_k = t_{k'}$ for some k, k' such that $k - k' \geq 2$. In this case, the product of step functions above vanishes, since $\theta(t_k - t_{k-1}) \dots \theta(t_{k'+2} - t_{k'+1})\theta(t_{k'+1} - t_k) = 0$[3]. Using this result, along with $\delta(t)\theta(t) = \frac{1}{2}\delta(t)$, we integrate out t_k for all odd k. Relabelling the remaining integrands, the resulting expression reads

$$M_d(\mathbf{q}, t) = \pi^l \int_0^t \prod_{k=1}^{l} dt_k \theta(t_{k+1} - t_k) \\ e^{-i(q_{2k+1}+q_{2k})t_k} \sqrt{J(-s_{d_{2k}} q_{2k+1}) J(s_{d_{2k}} q_{2k})}$$

Inserting the above expression for $M_d(\mathbf{q}, t)$ in Eq. (A.23), we obtain

$$U_R(t) \approx \sum_{l=0}^{\infty} \sum_{d} (-\pi)^l \int d^{2l}\mathbf{q} \int_0^t \prod_{k=1}^{l} dt_k \theta(t_{k+1} - t_k) \\ s_{d_{2k}} s_{d_{2k+1}} A(q_{2k})_{d_{2k}} A(q_{2k+1})_{d_{2k+1}} e^{-i(q_{2k+1}+q_{2k})t_k} \\ \sqrt{J(-s_{d_{2k}} q_{2k+1}) J(s_{d_{2k}} q_{2k})} \tag{A.26}$$

A.4 Derivation of master equation

Having rewritten the reduced time-evolution operator using the Markov approximation, we now show that it can be written as a time-ordered exponential. This in turn implies that ρ obeys a linear first-order differential equation.

To show this, we interchange the time integrals with the d sum and $\mathbf{q}$ integrals in Eq. (A.26), obtaining

$$U_R(t) = \sum_{l=0}^{\infty} \int_0^t \prod_{k=1}^{l} dt_k \theta(t_{k+1} - t_k) \mathcal{L}(t_k), \tag{A.27}$$

where the superoperator $\mathcal{L}(t)$ is given by

$$\mathcal{L}(t) = -\pi \sum_{d_1, d_2} s_{d_1} s_{d_2} \int dq_1 dq_2 \, A(q_1)_{d_1} A(q_2)_{d_2} e^{-i(q_1+q_2)t} \sqrt{J(-s_{d_2} q_1) J(s_{d_2} q_2)}. \tag{A.28}$$

[3] We recall that the sum over permutations takes into account interference between different orders of emissions that result in the same configuration of emitted photons. By assuming a Markovian bath, non-identical times of emissions result in completely non-overlapping states of the bath (i.e., the bath "learns" about the emission of a photon instantly), and hence we don't have interference between different orders of photon emissions.

We note that the sum on the right-hand side in Eq. (A.27) is simply a time-ordered exponential, and thus the reduced time-evolution operator $U_R(t)$ is given by

$$U_R(t) = \mathcal{T} e^{\int_0^t dt' \mathcal{L}(t')}. \tag{A.29}$$

Returning to the equation of motion (A.12) for ρ, and taking the time-derivative, we then arrive at the interaction picture master equation

$$\dot{\rho}(t) = \mathcal{L}(t) \circ \rho(t). \tag{A.30}$$

To obtain a simple expression for $\mathcal{L}(t)$, we introduce the operator

$$L(t) = \int dq \sqrt{2\pi J(q)} e^{-iqt} A(q). \tag{A.31}$$

Using this definition in Eq. (A.28), along with $\int dq \sqrt{2\pi J(-q)} e^{-iqt} A(q) = L^\dagger(t)$[4], we find

$$\mathcal{L}(t) = -\frac{1}{2} \sum_{d_1, d_2} s_{d_1} s_{d_2} L^{(-s_{d_2})}(t)_{d_1} L^{(s_{d_2})}(t)_{d_2},$$

where we used the shorthand $L^{(-1)} = L^\dagger$, $L^{(1)} = L$. Writing out the four terms in the d_1,d_2 sum explicitly,

$$\mathcal{L}(t) = -\frac{1}{2}(L^\dagger(t)_l L(t)_l + L(t)_r L^\dagger(t)_r) + \frac{1}{2}(L^\dagger(t)_r L(t)_l - L(t)_l L^\dagger(t)_r).$$

Note that the operator $\mathcal{L}(t)$ is an operator of the Lindblad form and hence $U_R(t)$ conserves the complete positivity and unit trace of ρ.

Using the above result in Eq. (A.30), along with the definitions of the superoperators X_l and X_r in Eq. (A.9), we then arrive at the master equation (which holds for general time-dependent Hamiltonians in the interaction picture)

$$\dot{\rho} = -\frac{1}{2}\{L^\dagger(t)L(t), \rho\} + L^\dagger(t)\rho L(t). \tag{A.32}$$

where the jump operator $L(t)$ was introduced in Eq. (A.31) above.

A.5 Master equation for periodically driven systems

Having derived the Master equation (A.32) for general time-dependent Hamiltonians, we now find $L(t)$ in the special case of a periodically driven system.

The jump operator $L(t)$ is defined Eq. (A.31) from the fourier transform of the operator $A(t) \equiv U_S^\dagger(t) A U_S(t)$. In the case we consider here, $U_S(t) = \mathcal{T} e^{-i\int_0^t dt' H_S(t')}$ is the time-evolution operator of the periodically driven system described by $H_S(t)$. As our starting point, we we write $A(t)$ in the basis of Floquet eigenstates $\{|\phi_a\rangle\}$ of the system:

$$A(t) = \sum_{ab} |\phi_a\rangle\langle\phi_b| A_{ab}(t). \tag{A.33}$$

[4]this follows from the Hermiticity of $A(t)$, which implies $A^\dagger(q) = A(-q)$

Here, by definition,

$$A_{ab}(t) = \langle\phi_a|U_S^\dagger(t)AU_S(t)|\phi_b\rangle. \tag{A.34}$$

Next, we note that $U_S(t)|\phi_a\rangle = e^{-i\varepsilon_a t}|\phi_a(t)\rangle$, where the $\{|\phi_a(t)\rangle = |\phi_a(t+T)\rangle\}$ denote the T-periodic Floquet states associated with the Hamiltonian $H_S(t)$. In terms of the Floquet states,

$$A_{ab}(t) = \langle\phi_a(t)|A|\phi_b(t)\rangle e^{-i(\varepsilon_b-\varepsilon_a)t}. \tag{A.35}$$

Thus $A_{ab}(t)$ is given by $e^{-i(\varepsilon_b-\varepsilon_a)t}$ times a T-periodic function, and we may write

$$A_{ab}(t) = \sum_n A^{ab}[n]e^{-i(\varepsilon_b-\varepsilon_a+\Omega n)t}. \tag{A.36}$$

Using the definition of the fourier transform, $A(t) = \int dq A(q)e^{-iqt}$, $A(q)$ can be written in terms of the coeficcients $\{A^{ab}[n]\}$ as

$$A(q) = \sum_{ab,n} \delta(q+\varepsilon_a-\varepsilon_b-\Omega n)|\phi_a\rangle\langle\phi_b|A^{ab}[n] \tag{A.37}$$

Inserting this in the definition of $L(t)$ in Eq. (A.31), we thus find, that for periodically driven systems

$$L(t) = \sum_{ab,n} |\phi_a\rangle\langle\phi_b|L^{ab}[n]e^{-i(\Omega n-\varepsilon_a+\varepsilon_b)t} \tag{A.38}$$

with

$$L^{ab}[n] = \sqrt{2\pi J(\varepsilon_b-\varepsilon_a+n\Omega)}A^{ab}[n]. \tag{A.39}$$

Here the coefficients $\{A^{ab}[n]\}$ were defined in Eqs. (A.35) and (A.36). From these equations, it follows that we can find them as

$$A^{ab}[n] = \frac{1}{T}\int_0^T dt\langle\phi_a(t)|A|\phi_b(t)\rangle e^{in\Omega t}. \tag{A.40}$$

A.5.1 Master equation in Schrodinger picture

The above result holds in the interaction picture. We obtain the Schrodinger picture master equation by reversing the rotating frame transformation that was generated by the unitary transformation $U_S(t) = \mathcal{T}e^{-i\int_0^t dt' H_S(t')}$. Doing this, we find

$$\dot\rho(t) = -i[H_S(t),\rho] + \tilde L^\dagger(t)\rho\tilde L(t) - \frac{1}{2}\{\tilde L^\dagger(t)\tilde L(t),\rho\} \tag{A.41}$$

where $\tilde L(t) = U_S(t)L(t)U_S^\dagger(t)$. Using $U_S(t)|\phi_a\rangle = e^{-i\varepsilon_a t}|\phi_a(t)\rangle$,

$$\tilde L(t) = \sum_{ab,n} |\phi_a(t)\rangle\langle\phi_b(t)|e^{-i\Omega nt}L^{ab}[n], \tag{A.42}$$

where the matrix elements $\{L^{ab}[n]\}$ were defined in Eqs. (A.39)-(A.40).

Appendix B

Appendix for Chapter 3

B.1 Time-domain expressions for the invariants ν_0 and ν_1

In this appendix we derive a time domain integral expression for the bulk invariant $w_m[U]$ in Eq. (3.9), which corresponds to the number of edge modes appearing in gap m when the system is defined in a geometry with edges. We directly show that this invariant is equivalent to the winding number invariant $W[U_\varepsilon]$ of Ref. [1], with ε set equal to a quasienergy value inside gap m:

$$W[U_m] = \int \frac{d^2k dt}{8\pi^2} \mathrm{Tr}\left\{ U_m^\dagger \partial_t U_m \left[U_m^\dagger \partial_{k_x} U_m, U_m^\dagger \partial_{k_y} U_m \right] \right\}. \tag{B.1}$$

Here U_m is a time-periodic evolution operator, satisfying $U_m(\mathbf{k}, T) = 1$, which is obtained from the original evolution U by a smooth deformation in which gap m of the quasienergy spectrum is kept open. Explicitly, the time-periodic evolution operator U_m can be obtained by deforming the final values of the phase bands $\phi_n(\mathbf{k}, T)$ to zero for $n = 1 \ldots m$, while the final values of the remaining bands are deformed to 2π.

In order to demonstrate the equivalence of the two invariants, i.e., to show $w_m[U] = W[U_m]$, we first consider two special cases and then discuss the general situation. In this appendix we label points in the three dimensional $\mathbf{k}, t$-space by a single dimensionless vector

$$\mathbf{s} = \left(\frac{\mathbf{k}}{2\pi/a}, \frac{t}{T} \right).$$

B.1.1 Winding number in case of no singularities

To begin, we first consider the case where $U_m(\mathbf{k}, t)$ has no topological singularities in the zone-edge gap. It is then possible to continuously deform the evolution operator U_m into one corresponding to a non-driven system, as described in Sec. 3.2. In doing so, the winding number $W[U_m]$, a topological invariant, cannot change its value. After the deformation, $W[U_m]$ is simply the winding number of a non-driven system described by the Hamiltonian

$$H_m(\mathbf{k}) = \frac{2\pi}{T} \sum_{n=m+1}^{N} P_n(\mathbf{k}, T). \tag{B.2}$$

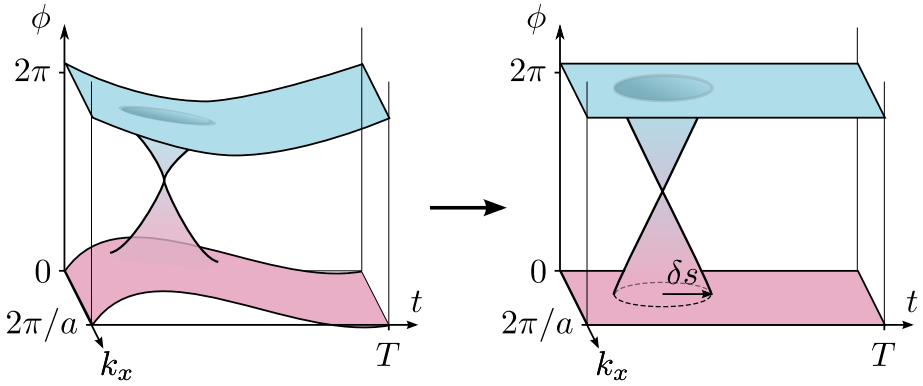

Figure B.1: The deformation of an isolated singularity discussed in Sec. B.1.2. In the figure, phase band 1 (blue) is shifted up by 2π for clarity of illustration.

The winding number of a system governed by such a Hamiltonian was found in Ref. [1] to be $\sum_{n=1}^{m} C_n$, where C_n is the Chern number of Floquet band n. Hence

$$W\left[U_m\right] = \sum_{n=1}^{m} C_n, \text{ (no zone-edge singularities).} \tag{B.3}$$

Note that the winding number will always be zero in the quasienergy zone-edge gap if the phase bands do not host any zone-edge singularities. This follows from the fact that the sum of Chern numbers for all bands must evaluate to zero, $\sum_{n=1}^{N} C_n = 0$.

B.1.2 Winding number in the case of one singularity

We now consider the case where $\phi_n(\mathbf{k}, T) = 0$ for all n, and $U_m(\mathbf{k}, t)$ has only one singularity in the zone-edge gap, located at $\mathbf{s}_0 = (\mathbf{k}_0/(2\pi/a), t_0/T)$. At the singularity, the two touching bands N and 1 have phases ϕ_d and $\phi_d - 2\pi$, where ϕ_d is a real number determined by details of the evolution. In this case we can deform the phase bands to zero for all $\mathbf{k}, t$, except in a small spherical neighbourhood of radius δs that surrounds the singularity (here lengths are computed with respect to the usual norm on the dimensionless vector $\mathbf{s}$). Within the neighborhood, all $N-2$ bands not involved in the singularity can still be flattened. The phase values of the two intersecting bands are deformed to evolve linearly from zero at the edge of the neighbourhood to π and $-\pi$ at the center (letting ϕ_d go continuously to π in the process), see Fig. B.1. Under the deformation we keep the eigenstates of $U_m(\mathbf{s})$ constant everywhere.

The deformed evolution operator $\tilde{U}_m$ is equal to the identity for all $\mathbf{s}$, except in the small region of radius δs that surrounds the singularity (see Fig. B.1). Within this neighbourhood, $\tilde{U}_m$ takes the form

$$\tilde{U}_m(\mathbf{s}) = \sum_{n\neq 1,N} |\chi_n\rangle\langle\chi_n| + \sum_{a,b=1,N} |\psi_a\rangle\langle\psi_b| M_{ab}(\mathbf{s}), \tag{B.4}$$

where $M_{ab}(\mathbf{s})$ is a 2×2 matrix whose eigenvectors are the eigenvectors of the matrix $(\mathbf{s}-\mathbf{s}_0)_j S_{jk}\sigma_k$. Here, the real invertible 3×3 matrix S was defined in Sec. 3.2.1, and $\{\sigma_k\}$ are the Pauli matrices.

From the description of the flattened phase bands above, we know that the logarithms of the eigenvalues of M must grow linearly from 0 at $|\mathbf{s}-\mathbf{s}_0| = \delta s$ to $-i\pi$ and $i\pi$ at $\mathbf{s} = \mathbf{s}_0$. For $|\mathbf{s}-\mathbf{s}_0| < \delta s$, M_{ab} thus takes the form

$$\begin{aligned} M_{ab}(\mathbf{s}) =& v_a^-(\mathbf{s}) v_b^{-*}(\mathbf{s}) e^{i\pi(|\mathbf{s}-\mathbf{s}_0|/\delta s - 1)} \\ &+ v_a^+(\mathbf{s}) v_b^{+*}(\mathbf{s}) e^{-i\pi(|\mathbf{s}-\mathbf{s}_0|/\delta s - 1)}. \end{aligned} \tag{B.5}$$

The vectors $v^-(\mathbf{s})$ and $v^+(\mathbf{s})$ are the eigenvectors of the traceless 2×2 Hermitian matrix $(\mathbf{s}-\mathbf{s}_0)_j S_{jk}\sigma_k$, corresponding to negative and positive eigenvalue, respectively. Since the matrix S is real and invertible, we can write it as $S = R_1 \Lambda R_2$, where R_1 and R_2 are orthogonal and Λ is a diagonal matrix with positive entries (this is the singular value decomposition of S, see e.g., Ref. [208]). A continuous deformation of the entries of Λ to 1 results in a orthogonality-preserving continuous interpolation of the eigenvectors $v^\pm(\mathbf{s})$ to the eigenvectors of $R_{jk}(\mathbf{s}-\mathbf{s}_0)_j\sigma_k$, where $R = R_1 R_2$. By continuously deforming the vectors $v^\pm$ in this way, $\tilde{U}_m$ is deformed into an evolution operator V_m still of the form (B.4), but with the matrix M given by

$$M(\mathbf{s}) = \begin{cases} 1, & |\mathbf{s}-\mathbf{s}_0| > \delta s \\ -\exp\left[\frac{-i\pi}{\delta s}(\mathbf{s}-\mathbf{s}_0)_i R_{ij}\sigma_j \cdot\right], & |\mathbf{s}-\mathbf{s}_0| < \delta s. \end{cases} \tag{B.6}$$

Recall that R is orthogonal and its determinant $|R|$ is the charge of the singularity, $q = |R_1||R_2| = |S|$, see Eq. (3.6). In Appendix B.1.4 we explicitly evaluate the winding number (B.1) of the evolution operator V_m. We find:

$$W[V_m] = -|R| \equiv -q. \tag{B.7}$$

Using the fact that the winding number could not change during the deformation from U_m to V_m, we thus establish

$$W[U_m] = -q. \tag{B.8}$$

In other words, if U_m contains one isolated singularity, the winding number of U_m is given by the corresponding charge of the singularity (with a minus sign).

B.1.3 The general case

We now consider the general case, where U_m has N topological singularities in the zone-edge gap, with charges $\{q_i^{(m)}\}$. In order to evaluate the winding number, we deform $U_m(\mathbf{k},t)$ as described in Sec. 3.3.1 and shown in Fig. 3.3. The deformed evolution is the identity everywhere except for in small isolated regions surrounding the singularities (region I), as well as in the short ramping time-interval δt at the end of the driving (region II).

The winding number (B.1) is defined as an integral over $\mathbf{k}, t$-space of the quantity $F_m(\mathbf{k},t) = \frac{1}{8\pi^2}\mathrm{Tr}\{U_m^\dagger \partial_t U_m \, [U_m^\dagger \partial_{k_x} U_m, \, U_m^\dagger \partial_{k_y} U_m]\}$. For the deformed, "band-flattened," system, F_m is only nonzero in each of the isolated regions that surround the singularities, and in the final ramp region II. We can therefore split up the integral of F_m into a sum of integrals over each of these nontrivial regions.

From the first special case we examined, i.e., for an evolution with no singularities, we know that the integral of $F_m(\mathbf{k},t)$ over region II equals $\sum_{n=1}^m C_n$, where $\{C_n\}$ are the Chern numbers

of Floquet bands $1 \dots m$. From the second special case, we know that the integral of $F_m(\mathbf{k}, t)$ over one of the regions surrounding a zone-edge singularity equals minus the charge of the singularity, i.e., $-q$.

Summing the integrals over all regions, we obtain:

$$W[U_m] = \sum_{n=1}^{m} C_n - \sum_{i=1}^{N} q_i^{(m)}. \tag{B.9}$$

Note that U_m can be constructed by deforming the phase bands of U only at the end of the driving. Therefore the net charge of all zone-edge singularities in the time-bulk should be the same for U and U_m. Thus $\sum_i q_i^{(m)} = \sum_i q_i^{(\mathrm{ZES})}$, where $\{q_i^{(\mathrm{ZES})}\}$ are the zone-edge singularity charges for the original system with evolution governed by U. Hence, we finally have the result for the number of edge modes in a two-dimensional system:

$$W[U_m] = \sum_{n=1}^{m} C_n - \sum_{i} q_i^{(\mathrm{ZES})} = w_m[U]. \tag{B.10}$$

This is what we set out to show.

B.1.4 Derivation of Eq. (B.8)

In this appendix we prove that the winding number (B.1) of an evolution operator V_m of the form in Eq. (B.4), with the matrix M given in (B.6), is equal to $-|R|$. We begin by inserting V_m from Eqs. (B.4) and (B.6) into Eq. (B.1), to obtain

$$W = \frac{\epsilon_{ijk}}{24\pi^2} \int_{|\mathbf{s}-\mathbf{s}_0|<\delta s} d^3\mathbf{s}\, \mathrm{Tr}\left\{ M^\dagger \partial_{\mathbf{s}_i} M\, M^\dagger \partial_{\mathbf{s}_j} M\, M^\dagger \partial_{\mathbf{s}_k} M \right\}, \tag{B.11}$$

where ε_{ijk} is the Levi-Civita symbol. Summation over repeated indices is used and will be used in the rest of this appendix.

In order to exploit the $\mathbf{s}$-space spherical symmetry of the deformed evolution V_m, we shift from Cartesian coordinates to spherical coordinates centred around $\mathbf{s}_0$, defined such that

$$\mathbf{s} - \mathbf{s}_0 \;\equiv\; (s\, \sin\theta \sin\phi,\; s\, \sin\theta \cos\phi,\; s\, \cos\theta). \tag{B.12}$$

After the coordinate transformation, W is expressed as

$$\begin{aligned} W = \frac{\epsilon_{ijk}}{24\pi^2} \int_0^{\delta s} ds \int_0^{\pi} d\theta \int_0^{2\pi} d\phi\; |J| J_{i\alpha} J_{j\beta} J_{k\gamma} \\ \cdot \mathrm{Tr}\left\{ M^\dagger \partial_\alpha M\, M^\dagger \partial_\beta M\, M^\dagger \partial_\gamma M \right\}, \end{aligned} \tag{B.13}$$

where J is the Jacobian matrix of the coordinate transformation, and the Greek letters α, β, γ run over the coordinates s, θ, ϕ. We now use the following useful identity for the Levi-Civita symbol that holds for any real invertible 3×3 matrix A [208]:

$$A_{i\alpha} A_{j\beta} A_{k\gamma} \epsilon_{ijk} = \frac{\epsilon_{\alpha\beta\gamma}}{|A|}. \tag{B.14}$$

With the help of this identity we see that the Jacobian matrices always cancel out:

$$W = \frac{\epsilon_{\alpha\beta\gamma}}{24\pi^2} \int_0^{\delta s} ds \int_0^{\pi} d\theta \int_0^{2\pi} d\phi \\ \mathrm{Tr}\left\{ M^\dagger \partial_\alpha M \, M^\dagger \partial_\beta M \, M^\dagger \partial_\gamma M \right\}.$$

Summing over the indices, we obtain:

$$W = \frac{1}{8\pi^2} \int_0^{\delta s} ds \int_0^{\pi} d\theta \int_0^{2\pi} d\phi \\ \mathrm{Tr}\left\{ M^\dagger \partial_s M \, [M^\dagger \partial_\theta M, \, M^\dagger \partial_\phi M] \right\}.$$

Using the cyclic property of the trace as well as the identity $\partial M M^\dagger = -M \partial M^\dagger$, we get

$$W = -\frac{1}{8\pi^2} \int_0^{\delta s} ds \int_0^{\pi} d\theta \int_0^{2\pi} d\phi \\ \mathrm{Tr}\left\{ M^\dagger \partial_s M \, [\partial_\theta M^\dagger, \, \partial_\phi M] \right\}. \tag{B.15}$$

We now consider the explicit canonical form of M, Eq. (B.6), in polar coordinates, in the region $|\mathbf{s} - \mathbf{s}_0| \leq \delta s$:

$$M(\mathbf{s}, \theta, \phi) = -\exp\left(-\frac{i\pi}{\delta s} (\mathbf{s} - \mathbf{s}_0) \cdot \tau \right), \tag{B.16}$$

where $\tau_i = R_{ij}\sigma_j$. Defining $\hat{s}(\theta, \phi) = (\mathbf{s} - \mathbf{s}_0)/s$, we evaluate each of the factors in the integrand

$$M^\dagger \partial_s M = -\frac{i\pi}{\delta s} \, \hat{s} \cdot \tau \\ \partial_\theta M = i \sin\left(\frac{\pi s}{\delta s} \right) \partial_\theta \hat{s} \cdot \tau \\ \partial_\phi M = i \sin\left(\frac{\pi s}{\delta s} \right) \partial_\phi \hat{s} \cdot \tau.$$

Hence, after performing the integral over s, we obtain

$$W = \frac{i}{16\pi} \int_0^{\pi} d\theta \int_0^{2\pi} d\phi \, \mathrm{Tr}\left\{ \hat{s} \cdot \tau \, [\partial_\theta \hat{s} \cdot \tau, \, \partial_\phi \hat{s} \cdot \tau] \right\}. \tag{B.17}$$

Working on the integrand, we note:

$$\mathrm{Tr}\left\{ (\hat{s}\cdot\tau)(\partial_\theta \hat{s}\cdot\tau)(\partial_\phi \hat{s}\cdot\tau) \right\} \\ = \hat{s}_i \, \partial_\theta \hat{s}_j \, \partial_\phi \hat{s}_k \, R_{ia} R_{jb} R_{kc} \, \mathrm{Tr}\left\{ \sigma_a \sigma_b \sigma_c \right\}. \tag{B.18}$$

Using the Pauli matrix identity $\mathrm{Tr}\{\sigma_i \sigma_j \sigma_k\} = 2i\epsilon_{ijk}$, we obtain

$$\mathrm{Tr}\left\{ (\hat{s}\cdot\tau)(\partial_\theta \hat{s}\cdot\tau)(\partial_\phi \hat{s}\cdot\tau) \right\} = \hat{s}_i \partial_\theta \hat{s}_j \partial_\phi \hat{s}_k \cdot 2i R_{ia} R_{jb} R_{kc} \epsilon_{abc} \\ = \hat{s}_i \partial_\theta \hat{s}_j \partial_\phi \hat{s}_k \cdot 2i |R| \epsilon_{ijk}.$$

Here we used the Levi-Civita symbol identity (B.14), and the fact that $|R|^{-1} = |R|$. Restoring antisymmetry in θ and ϕ, and going back to vector notation, we have

$$\begin{aligned} \mathrm{Tr}\,\{(\hat{s}\cdot\tau)[(\partial_\theta\hat{s}\cdot\tau),\,(\partial_\phi\hat{s}\cdot\tau)]\} &= 4i|R|\;\hat{s}\cdot(\partial_\theta\hat{s}\times\partial_\phi\hat{s}) \\ &= 4i|R|\sin\theta. \end{aligned} \tag{B.19}$$

Hence the integrand in Eq. (B.17) is simply $4i|R|$ times the surface area element of the sphere. We thus have

$$\begin{aligned} W &= \frac{i}{16\pi}\int_0^\pi \mathrm{d}\theta \int_0^{2\pi} \mathrm{d}\phi\; 4i|R|\sin\theta \\ &= -|R| \end{aligned}$$

Recalling that $q = \mathrm{sgn}|S| = |R|$, we see that the winding number contribution of an isolated singularity is given by the charge q of the singularity.

Appendix C

Appendix for Chapter 4

C.1 Magnetization as the response of quasienergy to a magnetic field

Here we derive Eq. (2) in the main text, showing that the single-period averaged magnetization $\langle M\rangle_T^{(n)}$ of a Floquet eigenstate $|\psi_n\rangle$ with quasienergy ε_n is given by the response of its quasienergy to an applied "probing" uniform magnetic field, B: $\langle M\rangle_T^{(n)} = -\frac{\partial\varepsilon_n}{\partial B}$. (Note that, in addition to the probing field B, a nontrivial field $B_0(\mathbf{r},t)$ may already be present in the system.) Throughout this work the magnetic field is given in units of [1/Area], such that the flux quantum has value 2π.

As a first step, we note that $\frac{\partial\varepsilon_n}{\partial B}$ can be written as

$$\frac{\partial\varepsilon_n}{\partial B} = \frac{i}{T}\langle\psi_n|\left(U^\dagger(T)\frac{\partial}{\partial B}U(T)\right)|\psi_n\rangle. \tag{C.1}$$

This relation can be checked using the spectral decomposition $U(T) = \sum_n |\psi_n\rangle\langle\psi_n|e^{-i\varepsilon_n T}$, together with the identity $\langle\psi_n|\frac{\partial}{\partial B}|\psi_n\rangle + \frac{\partial}{\partial B}[\langle\psi_n|]|\psi_n\rangle = 0$. Here $\frac{\partial}{\partial B}|\psi_n\rangle$ measures the change of Floquet eigenstate $|\psi_n\rangle$ when a uniform magnetic field B is introduced to the system.

We now use $U(T) = \mathcal{T}e^{-i\int_0^T dtH(t)}$ to obtain

$$U^\dagger(T)\frac{\partial}{\partial B}U(T) = -i\int_0^T dt\, U^\dagger(t)\frac{\partial H(t)}{\partial B}U(t). \tag{C.2}$$

Hence, substituting back into Eq. (C.1), we get

$$\frac{\partial\varepsilon_n}{\partial B} = \frac{1}{T}\int_0^T \langle\psi_n(t)|\frac{\partial H(t)}{\partial B}|\psi_n(t)\rangle, \tag{C.3}$$

where $|\psi_n(t)\rangle = U(t)|\psi_n\rangle$ is the time-evolved Floquet eigenstate at time t.

What is the nature of the operator $\frac{\partial H}{\partial B}$? By analogy to equilibrium systems, clearly it is suggestive of magnetization. However, similar to the magnetization density operator m_p discussed in the main text, the operator $\frac{\partial H}{\partial B}$ is gauge-dependent. Nonetheless, expectation values of $\frac{\partial H}{\partial B}$ taken in *stationary states* are in fact gauge invariant, and therefore physical (see next section).

The stationarity condition is satisfied for the full-period average of $\frac{\partial H}{\partial B}$ in a Floquet eigenstate, as appears on the right hand side of Eq. (C.3). Indeed this must be the case, since the quantity $\frac{\partial \varepsilon_n}{\partial B}$ on the left hand side is itself gauge-invariant.

To obtain an expression for $\frac{\partial H(t)}{\partial B}$, we consider the change of the Hamiltonian when the small uniform probing magnetic field B is introduced. In this case, the matrix elements $H_{ab}(t)$ of the Hamiltonian in the lattice site basis (here a, b refer to lattice site indices) acquire Peierl's phases: $H_{ab}(t) \to H_{ab}(t) e^{i \int_{\mathbf{r}_b}^{\mathbf{r}_a} d\mathbf{r} \cdot \mathbf{A}(\mathbf{r})}$, where the contour of integration is a straight line from site b to site a and $\mathbf{B} = \nabla \times \mathbf{A}$. Given that the result of Eq. (C.3) is gauge-independent, we work in the symmetric gauge below. This gauge choice highlights the direct relation to the magnetization defined in Eq. (1) of the main text. In the symmetric gauge, a uniform perpendicular "probing" magnetic field B is produced by the vector potential $\mathbf{A}(\mathbf{r}) = \frac{B}{2} \hat{\mathbf{z}} \times \mathbf{r}$. Using the identity $A \cdot (B \times C) = B \cdot (C \times A)$, we thus obtain the following modification of $H_{ab}(t)$ due to the probe field B :

$$\begin{aligned} H_{ab}(t) &\to H_{ab}(t) \exp\left[\frac{iB}{2} \int_{\mathbf{r}_b}^{\mathbf{r}_a} d\mathbf{r} \cdot (\hat{\mathbf{z}} \times \mathbf{r})\right] \\ &= H_{ab}(t) \exp\left[\frac{iB}{2} \hat{\mathbf{z}} \cdot \left(\int_{\mathbf{r}_b}^{\mathbf{r}_a} \mathbf{r} \times d\mathbf{r}\right)\right] \\ &= H_{ab}(t) \exp\left[\frac{iB}{2} \hat{\mathbf{z}} \cdot (\mathbf{r}_a \times (\mathbf{r}_a - \mathbf{r}_b))\right]. \end{aligned}$$

Here we used that $\mathbf{r}_a \times (\mathbf{r}_a - \mathbf{r}_b) = \mathbf{r}_b \times (\mathbf{r}_a - \mathbf{r}_b)$.

Taking the derivative of $H_{ab}(t)$ with respect to the probe field strength B, we obtain

$$\frac{\partial H_{ab}(t)}{\partial B} = \frac{i}{2} H_{ab}(t) \left(\mathbf{r}_a \times (\mathbf{r}_a - \mathbf{r}_b)\right) \cdot \hat{\mathbf{z}}. \tag{C.4}$$

This structure of the matrix elements of H implies that

$$\frac{\partial H(t)}{\partial B} = \frac{i}{2} \left(\mathbf{r} \times [\mathbf{r}, H(t)]\right) \cdot \hat{\mathbf{z}}. \tag{C.5}$$

Equation (C.5) can be verified by taking a matrix element with $\langle a|$ and $|b\rangle$ on the left and right, respectively, and comparing with Eq. (C.4). Comparing with Eq. (1) of the main text, and using $\dot{\mathbf{r}}(t) = -i[\mathbf{r}, H]$, we identify the right hand side above as minus the magnetization, $-M(t)$. Substituting this result into Eq. (C.3), we obtain Eq. (2) in the main text.

C.2 Gauge invariance of magnetization density

Here we show that the magnetization density operator $m_p(t)$, defined in Eq. (3) of the main text, yields gauge-independent time-averaged expectation values if and only if the density is stationary over the averaging interval τ, i.e., $\langle \dot{\rho} \rangle_\tau = 0$. In this case, we furthermore show that the magnetization density obeys the lattice version of Ampere's law given in Eq. (4) of the main text.

In the presence of a magnetic flux ϕ_p piercing through plaquette p, the matrix elements of the Hamiltonian in the lattice site basis are given by $H_{ab}(\phi_p) = e^{iA_{ab}(\phi_p)} H_{ab}(\phi_p = 0)$. (Here we work

in units where the lattice constant is 1). Here the vector potential $\{A_{ab}(\phi_p)\}$ should have the following property: for a sequence of sites $(a_1, a_2, \ldots a_N)$ forming a closed counterclockwise loop on the lattice, the phase $\sum_{n=1}^{N} A_{a_{n+1}a_n}(\phi_p)$ should equal ϕ_p if the loop encloses the plaquette p, while the sum should vanish otherwise (here we set $a_{N+1} = a_1$). The magnetization density operator is then given by

$$m_p(t) = -\frac{\partial H(t)}{\partial \phi_p} = -\sum_{\langle a,b\rangle} \frac{\partial H(t)}{\partial A_{ab}} \frac{\partial A_{ab}}{\partial \phi_p}, \tag{C.6}$$

where the sum runs over all pairs of sites on the lattice connected by bonds.

We note that there is a gauge freedom in choosing $A_{ab}(\phi_p)$: if the vector potential $\{A_{ab}(\phi_p)\}$ results in a flux ϕ_p on plaquette p, then so will a vector potential $\{A'_{ab}(\phi_p)\}$ that satisfies

$$A'_{ab}(\phi_p) = A_{ab}(\phi_p) + f_a(\phi_p) - f_b(\phi_p), \tag{C.7}$$

where $\{f_a(\phi)\}$ can be any set of scalar functions.

In order for $\langle m_p \rangle_\tau$ to be gauge-invariant, the time-averaged expectation value of the right hand side of Eq. (C.6) should remain unchanged if we replace A_{ab} with A'_{ab}. In order for this to be satisfied, we must have

$$\sum_{\langle a,b\rangle} \left\langle \frac{\partial H}{\partial A_{ab}} \right\rangle_\tau (g_a - g_b) = 0, \tag{C.8}$$

where $\{g_a = \frac{\partial f_a}{\partial \phi}\big|_{\phi=0}\}$ are arbitrary coefficients. Equation (C.8) is satisfied if we require that the net current flowing into or out of every site a on the lattice vanishes:

$$\sum_{b \in \text{n.n.}(a)} \langle I_{ab} \rangle_\tau = 0, \quad I_{ab}(t) = -\frac{\partial H(t)}{\partial A_{ab}}. \tag{C.9}$$

Here the sum runs over all sites b that are connected with a bond to site a. It is trivial to see that this condition ensures that the sum over terms proportional to g_a in Eq. (C.8) vanishes. The vanishing of the sum over terms proportional to g_b follows by relabeling.

The sum on the left hand side of Eq. (C.9) gives the net current flowing into site a, which is equal to the rate of change of density: $\sum_{b \in \text{n.n.}(a)} I_{ab} = \dot{\rho}_a$, where ρ_a is the density operator on site a. Therefore the gauge invariance condition for expectation values of the magnetization density, Eq. (C.8), is satisfied if and only if the density on every site is stationary over the time-window from 0 to τ: $\langle \dot{\rho}_a \rangle_\tau = 0$. This condition is the lattice-analogue of the condition that the current density in the continuum must be divergence-free.

C.2.1 Ampere's law on the lattice

To prove the lattice version of Ampere's law, we first consider the case where the vector potential is given by A_{ab} on a single bond ab, in the direction from site b to site a, and zero everywhere else. In this situation the magnetic flux is zero everywhere, except for the two plaquettes p and q adjacent to the bond ab, here taken such that the direction from site b to site a is counterclockwise

with respect to plaquette p. In these two neighboring plaquettes, the fluxes are given by $\phi_p = A_{ab}$ and $\phi_q = -A_{ab}$, respectively. Hence, with this choice of gauge (i.e., A nonzero on a single bond),

$$\frac{\partial H(t)}{\partial A_{ab}} = \frac{\partial H(t)}{\partial \phi_p} - \frac{\partial H(t)}{\partial \phi_q}. \tag{C.10}$$

Noting that $\frac{\partial H(t)}{\partial A_{ab}} = -I_{ab}(t)$, and $m_p = -\frac{\partial H(t)}{\partial \phi_p}$, we obtain an operator equation similar to Eq. (4) in the main text. However, this *operator equation* holds only in the specific gauge above, where A is nonzero only on the bond ab. Importantly, as shown above, the *time-averaged expectation value* of the right hand side is gauge-independent for times τ where the density is stationary, $\langle \dot{\rho} \rangle_\tau = 0$. Therefore Eq. (C.10) produces meaningful physical results, and reduces to Eq. (4) of the main text, when it is used to compute time-averaged expectation values in stationary states.

C.3 Relation to winding number

Here we show that the quantized value of the magnetization density for a fully-localized Floquet system on a torus, $\bar{m}_\infty$, is a topological invariant; its value is equal to $W[U]/T$, where $W[U]$ is the winding number introduced in Ref. [2]. Noting that the numbers $W[U]$ and $\bar{m}_\infty$ do not change when we increase the system size, provided that all Floquet eigenstates remain localized, we will consider the limit where the size L goes to infinity. In this section, we work in the Heisenberg picture.

In order to define the winding number $W[U]$, we consider the Hamiltonian $H(\mathbf{A}, t)$ of the system when a uniform vector potential $\mathbf{A}$ is introduced along the surface of the torus. Let $U(\mathbf{A}, t)$ be the corresponding evolution operator of the system. As an important ingredient in the computation of the winding number, we first define the effective Hamiltonian of the system, $H_{\text{eff},\varepsilon}(\mathbf{A})$, via: $U(\mathbf{A}, T) = e^{-iH_{\text{eff},\varepsilon}(\mathbf{A})T}$, where the eigenvalues of $H_{\text{eff},\varepsilon}(\mathbf{A})$ lie in the interval $[\varepsilon, \varepsilon + 2\pi/T)$. Here ε is chosen within one of the system's quasienergy gaps, which are present due to the finite extent of the system for any fixed L (see Ref. [2]). To find the system's winding number, we define the $2T$-periodic evolution $\tilde{U}_\varepsilon(\mathbf{A}, t)$, obtained by first evolving the system with Hamiltonian $H(\mathbf{A}, t)$ in the time-interval $[0, T]$, and then applying a static Hamiltonian $-H_{\text{eff},\varepsilon}(\mathbf{A})$ in the time-interval $[T, 2T]$. The evolution operator $\tilde{U}_\varepsilon(\mathbf{A}, t)$ is given by $U(\mathbf{A}, t)$ in the first half of the driving, from 0 to T, and by $e^{-iH_{\text{eff},\varepsilon}(\mathbf{A})(2T-t)}$ in the second half of the driving. In particular, the extended evolution satisfies $\tilde{U}_\varepsilon(\mathbf{A}, 2T) = 1$.

With the definition of $\tilde{U}_\varepsilon(\mathbf{A}, t)$ above, we obtain the winding number of the evolution via:

$$\begin{aligned} W[U] =& \frac{1}{8\pi^2} \int_0^{2T} dt \int_0^{2\pi/L} d^2\mathbf{A} \\ & \text{Tr}\left(\tilde{U}^\dagger \partial_t \tilde{U} \cdot \tilde{U}^\dagger \partial_{A_x} \tilde{U} \cdot \tilde{U}^\dagger \partial_{A_y} \tilde{U}\right) - x \leftrightarrow y. \end{aligned} \tag{C.11}$$

Given that W is independent of ε (see Ref. [2]), for brevity we drop the subscript ε on $\tilde{U}$ here and below.

As a first step in our derivation, we rewrite the above formula using basic identities for the time-evolution operator. We first use the identities $\partial_t \tilde{U} = -i\tilde{H}\tilde{U}$ and $\partial_{A_x} \tilde{U} \cdot \tilde{U}^\dagger = -\tilde{U}\partial_{A_x} \tilde{U}^\dagger$ to

obtain

$$W[U] = \frac{i\epsilon_{\alpha\beta}}{8\pi^2}\int_0^{2T} dt \int_0^{2\pi/L} d^2\mathbf{A}\,\mathrm{Tr}\left(\tilde{H}\partial_{A_\alpha}\tilde{U}\cdot\partial_{A_\beta}\tilde{U}^\dagger\right).$$

Here $\epsilon_{\alpha\beta}$ is the antisymmetric tensor, with $\alpha,\beta = \{x,y\}$. Next, we perform partial integration over A_α and obtain

$$\begin{aligned} W[U] = &\frac{i\epsilon_{\alpha\beta}}{8\pi^2}\int_0^{2T} dt\,\left[\int_0^{2\pi/L} dA_\beta \mathrm{Tr}\left(\tilde{H}\tilde{U}\cdot\partial_{A_\beta}\tilde{U}^\dagger\right)_{A_\alpha=0}^{A_\alpha=2\pi/L}\right. \\ &\left. - \int_0^{2\pi/L} d^2\mathbf{A}\,\mathrm{Tr}\left(\partial_{A_\alpha}\tilde{H}\tilde{U}\cdot\partial_{A_\beta}\tilde{U}^\dagger\right)\right]. \end{aligned} \tag{C.12}$$

We now make use of the fact that we can write $\tilde{H}(\mathbf{A}+\hat{\mathbf{e}}_\alpha 2\pi/L,t) = X_\alpha^\dagger \tilde{H}(\mathbf{A},t)X_\alpha$, where $\hat{\mathbf{e}}_\alpha$ is the α-unit vector, and $X_\alpha = e^{2\pi i x_\alpha/L}$ (see Ref. [2] for more details). Similarly, $\tilde{U}(\mathbf{A}+\hat{\mathbf{e}}_\alpha 2\pi/L,t) = X_\alpha^\dagger\tilde{U}(\mathbf{A},t)X_\alpha$. Using that $\partial_{A_\beta}X_\alpha = 0$ when $\alpha\neq\beta$, together with the cyclic property of the trace, we obtain

$$\mathrm{Tr}\left(\tilde{H}\tilde{U}\cdot\partial_{A_\beta}\tilde{U}^\dagger\right)_{\mathbf{A}=\left(\frac{2\pi}{L},A_\beta\right)} = \mathrm{Tr}\left(\tilde{H}\tilde{U}\cdot\partial_{A_\beta}\tilde{U}^\dagger\right)_{\mathbf{A}=\left(0,A_\beta\right)}.$$

Hence the integrand in the first term in Eq. (C.12) vanishes, and

$$W[U] = \frac{-i\epsilon_{\alpha\beta}}{8\pi^2}\int_0^{2T} dt \int_0^{2\pi/L} d^2\mathbf{A}\mathrm{Tr}\left(\partial_{A_\alpha}\tilde{H}\cdot\tilde{U}\partial_{A_\beta}\tilde{U}^\dagger\right). \tag{C.13}$$

Using the identity $\partial_{A_\beta}\tilde{U}^\dagger = -\tilde{U}^\dagger\partial_{A_\beta}\tilde{U}\tilde{U}^\dagger$, along with the cyclic property of the trace, we get

$$W[U] = \frac{i}{8\pi^2}\int_0^{2T} dt \int_0^{2\pi/L} d^2\mathbf{A}\mathrm{Tr}\left(\tilde{U}^\dagger\partial_{A_\alpha}\tilde{H}\tilde{U}\cdot\tilde{U}^\dagger\partial_{A_\beta}\tilde{U}\right).$$

Going to the thermodynamic limit $L\to\infty$, we treat the integrand as constant within the $\mathbf{A}$-interval $[0,2\pi/L]$ (cf. Ref. [209]). Thus we arrive at the formula

$$W[U] = \frac{i}{2L^2}\int_0^{2T} dt\,\mathrm{Tr}\left(\tilde{U}^\dagger\left(\partial_{A_\alpha}\tilde{H}\right)\tilde{U}\cdot\tilde{U}^\dagger\partial_{A_\beta}\tilde{U}\right). \tag{C.14}$$

What we have achieved so far, with Eq. (C.14), is to relate the winding number to two Heisenberg picture operators, $\tilde{U}^\dagger\partial_{\mathbf{A}}\tilde{U}$, and $\tilde{U}^\dagger\left(\partial_{\mathbf{A}}\tilde{H}\right)\tilde{U}$. Below we expose the physical meaning of each of these operators, and thereby link the winding number to the system's magnetization.

C.3.1 Displacement operator

Having transformed the original winding number formula (C.11) into the form of Eq. (C.14), we now introduce an additional operator that will be useful in making the final connection with the magnetization. Specifically, for a system with Hamiltonian $H(t)$, and evolution $U(t)$, we introduce the "displacement operator" $\Delta\mathbf{r}(t)$:

$$\Delta\mathbf{r}(t) \equiv -iU^\dagger(t)\partial_{\mathbf{A}}U(t). \tag{C.15}$$

With this definition, we note that $\partial_t \Delta\mathbf{r}(t) = U^\dagger(t)\left(-\partial_{\mathbf{A}} H(t)\right) U(t)$. The displacement operator can be seen as the Heisenberg picture operator that measures the displacement of a particle relative to its starting point, in the sense that displacement is the time-integral of the velocity. This definition is important because the standard position operator on the torus is complicated by the necessity of imposing a branch cut due to the periodic boundary conditions. The displacement operator in Eq. (C.15) is insensitive to this issue.

To further elucidate the physical meaning of the displacement operator $\Delta\mathbf{r}(t)$, we consider the case where the system has *open boundary conditions*, where the position operator $\mathbf{r}$ is naturally single-valued. In the lattice site basis, the Hamiltonian's matrix elements depend on the vector potential $\mathbf{A}$ in the following way:

$$H_{ab}(\mathbf{A}) = H_{ab} e^{i\mathbf{A}\cdot(\mathbf{r}_a - \mathbf{r}_b)}. \tag{C.16}$$

Consequently, $\frac{\partial H(t)}{\partial \mathbf{A}} = i[\mathbf{r}, H(t)]$, and we find $\partial_t \Delta\mathbf{r}(t) = \partial_t \mathbf{r}(t)$, where $\mathbf{r}(t) = U^\dagger(t)\mathbf{r}U(t)$ is the time-evolved position operator in the Heisenberg picture. Using the initial condition $\Delta\mathbf{r}(0) = 0$, we find

$$\Delta\mathbf{r}(t) = \mathbf{r}(t) - \mathbf{r}(0). \tag{C.17}$$

For a system with periodic boundary conditions (e.g., a torus), it is not possible to write $\Delta\mathbf{r}(t)$ as a difference of initial and final positions, as in the above equation. However, when $\Delta\mathbf{r}(t)$ acts on a state $|\psi\rangle$ that stays localized within a region S that is much smaller than the size of the torus, we can ignore the boundary conditions and write

$$\Delta\mathbf{r}(t)|\psi\rangle = (\mathbf{r}_S(t) - \mathbf{r}_S)|\psi\rangle, \tag{C.18}$$

where $\mathbf{r}_S$ is a position operator defined with a branch cut outside S. (We note that the right-hand side does not depend on the exact location of the branch cut, as long as it is located far outside the region S.)

C.3.2 Relationship with magnetization density

Having defined the displacement operator, we now rewrite the winding number formula (C.14) in terms of this operator. Using the definition in Eq. (C.15), we replace $\tilde{U}^\dagger \partial_{\mathbf{A}} \tilde{U}$ with $i\Delta\tilde{\mathbf{r}}(t)$, where $\Delta\tilde{\mathbf{r}}(t)$ is the displacement operator for the system governed by $\tilde{H}(t)$. Similarly, as noted in the text below Eq. (C.15), we may replace $\tilde{U}^\dagger(\partial_{\mathbf{A}}\tilde{H})\tilde{U}$ with $-\partial_t \Delta\tilde{\mathbf{r}}(t)$. Thus we obtain

$$W[U] = \frac{1}{2L^2}\int_0^{2T} dt\, \mathrm{Tr}\left(\Delta\tilde{\mathbf{r}}(t) \times \partial_t \Delta\tilde{\mathbf{r}}(t)\right). \tag{C.19}$$

The integrand in Eq. (C.19) above has a very similar form to that of the magnetization, Eq. (1) of the main text. It remains to show that this expression, which involves the displacement operator defined in Eq. (C.15), precisely reduces to the magnetization discussed in the main text.

Writing out the trace in terms of the (localized) Floquet eigenstates $\{|\psi_n\rangle\}$, and using Eq. (C.18), we obtain

$$W[U] = \frac{1}{2L^2}\int_0^{2T} dt \sum_n \langle\psi_n|(\tilde{\mathbf{r}}_n(t) - \mathbf{r}_n) \times \partial_t \tilde{\mathbf{r}}_n(t)|\psi_n\rangle.$$

Here $\tilde{\mathbf{r}}_n(t) \equiv \tilde{U}^\dagger(t)\mathbf{r}_n\tilde{U}(t)$, where $\mathbf{r}_n$ is a position operator, defined with a branch cut far away from the region where the state $|\psi_n\rangle$ is localized. Using that $\tilde{U}(2T) = 1$, such that $\tilde{\mathbf{r}}_n(2T) = \tilde{\mathbf{r}}_n(0) = \mathbf{r}_n$, we find

$$W[U] = \frac{1}{2L^2}\int_0^{2T} dt \sum_n \langle\psi_n|\tilde{\mathbf{r}}_n(t) \times \partial_t\tilde{\mathbf{r}}_n(t)|\psi_n\rangle. \tag{C.20}$$

In the first half of the driving, i.e., for $0 \le t \le T$, the system evolves according to the original Hamiltonian $H(t)$. Here $\tilde{\mathbf{r}}_n(t) = \mathbf{r}_n(t) \equiv U^\dagger(t)\mathbf{r}_nU(t)$, where $U(t)$ is the corresponding evolution operator of the original system. In the second half of the driving, from T to $2T$, the Hamiltonian of the system is given by $\tilde{H}(t) = -H_{\text{eff}}$, and the time-evolution operator is given by $\tilde{U}(t) = e^{-iH_{\text{eff}}(2T-t)}$. Using $\tilde{\mathbf{r}}_n(t) = \tilde{U}^\dagger(t)\mathbf{r}_n\tilde{U}(t)$, we then have (for $T \le t \le 2T$):

$$\tilde{\mathbf{r}}_n(t) \times \partial_t\tilde{\mathbf{r}}_n(t) = -ie^{iH_{\text{eff}}(2T-t)}\mathbf{r}_n \times [\mathbf{r}_n, H_{\text{eff}}]e^{-iH_{\text{eff}}(2T-t)}.$$

Using $H_{\text{eff}} = \sum_n P_n\varepsilon_n$, where $P_n = |\psi_n\rangle\langle\psi_n|$, we obtain

$$\langle\psi_n|\tilde{\mathbf{r}}_n(t) \times \partial_t\tilde{\mathbf{r}}_n(t)|\psi_n\rangle = -i\sum_m \langle\psi_n|\mathbf{r}_n \times [\mathbf{r}_n, P_m]|\psi_n\rangle\varepsilon_m.$$

Thus the integrand in Eq. (C.20) is actually constant over the interval $T \le t \le 2T$. This allows us to perform part of the integration and obtain

$$\begin{aligned} W[U] = &\frac{1}{2L^2}\int_0^{T} dt \sum_n \langle\psi_n|\mathbf{r}_n(t) \times \partial_t\mathbf{r}_n(t)|\psi_n\rangle \\ &+ \frac{iT}{2L^2}\sum_{m,n}\langle\psi_n|\mathbf{r}_n \times [\mathbf{r}_n, P_m]|\psi_n\rangle\varepsilon_m. \end{aligned} \tag{C.21}$$

We now argue that the last term in Eq. (C.21) must be zero. To do this, we note that for a fully-localized system, the winding number is independent of the choice of the quasienergy zone (i.e., the position of the branch cut ε in $H_{\text{eff},\varepsilon}$, see Ref. [2]). If we shift the quasienergy cut to the gap between ε_{m_0} and ε_{m_1}, where ε_{m_0} and ε_{m_1} are the lowest- and second lowest quasienergies, respectively, the quasienergy ε_{m_0} changes by $2\pi/T$, while all other quasienergies remain the same: $\varepsilon_{m_0} \to \varepsilon_{m_0} + 2\pi/T$. The invariance of the left-hand side of Eq. (C.21) under this shift of quasienergy zone implies that

$$\sum_n \langle\psi_n|\mathbf{r}_n \times [\mathbf{r}_n, P_{m_0}]|\psi_n\rangle = 0. \tag{C.22}$$

Since the branch cut could be placed anywhere in the spectrum, the argument above should in fact hold for any choice of m_0. Therefore the last term in Eq. (C.21) must vanish, and we arrive at

$$W[U] = \frac{1}{2L^2}\int_0^{T} dt \sum_n \langle\psi_n|\mathbf{r}_n(t) \times \partial_t\mathbf{r}_n(t)|\psi_n\rangle. \tag{C.23}$$

Following the discussion in the main text, we identify

$$\frac{1}{2T}\int_0^{T} dt\, \langle\psi_n|\mathbf{r}_n(t) \times \partial_t\mathbf{r}_n(t)|\psi_n\rangle = \langle M\rangle_T^{(n)} \tag{C.24}$$

as the time-averaged magnetization of Floquet eigenstate n. Hence

$$W[U] = \frac{T}{L^2}\langle M\rangle_T, \quad \langle M\rangle_T = \sum_n \langle M\rangle_T^{(n)}, \tag{C.25}$$

where $\langle M\rangle_T$ is the total magnetization of the system when all states are occupied (on a torus). Using $\langle M\rangle_T = L^2\bar{m}_\infty$, we finally arrive at

$$\bar{m}_\infty = \frac{W[U]}{T}. \tag{C.26}$$

This is what we set out to show: the magnetization density of a fully-localized Floquet system is a topological invariant, with its value equal to the winding number identified in Ref. [2], divided by the driving period, T.

C.4 Measurement of magnetization in a cold atoms experiment

In this section, we prove Eq. (10) in the main text. We show that the time-averaged magnetization can be measured via the net y-component of total (pseudo)-spin of a cloud of two-component cold atoms subjected to a spin-dependent artificial magnetic field. In this section, we will work in the Heisenberg picture. For an individual atom in the experiment, the wave function before the measurement is given by

$$|\psi\rangle = \frac{1}{\sqrt{2}}|\chi\rangle \otimes (|\uparrow\rangle + |\downarrow\rangle), \tag{C.27}$$

where $|\chi\rangle$ denotes the orbital part of the atom's wave function, and the tensor product separates the orbital and spin parts of the wave function. The time evolution operator of the system for the case where the spin-dependent effective field acts only on the $|\uparrow\rangle$ spin component is given by

$$\mathbb{U}(\tau) = U_B(\tau) \otimes |\uparrow\rangle\langle\uparrow| + U_0(\tau) \otimes |\downarrow\rangle\langle\downarrow|, \tag{C.28}$$

where $U_B(\tau)$ is the time-evolution operator (acting only on the system's orbital degrees of freedom) when a uniform field B is applied.

After an evolution time τ in the presence of the effective field B, the atom's wave function is given by

$$|\psi(\tau)\rangle = \frac{1}{\sqrt{2}}\left(U_B(\tau)|\chi\rangle \otimes |\uparrow\rangle + U_0(\tau)|\chi\rangle \otimes |\downarrow\rangle\right). \tag{C.29}$$

Hence, at time τ, the expectation value of the y-spin operator $\sigma_y = \frac{i}{2}(|\uparrow\rangle\langle\downarrow| - |\downarrow\rangle\langle\uparrow|)$ is given by

$$\langle\sigma_y(\tau)\rangle = \frac{i}{2}\langle\chi|\left(U_B^\dagger(\tau)U_0(\tau) - U_0^\dagger(\tau)U_B(\tau)\right)|\chi\rangle. \tag{C.30}$$

Using $U_B(\tau) = U_0(\tau) + B\frac{\partial}{\partial B}U_B(\tau)|_{B=0} + \mathcal{O}(B^2)$, valid in the linear response regime of weak fields, we obtain

$$\langle\sigma_y(\tau)\rangle = -iB\langle\chi|\left(U_0^\dagger(\tau)\frac{\partial}{\partial B}U_0(\tau)\right)|\chi\rangle + \mathcal{O}(B^2), \tag{C.31}$$

where for brevity we write $\frac{\partial}{\partial B}U_B(\tau)|_{B=0} \equiv \frac{\partial}{\partial B}U_0(\tau)$. To arrive at Eq. (C.31), we used the identity $\frac{\partial}{\partial B}U_0^\dagger \cdot U_0 = -U_0^\dagger \cdot \frac{\partial}{\partial B}U_0$. Using Eq. (C.2) we obtain the following result, which is valid on short times where the spin precession angle remains small:

$$\langle \sigma_y(\tau)\rangle = B\int_0^\tau dt\, \langle \chi(t)|M(t)|\chi(t)\rangle + \mathcal{O}(B^2). \tag{C.32}$$

Here we have introduced the operator $M(t)$ as a shorthand for $-\frac{\partial H(t)}{\partial B}$. We note that this operator, and its expectation values (for non-stationary states), in general depend on the implementation of the gauge field, see discussion below.

The above result, Eq. (C.32), holds for an individual atom. For a droplet of many non-interacting atoms the droplet's total y-spin $\langle S_y\rangle$ can be obtained by summing together their individual contributions:

$$\langle S_y(NT)\rangle = BNT\sum_j \langle M\rangle_{NT}^{(j)} + \mathcal{O}(B^2), \tag{C.33}$$

where the sum runs over all atoms j in the droplet, and $\langle M\rangle_\tau^{(j)}$ denotes the time-averaged expectation value of $M(t)$ for the atom j, taken over the interval $0 \le t \le \tau$. Importantly, for long times, $N \to \infty$, the particle density is stationary and $\langle M\rangle_{NT}^{(j)}$ becomes gauge independent. In this limit, $\sum_j \langle M\rangle_{NT}^{(j)} \to \langle\langle M\rangle\rangle$ and we find

$$\lim_{NT\to\infty} \frac{1}{BNT}\langle S_y(NT)\rangle = \langle\langle M\rangle\rangle + \mathcal{O}(B). \tag{C.34}$$

For a finite number of periods N, there will in general be a transient correction to the relation in Eq. (C.34) above. Consider a filled droplet, as described in the main text, where the many-body state is described by a single Slater determinant. Within such a state, atoms localized deep inside the bulk of the droplet (i.e., centered many localization lengths from its boundary), where all sites are filled, can be taken to be occupying Floquet eigenstates. For an atom j initialized in a Floquet eigenstate n, $\langle M\rangle_{NT}^{(j)} = -\frac{\partial \varepsilon_n}{\partial B}$ for any integer number of periods, N. Thus atoms in the bulk do not give any transient corrections to Eq. (C.34). However, an atom j localized near the boundary of the droplet does not generically occupy a single Floquet eigenstate. In this case, the contribution of atom j to the total density is not stationary over a single period, and $\langle M\rangle_{NT}^{(j)}$ generally depends on N. Thus the motion of atoms localized in a strip of width $\sim \xi$ along the boundary of the droplet produces a transient deviation of $\frac{1}{BNT}\langle S_y(NT)\rangle$ from its long-time asymptotic value $\langle\langle M\rangle\rangle$.

The non-universal transient depends on details of the implementation, including in particular the choice of "gauge" used for producing the effective spin-dependent magnetic field. That is, the spin rotation of an atom moving through the lattice depends explicitly on the "vector potentials" $\mathbf{A}_\uparrow$ and $\mathbf{A}_\downarrow$ for up and down spins, respectively, and not only on the effective magnetic fields $\mathbf{B}_\uparrow = \nabla \times \mathbf{A}_\uparrow$ and $\mathbf{B}_\downarrow = \nabla \times \mathbf{A}_\downarrow$. Independent "gauge" transformations of $\mathbf{A}_\uparrow$ and $\mathbf{A}_\downarrow$ correspond to position-dependent spin rotations around the z-axis. Since the system is initialized and measured in a fixed, spatially uniform frame, there is no symmetry under spin-dependent gauge transformations.

We now estimate the magnitude of the transient correction. To do so, we consider the case of a circular droplet of radius R, where the magnetic field is implemented in the symmetric gauge (here the origin of the coordinate system is located in the droplet's center). In the symmetric gauge, recall from Sec. C.1 that $M(t) = -\frac{\partial H(t)}{\partial B} = \frac{1}{2}\hat{\mathbf{z}} \cdot (\mathbf{r} \times \dot{\mathbf{r}}(t))$. For an atom at the boundary of the droplet we write $\mathbf{r}(t) = \mathbf{R} + \delta\mathbf{r}(t)$, where $\mathbf{R} = \langle\langle \mathbf{r}(t) \rangle\rangle$ is a vector of length $\sim R$ pointing from the origin to the atom's long-time-averaged position, and $\delta\mathbf{r}(t)$ describes the motion around this point, with $|\delta\mathbf{r}| \sim \xi$. The time-averaged expectation value of M for an atom in the boundary region is then

$$\langle M \rangle_{NT}^{(j)} = \frac{1}{2}\hat{\mathbf{z}} \cdot [\mathbf{R} \times \langle \delta\dot{\mathbf{r}} \rangle_{NT} + \langle \delta\mathbf{r} \times \delta\dot{\mathbf{r}} \rangle_{NT}] \,. \tag{C.35}$$

The first term yields a contribution to $\langle M \rangle_{NT}$ of order $R\left\langle \dot{r}_{\parallel} \right\rangle_{NT}$, where $\dot{r}_{\parallel}(t)$ denotes the tangential component of the atom's velocity along the boundary. Since the atom must remain confined within a region of linear dimension ξ for all times, the N-period average of the tangential velocity takes a typical value of order ξ/NT. Therefore we expect the corresponding transient contribution to $\langle M \rangle_{NT}^{(j)}$ to have a magnitude at most $\sim \frac{R\xi}{NT}$. Assuming that the atoms are initially randomly distributed within their respective localization areas (this is assured by letting particle density in the droplet reach a steady profile before the measurement begins), the *sign* of $\left\langle \dot{r}_{\parallel} \right\rangle_{NT}$ is expected to be random. Any transient contributions to $\langle M \rangle_{NT}^{(j)}$ from the second term in Eq. (C.35) involving $\delta\mathbf{r} \times \delta\dot{\mathbf{r}}$ are expected to be relatively suppressed by a factor ξ/R, and we ignore them below.

Having estimated the scale of the transient contribution to $\langle M \rangle_{NT}^{(j)}$ for each boundary atom, we now infer the net contribution of all atoms to the net transient deviation of $\frac{1}{BNT}\langle S_y(NT) \rangle$ from the asymptotic value $\langle\langle M \rangle\rangle$. First, note that total number of atoms in the boundary region (a strip of width ξ around the perimeter of the droplet) is of order $R\xi/a^2$. Assuming a random sign for the contribution of each atom, we get a net transient correction with magnitude of order $\sqrt{\frac{R\xi}{a^2}} \cdot \frac{R\xi}{NT}$. Using $A_{\text{loc}} = \xi^2$, and $A_{\text{filled}} \sim R^2$, we thus obtain

$$\sum_j \langle M \rangle_{NT}^{(j)} = \langle\langle M \rangle\rangle + \frac{1}{NT}\mathcal{O}\left(\frac{A_{\text{loc}} A_{\text{filled}}}{a\sqrt{R\xi}}\right). \tag{C.36}$$

While this result was obtained for a field implemented in the symmetric gauge, analogous arguments to those above can be used for other natural implementations, e.g. the Landau gauge, to show that the transient should have the same magnitude as above.

Using Eq. (C.36) in Eq. (C.33), we see that

$$\frac{\langle S_y(NT) \rangle}{BNT} = \langle\langle M \rangle\rangle + \frac{1}{NT}\mathcal{O}\left(\frac{A_{\text{loc}} A_{\text{filled}}}{a\sqrt{R\xi}}\right) + \mathcal{O}(B). \tag{C.37}$$

Hence the cloud's total magnetization can be extracted from the asymptotic behaviour of the growth rate of $\langle S_y(\tau) \rangle$ in the long-time limit. The result for the average y-spin *per particle* $\langle \overline{\sigma}_y(NT) \rangle$, in Eq.(10) in the main text, is obtained by dividing both sides of Eq. (C.37) with the total number of atoms, A_{filled}/a^2.

The "long time limit" in which the magnetization can be extracted should be understood as a time that is long compared with the damping of transients due to the system's initialization, but

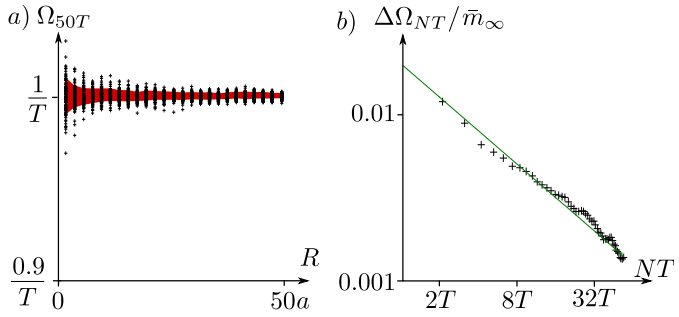

Figure C.1: Statistical behaviour of the normalized growth rate Ω_{NT}, whose saturation value yields the long-time-averaged magnetization density. a) Normalized growth rate Ω_{NT} as function of droplet size R, obtained for 100 disorder realizations, with parameters set as in the main text (for each R, each realization corresponds to one black cross). The red shading indicates the interval within one standard deviation from the data points' mean. b) Deviation $\Delta\Omega_{NT}$ of the net y-spin growth rate from the expected saturation value $\bar{m}_\infty = 1/T$, as a function of the averaging time NT, taken as an rms-average over 100 disorder realizations. The data are shown in a logarithmic plot.

still short enough that the atoms' spin precession angle is small. The necessary separation of timescales can be guaranteed both by working at small fields, B, and by taking a large enough droplet (since the transient correction to $\langle\overline{\sigma}_y(NT)\rangle$ decays as $1/\sqrt{R}$). In practice, our numerics show that the transients can be made quite small for square droplets of only a few tens of lattice sites per side (see below and main text).

Finally, we note that our results were derived for a tight-binding model with one (s-type) orbital per site. This means that each on-site orbital does not carry any intrinsic magnetization. Due to mixing with higher bands, small non-quantized contributions to the magnetization density may arise, as discussed in the main text. However, such contributions are strongly suppressed when the driving is adiabatic with respect to the gap to higher bands, and gap is large compared to the bandwidth. In this limit, over one driving period the center of mass of the orbital on each site shifts by a distance that is small compared with the lattice spacing. The non-quantized contribution to the magnetization density (in units of the driving frequency) is proportional to the area swept out by the center of mass, divided by the area of the unit cell, and is therefore small compared to $\bar{m}_\infty = 1/T$ in the AFAI phase.

C.5 Numerical simulation

Here we provide additional details from the numerical simulations, beyond what was discussed in the main text. The magnetic field in the simulation was implemented in the Landau gauge, $\mathbf{A} = (0, -B(x - x_0))$, where x_0 is located in the center of the lattice.

To explore the generic behavior of the system in the parameter regime used in the main text, we find and diagonalize the Floquet operator for 100 random disorder realizations, on

a lattice of 80×80 sites with periodic boundary conditions. Among all Floquet eigenstates across these 100 realizations, we find the largest localization length to be $11.7a$, where a is the lattice constant. Thus we are well within the fully-localized, AFAI regime. We furthermore have compiled statistics to demonstrate how the normalized growth rate $\Omega_{NT} \equiv \frac{1}{Ba^2NT}\langle\overline{\sigma}_y(NT)\rangle$ converges to the quantized value with system size and averaging time, which we now discuss.

In Fig. C.1a we show the time-averaged magnetization density after 50 periods as function of R (the side length of the filled squared droplet) for each of the 100 realizations. For each value of R, each black cross indicates the the value obtained for a specific realization. The red area marks the interval within one standard deviation from the mean value of Ω_{50T}, obtained from the 100 realizations. For *all* disorder realizations we see that Ω_{50T} rapidly converges to the quantized value as the size of the filled region, L, is increased.

To see how the average magnetization converges to the quantized value with the averaging time, NT, we investigate the deviation $\Delta\Omega_{NT}$ of Ω_{NT} from the quantized value $\bar{m}_\infty = 1/T$ as a function of N. The value of $\Delta\Omega_{NT}$ is obtained as a root-mean-squared deviation, taken over the 100 realizations, in the case where a region of 50×50 sites is initially occupied. The data are shown in a log-log plot in Fig. C.1b. The linear trend indicates that the deviation decreases with a power-law scaling behaviour. From a linear fit (green line), we find that the deviation from the quantized value decreases as $(NT)^{-0.64}$.

Appendix D

Appendix for Chapter 5

D.1 Hamiltonian in the rotating frame.

Here we explicitly compute the transformed interaction Hamiltonian in the rotating frame, $\tilde{H}_{\text{int}}(t) \equiv Q^\dagger(t) H_{\text{int}} Q(t)$. The interacting part of the Hamiltonian is a sum of terms:

$$H_{\text{int}} = \sum_{\mathbf{r},i} H^{(i)}_{\text{int},\mathbf{r}}, \quad H^{(i)}_{\text{int},\mathbf{r}} = \lambda n_{\mathbf{r}} n_{\mathbf{r}+\mathbf{b}_i}, \tag{D.1}$$

where $i = 1, \ldots, 4$, with $\mathbf{b}_1 = -\mathbf{b}_3 = (a, 0)$ and $\mathbf{b}_2 = -\mathbf{b}_4 = (0, a)$. In the rotating frame, the transformed interaction Hamiltonian is computed using Eq. (D.1) with

$$\tilde{H}^{(i)}_{\text{int},\mathbf{r}}(t) = \lambda \tilde{n}_{\mathbf{r}}(t) \tilde{n}_{\mathbf{r}+\mathbf{b}_i}(t), \tag{D.2}$$

where $\tilde{n}_{\mathbf{r}}(t) \equiv Q^\dagger(t) n_{\mathbf{r}} Q(t)$ is the time-evolved site occupation operator.

We now explicitly compute $\tilde{n}_{\mathbf{r}}(t)$ for the first segment of the driving protocol, $0 \le t < \alpha T/4$. From this we will be able to infer the form of the terms for all later times. Note that the direction of hopping is opposite for particles initially in the A or B sublattice. Therefore, in order to explicitly write $\tilde{n}_{\mathbf{r}}(t)$, we introduce an index $\sigma_{\mathbf{r}} = 1$ for $\mathbf{r}$ in the A sublattice, and $\sigma_{\mathbf{r}} = -1$ for $\mathbf{r}$ in the B sublattice. A straightforward computation gives:

$$n_{\mathbf{r}}(t) = \cos^2(Jt) c^\dagger_{\mathbf{r}} c_{\mathbf{r}} + \sin^2(Jt) c^\dagger_{\mathbf{r}+\sigma_{\mathbf{r}}\mathbf{b}_1} c_{\mathbf{r}+\sigma_{\mathbf{r}}\mathbf{b}_1} + \frac{i}{2} \sin(2Jt)(c^\dagger_{\mathbf{r}} c_{\mathbf{r}+\sigma_{\mathbf{r}}\mathbf{b}_1} - h.c.), \quad 0 \le t < \alpha T/4. \tag{D.3}$$

Note that condition (3) of the main text, $J\alpha T/4 = \pi/2$, yields a simple form for $n_{\mathbf{r}}(t)$ at the end of the segment: $n_{\mathbf{r}}(\alpha T/4) = n_{\mathbf{r}+\sigma_{\mathbf{r}}\mathbf{b}_1}$. Similar expressions are obtained for driving segments 2-4.

The full expression for $\tilde{n}_{\mathbf{r}}(t)\tilde{n}_{\mathbf{r}+\mathbf{b}_i}(t)$ is too cumbersome to write out. For the first segment, using Eq. (D.3), it is evident that there are three kinds of terms:

- density-density interaction between nearest and next-nearest neighbor sites.
- hopping between nearest-neighbor sites with amplitude that depends on density on one of the nearby sites (terms such as $c^\dagger_{\mathbf{r}} c_{\mathbf{r}} c^\dagger_{\mathbf{r}+\mathbf{b}_i} c_{\mathbf{r}+\mathbf{b}_i-\mathbf{b}_1}$),

- hopping of pairs of particles (terms such as $c^\dagger_{\mathbf{r}} c_{\mathbf{r}+\mathbf{b}_1} c^\dagger_{\mathbf{r}+\mathbf{b}_i} c_{\mathbf{r}+\mathbf{b}_i-\mathbf{b}_1}$).

In the remaining three segments, $\tilde{n}_{\mathbf{r}}(t)$ can be constructed from Eq. (D.3), starting the evolution in each segment with the result of the previous one, by 90° rotations and translations in the x- and/or y-directions. At any time, $\tilde{n}_{\mathbf{r}}(t)$ has its support only on the nearest- and next-nearest neighbor sites of $\mathbf{r}$. In these later segments, the terms in $\tilde{H}_{\rm int}(t)$ are also of the three types described above, although the distance between coupled sites may be larger than in the first segment. The distances between coupled sites in the term $\tilde{n}_{\mathbf{r}}\tilde{n}_{\mathbf{r}+\mathbf{b}_i}$ are always bounded by $(1+2\sqrt{2})a$, since $\tilde{n}_{\mathbf{r}}$ has all of its support within a radius of $\sqrt{2}a$ from $\mathbf{r}$.

The above discussion shows that $\tilde{H}_{\rm int}(t)$ is always local with a strictly finite range. This transformed interaction has an off-diagonal part in the site occupation number basis, whose time-averaged component has a magnitude of order $\alpha\lambda$. To see this, note that $\tilde{H}(t)$ only has off-diagonal components in the interval $0 \le t < \alpha T$, and these have magnitude λ.

D.2 Other protocols.

The arguments used in this paper can be extended to other driving protocols. As an example, we consider a setup in which both $H_{\rm dis}$ and $H_{\rm int}$ act throughout the whole driving period. We still assume that $W, \lambda \ll \omega$.

Similar to the analysis above, we employ a unitary transformation $Q(t)$ to eliminate the largest part of the time-dependent Hamiltonian, $H_{\rm id}(t)$. We are left with transformed terms $\tilde{H}_{\rm dis}(t)$, $\tilde{H}_{\rm int}(t)$. One important difference compared to the main protocol discussed in the text is that the transformed disorder Hamiltonian in this case also contains finite-ranged hopping terms, of the order αW. In the absence of interactions ($\lambda = 0$), the system is in the localized phase for small disorder $W \ll \omega$, as shown in Ref. [2]. Moreover, tuning parameter α allows one to tune the localization length in the single-particle problem: at very small α (corresponding to very strong hopping during first four segments of the period), the localization length can be made much shorter than the lattice constant.

The interaction terms transform in the same way as described in the previous subsection. Provided λ is sufficiently small compared to W, these terms will not delocalize the system. We note that the presence of single-particle hopping terms originating from the disorder Hamiltonian will reduce the critical value of the interaction strength at which delocalization occurs. Residual hopping outside of $H_{\rm ideal}(t)$ (i.e., imperfect hopping "π-pulses") will have a similar effect. We thus conclude that AFI phase is generally stable with respect to weak interactions, irrespective of the precise driving protocol.

D.3 Localization controlled by α.

Here we briefly comment on how α controls the localization properties of models (i) and (ii) discussed in the main text. This analysis applies to both models. After applying the rotating frame transformation, Eq. (6) of the main text, we write the transformed Hamiltonian $\tilde{H}(t)$, Eq. (7), as $\tilde{H}(t) = \bar{H} + \delta\tilde{H}(t)$. Here $\bar{H}$ is the time-average of $\tilde{H}(t)$. We further decompose $\bar{H}$ as $\bar{H} = H_{\rm int} + \bar{H}_{\rm dis} + \mathcal{O}(\alpha W, \alpha\lambda)$, where $\bar{H}_{\rm dis}$ is the time average of $H_{\rm dis}(t)$ over the fifth segment.

The $\mathcal{O}(\alpha W, \alpha\lambda)$ corrections arise due to the transformation during the window $0 \leq t < \alpha T$ where the hopping is applied.

Both H_{int} and $\bar{H}_{\text{dis}}$ are diagonal in the site occupation number basis. The off-diagonal contributions to $\bar{H}$, contained in the $\mathcal{O}(\alpha W, \alpha\lambda)$ terms, can be made arbitrarily small by taking α small enough. In this way we can ensure that, in the absence of the time-dependent terms $\delta\tilde{H}(t)$, $\bar{H}$ describes a many-body localized system.

Next, we consider the oscillating part of $\tilde{H}(t)$, $\delta\tilde{H}(t)$, which has a magnitude of order W, λ, varies rapidly in the interval $0 \leq t < \alpha T$, and is constant for the rest of the period. Turning to the Fourier transform of $\delta\tilde{H}(t)$, these properties dictate that its n-th Fourier component is of order $\alpha W, \alpha\lambda$ for $|n| \lesssim \frac{2\pi}{\alpha}$, and falls off as $1/n$ for large n. In the limit $\omega \gg \alpha\lambda, \alpha W$, even the lowest harmonics correspond to high frequencies in the rotating frame, and therefore the system remains localized. For ω comparable to or greater than W, λ, the amplitude of the oscillating terms can be made arbitrarily small by taking $\alpha \to 0$. This again brings the system into the Floquet-MBL regime.

D.4 Stability of time crystals

To demonstrate the universality of our approach, we now outline an argument for the stability of the discrete time crystal (DTC) [49, 50]. The DTC is an example of an anomalous Floquet phase where the discrete time-translational symmetry of the drive, $t \to t + T$, is broken. We note that the stability of DTCs has been previously investigated numerically and through other analytical arguments in Refs. [45, 49, 50].

First, following Ref. [49], we consider a solvable driving protocol for a one dimensional spin-1/2 chain, which illustrates the basic physics of the DTC:

$$H_0(t) = f(t)H_x + [1 - f(t)]H_{\text{dis}}, \tag{D.4}$$

where $f(t) = 1$ for $t \in [nT, nT + T/2]$ and zero otherwise. With this protocol, the first (second) term in the Hamiltonian is turned on during the first (second) half-period. The Hamiltonian H_x induces a global spin rotation around the x axis. The strength of the uniform applied x-field is chosen such that the evolution over the first half-period gives a perfect π-pulse:

$$H_x = \frac{\pi}{T}\sum_i \sigma_i^x. \tag{D.5}$$

The disorder Hamiltonian is chosen as a random, nearest-neighbor Ising interaction:

$$H_{\text{dis}} = \sum_{\langle ij\rangle} J_{ij}\sigma_i^z\sigma_j^z, \quad J_{ij} \in [\bar{J} - W, \bar{J} + W], \tag{D.6}$$

where $\bar{J}$ sets the average interaction strength, and W is the width of the distribution of random couplings.

The evolution generated by protocol (D.4) can be solved exactly. For simplicity, consider an initial product state $|\Psi(0)\rangle = \bigotimes_i |\sigma_i\rangle \equiv |\{\sigma_i\}\rangle$, in which each spin points up or down along z, $\sigma_i = \pm 1$. (The argument works for all such configurations.) During the first half-period, each

spin is flipped: $|\{\sigma_i\}\rangle \to |\{-\sigma_i\}\rangle$. Note that the state remains a product state in the z-basis. During the second half of the period, the state acquires a dynamical phase due to the Ising interaction (D.6). Over the next driving period, a second π-pulse flips all spins back to their initial configuration. In total, the local z-projection $\langle\sigma_i^z\rangle$ of each spin oscillates with twice the period of the drive. Remarkably, this behavior is stable with respect to generic T-periodic perturbations of the Hamiltonian.

To show the stability of DTCs using our approach, we add a small local, but otherwise generic perturbation to the time-dependent Hamiltonian (D.4):

$$H(t) = H_0(t) + \lambda H_{\text{pert}}(t), \;\; \lambda \ll 1. \tag{D.7}$$

We assume that $H_{\text{pert}}(t)$ shares the same periodicity as the drive, $H_{\text{pert}}(t+T) = H_{\text{pert}}(t)$.

Similar to the AFI discussed in the main text, this problem is not in the high-frequency limit. More specifically, the frequency ω is comparable to the amplitude of the local field in H_x, as it must be in order to induce a spin flip during one half-cycle. Similar to our analysis of the AFI, we move to a rotating frame which removes the large-scale micromotion (i.e., the repeated π-pulses). This is accomplished via the transformation $|\Phi(t)\rangle = S^\dagger(t)|\Psi(t)\rangle$, with

$$S(t) = \mathcal{T} e^{-i\int_0^t ds f(t) H_x(s)}. \tag{D.8}$$

We note that $S(nT) = P^{n\,(\text{mod }2)}$, where

$$P = \prod_i (i\sigma_i^x) \tag{D.9}$$

is a global spin-flip operator.

Taking into account the fact that the Ising disorder Hamiltonian commutes with $S(t)$, the Hamiltonian in the rotating frame is given by:

$$\tilde{H}(t) = [1 - f(t)]H_{\text{dis}} + S^\dagger(t) H_{\text{pert}}(t) S(t). \tag{D.10}$$

Interestingly, the periodicity of the dressed perturbation $\tilde{H}_{\text{pert}}(t) = S^\dagger(t) H_{\text{pert}}(t) S(t)$ may be reduced to $2T$-periodicity. This is easy to see, for example, for $H_{\text{pert}}(t) = g(t)\sum_i \sigma_i^y$, using Eq. (D.9) and $g(t+T) = g(t)$. Importantly, this term remains *local*, since $S(t)$ [Eq. (D.8)] simply describes spin rotations over the first half-period.

Having eliminated the large term (D.5), we see that for sufficiently small interactions, $\bar{J}, W \ll \omega$, the transformed Hamiltonian in the rotating frame *is* in the high-frequency driving regime. Therefore, by the perturbation theory of Ref. [109], we can argue that for a sufficiently weak perturbation, $\lambda \ll W$, the system is in the MBL phase. Thus the time-evolved wave function (in the rotating frame), $|\Phi(t)\rangle = \tilde{U}|\Phi(0)\rangle$, with $\tilde{U}(t) = \mathcal{T} e^{-i\int_0^t \tilde{H}(s) ds}$, retains the memory of the initial state.

Finally, we discuss why MBL of the transformed problem (D.10) implies persistent oscillations of physical observables with a doubled period. As above, choose the initial state to be a product state $|\Psi(0)\rangle = |\{\sigma_i\}\rangle$. Then, MBL implies that the local magnetization evaluated in the rotating frame, $\langle\tilde{\sigma}_i^z(t)\rangle := \langle\Phi(t)|\sigma_i^z|\Phi(t)\rangle$, remains close to its initial value for all $t \to \infty$ (at least in the

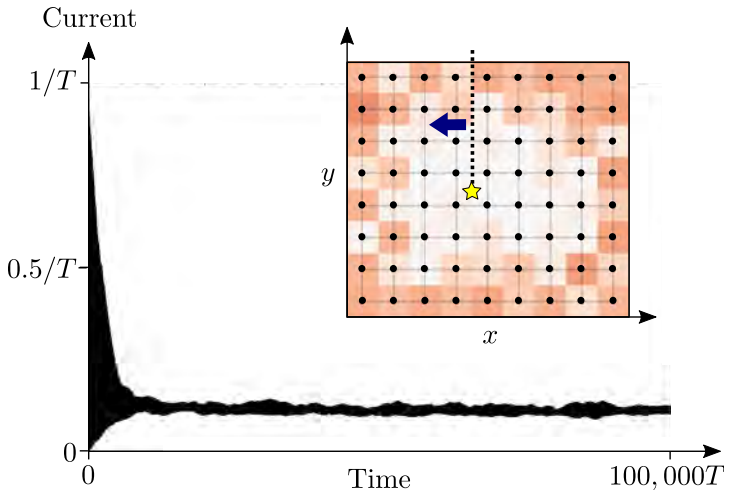

Figure D.1: Persistent current in the AFI with particles initialized along its edge. Here we show the period-averaged current, I_n, as a function of time. The inset shows the cut through which the current is calculated.

strong-disorder limit $\lambda \ll W \ll \omega$). Then, using Eq. (D.9) and the fact that $P^\dagger \sigma_i^z P = -\sigma_i^z$, we relate the physical local magnetization at stroboscopic times to $\langle \tilde{\sigma}_i^z(t) \rangle$:

$$\langle \sigma_i^z(nT) \rangle = \langle \Psi(nT) | \sigma_i^z | \Psi(nT) \rangle = (-1)^n \langle \tilde{\sigma}_i^z(nT) \rangle. \tag{D.11}$$

Since $\langle \tilde{\sigma}_i^z(nT) \rangle$ remains close to its initial value, we have shown that the magnetization oscillates with period $2T$, persisting to the limit $t \to \infty$.

D.5 Circulating current

For the simulation where particles are initialized along the edge, Fig. 4, we have calculated the current flowing across a line that extends from the middle of the system through its boundary, see inset of Fig. D.1. The period-averaged current, $I_n = \int_{nT}^{(n+1)T} dt I(t)$, where $I(t)$ is the instantaneous current through the cut, is shown in Fig. D.1. The current exhibits large oscillations at short times, due to the fact that the particles that circulate around the perimeter initially have a nonuniform density profile. At later times, the density of particles along the edge becomes uniform, and the value of the current settles to a nearly constant, nonzero value. This persistent current is a signature of the chiral nature of the AFI edge.

Appendix E

Appendix for Chapter 6

E.1 Magnetization density in closed geometries

In this section, we provide a rigorous definition of magnetization density in closed geometries. Specifically, we show how to define the time-averaged magnetization operator $\bar{m}_p$ (defined in Eq. (6.3) of the main text) in closed geometries. In the case of a closed geometry, such as a torus, the operator $m_p(t) = \frac{\partial H(t)}{\partial \phi_p}$ is not completely defined: due to Dirac's magnetic flux quantization condition, the flux in a single plaquette cannot be changed continuously without a compensating flux change somewhere else that keeps the total flux through the system constant.

Although the quantization of magnetic flux on closed surfaces prevents a continuous variation of total magnetic flux, it *is* possible to continuously vary the magnetic flux locally in the system, as long as a compensating flux is introduced elsewhere in the system. Therefore Eq. (6.3) of the main text naturally provides a definition for *differences* between magnetization densities in compact geometries. Specifically, on the torus, the difference in the magnetization densities on two plaquettes p and q is given by

$$m_p(t) - m_q(t) = \frac{\partial H(t)}{\partial \phi_{pq}}. \tag{E.1}$$

Here $\frac{\partial H}{\partial \phi_{pq}}$ measures the response of the Hamiltonian to the simultaneous insertion of a magnetic flux ϕ_{pq} in plaquette p and a compensating flux $-\phi_{pq}$ in plaquette q that keeps the total flux through the system zero. Following the same arguments as in Sec. 6.2.1 of the main text, the long-time averaged expectation value of $m_p(t) - m_q(t)$ in some given state $|\Psi\rangle$ can be found as $\langle\!\langle m_p - m_q \rangle\!\rangle = \langle\Psi|\bar{m}_p - \bar{m}_q|\Psi\rangle$, where

$$\bar{m}_p - \bar{m}_q \equiv \lim_{\tau\to\infty} \frac{1}{\tau} \int_0^\tau dt U^\dagger(t) \frac{\partial H}{\partial \phi_{pq}} U(t). \tag{E.2}$$

In the same way as in Sec. 6.2.1 of the main text, the operator $\bar{m}_p - \bar{m}_q$ is an integral of motion, and can be expanded in terms of the LIOMs $\{\hat{n}_a\}$:

$$\bar{m}_p - \bar{m}_q = \sum_{a_1} \mu^{pq}_{a_1} \hat{n}_{a_1} + \sum_{a_1 a_2} \mu^{pq}_{a_1 a_2} \hat{n}_{a_1} \hat{n}_{a_2} + \dots. \tag{E.3}$$

Moreover, as for the case of open geometries (see Footnote 5 of Chapter 6), the coefficient $\mu^{pq}_{a_1\dots a_k}$ is suppressed by an exponential factor $e^{-d_i/\xi}$ for each LIOM $\hat{n}_{a_i}$ that is located far away from both plaquettes p and q. Here d_i is the minimal distance from the center of LIOM $\hat{n}_{a_i}$ to either of the plaquettes p and q. This is a consequence of Ampere's law: specifically, Ampere's law law dictates that the difference in the magnetization densities of two plaquettes p and q is given by the total current that passes through a cut between the plaquettes: $\langle\langle m_p - m_q\rangle\rangle = -\sum_n \langle\langle I_{p_{n+1}p_n}\rangle\rangle$, where $(p_1, p_2, \dots)$ can be any sequence of neighbouring plaquettes that goes from plaquette q to plaquette p. Changing the value of the LIOM $\hat{n}_{a_i}$ (by acting on the state of the system with either $\hat{f}_{a_0}$ or $\hat{f}^\dagger_{a_0}$) can then maximally affect $\langle\langle m_p - m_q\rangle\rangle$ by an amount of order $e^{-d_i/\xi}$, since the sequence of plaquettes $(p_1, p_2, \dots)$ can always be chosen to remain separated from the center of the LIOM $\hat{n}_{a_0}$ by a distance larger than d_i. Thus, $\mu^{pq}_{a_1\dots a_k}$must be exponentially suppressed in d_i/ξ for each of the LIOMs $\hat{n}_{a_i}$.

The above considerations show that the only terms in Eq. (E.3) that can take significant values are those where each of the involved LIOMs $\hat{n}_{a_1}\dots\hat{n}_{a_k}$ is located near either plaquette p or q. We now show that, in the case where plaquettes p and q are separated by a distance $d \gg \xi$ from each other, all of the involved LIOMs are located near the *same* plaquette for a term to contribute significantly. Specifically, we show that $\mu^{pq}_{a_1\dots a_k}$ is exponentially suppressed in d/ξ if one of the LIOMs $\hat{n}_{a_1}\dots\hat{n}_{a_k}$ are located near plaquette p, while another is located near plaquette q. In order to do this, we consider a third plaquette r on the torus, which is also separated from plaquettes p and q by a distance of order L. From Ampere's law, it follows that $\bar{m}_p - \bar{m}_q + (\bar{m}_q - \bar{m}_r) = \bar{m}_p - \bar{m}_r$. This implies that

$$\mu^{pq}_{a_1\dots a_k} = \mu^{pr}_{a_1\dots a_k} - \mu^{qr}_{a_1\dots a_k}. \tag{E.4}$$

We recall that $\mu^{pr}_{a_1\dots a_k}$ vanishes expoentially with the distance from any of the LIOMs $\hat{n}_{a_1}\dots\hat{n}_{a_k}$ to either plaquette p or r. Since one of the LIOMs $\hat{n}_{a_1}\dots\hat{n}_{a_k}$ is located near plaquette q, $\mu^{pr}_{a_1\dots a_k}$ must then be of order $e^{-d/\xi}$. Here we use that plaquette q is located a distance d from plaquette p, and a distance $\sim L > d$ from plaquette r. Noting that another of the LIOMs $\hat{n}_{a_1}\dots\hat{n}_{a_k}$ is located near plaquette p, the same arguments show that $\mu^{pr}_{a_1\dots a_k}$ must also be of order $e^{-d/\xi}$. Using Eq. (E.4), we conclude that $\mu^{pq}_{a_1\dots a_k}$ must be exponentially small in d/ξ. In this way, we conclude that $\mu^{pq}_{a_1\dots a_k}$ is exponentially suppressed in d/ξ unless all LIOMs $a_1\dots a_k$ are located near the same plaquette (p or q).

The above considerations show that the significant terms in the expansion (E.3) can be divided into two groups: terms where the LIOMs $\hat{n}_{a_1}\dots\hat{n}_{a_k}$ are located near plaquette p, and terms where the LIOMs $\hat{n}_{a_1}\dots\hat{n}_{a_k}$ are located near plaquette q. This allows us to write $\bar{m}_p - \bar{m}_q$ in the form

$$\begin{aligned}\bar{m}_p - \bar{m}_q = &\left(\sum_a \mu^p_a \hat{n}_a + \sum_{a,b} \mu^p_{ab}\hat{n}_a\hat{n}_b + \dots\right)\\ &- \left(\sum_a \mu^q_a \hat{n}_a + \sum_{a,b} \mu^q_{ab}\hat{n}_a\hat{n}_b + \dots\right)\end{aligned} \tag{E.5}$$

where $\mu^p_{a_1\dots a_k}$ decays exponentially with the distance from any of the LIOMs $\hat{n}_{a_1}\dots\hat{n}_{a_k}$ to

plaquette p. We identify $\bar{m}_p$ as the first term, and $\bar{m}_q$ as the second term. As defined above $\bar{m}_p$ obeys Ampere's law and thus has all the defining properties of magnetization density.

Note that, for finite systems, $\bar{m}_p$ is only well-defined up to a correction of order $e^{-L/\xi}$ due to the exponentially decaying tails of the coefficients $\{\mu^{pq}_{a_1\dots a_k}\}$. Here, the value of the correction depends on how exactly the above distinction between coefficients $\{\mu^{pq}_{a_1\dots a_k}\}$ is implemented. For large systems, this correction is negligible, and the magnetization density $\bar{m}_p$ is thus a meaningful physical object.

E.2 Response of system to the insertion of a magnetic flux

Here we provide technical details of the discussion in Sec. 6.3.1 of the main text, where the quantization of the invariants $\{\mu_k\}$ as integers is proven.

Specifically, we establish here the relation between the magnetization of Floquet eigenstates and the response of the corresponding quasienergy to the insertion of a magnetic field (Eq. (6.14) in the main text):

$$\sum_p \ell^2 \langle \Psi_{a_1\dots a_k} | \bar{m}_p | \Psi_{a_1\dots a_k} \rangle = -\frac{\partial E_{a_1\dots a_k}}{\partial B}, \tag{E.6}$$

where $\frac{\partial E_{a_1\dots a_k}}{\partial B}$ denotes the response of the quasienergy $E_{a_1\dots a_k}$ to the insertion of a uniform magnetic field B in the region of support of the state $|\Psi_{a_1\dots a_k}\rangle$. Moreover, we show here the the derivative $\frac{\partial E_{a_1\dots a_k}}{\partial B}$ is well-approximated from the response of the system's quasienergy spectrum to the insertion of a (weak) uniform field $B_0 = \frac{2\pi}{L^2}$ corresponding to precisely one flux quantum piercing the torus (Eq. (6.15) in the main text). Specifically, we show that, for any finite value of k, it is possible to label the eigenstates $\{|\tilde{\Psi}_a\rangle\}$ and quasienergies $\{\tilde{E}_a\}$ of the one-flux system, such that, for *each* choice of the LIOM indices $a_1 \dots a_k$,

$$\tilde{E}_{a_1\dots a_k} = E_{a_1\dots a_k} + B_0 \frac{\partial E_{a_1\dots a_k}}{\partial B} + \mathcal{O}\left(A_S B_0 \sqrt{\ell/L}\right), \tag{E.7}$$

The derivative $\frac{\partial E_{a_1\dots a_k}}{\partial B}$ may thus be well-approximated by the difference $(\tilde{E}_{a_1\dots a_k} - E_{a_1\dots a_k})/B_0$ in the thermodynamic limit $L \to \infty$. This step is crucial for the proof of quantization of the invariants $\{\mu_k\}$ in the main text.

Note that Eq. (E.7) does not follow trivially from first-order perturbation theory in the field B_0: Specifically, since the system's quasienergy spectrum undergoes exponentially many avoided crossings under a continuous perturbation of the system (due to resonances between far-separated Floquet eigenstates), first-order perturbation theory breaks down for the system. Instead, we establish Eq. (E.7) with an alternative approach, using the localization of the Floquet eigenstates $|\Psi_{a_1\dots a_k}\rangle$.

In order to follow this approach, we use a succession of auxillary results which are not discussed in detail in the main text, but are crucial for the proof of Eqs. (E.6) and (E.7). The line of arguments proceed as follows: we first show explicitly how the magnetic field B_0 can be implemented in the system (Sec. E.2.1). Subsequently, we show that it is always possible to choose a gauge where the Hamiltonian H_1 of the one-flux system locally resembles the Hamiltonian H of the zero-flux system (Sec. E.2.2), and likewise for the Floquet operators U_1 and U (Sec. E.2.3).

From this, we demonstrate that the k-particle Floquet eigenstates and quasienergies of a many-body localized system are robust to perturbations, such as the insertion of the weak magnetic field B_0 (Sec. E.2.4). Finally, using this result, we prove Eqs. (E.6) and (E.7) (Sec. E.2.5), which is the goal of this appendix.

E.2.1 Implementation of magnetic flux

Here we briefly discuss how the magnetic flux is implemented. The system we consider consists of interacting fermions on a lattice with the geometry of a torus, of dimensions $L \times L$. The Hamiltonian of the system takes the form

$$H(t) = \sum_{\alpha\beta} \hat{c}_\alpha^\dagger \hat{c}_\beta J_{\alpha\beta}(t) + H_{\text{int}}(t) \tag{E.8}$$

where c_α annihilates a fermion on site α in the lattice. Here the first term contains both hopping and on-site potentials, including disorder, while the term H_{int} accounts for interactions (we allow both parts of the Hamiltonian to be time-dependent, with periodicity T). In order to keep the discussion clear and simple, we consider the case of a square lattice model with nearest-neighbour hoppings, and a density-density interaction described by $H_{\text{int}} = \sum_{\alpha,\beta} \rho_\alpha \rho_\beta V_{\alpha\beta}$, where $\rho_\alpha = \hat{c}_\alpha^\dagger \hat{c}_\alpha$. In the general case of a quasilocal Hamiltonian, the results below can also be derived using similar arguments.

In this subsection we are interested in finding the Hamiltonian H_1 of the system when the uniform magnetic field $B_0 = \frac{2\pi}{L^2}$ is insterted, corresponding to one flux quantum through the surface of torus. Having assumed H_{int} to consist of density-density interactions, only the first term in Eq. (E.8) is affected by magnetic flux, and the Hamiltonian H_1 can be found as

$$H_1 = \sum_{\alpha\beta} \hat{c}_\alpha^\dagger \hat{c}_\beta J_{\alpha\beta}(t) e^{-i\theta_{\alpha\beta}} + H_{\text{int}}(t), \tag{E.9}$$

Here, the Peierl's phases $\{\theta_{\alpha\beta}\}$ should ensure that the total phase acquired by traversing a closed loop [1] on the torus be given by $B_0 A_S \,(\text{mod } 2\pi)$, where A_S is the area enclosed by the loop[2]. The phases $\{\theta_{\alpha\beta}\}$ are not uniquely defined, but depend on the gauge used for the one-flux Hamiltonian H_1.

The goal of the following is to show that the flux B_0 only weakly perturbs the system locally. To do this, we are interested in finding a gauge where the Peierl's phases $\theta_{\alpha\beta}$ are much smaller than 1 for bonds located in a particular finite region R of the lattice. The region R should have

[1] Note that we we only consider loops with zero windings around the handles of the torus. The application of a magnetic field through the torus technically also requires a specification of Aharonov-Bohm phase acquired when traversing a closed trajectory with a nontrivial winding on the torus. This is equivalent to specyfing the gauge-independent magnetic flux through the handles of the torus, as function of y and x. For the gauge choice in Eq. [PeierlsPhases:eq:app:stab], one can verify that the phase acquired by traversing the closed curve with x constant is given by $2\pi(x - x_0)/L$, while the phase acquired with the curve with y constant is given by $2\pi y/L$. However, due to localization, the system is exponentially insensitive to the exact choice of flux through the handles, since MBL implies that particles will remain confined in small, finite regions on the torus. For this reason, this subtelty is not discussed further in the main text.

[2] The fact that the total flux on the torus is given by an integer multiple of 2π, means that this requirement does not require a specification of the interior region of the loop.

disk geometry and area A_R, and be centered around the location $\mathbf{r}_0 = (x_0, y_0)$ in the lattice. We assume furthermore for simplicity that $\mathbf{r}_0$ is far away from either of the branch cuts of the position operator at $x = L$ and $y = L$. This can be achieved with the following Landau-type gauge: we let θ_α^x denote the Peierl's phase on the bond that goes in the positive x-direction from the site α (and definine θ_α^y in a similar fashion), let these be given by

$$\theta_\alpha^y = B_0(x_\alpha - x_0)\ell \quad \theta_\alpha^x = B_0 L y_\alpha \delta_{x_\alpha, L}. \tag{E.10}$$

Here (x_α, y_α) denote the coordinates of site α, and δ_{ab} denotes the Kronecker delta symbol, such that $\delta_{x_\alpha,L}$ takes value 1 if $x_\alpha = L$, while $\delta_{x_\alpha,L} = 0$ for all other values of x_α, where ℓ is the lattice constant of the system. The phases θ_α^y ensure that a trajectory encircling a plaquette acquries a phase of $B_0\ell^2$, if the trajectory does not cross the branch cut of the x-position operator at $x = 0$. The phase θ_α^x ensures that the phase is also given by $B_0\ell^2 (\mathrm{mod}\ 2\pi)$ for trajectories encircling plaquettes across the branch cut.

To see that the gauge choice in Eq. (E.10) implies that the Peierl's phases are much smaller than 1 in the region R, note that $\mathbf{r}_0$ is located far from the branch cut at $x = 0$, and hence $\theta_\alpha^x = 0$ for all sites in the region R. To see that θ_α^y is much smaller than 1, note that $|x_\alpha - x_0| \leq \sqrt{A_R}$ when the site α is located within R. This follows from the fact that R has disk geometry, and is centered around $\mathbf{r}_0$. Thus θ_α^y is of order $\sqrt{A_R}\ell/L^2$ for sites within R, and therefore much smaller than 1.

E.2.2 Response of the Hamiltonian

An important result that we will use extensively in the following is that, for large systems, the insertion of the uniform field B_0 only weakly perturbs the system, up to a gauge transformation. To see this, we consider the restriction of the Hamiltonians H_1 and H to the finite region R that was introduced in the previous subsection. In the following, we let $\mathcal{O}_R$ denote the restriction of an operator $\mathcal{O}$ to the region R. Specifically, $\mathcal{O}_R$ is contstructed by eliminating all terms of the operator $\mathcal{O}$ that involve fermionic creation or annihilation operators $\hat{c}_\alpha, \hat{c}_\alpha^\dagger$ on sites located outside R. Using this definition, we have, from Eq. (E.9), that

$$(H_1(t) - H(t))_R = \sum_{\alpha\beta \in R} J_{\alpha\beta}(t)\hat{c}_\alpha^\dagger \hat{c}_\beta (e^{-i\theta_{\alpha\beta}} - 1). \tag{E.11}$$

where the Peierl's phases $\{\theta_{\alpha\beta}\}$ are given in Eq. (E.10). Below, we show that $(H_1 - H)_R$ is small when the system size is large. Specifically, we will find an upper bound for the norm[3] $\|(H_1 - H)_R\|$. In order to do this, we make use of the fact that $\|M\| \leq \sqrt{\mathrm{Tr}(M^\dagger M)}$, such that

$$\|(H_1 - H_0)_R\|^2 \leq \sum_{\alpha_i, \beta_i \in R} K^*_{\alpha_1\beta_1} K_{\alpha_2\beta_2} \mathrm{Tr}(\hat{c}^\dagger_{\beta_1}\hat{c}_{\alpha_1}\hat{c}^\dagger_{\alpha_2}\hat{c}_{\beta_2}),$$

where $K_{\alpha\beta} \equiv J_{\alpha\beta}(e^{i\theta_{\alpha\beta}} - 1)$. Noting that $\theta_{\alpha_i\beta_i} = 0$ if $\alpha_i = \beta_i$, we see that the terms above are only nonvanishing when $\alpha_1 = \alpha_2$ and $\beta_1 = \beta_2$. Thus, we find

$$\|(H_1 - H_0)_R\|^2 \leq \sum_{\alpha,\beta \in R} |J_{\alpha\beta}|^2 |e^{-i\theta_{\alpha\beta}} - 1|^2. \tag{E.12}$$

[3]Here $\|M\|$ refers to the maximum singular value norm $\|M\| \equiv \max_{|\psi\rangle} \sqrt{\langle\, \psi|M^\dagger M|\psi\,\rangle \,/\, \langle\psi|\psi\rangle}$.

We now seek to estimate the maximal scale of the right hand side above. We recall from the discussion in the end of Subsection E.2.1 that the Peierl's phases $\{\theta_{\alpha\beta}\}$, as given in Eq. (E.10), are of order $\sqrt{A_R}\ell/L^2$ for bonds within the region R. This implies that the value of each nonvanishing term in the sum in Eq- (E.12) is of order $J^2 A_R \ell^2/L^4$ or less, where J denotes the typical scale of the (off-diagonal) tunnelling coefficients $\{J_{\alpha\beta}\}$. To estimate the number of nonvanishing terms in the sum, we recall, from the assumptions made in the beginning of Subsection E.2.1, that the tunneling coefficients $J_{\alpha\beta}$ may only couple nearest-neighbour pairs of sites in the lattice. Hence, for each choice of the index α, $J_{\alpha\beta}$ may only be nonvanishing for four choices of the index β. These considerations show that there only is of order A_R nonvanishing terms in the sum above. Using that each nonvanishing term is of order $J^2 A_R \ell^2/L^4$ or less, we find that $\|(H_1 - H)_R\|^2 \lesssim A_R^2 L^{-4} J^2$. Here $a \lesssim b$ indicates that a is smaller than b, or of order b. Thus we conclude that

$$\|(H_1 - H)_R\| \lesssim J A_R/L^2. \tag{E.13}$$

This result can be extended to hold for any region in the torus, with a proper gauge choice of H_1.

E.2.3 Response of the Floquet operator

We now use the above result to show that the Floquet operator U_1 of the one-flux system is approximately identical to the Floquet operator U of the zero-flux system, within the region R. Specifically, we show here that $\|(U - U_1)|\psi\rangle\|$ is much smaller than 1 for any state $|\psi\rangle$ that has its full support within the region R[4]. Here, $|\psi\rangle$ having its full support in the region R means that $\langle\psi|\hat{c}_\alpha^\dagger \hat{c}_\alpha|\psi\rangle = 0$ for all sites α which are not located within the region R. As a first step, we note[5] that $\|(U - U_1)|\psi\rangle\| = \|(U_1^\dagger U - 1)|\psi\rangle\|$. Using that $U_1^\dagger U - 1 = \int_0^T dt\, \partial_t (U_1^\dagger(t) U(t))$ along with the chain rule, we find

$$(U_1^\dagger U - 1)|\psi\rangle = -i\int_0^T dt\, U_1^\dagger(t)[H(t) - H_1(t)]U(t)|\psi\rangle. \tag{E.14}$$

We now make use of the fact that the time-evoution operator $U(t)$ is local at all times $0 \leq t \leq T$, due to the finite Lieb-Robinson velocity v of the system. Thus the state $U(t)|\psi\rangle$ has all of its support on sites within the region $\bar{R}$ which contains all sites located within a distance $\sim vT$ from R, up to a exponentially small correction. This implies that $\mathcal{O}|\psi\rangle = \mathcal{O}_{\bar{R}}|\psi\rangle$ for any local operator $\mathcal{O}$ (up to an exponentially small correction which we ignore in the following). Hence

$$[H_1(t) - H(t)]U(t)|\psi\rangle = [H_1(t) - H(t)]_{\bar{R}} U(t)|\psi\rangle \tag{E.15}$$

Using this result in Eq. (E.14), along with the triangle inequality

$$\|(U_1^\dagger U - 1)|\psi\rangle\| \leq \int_0^T dt\, \|U_1^\dagger(t)[H(t) - H_1(t)]_{\bar{R}} U(t)|\psi\rangle\|.$$

Next, we use that $\|U_1^\dagger(t)[H(t) - H_1(t)]_{\bar{R}} U(t)|\psi\rangle\| \leq \|[H(t) - H_1(t)]_{\bar{R}}\|$, and thus

$$\|(U_1^\dagger U - 1)|\psi\rangle\| \leq \int_0^T dt\, \|[H(t) - H_1(t)]_{\bar{R}}\|. \tag{E.16}$$

[4]Here $\||\psi\rangle\| = \sqrt{\langle\psi|\psi\rangle}$ refers to the usual Hilbert space norm.

[5]This can be verified using $\|U|\Psi\rangle\| = \||\Psi\rangle\|$ for any unitary operator U.

Using inequality (E.13) from the previous subsection, we recall that $\|H_1(t) - H(t)\| \lesssim JA_{\bar{R}}/L^2$. We take the linear dimension of R to be larger than vT (but still much smaller than L), and hence the regions $\bar{R}$ and R approximately have the same area A_R: $A_{\bar{R}} = A_R + \mathcal{O}(vT\sqrt{A_R})$. Setting $A_{\bar{R}} \approx A_R$ in the following, and using inequality (E.13) in the above, we find

$$\|(U^\dagger U_1 - 1)|\psi\rangle\| \lesssim JTA_R/L^2. \tag{E.17}$$

We thus conclude that $\|(U_1 - U)|\psi\rangle\| \lesssim JTA_R/L^2$. As for the Hamiltonian, this result can be extended to hold for any region R in the torus, by using a proper gauge for U_1.

The result in Eq. (E.17) shows that (when picking a proper gauge) the Floquet operators of the one- and zero flux systems give nearly identical results when acting on a state which is confined to a finite region on the torus whose area is much smaller than the size of the torus. In this sense, the insertion uniform magnetic field B_0 only weakly modifies the Floquet operator for large systems.

E.2.4 Response of Floquet eigenstates and quasienergy spectrum

We now use the result in Eq. (E.17) to show that the quasienergy spectrum and Floquet eigenstates of the system are robust to perturbations, and only weakly affected by the insertion of the uniform magnetic field B_0. Specifically, due to many-body localization, each Floquet eigenstate of the one- and zero flux systems each has its full support within a finite region S on the torus, with area A_S, up to a correction exponentially small in $\sqrt{S}/\xi$. Using this fact, we show below that, with a probability that goes to 1 in the thermodynamic limit, the k-particle eigenstates $\{|\tilde{\Psi}_{a_1\ldots a_k}\rangle\}$ of U_1 can be labelled such that, for *each* choice of the LIOM indices $a_1 \ldots a_k$,

$$\tilde{E}_{a_1\ldots a_k} = E_{a_1\ldots a_k} + \mathcal{O}(JB_0A_S), \tag{E.18}$$

while

$$|\tilde{\Psi}_{a_1\ldots a_k}\rangle = |\Psi_{a_1\ldots a_k}\rangle + \mathcal{O}(A_S L^{-2+\eta}\ell^{-\eta}). \tag{E.19}$$

Here the latter result holds up to a gauge transformation, and η can be any number greater than $2/3$. In particular, by picking $2/3 < \eta < 2$, we see that, with probability 1 in the thermodynamic limit, *each* eigenstate of U_1 is identical to an eigenstate of U (up to gauge transformation, and a vanishing correction). Noting that, in the thermodynamic limit, and for $2/3 < \eta < 1$, $A_S < \ell^{1+\eta}L^{1-\eta}$, we find that $|\tilde{\Psi}_{a_1\ldots a_k}\rangle = |\Psi_{a_1\ldots a_k}\rangle + \mathcal{O}(\ell/L)$, which is the result quoted above Eq. (6.15) in the main text.

Due to the possibility that the introduction of the field B_0 induces a resonance between two Floquet eigenstates of U, there does exist disorder realizations where one (or more) of the eigenstates of U_1 is a hybridization of two eigenstates of U. In this case, Eq. (E.19) will not hold for each Floquet eigenstate of the system. However, as we show here, Eq. (E.19) is only violated for a set of disorder realizations with meausre zero in thermodynamic limit. In this way, Eqs. (E.19) and (E.18) hold for *almost all* disorder realizations in the thermodynamic limit.

To show that Eqs. (E.18) and (E.19) hold, we first consider the case $k = 1$ (i.e., we establish the relationship for each single-particle Floquet eigenstate). Subsequently, we generalize this result to larger numbers of particles. In the following, we neglect corrections that are exponentially small in system size, only keeping power law corrections.

Single-particle eigenstates

Here we show that relationship in Eqs. (E.19) holds for the single-particle case, with a probability that goes to 1 in the thermodynamic limit.

As a first step, we note that the one-flux system is also many-body localized[6]. Thus each single-particle eigenstate $|\tilde{\Psi}\rangle$ of U_1 almost surely has its full support within a finite region S of the torus, of linear dimension $d \sim \xi$, up to an exponentially small correction. This implies that each eigenstate $|\tilde{\Psi}\rangle$ of U_1 can only overlap significantly with a a finite number $N_1 \sim A_S/\ell^2$ of eigenstates $|\Psi_a\rangle$ of U (up to an exponentially small correction); namely the eigenstates $|\Psi_a\rangle$ that are located in the vicinity of S. We now use this fact to show that, for each eigenstate $|\tilde{\Psi}\rangle$ of U_1 with quasienergy $\tilde{E}$, there exists a *unique* significantly overlapping eigenstate $|\Psi_a\rangle$ whose quasienergy E_a satisfies

$$|\tilde{E} - E_a| < \ell/LT. \tag{E.20}$$

We use this as our basis for the labelling of eigenstates of U_1. Subsequently, we show that Eqs. (E.19) and (E.18) holds for this choice of labelling.

In order to prove Eq. (E.20), it is convenient to make use of the properties of the zero-flux system's quasienergies. For a given single-particle eigenstate $|\tilde{\Psi}\rangle$ of U_1 with quasienergy $\tilde{E}$, we let $|\Psi_{a_1}\rangle \dots |\Psi_{a_{N_1}}\rangle$ denote the N_1 eigenstates of U that may significantly overlap with $|\tilde{\Psi}\rangle$. We order the indices $a_1 \dots a_{N_1}$ according to how close the associated quasienergies $\{E_{a_i}\}$ are to $\tilde{E}$, such that $|E_{a_1} - \tilde{E}| \leq |E_{a_2} - \tilde{E}| \dots \leq |E_{a_{N_1}} - \tilde{E}|$ (mod $2\pi/T$)[7]. With this ordering of the indices, it follows that[8]

$$|\tilde{E} - E_{a_i}| \geq \frac{1}{2}|E_{a_2} - E_{a_1}| \,(\text{mod } 2\pi/t), \text{ for } \quad i \geq 2. \tag{E.21}$$

We now note that the two Floquet eigenstates $|\Psi_{a_1}\rangle$ and $|\Psi_{a_2}\rangle$ whose quasienergies are closest to $\tilde{E}$ are located in the same region on the torus. Hence their respective quasienergies E_{a_1} and E_{a_2}. are subject to level repulsion, when the quasienergy difference $|E_{a_1} - E_{a_2}|$ is sufficiently small. The distribution of the gaps between eigenvalues that experience level repulsion is described by a Wigner-dyson distribution [210]. Noting that the Floquet operator U is unitary, the probability distribution for the value of $|E_{a_1} - E_{a_2}|$ near zero (given a random choice of the state $|\tilde{\Psi}\rangle$) therefore resembles a Wigner-dyson distribution for the Gaussian Unitary Ensemble. In particular, letting $p(x)$ denote the probability density that $|E_{a_1} - E_{a_2}| = x$, we have, in the limit $x \to 0$ that

$$p(x) \propto x^2 T^3/N_1 \tag{E.22}$$

Using the result in Eq. (E.22), we now seek to compute the expected number $N(x)$ of choices of the eigenstate $|\tilde{\Psi}\rangle$ (among all L^2/ℓ^2 single-particle eigenstates of U_1) for which $|E_{a_1} - E_{a_2}|$ is smaller than a given value x. This number can be found as

$$N(x) = L^2/\ell^2 \int_0^x dx' p(x'). \tag{E.23}$$

[6] We assume that MBL is robust to perturbations, and thus U_1 also describes a many-body localized system

[7] Here the inequality modulo $2\pi/T$ is defined such that $|a| < |b|(\text{mod } k)$ means that $\min_{z\in\mathbb{Z}} |a + zk| < \min_{z\in\mathbb{Z}} |b + zk|$

[8] Specifically, since $|E_{a_2} - \tilde{E}| \geq |E_{a_1} - \tilde{E}|(\text{mod } 2\pi/t)$, we have $|\tilde{E} - E_{a_i}| \geq \frac{1}{2}(|E_{a_2} - \tilde{E}| + |\tilde{E} - E_{a_1}|)(\text{mod } 2\pi/t)$. Moreover, one can verify that $|a| + |b| \geq |a + b|(\text{mod } 2\pi/T)$, from which the result follows

In the limit where $x \ll 1/T$, we may use the scaling behaviour in Eq. (E.22) for $p(x)$. Evaluating the integral above in this case, we find that $N(x)$ scales as $x^3\, N_1 L^2 T^3/\ell^2$ for small x. Picking $x = T^{-1}(\ell/L)^\eta$, where $\eta > 2/3$, we see that the expected number of eigenstates $|\tilde{\Psi}\rangle$ for which $|E_{a_1} - E_{a_2}| < (\ell/L)^\eta/T$ goes to zero as $L^{2/3-\eta}$ in the thermodynamic limit. Using the inequality in Eq. (E.21), we conclude that, for *each* choice of the eigenstate $|\tilde{\Psi}\rangle$, it holds with probability 1 in the thermodynamic limit that

$$|E - E_{a_i}| > (\ell/L)^\eta T^{-1}, \tag{E.24}$$

when $i \geq 2$. Here η can be any number greater than 2/3. By picking $\eta = 1$, we conclude that the inequality (**??**) can maximally be satisfied for *one* of the signfificantly overlapping eigenstates $\{|\Psi_{a_i}\rangle\}$, namely $|\Psi_{a_1}\rangle$.

We now show that $|\tilde{E} - E_{a_1}|$ must be smaller than ℓ/LT in the thermodynamic limit, thus proving the inequality (E.20). To do this, we pick the gauge for U such that the inequality (E.17) holds for states that have their full support in the region S, where $|\tilde{\Psi}\rangle$ is confined. We consider the overlap $\lambda_i \equiv \langle \Psi_{a_i}|\tilde{\Psi}\rangle$ of $|\tilde{\Psi}\rangle$ with the one of the significantly overlapping single-particle eigenstates $\{|\Psi_{a_i}\rangle\}$ (for all other eigenstates of U, the overlap will be exponentially suppressed). As a first step we note that $|\Psi_a\rangle$ and $|\tilde{\Psi}\rangle$ are eigenstates of U and U_1, respectively, and thus λ_i can be found as

$$\lambda_i = \frac{\langle \Psi_a|U^\dagger U_1 - 1|\tilde{\Psi}\rangle}{e^{-i(\tilde{E}-E_a)T} - 1} - \tag{E.25}$$

Since $|\tilde{\Psi}\rangle$ has its full support in the region S (up to an exponentially small correction), we find from the inequality (E.17) that $|\langle \Psi_a|U^\dagger U_1 - 1|\tilde{\Psi}\rangle| \lesssim JTA_S/L^2$. Hence

$$|\lambda_i| \lesssim \frac{JTA_S L^{-2}}{|e^{-i(\tilde{E}-E_{a_i})T} - 1|}, \tag{E.26}$$

Inequality (E.24) implies that $|e^{-i(\tilde{E}-E_a)T} - 1| > |e^{-i(\ell/L)^\eta} - 1|$ in the thermodynamic limit, when $i \geq 2$ (for almost all disorder realizations). Using this fact, and taking the limit $L \to \infty$ (in which $|e^{-i(\ell/L)^\eta} - 1| \to (\ell/L)^\eta$) we conclude that

$$|\lambda_i| < A_S L^{-2+\eta} \ell^{-\eta}, \tag{E.27}$$

for $i \geq 2$, and for almost all disorder realizations. Here we suppressed all factors with irrelevant scaling in the thermodynamic limit.

We now note that, up to an exponentially small correction, $\sum_{i=1}^{N_1} |\lambda_i|^2 = 1$, and hence $|\lambda_1|^2 = 1 - \sum_{i=2}^{N_1} |\lambda_{a_i}|^2$. Taking the square root, and using the inequality (E.27), we thus find that

$$|\lambda_1| = 1 + \mathcal{O}(A_S^2 L^{-4+2\eta} \ell^{-2\eta}), \tag{E.28}$$

where we again suppressed factors with irrelevant scaling behavoiur. Picking $\eta = 1$, we see that $|\lambda_1| = 1 + \mathcal{O}(A_S^2 L^{-2}\ell^{-2})$ in the thermodynamic limit. Using this result in the inequality (E.26), we conclude that the quasienergy difference $|E_{a_1} - \tilde{E}|$ must be smaller than (or of order) $JA_S L^{-2}$. Thus $|E_{a_1} - \tilde{E}|$ is smaller than ℓ/LT in the thermodynamic limit. Thus we conclude that, with a probability that goes to 1 in the thermodynamic limit, and for each eigenstate $|\tilde{\Psi}\rangle$ of U_1, the

inequality (E.20) is satisfied for one and only one of the eigenstates of U that significantly overlaps with $|\tilde{\Psi}\rangle$. This concludes the proof of Eq. (E.20).

We use Eq. (E.20) as a basis for labelling the eigenstates of U_1. Specifically, we label the single-particle eigenstates of U_1 such that $|\tilde{\Psi}_a\rangle$ denotes the eigenstate for which the eigenstate $|\Psi_a\rangle$ satisfies Eq. (E.20). To show that the Eqs. (E.19) and (E.18) holds with this labelling, we recall from the discussion below Eq. (E.28) that $|E_a - \tilde{E}_a|$ must be smaller than (or of order) JA_SL^{-2}. Using $B_0 = 2\pi L^{-2}$, we thus establish

$$\tilde{E}_a = E_a + \mathcal{O}(JA_SB_0). \tag{E.29}$$

Next, we note, from the definition of λ_i that $\lambda_1 = \langle\tilde{\Psi}_a|\Psi_a\rangle$. Thus Eq. (E.28) implies that

$$|\tilde{\Psi}_a\rangle = |\Psi_a\rangle + \mathcal{O}(A_SL^{-2+\eta}\ell^{-\eta}), \tag{E.30}$$

where η can be any number greater than 2/3. Thus Eqs. (E.18) (E.19) hold in the single-particle case.

Two-particle eigenstates

Having established the relationship in Eq. (E.19) for single-particle Floquet eigenstates, we now show that it also holds for all two-particle eigenstates. In order to do this, we consider a two-particle Floquet eigenstate $|\tilde{\Psi}\rangle$ of the one-flux system, with quasienergy $\tilde{E}$. In the following, we divide our argumentation into two cases, depending on whether or not the two particles are located in the same region, i.e., within a distance $\lesssim \xi$ from each other.

Nearby LIOMs — We first consider the case where the two particles are located in the same region S, a distance $\lesssim \xi$ from each other. In this case, for a Floquet eigenstate $|\Psi_{ab}\rangle$ of the one-flux system to significantly overlap with $|\tilde{\Psi}\rangle$, the LIOMs $\hat{n}_a$ and $\hat{n}_b$ must also be located in the same region. This implies that there only are of order $N_2 \sim \binom{A_R/a^2}{2}$ choices of distinct LIOMs a, b for which $|\Psi_{ab}\rangle$ to significantly overlaps with $|\tilde{\Psi}\rangle$. Here $A_S \lesssim 2\xi^2$ denotes the area of the region in which the state $|\tilde{\Psi}\rangle$ has its support (up to an exponentially small correction).

The arguments above establishes that $|\tilde{\Psi}\rangle$ may only overlap with a finite number of eigenstates $\{|\Psi_{ab}\rangle\}$ of U that have their full support in the same region S (up to an exponentially small correction). Using the same arguments as for the single particle case (see above subsection), one can then show that, for almost all disorder realizations in the thermodynamic limit, there exists a unique two-particle eigenstate $|\Psi_{ab}\rangle$ of U for each two-particle eigenstate $|\tilde{\Psi}\rangle$ of U_1 such that (up to a gauge transformation)

$$|\tilde{\Psi}\rangle = |\Psi_{ab}\rangle + \mathcal{O}(A_SL^{\eta-2}\ell^{\eta}), \tag{E.31}$$

where η can be any number larger than 2/3, and

$$\tilde{E} = E_{ab} + \mathcal{O}(JA_SB_0). \tag{E.32}$$

Separated LIOMs — Next, we consider the case where $|\tilde{\Psi}\rangle$ describes a state where the two particles are separated by a large distance $\delta \gg \xi$. In this case, the LIOM structure of the Floquet operator U_1 (Eq. (6.1) in the main text) implies that $|\tilde{\Psi}\rangle$ may be written as a direct product of two single-particle eigenstates $|\tilde{\Psi}_a\rangle$ and $|\tilde{\Psi}_b\rangle$, up to a correction exponentially small in the distance δ. Here a and b refer to the labelling of the single-particle eigenstates of U_1 that was established in the previous subsection. Letting S_a and S_b denote the two well-separated regions where the states $|\tilde{\Psi}_a\rangle$ and $|\tilde{\Psi}_b\rangle$, respectively, have their support (up to an exponentially small correction), we have:

$$|\tilde{\Psi}\rangle = |\tilde{\Psi}_a\rangle_{S_a} \otimes |\tilde{\Psi}_b\rangle_{S_b} \otimes |0\rangle + \mathcal{O}(e^{-\delta/\xi}). \tag{E.33}$$

Here $|\Psi\rangle_S$ denotes the restriction of the state $|\Psi\rangle$ to the Fock space of the region S (defined from the projection of $|\Psi\rangle$ into the subspace with no particles outside region S). The state $|0\rangle$ refers to the vacuum in the complementary region to S_a and S_b. Since the two particles in the state $|\tilde{\Psi}\rangle$ are separated by a distance much larger than ξ, the regions S_a and S_b do not overlap.

We now recall from Eq. (E.30) that $|\tilde{\Psi}_a\rangle$ is approximately identical to a single-particle eigenstate $|\Psi_a\rangle$ of the zero-flux system's Floquet operator U (for all but a measure zero set of disorder realizations). Specifically, up to a gauge transformation, $|\tilde{\Psi}_a\rangle = |\Psi_a\rangle + \mathcal{O}(A_{S_a} L^{-2-\eta} \ell^{\eta})$, where η can be any number greater than 2/3. The eigenstate $|\Psi_a\rangle$ moreover has its full support in the same region S_a as $|\tilde{\Psi}_a\rangle$ (up to an exponentially small correction). Letting V_a being the unitary operator that generates the transformation to the gauge in which Eq. (E.34) holds for $|\tilde{\Psi}_a\rangle$, we have

$$|\tilde{\Psi}_a\rangle_{S_a} = V_a |\Psi_a\rangle_{S_a} + \mathcal{O}(A_{S_a} L^{-2-\eta} \ell^{\eta}). \tag{E.34}$$

Here we suppressed the exponentially small correction due to the restriction of the states $|\tilde{\Psi}_a\rangle$, $|\Psi_a\rangle$ to the region S_a (this can be taken to be subleading relative to the power-law correction above). Using the relation (E.34) for the states $|\tilde{\Psi}_a\rangle_{S_a}$ and $|\tilde{\Psi}_b\rangle_{S_b}$ in Eq. (E.33), we obtain

$$|\tilde{\Psi}\rangle = V_a V_b |\Psi_a\rangle_{S_a} \otimes |\Psi_b\rangle_{S_b} \otimes |0\rangle + \mathcal{O}(A_S L^{-2+\eta} \ell^{-\eta}), \tag{E.35}$$

where $A_S = A_{S_a} + A_{S_b}$.

We now note that the product of the two gauge transformations V_a and V_b is itself a gauge transformation. We further note that, due to the LIOM structure (Eq. (6.1) in the main text) of the Floquet operator U, the direct product $|\Psi_a\rangle_{S_a} \otimes |\Psi_b\rangle_{S_b} \otimes |0\rangle$ is identical to the Floquet eigenstate $|\Psi_{cd}\rangle$ of the zero-flux system, up to a correction exponentialy small in $\mathcal{O}(e^{-\delta/\xi})$, which we ignore in the following. We thus concluce that (up to a gauge transformation),

$$|\tilde{\Psi}\rangle = |\Psi_{cd}\rangle + \mathcal{O}(A_S L^{-2+\eta} \ell^{-\eta}), \tag{E.36}$$

To establish the analogous result for the quasienergies, we note that the exponential decay of the quasienergy coefficients $\tilde{\varepsilon}_{a_1 \ldots a_k}$ for the Floquet operator U_1 (see Eq. (6.1) in the main text) with the distance between the LIOMs labelled by $a_1 \ldots a_k$ implies that $\tilde{E}_{ab} = \tilde{E}_a + \tilde{E}_b + \mathcal{O}(e^{-d/\xi})$. Recalling from Eq. (E.29) that $\tilde{E}_a = E_a + \mathcal{O}(J A_{S_a} B_0)$, we conclude that

$$\tilde{E} = E_{ab} + \mathcal{O}(J A_S B_0). \tag{E.37}$$

The two cases we considered above show that, in the thermodynamic limit (for all but a measure zero set of disorder realizations), *each* two-particle eigenstate $|\tilde{\Psi}\rangle$ of U_1 is identical to a

unique eigenstate of U, up to a gauge transformation, and a correction of order $\mathcal{O}(A_S L^{-2+\eta}\ell^{-\eta})$. Here η can be any number greater than 2/3, and A_S dentoes denotes the area of the region in which the state $|\tilde{\Psi}\rangle$ has its support (up to an exponentially small correction). We may thus label the two-particle eigenstates of U_1 such that Eq. (E.18) and (E.19) hold with $k = 2$, and for each choice of the LIOM indices a_1 and a_2.

k-particle-eigenstates

For the general case of a k-particle eigenstate $|\tilde{\Psi}\rangle$ of U_1, we we can apply the same steps as for the two-particle case. We divide our arguments into two cases, depending on whether or not $|\tilde{\Psi}\rangle$ describes a state where *all* of the particles are located within the same region.

In the case where all particles are located within the same region, we use the fact that this type of eigenstate may only overlap with a finite, size-independent number N_k of eigenstates $\{|\Psi_{a_1\ldots a_k}\rangle$ of U. Using the same arguments as for the single-particle case, we then find that, for all but a measure zero set of disorder realizations in the thermodynamic limit, there exists a unique eigenstate $|\Psi_{a_1\ldots a_k}\rangle$ of U such that (up to a gauge transformation),

$$|\tilde{\Psi}\rangle = |\Psi_{a_1\ldots a_k}\rangle + \mathcal{O}(A_S L^{\eta-2}\ell^{\eta}), \tag{E.38}$$

$$\tilde{E} = E_{a_1\ldots a_k} + \mathcal{O}(J A_S B_0). \tag{E.39}$$

Here A_S denotes the area in which the eigenstate $|\Psi_{a_1\ldots a_k}\rangle$ has its support (up to an exponentially small correction), and η can be any number greater than 2/3.

All other eigenstates of U_1 (i.e., the eigenstates where all particles are *not* located in the same region on the torus) can be written as a direct products of eigenstates with fewer than k particles, up to an exponentially small correction. Following the same line of arguments as for the analogous two-particle case, the relationships (E.19) and(E.18) can then be demonstrated to hold for this class of eigenstates using the fact that Eq. (E.19) and (E.18) hold for eigenstates with less than k particles.

E.2.5 Relationship between magnetization density and quasienergy

Having established the auxillary results in Secs. E.2.1-E.2.4, we are now ready to prove Eqs. (E.6) and (E.7), which is the goal of this appendix. In the following, we neglect corrections that are exponentially small in system size, only keeping power law corrections.

Proof of Eq. (E.6)

We first prove the relationship between the quasienergies in Eq. (E.6). Specifically, we show that, for a Floquet eigenstate $|\Psi_{a_1\ldots a_k}\rangle$,

$$\sum_p \ell^2 \langle \Psi_{a_1\ldots a_k}|\bar{m}_p|\Psi_{a_1\ldots a_k}\rangle = \frac{\partial E_{a_1\ldots a_k}}{\partial B} \tag{E.40}$$

where $\frac{\partial E_{a_1\ldots a_k}}{\partial B}$ denotes the response of the quasienegy $E_{a_1\ldots a_k}$ to a uniform magnetic field through the region of support of the eigenstate $|\Psi_{a_1\ldots a_k}\rangle$ (see discussion below).

In order to prove Eq. (6.14), we consider a Floquet eigenstate $|\Psi_{a_1\ldots a_k}\rangle$ which has its full support in a region S (up to an exponentially small correction) whose area is given by A_S. We let $U(B)$ be the Floquet operator of the system in the case where a uniform magnetic field B is applied through the region S, while a compensating magnetic flux $A_S B$ is applied through a plaquette q somewhere outside S. This configuration of magnetic field keeps the total flux through the torus zero, thus allowing for a contiunuous variation of the field B (in contrast to the case discussed in Appendix E.1). We establish Eq. (E.6) by computing the expectation value of $\frac{\partial U}{\partial B}$ at $B = 0$ in the state $|\Psi_{a_1\ldots a_k}\rangle$.

We find the operator $\frac{\partial U}{\partial B}$ from direct differentiation of the time-ordered exponential $U = \mathcal{T} e^{-i\int_0^T dt H(t)}$:

$$\frac{\partial U}{\partial B} = -iU \int_0^T dt\, U^\dagger(t) \frac{\partial H(t)}{\partial B} U(t). \tag{E.41}$$

From the definition of $U(B)$ in the above paragraph, it follows that $\frac{\partial H}{\partial B}$ can be written as $\frac{\partial H}{\partial B} = \sum_{p\in S} \ell^2 \frac{\partial H}{\partial \phi_p} - A_S \frac{\partial H}{\partial \phi_q}$. Using this identity, along with the definition of magnetization density as $m_p(t) = \frac{\partial H(t)}{\partial \phi_p}$, we find

$$\frac{\partial U}{\partial B} = -iU \int_0^T dt\, U^\dagger(t) \left(\sum_{p\in R} \ell^2 m_p(t) - A_R m_q(t) \right) U(t).$$

We now take the expectation value of the above in the Floquet eigenstate $|\Psi_{a_1\ldots a_k}\rangle$. We introduce for brevity the shorthand notation $\langle \mathcal{O} \rangle$ for the expectation value of an operator $\mathcal{O}$ in the state $|\Psi_{a_1\ldots a_k}\rangle$: $\langle \mathcal{O} \rangle \equiv \langle \Psi_{a_1\ldots a_k} | \mathcal{O} | \Psi_{a_1\ldots a_k} \rangle$. Since $U(T+t)|\Psi_{a_1\ldots a_k}\rangle = e^{-iE_{a_1\ldots a_k}T} U(t) |\Psi_{a_1\ldots a_k}\rangle$, one can then verify that

$$\int_0^T dt\, \langle U^\dagger(t) m_p(t) U(t) \rangle = \lim_{\tau\to\infty} \frac{T}{\tau} \int_0^\tau dt\, \langle U^\dagger(t) m_p(t) U(t) \rangle.$$

Thus, using the definition of $\bar{m}_p$ in Eq. (6.5) of the main text, we find

$$\int_0^T dt \langle U^\dagger(t) m_p(t) U(t) \rangle = \langle \bar{m}_p \rangle T. \tag{E.42}$$

Using $\langle \Psi_{a_1\ldots a_k} | U(T) = e^{-iE_{a_1\ldots a_k}T} \langle \Psi_{a_1\ldots a_k}|$, we then find

$$\left\langle \frac{\partial U}{\partial B} \right\rangle = -iT e^{-iE_{a_1\ldots a_k}T} \left\langle \sum_{p\in S} \ell^2 \bar{m}_p - A_R \bar{m}_q \right\rangle.$$

We now make use of the fact that the state $|\Psi_{a_1\ldots a_k}\rangle$ has its full support in the region S, up to an exponentially small correction. We note that $\bar{m}_q$ only has support in the region around plaquette q, outside S, (up to a correction of order $e^{-L/\xi}$ which we ignore), and hence $\langle \Psi_{a_1\ldots a_k} | \bar{m}_q | \Psi_{a_1\ldots a_k} \rangle = 0$. Moreover, since $\langle \Psi_{a_1\ldots a_k} | \bar{m}_p | \Psi_{a_1\ldots a_k} \rangle$ is only nonzero if p is in the region S (again up to an exponentially small correction), $\sum_{p\in S} \langle \Psi_{a_1\ldots a_k} | \bar{m}_p | \Psi_{a_1\ldots a_k} \rangle = \sum_p \langle \Psi_{a_1\ldots a_k} | \bar{m}_p | \Psi_{a_1\ldots a_k} \rangle$. Using these two results in the above, we find

$$\left\langle \frac{\partial U}{\partial B} \right\rangle = -ie^{-iE_{a_1\ldots a_k}T} \sum_p \ell^2 \langle \bar{m}_p \rangle T. \tag{E.43}$$

As a next step, we rewrite $\frac{\partial U}{\partial B}$ in terms of the spectral decomposition

$$U = \sum_{a_1 \ldots a_k} |\Psi_{a_1 \ldots a_k}\rangle\langle\Psi_{a_1 \ldots a_k}| e^{-iE_{a_1 \ldots a_k} T}, \tag{E.44}$$

obtaining

$$\begin{aligned}\frac{\partial U}{\partial B} = &\sum_{a_1 \ldots a_k} -iT \frac{\partial E_{a_1 \ldots a_k}}{\partial B} e^{-iE_{a_1 \ldots a_k} T} |\Psi_{a_1 \ldots a_k}\rangle\langle\Psi_{a_1 \ldots a_k}| \\ &+ \sum_{a_1 \ldots a_k} e^{-iE_{a_1 \ldots a_k} T} \frac{\partial}{\partial B} (|\Psi_{a_1 \ldots a_k}\rangle\langle\Psi_{a_1 \ldots a_k}|).\end{aligned}$$

Using that $\langle\Psi_{a_1 \ldots a_k}| \frac{\partial}{\partial B} (|\Psi_{b_1 \ldots b_k}\rangle\langle\Psi_{b_1 \ldots b_k}|) |\Psi_{a_1 \ldots a_k}\rangle = 0$ for any choice of the LIOM indices $\{b_1 \ldots b_k\}$, we thus find

$$\langle\Psi_{a_1 \ldots a_k}| \frac{\partial U}{\partial B} |\Psi_{a_1 \ldots a_k}\rangle = -iT \frac{\partial E_{a_1 \ldots a_k}}{\partial B} e^{-iE_{a_1 \ldots a_k} T}. \tag{E.45}$$

Comparing with Eq. (E.43) we identify

$$\frac{\partial E_{a_1 \ldots a_k}}{\partial B} = \sum_p a^2 \langle\Psi_{a_1 \ldots a_k}| \bar{m}_p |\Psi_{a_1 \ldots a_k}\rangle \tag{E.46}$$

This was what we wanted to show.

Proof of Eq. (E.7)

Here we prove the relationship Eq. (E.7), showing that the derivative $\frac{\partial E_{a_1 \ldots a_k}}{\partial B}$ is well-approximated from the response of the system's quasienergy spectrum to the insertion of the uniform field $B_0 = \frac{2\pi}{L^2}$:

$$\tilde{E}_{a_1 \ldots a_k} = E_{a_1 \ldots a_k} + B_0 \frac{\partial E_{a_1 \ldots a_k}}{\partial B} + \mathcal{O}(A_R^2 B_0^2). \tag{E.47}$$

In order to prove this result, we consider, as in the previous subsection, a Floquet eigenstate $|\Psi_{a_1 \ldots a_k}\rangle$, with full support within the region S (up to an exponentially small correction). We let A_S denote the area of the region S, and take this to be much smaller than the area of the torus. The region S may consist of several simply connected regions $\{S_i\}$ that are disconnected from each other and spread throughout the torus. We let $H_S(B)$ be the Hamiltonian of the system, restricted to the region S, in the presence of a uniform perpendicular magnetic field B (since the region S is not a closed geometry, the field B can be varied continuously, in contrast to the case discussed in Appendix E.1). The region S should be large enough that the Hamiltonian H_R adequately describes the dynamics of the system wihtin a drivng period, when initialized in the state $|\Psi_{a_1 \ldots a_k}\rangle$[9], up to exponentially small corrections in system size, which we neglect in the following. In the case where S consists of several disconnected regions, $H_S(B)$ can be written as $H_S(B) = \sum_i H_{S_i}(B)$, where $H_{S_i}(B)$ is the restriction of H to the region S_i.

[9]For example, we may take S to contain all sites within a distance $\sim vT$ from the region of support of the state $|\Psi_{a_1 \ldots a_k}\rangle$, where v is the Lieb-Robinsion velocity of the Hamiltonian.

The Hamiltonian $H_{S_i}(B)$ is given in Eq. (E.9) in Sec. E.2.1, where the the Peierl's phases are given in Eq. (E.10), where x_0 is located in the center of the region S_i. With this choice of gauge, arguments similar to those made in Sec. E.2.2 imply that

$$\|\frac{\partial H_{S_i}(B)}{\partial B}\| \lesssim A_{S_i} J \tag{E.48}$$

where A_{S_i} is the area of the region S_i, and J denotes the typical scale of the (off-diagonal) tunneling coefficients $\{J_{\alpha\beta}\}$. Since $\|\frac{\partial H}{\partial B}\| \leq \sum_i \|\frac{\partial H_{S_i}}{\partial B}\|$, we thus have

$$\|\frac{\partial H_S}{\partial B}\| \lesssim A_S J \tag{E.49}$$

This result holds for any value of B.

We now let $U_S(B)$ be the Floquet operator generated by $H_S(B)$. By direct differentiation of the time-ordered exponential $U_S(B) = \mathcal{T} e^{-i\int_0^T dt H_S(B,t)}$, we find

$$\frac{\partial U_S}{\partial B} = -iU_S(B)X(B). \tag{E.50}$$

Here

$$X(B) \equiv \int_0^T dt U_S^\dagger(B,t) \frac{\partial H_S(B,t)}{\partial B} U_S(B,t), \tag{E.51}$$

and $U_S(B,t) \equiv \mathcal{T} e^{-i\int_0^t dt' H_S(B,t')}$ is the time-evolution operator in the presence of the field B. Using the triangle inequality, together with the fact that $\|V\mathcal{O}\| = \|\mathcal{O}\|$ for any unitary operator V, and making use of Eq. (E.49),we find that $\|X\| \sim A_S J T$. Using this result in the differential equation above, it follows that

$$U_S(B_0) = U_S(0) - iB_0 \frac{\partial U_S}{\partial B} + \mathcal{O}(B_0^2 A_S^2 J^2 T^2). \tag{E.52}$$

To prove Eq. (E.7), we consider the expectation value of $U_S(B_0)$ given the Floquet eigenstate $|\Psi_{a_1\ldots a_k}\rangle$. In the following, we will, as in Subsection E.2.5 use the shorthand notation $\langle\mathcal{O}\rangle \equiv \langle\Psi_{a_1\ldots a_k}|\mathcal{O}|\Psi_{a_1\ldots a_k}\rangle$. We note that the Hamiltonian $H_S(B)$ adequately describes the dynamics of the system when initialized in the state $|\Psi_{a_1\ldots a_k}\rangle$. Thus, up to an exponentially small correction, the time-evolution of $|\Psi_{a_1\ldots a_k}\rangle$ generated by $H_S(B_0)$ should be identical to the time-evolution generated by the Hamiltonian H_1 of the (full) one-flux system. In particular, suppressing the exponentially small correction, $U_S(B_0)|\Psi_{a_1\ldots a_k}\rangle = U_1|\Psi_{a_1\ldots a_k}\rangle$, where U_1 is the Floquet operator of the system in the presence of the uniform magnetic field B_0. Hence,

$$\langle U_S(B_0)\rangle = \langle U_1\rangle, \tag{E.53}$$

At the same time, the time-evolution of $|\Psi_{a_1\ldots a_k}\rangle$ generated by $H_S(0)$ should be identical to the time-evolution generated by the Hamiltonian H of the zero-flux system, and thus (up to an exponentially small correction, which we suppress in the following),

$$\langle U_S(0)\rangle = e^{-iE_{a_1\ldots a_k}T}, \tag{E.54}$$

Finally, the fact that H_R adequately describes the evolution of the state $|\Psi_{a_1\ldots a_k}\rangle$ implies that

$$\left\langle \frac{\partial U_R}{\partial B} \right\rangle = \left\langle \frac{\partial U}{\partial B} \right\rangle, \tag{E.55}$$

where $U(B)$ is the Floquet operator introduced in Subsection E.2.5 that describes the system in the presence of a local uniform field B in the region S. Using Eqs. (E.53)-(E.55), along with Eq. (E.52), we find

$$\langle U_1 \rangle = e^{-iE_{a_1\ldots a_k}T} - iB_0 \left\langle \frac{\partial U}{\partial B} \right\rangle + \mathcal{O}(B_0^2 A_R^2 J^2 T^2),$$

We now recall from Eq. (E.45) in subsection E.2.5 that $\left\langle \frac{\partial U}{\partial B} \right\rangle = -iT \frac{\partial E_{a_1\ldots a_k}}{\partial B} e^{-iE_{a_1\ldots a_k}T}$. Thus

$$\begin{aligned}\langle U_1 \rangle = e^{-iE_{a_1\ldots a_k}T} \left[1 - iB_0 \frac{\partial E_{a_1\ldots a_k}}{\partial B} T\right] \\ + \mathcal{O}(B_0^2 A_R^2 J^2 T^2).\end{aligned} \tag{E.56}$$

In order to link $\frac{\partial E_{a_1\ldots a_k}}{\partial B}$ with the quasienergy difference $\tilde{E}_{a_1\ldots a_k} - E_{a_1\ldots a_k}$, we use the result (E.19) that relates the eigenstates of U_1 and U:

$$|\langle \Psi_{a_1\ldots a_k} | \tilde{\Psi}_{a_1\ldots a_k} \rangle|^2 = 1 + \mathcal{O}(A_S^2 L^{-4+2\eta} \ell^{-2\eta}), \tag{E.57}$$

for some eigenstate $|\tilde{\Psi}_{a_1\ldots a_k}\rangle$ of U_1, and for any value of η greater than $2/3$. Picking $2/3 < \eta < 3/4$, and using that, in this case, $A_S < L^{-2\eta+3/2} \ell^{2\eta+1/2}$ in the thermodynamic limit, we may write

$$|\langle \Psi_{a_1\ldots a_k} | \tilde{\Psi}_{a_1\ldots a_k} \rangle|^2 = 1 + \mathcal{O}(A_S B_0 \sqrt{\ell/L}), \tag{E.58}$$

where we also used that $B_0 = 2\pi/L^2$.

Eq. (E.58) implies that the projection of $|\Psi_{a_1\ldots a_k}\rangle$ into the subspace orthogonal to $|\tilde{\Psi}_{a_1\ldots a_k}\rangle$ must have squared norm of order $A_S B_0 \sqrt{\ell/L}$ or smaller. Using these facts, along with the spectral decomposition of U_1, we find that

$$\langle U_1 \rangle = e^{-i\tilde{E}_{a_1\ldots a_k}T} + \mathcal{O}(A_S B_0 \sqrt{\ell/L}). \tag{E.59}$$

Using that $\tilde{E}_{a_1\ldots a_k} - E_a$ is of order $J A_S B_0$, we thus have

$$\begin{aligned}\langle U_1 \rangle = e^{-iE_{a_1\ldots a_k}T} \left[1 - i(\tilde{E}_{a_1\ldots a_k} - E_{a_1\ldots a_k})T\right] \\ + \mathcal{O}(A_S B_0 \sqrt{\ell/L}),\end{aligned}$$

where we suppressed a correction of order B_0^2 which is subleading in L (recall that $B_0 = 2\pi/L^2$). Comparing with Eq. (E.45), and using that $(\tilde{E}_{a_1\ldots a_k} - E_{a_1\ldots a_k})$ is of order $J B_0 A_S$, we thus we thus find that

$$\tilde{E}_{a_1\ldots a_k} = E_{a_1\ldots a_k} + B_0 \frac{\partial E_{a_1\ldots a_k}}{\partial B} T + \mathcal{O}(A_S B_0 \sqrt{\ell/L}).$$

This was what we wanted to prove.

E.3 Specific model with nonzero ν_2

In this appendix, we give an explicit example of a model, where one of the higher invariants μ_k is nonzero. Specificially, we will demonstrate that the invariant μ_2 takes value 2 for the model we consider.

The model is a modified version of AFI model studied in Sec. **??** (see also Refs. [1,2,6,7]). The model consists of interacting spin-1/2 fermions on a bipartite square lattice of dimensions $L \times L$, and with lattice constant ℓ. The Hamiltonian of the system $H_{\rm dr}(t)$ consists of time-dependent conditional tunneling terms. The driving protocol is divided into four segments, each of duration $T/4$. In the nth segment, the $H_{\rm dr}(t)$ is given by H_n, where

$$H_n = \frac{2\pi}{T} \sum_{\mathbf{r}\in A} \sum_{s=\uparrow,\downarrow} \hat{\Gamma}_{\mathbf{r}} \hat{\Gamma}_{\mathbf{r}+\mathbf{b}_n} (\hat{c}^\dagger_{\mathbf{r}+\mathbf{b}_n,s} \hat{c}_{\mathbf{r},s} + \text{h.c.}) \hat{\Gamma}_{\mathbf{r}} \hat{\Gamma}_{\mathbf{r}+\mathbf{b}_n}. \tag{E.60}$$

Here $\hat{c}_{\mathbf{r},s}$ annihilates a fermion on site $\mathbf{r}$ with spin s, and the vectors $\{\mathbf{b}_n\}$ are given by $\mathbf{b}_1 = -\mathbf{b}_3 = (\ell, 0)$ and $\mathbf{b}_2 = -\mathbf{b}_4 = (0, \ell)$. The $\mathbf{r}$-sum above runs over all sites in sublattice A of the bipartite lattice. Finally, the operator $\hat{\Gamma}_{\mathbf{r}}$ is defined as $\hat{\Gamma}_{\mathbf{r}} \equiv (1 - \rho_{\mathbf{r},\uparrow}\rho_{\mathbf{r},\downarrow})$, where $\rho_{\mathbf{r},s} \equiv \hat{c}^\dagger_{\mathbf{r},s}\hat{c}_{\mathbf{r},s}$. In this way, $\Gamma_{\mathbf{r}}|\Psi\rangle = 0$ for a state $|\Psi\rangle$ where site $\mathbf{r}$ is occupied by two fermions, while $\hat{\Gamma}_{\mathbf{r}}|\Psi\rangle = |\Psi\rangle$, if site $\mathbf{r}$ is occupied by zero, or one fermion. As defined above, H_n turns hopping on bonds between site $\mathbf{r}$ and site $\mathbf{r} + \mathbf{b}_n$ (for each site $\mathbf{r}$ in sublattice A) whenever the two coupled sites $\mathbf{r}$ and $\mathbf{r} + \mathbf{b}_n$ hold only one fermion. The tunneling strength of $2\pi/T$ ensures that a particle located on site $\mathbf{r}$ is perfectly transferred to the site $\mathbf{r} + \mathbf{b}_n$ in the nth segment (and vice versa) in this case. If there are two or more particles on the sites $\mathbf{r}$, $\mathbf{r} + \mathbf{b}_n$, H_n yields zero when acting on the state. In this case, the configuration of particles on these two sites does not change in segment n.

E.3.1 Dynamics of the model

To characterize the topology of the model, we first analyze the dynamics of the model. We begin by discussing the properties of the model in the single-particle subspace, before we move on to the two-particle subspace. We discuss the time-evolution and identify the Floquet eigenstates of the model.

Single-particle subspace

In the single-particle subspace, we may set $\hat{\Gamma}_{\mathbf{r}} = 1$ for all sites $\mathbf{r}$ (since $\rho_{\mathbf{r},\uparrow}\rho_{\mathbf{r},\downarrow}$ gives zero when acting on any single-particle state). In this case, the model is identified the clean limit of the AFAI model studied in Refs. [1, 2, 6], with spinful (rather than spinless) fermions. In this case, each fermion encircles a plaquette during the driving period in the clockwise direction. The Floquet operator of the system in this subspace is given by the identity, and the Floquet eigenstates of the system can be taken to be the states $\{|\psi_{\mathbf{r},s}\rangle\}$, where $|\psi_{\mathbf{r},s}\rangle \equiv \hat{c}^\dagger_{\mathbf{r},s}|0\rangle$.

Two-particle subspace

Next, we consider the dynamics of the system in the two-particle subspace. In this subspace, there are three classes of initial states that result in qualitatively different time evolutions.

In case 1, the two particles are initially located on the same site $\mathbf{r}$. We refer to this state as $|\psi^1_{\mathbf{r}}\rangle$. For this class of initial states, the two particles remain confined on the same site $\mathbf{r}$ during the full driving period, since hopping to and from the site is turned off by the operator $\hat{\Gamma}_{\mathbf{r}}$. Thus, letting $U(t)$ denote the time-evolution operator of the system, $U(t)|\psi^1_{\mathbf{r}}\rangle = |\psi^1_{\mathbf{r}}\rangle$ for all t.

In case 2, the first particle is located on site $\mathbf{r}$ in sublattice A (with spin s_1), and the second particle is located on one of the four sites $\mathbf{r}+\Delta\mathbf{r}_1, \ldots \mathbf{r}+\Delta\mathbf{r}_4$ on sublattice B (with spin s_2). Here $\Delta\mathbf{r}_1 = (\ell, 0)$, $\Delta\mathbf{r}_2 = (2\ell, -\ell)$, $\Delta\mathbf{r}_3 = (\ell, -2\ell)$, and $\Delta\mathbf{r}_4 = (0, -\ell)$. We refer this state as $|\psi^2_{\mathbf{r},n;s_1,s_2}\rangle$. During the time-evolution of $|\psi^2_{\mathbf{r},n;s_1,s_2}\rangle$, the two particles in the system are always located on distinct sites. However, during segment n, the two particles are located at two adjacent sites, between which hopping is turned on. Thus, the two particles do not tunnel in segment n (they still tunnel in all three remaining segments). Using this fact, one can verify that the two fermions have switched places after one driving period, and hence $U(T)|\psi^2_{\mathbf{r},n;s_1,s_2}\rangle = |\psi^2_{\mathbf{r},n;s_2,s_1}\rangle$[10].

Case 3 covers all remaining states. We refer to these states as $|\psi^3_{\mathbf{r}_1,s_1;\mathbf{r}_2,s_2}\rangle$, such that $|\psi^3_{\mathbf{r}_1,s_1;\mathbf{r}_2,s_2}\rangle \equiv \hat{c}^\dagger_{\mathbf{r}_1,s_1} c^\dagger_{\mathbf{r}_2 s_2}|0\rangle$. For this class of initial particle configurations, the particles hop in each of the four segments, and each particle encircles one plaquette in the lattice in clockwise direction. After one driving period, both particles have returned to their initial locations, and one can verify that $U(T)|\psi^3_{\mathbf{r}_1,s_1;\mathbf{r}_2,s_2}\rangle = |\psi^3_{\mathbf{r}_1,s_1;\mathbf{r}_2,s_2}\rangle$.

The three cases above show that the Floquet operator of the two-particle system has two distinct eigenvalues, 1 and -1. The Floquet eigenstates with quasienergy -1 are the "singlet states" $|\psi^{2S}_{\mathbf{r},n}\rangle \equiv \frac{1}{\sqrt{2}}(|\psi^2_{\mathbf{r},n;\uparrow\downarrow}\rangle - |\psi^2_{\mathbf{r},n;\downarrow\uparrow}\rangle)$. All other of the above states (i.e, the states $|\psi^1_{\mathbf{r}}\rangle$, $|\psi^3_{\mathbf{r}_1,s_1;\mathbf{r}_2,s_2}\rangle$ and the spin-triplet combinations $\{|\psi^{2T}_{\mathbf{r},n;i}\rangle\}$ of the states $\{|\psi^2_{\mathbf{r},n;s_1,s_2}\rangle\}$) are Floquet eigenstates with quasienergy zero. Note that all two-particle Floquet eigenstates of the model are localized.

E.3.2 Topological characterization of the model

Having identified the one- and two-particle Floquet eigenstates of the model, we now characterize the topology of the model. We first consider the single-paticle subspace, after which we consider the two-particle subspace.

Single-particle subspace

To find the value of the coefficient μ_1, we consider the response of the single-particle quasienergies to the insertion of a magnetic flux. In the presence of a (locally) uniform magnetic field B, a particle initially located on site $\mathbf{r}$ acquires an Abrahamov-Bohm phase of $-B\ell^2$ during the driving period, as it encircles a plaquette in the clockwise direction. Thus, its quasienergy in the presence of the magnetic field B is given by $-B\ell^2/T$. This holds for all Floquet eigenstates in the system. Next, we note from Eq. (6.13)-(6.14) in the main text that the trace of the magnetization density

[10]The phase factor of 1 arises, since each particle acquires a phase $-i$ during each hop. Each particle hops 3 times, and hence, the total phase acquired is given by $i^6 = -1$. However, the two fermions have furthermore switched places, which means that the state acquires another factor of -1.

in the k-particle subspace $\bar{M}_k \equiv \mathrm{Tr}_k \bar{m}_p$ can be found as

$$\bar{M}_k = \frac{1}{L^2} \sum_{a_1 \ldots a_k} \frac{\partial E_{a_1 \ldots a_k}}{\partial B} \tag{E.61}$$

We now use the above relation to compute $\bar{M}_1$. Noting that $\frac{\partial E_a}{\partial B} = -\ell^2/T$ for each single-particle Floquet eigenstate, and that there are $D \equiv 2L^2/\ell^2$ distinct single-particle Floquet eigenstates in total, we find that $M_1 = -\frac{2}{T}$. As a final step, we recall from the discussion in Sec. 6.3.1 that $M_1 = \mu_1/T$. Thus we conclude that

$$\mu_1 = -2. \tag{E.62}$$

Two-particle states

We now compute the invariant μ_2 from the response of the two-particle quasienergies to the insertion of a local magnetic field B.

The Floquet eigenstates of type 1 do not result in any current in the system, and their quasienergies are unaffected by the magnetic field. For the Floquet eigenstates of type $2S$ and $2T$, one can verify that each of the two particles encircle two plaquettes after two driving periods, in clockwise direction (at this point, the final state is identical to the initial state). Hence these Floquet eigenstates pick up an additional phase $-2\ell^2/T$ after a single driving period. The quasienergies of the type $2S$ Floquet eigenstate in the presence of the field B is thus given by $\pi/T - 2\ell^2/T$, while the quasienergy of the type $2T$ Floquet eigenstate is given by $-2\ell^2/T$. For the type-3 Floquet eigenstates, each particle encircles a plaquette clockwise during the driving period, and hence picks up a phase of $-2\ell^2/T$. We thus conclude that $\frac{\partial E}{\partial B} = -2\ell^2/T$ for all Floquet eigenstates, except for those of type 1. For Floquet eigenstates of type 1, $\frac{\partial E}{\partial B} = 0$.

We use this result in Eq. (E.61) to compute $\bar{M}_2$. Noting that there are $\binom{D}{2}$ distinct two-particle Floquet eigenstates (where $D = 2L^2/\ell^2$ is the number of distinct single-particle states), and that $\frac{\partial E}{\partial B} = \frac{-2\ell^2}{T}$ for all Floquet eigenstates except for those of type 1, we find that

$$\bar{M}_2 = \frac{1}{L^2}\left[\binom{D}{2} - N_1\right]\frac{-2\ell^2}{T}. \tag{E.63}$$

Here N_1 counts the number of distinct Floquet eigenstates of type 1. Since there is one Floquet eigenstate of type 1 per lattice site, we find $N_1 = D/2$. Using this result, along with $\binom{D}{2} = \frac{D(D-1)}{2}$, and $\frac{\ell^2}{L^2} = \frac{2}{D}$, we thus find

$$\bar{M}_2 T = -2(D-2). \tag{E.64}$$

Next, we recall that $\bar{M}_k = \frac{1}{T}\sum_n \binom{D-n}{k-n}\mu_n$. Thus, $\bar{M}_2 T = (D-1)\mu_1 + \mu_2$. Since $\mu_1 = -2$, we hence identify

$$\mu_2 = 2. \tag{E.65}$$

E.3.3 Robustness of the invariants

The discussion here showed that the model in Eq. (E.60) is characterized by a nonzero, quantized value of the "higher" invariant μ_2. Although the quantization of μ_2 appears to be the result

of fine-tuning to a special point, where the Hamiltonian generates perfect "pi-pulses" in each segment, we stress that it is topologically robust: the discussion in the main text shows that the invariant μ_2 is invariant under perturbations that preserve localization within the one- and two-particle subspaces.

For instance, one can tune the model slightly away from this special point described above, by adding a constant on-site disorder potential H_{dis}, given by

$$H_{\text{dis}} = \sum_{\mathbf{r}} \sum_{s=\uparrow,\downarrow} w_{\mathbf{r},\mathbf{s}} \hat{\rho}_{\mathbf{r},s}, \tag{E.66}$$

where the numbers $w_{\mathbf{r},\mathbf{s}}$ are randomly drawn from the interval $[-W, W]$. For disorder strengths W smaller than some critical value, we expect the model to remain localized within the one- and two-particle subspaces. Thus, as the disorder strength in the model is increased gradually from 0 to W, the value of the invariant μ_2 cannot change, and hence the time evolution generated by $H(t) \equiv H_{\text{dr}}(t) + H_{\text{dis}}$ is characterized by a quantized, nonzero value of the invariant μ_2 (specifically $\mu_2 = 2$).

Appendix F

Appendix for Chapter 7

F.1 Dimensional reduction and quantized response

Let us begin by showing that the dimensional reduction of magnetization gives quantization of the work polarization. In Ref. [6], it is shown that the time-averaged magnetization density $\langle M \rangle = \sum_{n=1}^{N} \langle M \rangle_n$ of the anomalous Floquet Anderson insulator after summing over localized single particle Floquet eigenstates $|\psi_n\rangle$ is quantized as

$$\langle M \rangle = \frac{N}{T}\nu,$$

where $N = L^2$ is the number of unit cells for an $L \times L$ system with N_{orb} orbitals/sublattices and both the particle charge q and lattice constant a are set to 1. This may be rewritten as average quantization of $\langle M \rangle_n$:

$$\begin{aligned} \overline{\langle M \rangle_n} \equiv \frac{\langle M \rangle}{N} = \frac{\nu}{T} &= \frac{1}{N}\sum_n \left(\frac{1}{2T}\int_0^T dt \langle \psi_n | \mathbf{r} \times \partial_t \mathbf{r} | \psi_n \rangle \right) \\ &= \frac{1}{N}\sum_n \left(\frac{1}{2T}\int_0^T dt \langle \psi_n | \left[\hat{x}\partial_t \hat{y} - \hat{y}\partial_t \hat{x} \right] | \psi_n \rangle \right). \end{aligned}$$

Noting that the velocity operator is $\partial_t \hat{y} = (L/2\pi\hbar)\int dk_y (\partial \hat{H}/\partial k_y)$ and utilizing antisymmetry of the integrand with respect to k_x and k_y, we see that

$$\frac{\nu}{T} = \frac{1}{2\pi\hbar L}\left[\int dk_y \sum_n \left(\frac{1}{T}\int_0^T dt \langle \psi_n | \hat{x}\partial_{k_y} H | \psi_n \rangle \right) \right]. \tag{F.1}$$

Upon dimensional reduction, $k_y \to \lambda$, the expression in square brackets is none other than the sum of the work polarization P_W^n over $N_{\text{orb}}L$ single particle eigenstates of the one-dimensional problem. Thus the average work polarization per unit cell,

$$\overline{P}_W = \frac{1}{L}P_W^n = \nu\hbar\Omega \tag{F.2}$$

is quantized as promised.

Let us now elaborate on how Eq. F.2 yields quantized responses near the edge of a filled region as discussed in the main text. Let us begin by considering the many-body Floquet eigenstate $|\Psi(\lambda)\rangle$ obtained by filling all Floquet eigenstates $\{|\psi_n(\lambda)\rangle\}$ that are located in a finite region S of the chain, of length ℓ, as indicated in Fig. 1 from the main text. For a site x_0 outside the filled region, the force density ρ^F_x is trivially zero for all values of λ and t, and hence the system can't absorb any energy here. For a site x_0 in the bulk of the filled region, ρ^F_x also vanishes when averaged over λ and t:

$$\bar{\rho}^F_x \equiv \frac{1}{2\pi T}\int_0^T dt \int_0^{2\pi} d\lambda \langle \Psi(\lambda,t)\ |\frac{\partial \rho^E_x(\lambda,t)}{\partial \lambda}|\Psi(\lambda,t)\rangle = 0. \tag{F.3}$$

To see how the above result follows, we insert the explicit form for ρ^E_x in second quantized notation,

$$\rho^E_x(\lambda,t) = \frac{1}{2}\sum_{x',\alpha,\alpha'} (H_{\alpha',x';\alpha,x}(\lambda,t)c^\dagger_{\alpha',x'}c_{\alpha,x} + H_{\alpha,x;\alpha',x'}(\lambda,t)c^\dagger_{\alpha,x}c_{\alpha',x'}), \tag{F.4}$$

where $H_{\alpha',x';\alpha,x}$ is the single particle matrix element. Noting that that for sites a, b in the bulk $\langle\Psi(\lambda,t)|c^\dagger_{\alpha,a}c_{\beta,b}|\Psi(\lambda,t)\rangle = \delta_{ab}\delta_{\alpha,\beta}$ for all values of t and λ, we find

$$\bar{\rho}^F_{x_0} = \int_0^{2\pi} d\lambda \sum_\alpha \frac{\partial H_{\alpha,x_0;\alpha,x_0}(\lambda,t)}{\partial\lambda} = 0, \tag{F.5}$$

where the last equality follows from $H(\lambda=0,t) = H(\lambda=2\pi,t)$. Finally, if the localization length is much less than the filled region size, $\xi \ll \ell$, we may treat all the energy pumping as occurring directly at the density edge and the result from the main text follows.

While the above arguments from dimensional reduction hold perfectly in the case where states are fully localized and may be adiabatically tracked upon varying λ, it is important to note that this is indeed not the case for the models we consider except at the fine-tuned point $W = \alpha = 0$. We have indeed seen this in the numerical results for finite disorder, as the lack of a well-defined adiabatic limit gives rise to a smooth crossover from topological to non-topological, rather than a sharp transition as in the two-dimensional case. Healing the above arguments when this limit is not satisfied is a subtle issue which we will address in a follow up work to appear shortly [173]. In particular, we will show that a more careful derivation of the quantized work polarization (or indeed the magnetization in the absence of localization) gives rise to non-topological terms as well as the topological contribution. We will argue that non-topological contributions are suppressed exponentially as $e^{-L/\xi}$ in the presence of arbitrarily weak localization, while the topological contribution is only slowly destroyed in a system-size-independent manner as disorder strength is increased.

F.2 Quantized response of fine-tuned model

Let us quickly see analytically that we achieve work quantization for the fine-tuned model with $J = J_{\text{tuned}}$. This model has the nice property that for $t = nT/5$, the Floquet eigenstates are simply localized on each site. The force density is clear zero except during periods 2 and 4, as $h_{1,3,5}$ are independent of λ. Consider the bulk state indicated by the black arrow in Fig. 2a

from the main text, starting on the A sublattice of site x. During step 2, let us write the 2-site Hamiltonian connecting $|x, B\rangle$ to $|x+1, A\rangle$: $H_2 \to -J(\sigma^x \cos\lambda + \sigma^y \sin\lambda)$. Time evolving this effective spin-1/2 starting from the state $|\uparrow\rangle$, we see that $\langle \partial_\lambda H\rangle = -J \sin[\pi(t - T/5)/(T/5)]$, which averages to $2J/\pi$ over the period $T/5 < t < 2T/5$. This force is evenly split between sites x and $x+1$. During step 4, it has average force is similarly $-2J/\pi$, entirely on site x. Summing these up, along with zero responses during the other three steps, and integrating over λ, we see that the work polarization is

$$P_W \equiv \int d\lambda P_F = \left(\frac{1}{5}\right)(2\pi)\left(\frac{2J}{\pi}\right)[(x+1/2) - x] = \frac{\hbar\Omega}{2}. \tag{F.6}$$

One may readily check that starting at site $|x, B\rangle$ gives the same result, such that the work polarization for a filled unit cell is the quantized value $\hbar\Omega$, as promised.

F.3 Additional numerics

In this section, we numerically address two potential sources of concern. First, the data in Figure 3 of the main text seem to give anomalous behavior at low values of disorder. For instance, at the smallest value of $W = 0.1$, the pumped energy seems to first decrease as a function of α before increasing and then decreasing again. We will show data to confirm that some of this non-monotonicity is the result of finite size effects due to the fact that the phase diagram is taken at fixed $L = 100$ and $N_c = N_\lambda$. Second, in the main text we only show data for the system with the left half filled. Here we provide additional support for our argument of quantization of P_W independent of filling by consider three other initial conditions.

In order to understand what is happening in the low disorder regime, we first note that analytically one may show that the band structure undergoes a simple topological transition at $\alpha = 1/2$ from $\nu = 1$ for $0 < \alpha < 1/2$ to $\nu = 0$ for $1/2 < \alpha < 1$. It is natural, therefore, to expect that in the limit of weak but finite disorder, this transition should become asymptotically exact. However, in the same weak disorder limit, the correlation length and associated time scales become very large. Therefore, data for finite values of L, N_c, and N_λ is not as readily converged as elsewhere in the phase diagram.

However, while time consuming, convergence may indeed be observed numerically. We begin by considering two small values of disorder strength: $W = 0.05$ and $W = 0.1$. Note that $W = 0.1$ is the lowest value show in Figure 3a of the main text. We next calculate Floquet eigenstates and determine their inverse participation ratios, ξ, which in turn are averaged over states, λ, and disorder realizations. This averaged ξ is then a useful proxy for the localization length. We then take $L \gg \xi$ to ensure no effect of finite localization length is observed. In practice, $L = 1200$ is found to be sufficient. Next we solve the dynamics for many disorders realization and different values of N_c and N_λ. The effect of N_λ is particularly straightforward, as it amounts to suppressing and order one transient by averaging. Therefore, we find that for fixed N_c, the data is very well fit by a functional form $a + b/N_\lambda$ for $N_\lambda > 100$. We use this to extrapolate to the $N_\lambda = \infty$ limit and, finally, numerically confirm independence with N_c from 50 to 150.

The data shown in Fig. F.1a has been converged according to this procedure. It is clearly seen that the decreased of E_{abs} near $\alpha = 0.4$ is suppressed, and thus was due to finite size

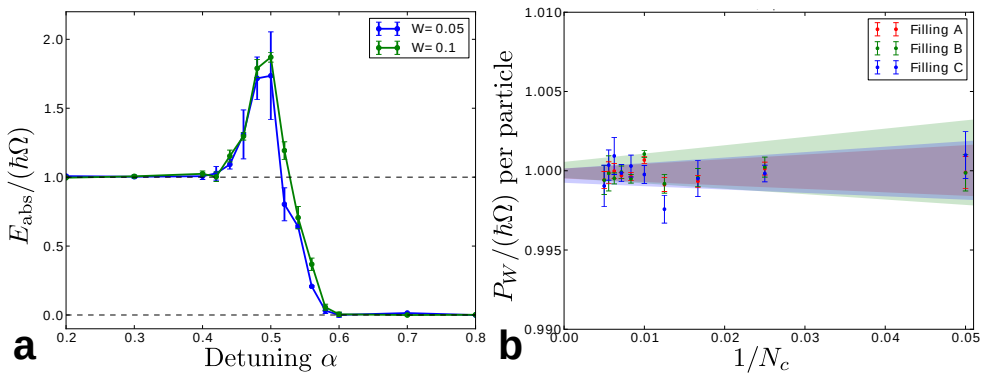

Figure F.1: Additional numerical support. (a) Energy absorbed for the same initial conditions as in the main text after extrapolating L, N_c, and N_λ to infinity. We expect the data to approach a sharp transition at $\alpha = 1/2$ in the $W \to 0^+$ limit but are unable to rule out other interesting phenomena near this point for these finite values of W. (b) Work polarization extrapolated to the same $L, N_c, N_\lambda \to \infty$ limit for a fixed $W = 1$, $\alpha = 0.2$ for which good quantization is expected. The results are well quantized independent of initial condition.

effects. However, there remains non-monotonic behavior near $\alpha = 0.5$, which is the location of the topological phase transition in the absence of disorder. In general, there is expected to be a singularity near this point. Based on the above arguments, we expect the singularity to become sharper and eventually resolve to a direct topological transition in the limit $W \to 0^+$. Our data suggests that the transitions is perhaps sharpening slightly as W is decreased, but does not rule out the possibility of a new topological phase or other non-trivial phenomenon in the vicinity of $\alpha = 1/2$ at finite disorder strength.

Our second goal is to demonstrate the initial condition independence of our results. In the main text, we work with an initial condition in which the left half of the system is filled, allowing us to convert a quantized work polarization into quantized energy absorption. Here, as we consider more generic initial conditions, we instead directly measure work polarization P_W and extrapolate to $N_\lambda \to \infty$ using the same procedure as above. In particular, we consider to point $W = 1$, $\alpha = 0.2$, which yielded a well-quantized value of E_{abs}. We then consider the following initial conditions:

(A) Every site from $L/4$ to $3L/4$ half-filled

(B) Every site from $L/4$ to $3L/4$ half-filled with an added "charge density wave": $A\cos(2\pi(x - L/4)/(L/2))$

(C) A single random filling of sites $L/4$ to $3L/4$

These initial condition are simulated and disorder averaged. We find stronger effects of N_c compared to the case of E_{abs}, so they have also been extrapolated in $1/N_c$ to the adiabatic limit. The results, found in Fig. F.1, are quantized to better than one part in a thousand, confirming the independence of our results on initial conditions.

F.4 Winding number of micromotion versus extended time evolution

In earlier work [1], the winding number for a given branch cut ϵ_{cut} is defined as that of the following unitary:

$$\tilde{U}(t) = \begin{cases} U(t), & 0 < t < T \\ e^{iH_F(t-T)}U(T), & T < t < 2T \end{cases}$$

where H_F is chosen such that its eigenvalues range from ϵ_{cut} to $\epsilon_{\text{cut}} + \hbar\Omega$. We can relate this to the micromotion invariant defined in the main text via a band-flattening procedure. First, note that $U(t) = P(t)e^{-iH_F t}$. Define the family of unitaries $U(t,s) \equiv P(t)e^{-isH_F t}$, such that

$$\tilde{U}(s,t) = \begin{cases} U(s,t), & 0 < t < T \\ e^{isH_F(t-T)}U(s,T), & T < t < 2T. \end{cases}$$

At $s = 1$, we recover the original result of Rudner et al. At $s = 0$, we have band-flattened H_F, such that

$$\tilde{U}(0,t) = \begin{cases} P(t), & 0 < t < T \\ \mathbb{1}, & T < t < 2T. \end{cases}$$

Hence $\nu\left[\tilde{U}(s=0)\right] = \nu[P]$. But s clearly implements a smooth transformation on the family of unitaries, and thus can't change the winding number. So we conclude that $\nu\left[\tilde{U}\right] = \nu[P]$.

Appendix G

Appendix for Chapter 8

G.1 Derivation of Eq. (8.27)

Here we derive Eq. (G.1), showing that when $\alpha \ll 1$, $\mathbf{L}_{\text{slow}}$ is given by $\lambda_0 \mathbf{S}_0$, where λ_0 was a constant of motion. Here $\mathbf{S}_0$ was defined in Eq. (G.7). Our starting point is the equations of motion (8.26),(8.25) for the slow and fast components of $\mathbf{L}$. In the main trext, we concluded from these equations that the magnitude of $\mathbf{L}_{\text{slow}}$ and $\mathbf{L}_{\text{fast}}$ were constants of motion λ_0, λ_1. We note here that the equations imply that their dot product $\mathbf{L}_{\text{slow}} \cdot \mathbf{L}_{\text{fast}}$ is also a constant of motion. Since $\mathbf{L}_{\text{slow}}$ and $\mathbf{L}_{\text{fast}}$ oscillate at different time scales, their dot product can only be a constant of motion if takes value zero – i.e., if $\mathbf{L}_{\text{fast}}$ precesses in the plane perpendicular to $\mathbf{L}_{\text{slow}}$.

Having established the existence of these constants of motion, we consider the equation of motion (8.26) for $\mathbf{L}_{\text{slow}}$. We first decompose $\mathbf{L}_{\text{slow}}$ in its components parallel and perpendicular to $\hat{n}$:

$$\mathbf{L}_{\text{slow}} = \ell \hat{n} + \Delta \mathbf{L}, \tag{G.1}$$

where $\Delta \mathbf{L}$ is orthogonal to $\hat{n}$, and the scalar ℓ may depend on time. Inserting this decomposition into the equation of motion for $\mathbf{L}_{\text{slow}}$, we have

$$\ell \dot{\hat{n}} + \dot{\ell} \hat{n} + \Delta \dot{\mathbf{L}} = \eta h \hat{n} \times \Delta \mathbf{L}. \tag{G.2}$$

Next, we take the cross-product with $\hat{n}$ from the left and use $\hat{n} \times \hat{n} = 0$, and $\hat{n} \times (\hat{n} \times \mathbf{v}) = -\mathbf{v}$ to isolate $\Delta \mathbf{L}$:

$$\Delta \mathbf{L} = -\frac{\ell}{\eta h} \hat{n} \times \dot{\hat{n}} - \frac{1}{\eta h} \hat{n} \times \Delta \dot{\mathbf{L}}. \tag{G.3}$$

We now note, that, in the equation of motion (8.26) for $\mathbf{L}_{\text{slow}}$, the right hand side has magnitude $\eta h |\Delta \mathbf{L}|$, while the magnitude of the left hand side is, from the definition of $\mathbf{L}_{\text{slow}}$, at most of order $\lambda_0 \Omega_0$. This implies that $\Delta \mathbf{L}$ must be of order $\Omega_0 \lambda_0 / \eta h = \alpha \lambda_0$, which in turn implies $\Delta \dot{\mathbf{L}} \sim \mathcal{O}(\alpha \Omega \lambda_0)$. This allows us to write

$$\Delta \mathbf{L} = -\frac{\ell}{\eta h} \hat{n} \times \dot{\hat{n}} + \mathcal{O}(\alpha^2 \lambda_0). \tag{G.4}$$

We see from the above that $\Delta \mathbf{L} \sim \mathcal{O}(\alpha \lambda_0)$, and hence the correction on the right hand side is subleading in α.

To find ℓ, we note that, since $\hat{n}$ and $\Delta\mathbf{L}$ are orthogonal, $\mathbf{L}_{\text{slow}}^2 = \ell^2 + \Delta\mathbf{L}^2$, and $\Delta\mathbf{L} \sim \mathcal{O}(\alpha\lambda_0)$. Using $\mathbf{L}_{\text{slow}}^2 = \lambda_0^2$, this implies

$$\ell = \lambda_0 + \mathcal{O}(\alpha^2\lambda_0). \tag{G.5}$$

Using this expression for ℓ along with the expression (G.4) for $\Delta\mathbf{L}$ in Eq. (G.1), we find

$$\mathbf{L}_{\text{slow}} = \lambda_0\mathbf{S}_0 + \mathcal{O}(\alpha^2\lambda_0), \tag{G.6}$$

where λ_0 was a constant of motion, and

$$\mathbf{S}_0 = \hat{n} - \frac{1}{\eta h}\hat{n} \times \dot{\hat{n}} \tag{G.7}$$

The values of the constants of motion can be found using $\mathbf{L} = \mathbf{L}_{\text{slow}} + \mathbf{L}_{\text{fast}}$, and that $\mathbf{L}_{\text{fast}} \cdot \mathbf{L}_{\text{slow}} = 0$, which implies that $\mathbf{L} \cdot \mathbf{L}_{\text{slow}} = \lambda_0^2$. Using the expression (G.6) for $\mathbf{L}_{\text{slow}}$ in this identity, we then find

$$\mathbf{S}_0 \cdot \mathbf{L} = \lambda_0 + \mathcal{O}(\alpha^2 L). \tag{G.8}$$

Thus, up to a small correction of order $\alpha^2 L$, λ_0 can be found from the initial value of $\mathbf{S}_0 \cdot \mathbf{L}$. We can use this result to find the constant of motion λ_1. Using that $\mathbf{L}_{\text{slow}} \cdot \mathbf{L}_{\text{fast}} = 0$, $L^2 = \lambda_1^2 + \lambda_0^2$. Inserting this in the above, we find that $|\mathbf{L}_\perp| = \lambda_1 + \mathcal{O}(\alpha^2 L)$, where $\mathbf{L}_\perp$ is the component of $\mathbf{L}$ perpendicular to $\mathbf{S}_0$.

The above discussion shows that $\mathbf{S}_0 \cdot \mathbf{L}$ and $|\mathbf{L}_\perp|$ are constants of motion, up to small fluctuations of magnitude $\alpha^2 L$. This implies that $\mathbf{L}$ precesses around $\mathbf{S}_0$, at the speed $\sim \eta h$, and with a fixed radius of precession given by λ_1.

G.2 Alignment of L with $\mathbf{S}_0$

Here we derive the result in Sec. 8.4.3, showing that the angular moment $\mathbf{L}$ aligns itself with $\mathbf{S}_0$ when it is subject to dissipation, provided that the dissipation strength γ satisfies the condition $\alpha^2 \ll \gamma \ll 1$. Our starting point is the equation of motion in Eq. (8.29), in the case where $\mathbf{v}_{\text{dis}}(\mathbf{L}, \dot{\mathbf{L}}) = -\frac{\gamma}{L}\dot{\mathbf{L}}$:

$$\dot{\mathbf{L}} = -\eta\mathbf{h}(t) \times \mathbf{L} - \frac{\gamma}{L}\dot{\mathbf{L}} \times \mathbf{L}. \tag{G.9}$$

In order to show that $\mathbf{L}$ aligns itself with $\mathbf{S}_0$, we apply a rotating frame transformation $R(t)$ in the above equation that keeps the instanteneous field $\mathbf{h}(t)$ pointing along the z axis: $R(t)\hat{n} = \hat{\mathbf{z}}$. Since $R(t)$ is a time-dependent orthogonal matrix, it obeys a differential equation of the form

$$\dot{R}(t)\mathbf{v} = R(t)(\omega(t) \times \mathbf{v}) \tag{G.10}$$

for some time-dependent (angular velocity) vector $\omega(t)$. The angular velocity vector $\omega(t)$ uniquely defines $R(t)$ together with an initial condition for $R(t)$. In our case, $R(t)$ must satisfy $\frac{d}{dt}(R(t)\hat{n}(t)) = 0$. Using Eq. (G.10), we find that ω must satisfy $\omega \times \hat{n} = -\dot{\hat{n}}$. Taking the cross product from the left with $\hat{n}$, and using $(\hat{n} \times \mathbf{v}) \times \hat{n} = \mathbf{v}$, we find that $\omega = \dot{\hat{n}} \times \hat{n}$. Along with an initial condition for $R(t)$ which turns out to be unimportant in the followng, $R(t)$ is uniquely defined from the differential equation (G.10) with $\omega = \dot{\hat{n}} \times \hat{n}$.

Having found the rotating frame transformation R that aligns $\hat{n}(t)$ with the z-axis, we now consider the equations of motion of the angular moment $\mathbf{M} \equiv R\mathbf{L}$ in this rotating frame. Using $\dot{\mathbf{M}} = R\dot{\mathbf{L}} + \dot{R}\mathbf{L}$ along with Eq. (8.29), we find

$$\dot{\mathbf{M}} = R\left[\left(\eta\mathbf{h} - \frac{\gamma}{L}\dot{\mathbf{L}}\right) \times \mathbf{L}\right] + \dot{R}\mathbf{L}. \tag{G.11}$$

As our next step, we use that $R(\mathbf{a} \times \mathbf{b}) = (R\mathbf{a} \times R\mathbf{b})$, along with Eq. (G.10), obtaining

$$\dot{\mathbf{M}} = R\left(\eta\mathbf{h} - \omega - \frac{\gamma}{L}\dot{\mathbf{L}}\right) \times R\mathbf{L}. \tag{G.12}$$

We note that $\eta\mathbf{h} - \omega = \eta h\mathbf{S}_0$, where $\mathbf{S}_0$ was defined in Eq. (G.7) above. Multiplying R into the first parenthesis, and using $R\dot{\mathbf{L}} = \dot{\mathbf{M}} - \dot{R}\mathbf{L}$, we find

$$\dot{\mathbf{M}} = \left(\eta h\hat{\mathbf{z}} - R\omega - \frac{\gamma}{L}(\dot{\mathbf{M}} - \dot{R}\mathbf{L})\right) \times \mathbf{M}. \tag{G.13}$$

Next,we use $\dot{R}\mathbf{L} = R(\omega \times \mathbf{L}) = R\omega \times \mathbf{M}$, to find

$$\dot{\mathbf{M}} = \left(\mathbf{J}(\mathbf{M}) - \frac{\gamma}{L}\dot{\mathbf{M}}\right) \times \mathbf{M}, \tag{G.14}$$

where

$$\mathbf{J}(\mathbf{M}) = \eta h\hat{\mathbf{z}} - R\omega + \frac{\gamma}{L}(R\omega \times \mathbf{M}). \tag{G.15}$$

We now consider the dynamics that result from the above equation of motion for $\mathbf{M}$. If h and ω were stationary, $\mathbf{M}$ would relax to a stationary point of the equations of motion with the relaxation rate $\Gamma_{\mathbf{L}} \sim \gamma|\mathbf{J}| \approx \gamma\eta h$. The stationary point is found at $\mathbf{J}(\mathbf{M}_0) \times \mathbf{M}_0 = 0$, which implies that $\mathbf{M}_0$ must be parallel to $\mathbf{J}(\mathbf{M}_0)$. Using $|\mathbf{M}| = L$ we find that $\mathbf{J}(\mathbf{M}) = \eta h\hat{\mathbf{z}} - R\omega + \mathcal{O}(\gamma\Omega_0)$, which implies that the stationary point lies at

$$\mathbf{M}_0 = \hat{\mathbf{z}}L - \frac{L}{\eta h}R\omega + \mathcal{O}(\gamma\alpha L) \tag{G.16}$$

Since the second term above is of order αL, we may ignore the third term if $\gamma \ll 1$, and in this case find that $\mathbf{J}$ will relax to

$$\mathbf{M}_0 = \hat{\mathbf{z}}L - \frac{L}{\eta h}R\omega. \tag{G.17}$$

Since $R^T\hat{\mathbf{z}} = \hat{n}$, we identify $\mathbf{M}_0$ as $LR\mathbf{S}_0$. Reverting the rotating frame transformation, we thus find that relaxation of $\mathbf{M}$ to $\mathbf{M}_0$ implies that $\mathbf{L}$ relaxes to $L\mathbf{S}_0$.

Above, we found that $\mathbf{M}$ relaxes to $\mathbf{M}_0$ if ω and h were stationary (assuming $\gamma \ll 1$). In the system we study, however, ω and h change in time, although slowly, which implies that the stationary point $\mathbf{M}_0$ moves on the unit sphere. If the angular velocity $\omega_{\mathbf{M}_0}$ of $\mathbf{M}_0$ is much smaller than the relaxation rate $\Gamma_{\mathbf{L}}$, $\mathbf{M}(t)$ will remain relaxed and point along $\mathbf{M}_0(t)$ at all times. To find the angular velocity at which $\mathbf{M}_0$ changes in time, we note that $R\omega \sim \mathcal{O}(\Omega_0)$, and furthermore oscillates on the same frequency scale Ω_0. Hence the second term in the above equation is at most of order αL, and oscillates on frequency scale Ω_0. On the other hand, the first term is fixed along

the z-axis, and has magnitude L. Hence $\mathbf{M}_0$ itself changes with angular velocity $\omega_{\mathbf{M}_0} \sim \mathcal{O}(\Omega_0\alpha)$. Recalling that $\Gamma_{\mathbf{L}} \sim \gamma\eta h$, the requirement $\Gamma_{\mathbf{L}} \gg \omega_{\mathbf{M}_0}$ is thus met if $\gamma \gg \alpha^2$.

Reverting the rotating frame transformation, the above discussion shows that $\mathbf{L}(t)$ will always remain aligned with $L\mathbf{S}_0(t)$ if

$$\alpha^2 \ll \gamma \ll 1, \tag{G.18}$$

which was what we wanted to show.

G.3 Correction to Eq. (8.35)

Here we show that the correcting term $\Delta\dot{E}$ in Eq. (8.35) goes to zero as $\frac{\lambda_0\omega}{\tau}$ when averaged over a time-window of width τ.

To show this, we insert $\dot{\hat{\mathbf{n}}} = (\partial_t + \dot{\phi}\partial_\phi + \dot{A}\partial_A)\hat{\mathbf{n}}$ in the expression Eq. (8.34) for $\dot{E}$, obtaining

$$\dot{E} = -\eta\omega\lambda_0\partial_\phi h + \omega\lambda_0\,\hat{\mathbf{n}}\cdot([\partial_t + \dot{A}\partial_A]\hat{\mathbf{n}}\times\partial_\phi\hat{\mathbf{n}}). \tag{G.19}$$

Comparing with Eq. (8.35), the correction $\Delta\dot{E}$ is thus given by

$$\Delta\dot{E} = \omega\lambda_0\dot{A}\,\hat{\mathbf{n}}\cdot(\partial_A\hat{\mathbf{n}}\times\partial_\phi\hat{\mathbf{n}}). \tag{G.20}$$

Noting that A changes insignificantly on the time scales of the two modes, the arguments made in the paragraph below Eq. (8.35) imply that

$$\Delta\dot{E} = \frac{\omega\lambda_0\dot{A}}{2\pi T}\int_0^T dt\int_0^{2\pi} d\phi\,\hat{\mathbf{n}}\cdot(\partial_A\hat{\mathbf{n}}\times\partial_\phi\hat{\mathbf{n}}). \tag{G.21}$$

We can find the time-averaged value of $\Delta\dot{E}$ over a time-window of width τ as $\Delta E(\tau)/\tau$, where $\Delta E(\tau)$ is the integral of $\Delta\dot{E}$ over the time-interval from 0 to τ. This can be computed as

$$\Delta E(\tau) = \frac{\omega\lambda_0}{2\pi T}\int_0^T dt\int_{A(0)}^{A(\tau)} dA\int_0^{2\pi} d\phi\,\hat{\mathbf{n}}\cdot(\partial_A\hat{\mathbf{n}}\times\partial_\phi\hat{\mathbf{n}}).$$

For fixed t, we recognize the A,ϕ-integral as the solid angle on the unit sphere covered by the image of the two-dimensional manifold $\mathcal{M} = \{(A,\phi)|A\in[A(0),A(\tau)],\phi\in[0,2\pi]\}$ with respect to the mapping $\hat{\mathbf{n}}(A,\phi,t)$. From the definition of $\mathbf{h}(A,\phi,t)$ in Eq. (8.6), we see that, for any fixed value of t, the mapping $\hat{\mathbf{n}}(A,\phi,t)$ at most covers a given point on the unit sphere once for ϕ in the interval $[0,2\pi]$. Hence the solid angle covered by the image $\hat{\mathbf{n}}(\mathcal{M})$ must be smaller than the area 4π of the unit sphere. Thus, for any value of t, the A,ϕ integral above is bounded by 4π. This implies that

$$|\Delta E(\tau)| \le 2\omega\lambda_0. \tag{G.22}$$

The time-averaged value of $\Delta\dot{E}$ hence goes to zero as $2\omega\lambda_0/\tau$ with the averaging time τ.

G.4 Multiple modes

To find the equations of motion, we reexpres the Hamiltonian in terms of conjugate pair of variables Z and Z^*, with $Z = e^{\pm i\phi}$, where the sign depends on the chirality of the mode. Their possion bracket is $\{Z, Z^*\} = \frac{1}{L_0}$. To find the equation of motion for Z_n, we apply the chain rule: $\frac{dZ_n}{dt} = \frac{\partial Z_n}{\partial \phi_n}\frac{d\phi_n}{dt} + \frac{\partial Z_n}{\partial A_n^2}\frac{dA_n^2}{dt}$. Using the fact that for any function f of the dynamical variables $\{x_i\}$, $\sum_i \frac{\partial f}{\partial x_i}\{x_i, H\} = \{f, H\}$, we obtain

$$\dot{Z}_n = \{Z_n, H\} - \gamma_n A_n^2 \frac{\partial Z_n}{\partial A_n^2} \tag{G.23}$$

From the definition of Z we have $\frac{\partial Z}{\partial A} = \frac{1}{A}Z$, and using that only H_n has a nonzero Poisson bracket with Z_n, we find

$$\dot{Z}_n = \{Z_n, H_n\} - \frac{\gamma_n}{2} Z_n. \tag{G.24}$$

In terms of the variables Z, Z^*, the Hamiltonian is given by

$$H_n = \omega_n L_0 |Z_n|^2 + \frac{\eta_n}{2}(Z_n \Phi + Z_n^* \Phi^*) \tag{G.25}$$

where $\Phi = (L_y + iL_z)$, and $\omega_n \equiv |n|\omega$. Cf. the discussion in the main text, we assume that the other modes than $n = 1$ do not affect the motion of the spin in any significant way, and we thus treat Φ as an external drive $\Phi(t) \equiv L_x(t) + iL_z(t)$. Neglecting the subscripts on Z_n, the equation of motion for Z is

$$\dot{Z} = \left(-i\omega_n - \frac{\gamma_n}{2}\right) Z + \frac{\eta_n}{2L_0}\Phi(t). \tag{G.26}$$

To obtain an estimate for the typical amplitude of mode n, we compute the average value $\overline{|Z^2|}$ of its squared amplitude $A^2 = |Z|^2$. By taking the square root of this, we find the rms amplitude in mode n, and by multiplying $\overline{|Z^2|}$ with $\omega_n L_0$, we find the average energy stored in mode n.

To ease this computation, we consider the time-derivative of the field energy $E = \omega_n L_0 |Z|^2$. Using $\frac{d|Z^2|}{dt} = \dot{Z}Z^* + Z\dot{Z}^*$, We find

$$\frac{dE}{dt} = -\gamma\omega_n L_0 |Z|^2 + \frac{\eta_n \omega_n}{2}(\Phi Z^* + \Phi^* Z). \tag{G.27}$$

We identify the first term as the energy loss due to dissipation, and the second term as the energy transferred to the mode from the drive. Taking the long-time average, and using the fact that the energy in the mode remains bounded [1], $\overline{\frac{dE}{dt}} = 0$. Using this in the above, we find after a few steps,

$$\overline{|Z^2|} = \frac{\eta_n}{\gamma_n L_0} \mathrm{Re}\,(\overline{\Phi^* Z}). \tag{G.28}$$

[1] To see this, note that the energy pumped in from the field is bounded by $\eta\omega AL$, while the energy lost to dissipation is of order $A^2\omega\gamma L_0$. For sufficiently large values, the energy can thus only decrease, and it hence remains bounded.

Now, using the fourier transforms of $Z(t)$, and likewise with Φ, we obtain [2]

$$\overline{\Phi^* Z} = \int d\omega \Phi^*(-\omega) Z(\omega) = \int d\omega \Phi(\omega)^* Z(\omega) \tag{G.29}$$

The fourier transform $Z(\omega)$ has units $\frac{1}{\sqrt{\omega}}$, and can be found by fourier transforming the equation of motion for $Z(\omega)$:

$$-i\omega Z(\omega) = \left(-i\omega_n - \frac{\gamma_n}{2}\right) Z(\omega) + \frac{\eta_n}{2L_0}\Phi(\omega) \tag{G.30}$$

Thus,

$$Z(\omega) = \frac{\eta_n}{2L_0} \frac{\Phi(\omega)}{-i(\omega - \omega_n - i\gamma_n/2)}, \tag{G.31}$$

and

$$\overline{|Z^2|} = \mathrm{Re}\left[\frac{-i\eta_n^2}{2\gamma_n L_0^2} \int d\omega \frac{|\Phi(\omega)|^2}{\omega - \omega_n - i\gamma_n/2})\right]. \tag{G.32}$$

Taking the imaginary part,

$$\overline{|Z^2|} = \frac{\eta_n^2}{2L_0^2} \int d\omega \frac{|\Phi(\omega)|^2}{(\omega - \omega_n)^2 + (\gamma_n/2)^2} \tag{G.33}$$

Numerical studies show that $|\Phi^2(\omega)|$ contains a few sharp peaks, at integer multiples of ω and Ω, and combinations of these:

$$|\Phi^2(\omega)| \approx \sum_k L^2 \delta(\omega - q_{kl}) \Phi_{kl}^2 \tag{G.34}$$

where $q_{kl} = k\omega + l\Omega$, and the coefficients have dimension L, and decrease with higher k and l. If there is a phase-shift mirror, the frequencies will not coincide with ω_n, except for high-order coefficients

$$\overline{|Z^2|} \approx \frac{\eta_n^2 |\Phi(\omega_n)|^2}{\gamma_n L_0^2}. \tag{G.35}$$

Numerical studies show that Φ_n is typically of order $0.02L$ (the scale 0.02 is universal for a wide range of drives).

Alternatively, if $\Phi(\omega)$ has a sharp peak at ω_n, of height Φ_n,

$$\overline{\Phi^* Z} \approx \frac{\eta}{\gamma L_0} \Phi_n^2 \tag{G.36}$$

so in this case, we may set $\Phi(\omega_n) = \frac{\Phi_n}{\sqrt{2\pi\gamma}}$. The rms average of the dimensionless amplitude of the mode is

$$\bar{A}_n \sim \sqrt{\bar{E}/\omega L_0} \sim \sqrt{\frac{\eta^2}{\gamma L_0^2} |\Phi(\omega_n)|^2} \tag{G.37}$$

[2] The Fourier transform $Z(\omega)$ is defined as $\lim_{T\to\infty} \frac{1}{\sqrt{2\pi T}} \int_0^T dt e^{i\omega t} Z(t)$.' $Z(\omega)$ is a Wiener meausre, and the limit of $Z(\omega)$ and is strictly speaking not well defined, but $|Z^2(\omega)|$ exists and is dimensionles, and satisfies $\int d\omega Z^2(\omega) = \overline{|Z^2|}$. The inverse mapping is defined as follows: let $Z_T(t)$ be T-periodic, and given by $Z(t)$ for $t \in [0, T)$, while $Z(t) = Z(t + T)$ for later times. Writing $Z(t) = \Sigma_n Z_n e^{-in\Delta\omega t}$, the nth fourier component Z_n goes to $\sqrt{\Delta\omega} Z(n\Delta\omega)$, where $\Delta\omega = \frac{2\pi}{T}$.

For sharp peaks,

$$\bar{A}_n \sim \frac{\eta L}{\gamma_n L_0} |\tilde{\Phi}_n|. \tag{G.38}$$

Bibliography

[1] Mark S. Rudner, Netanel H. Lindner, Erez Berg, and Michael Levin. Anomalous edge states and the bulk-edge correspondence for periodically driven two-dimensional systems. *Phys. Rev. X*, 3:031005, Jul 2013.

[2] Paraj Titum, Erez Berg, Mark S. Rudner, Gil Refael, and Netanel H. Lindner. Anomalous floquet-anderson insulator as a nonadiabatic quantized charge pump. *Phys. Rev. X*, 6:021013, May 2016.

[3] Ivar Martin, Gil Refael, and Bertrand Halperin. Topological frequency conversion in strongly driven quantum systems. *Phys. Rev. X*, 7:041008, 2017.

[4] Frederik Nathan. Topological classification of floquet-bloch systems. Master's thesis, University of Copenhagen, 2015.

[5] Frederik Nathan and Mark S Rudner. Topological singularities and the general classification of floquet–bloch systems. *New Journal of Physics*, 17(12):125014, 2015.

[6] Frederik Nathan, Mark S. Rudner, Netanel H. Lindner, Erez Berg, and Gil Refael. Quantized magnetization density in periodically driven systems. *Phys. Rev. Lett.*, 119:186801, Oct 2017.

[7] Frederik Nathan, Dmitry Abanin, Erez Berg, Netanel H. Lindner, and Mark S. Rudner. Stability of anomalous floquet insulators. arXiv:1712.02789, 12 2017.

[8] Michael H. Kolodrubetz, Frederik Nathan, Snir Gazit, Takahiro Morimoto, and Joel E. Moore. Topological floquet-thouless energy pump. *Phys. Rev. Lett.*, 120:150601, april 2018.

[9] Liang Fu and C. L. Kane. Time reversal polarization and a Z_2 adiabatic spin pump. *Phys. Rev. B*, 74:195312, Nov 2006.

[10] Liang Fu, C. L. Kane, and E. J. Mele. Topological insulators in three dimensions. *Phys. Rev. Lett.*, 98:106803, 2007.

[11] B. Andrei Bernevig, Taylor L. Hughes, and Shou-Cheng Zhang. Quantum spin hall effect and topological phase transition in hgte quantum wells. *Science*, 314(5806):1757–1761, 2006.

[12] Markus König, Steffen Wiedmann, Christoph Brüne, Andreas Roth, Hartmut Buhmann, Laurens W. Molenkamp, Xiao-Liang Qi, and Shou-Cheng Zhang. Quantum spin hall insulator state in hgte quantum wells. *Science*, 318:766, 2007.

[13] D. Hsieh, D. Qian, L. Wray, Y. Xia, Y. S. Hor, R. J. Cava, and M. Z. Hasan. A topological dirac insulator in a quantum spin hall phase. *Nature*, 452(7190):970–974, April 2008.

[14] K. v. Klitzing, G. Dorda, and M. Pepper. New method for high-accuracy determination of the fine-structure constant based on quantized hall resistance. *Phys. Rev. Lett.*, 45:494–497, Aug 1980.

[15] D. J. Thouless, M. Kohmoto, M. P. Nightingale, and M. den Nijs. Quantized hall conductance in a two-dimensional periodic potential. *Phys. Rev. Lett.*, 49:405–408, Aug 1982.

[16] A Yu Kitaev. Unpaired majorana fermions in quantum wires. *Physics-Uspekhi*, 44(10S):131, 2001.

[17] C. L. Kane and E. J. Mele. Z_2 topological order and the quantum spin hall effect. *Phys. Rev. Lett.*, 95:146802, Sep 2005.

[18] Alexei Kitaev. Periodic table for topological insulators and superconductors. *AIP Conference Proceedings*, 1134(1):22–30, 2009.

[19] Shinsei Ryu, Andreas P Schnyder, Akira Furusaki, and Andreas W W Ludwig. Topological insulators and superconductors: tenfold way and dimensional hierarchy. *New Journal of Physics*, 12(6):065010, 2010.

[20] Wang Yao, A. H. MacDonald, and Qian Niu. Optical Control of Topological Quantum Transport in Semiconductors. *Physical Review Letters*, 99(4):047401, jul 2007.

[21] Takashi Oka and Hideo Aoki. Photovoltaic hall effect in graphene. *Phys. Rev. B*, 79:081406, Feb 2009.

[22] Jun-ichi Inoue and Akihiro Tanaka. Photoinduced Transition between Conventional and Topological Insulators in Two-Dimensional Electronic Systems. *Physical Review Letters*, 105(1):017401, jun 2010.

[23] Takuya Kitagawa, Erez Berg, Mark Rudner, and Eugene Demler. Topological characterization of periodically driven quantum systems. *Phys. Rev. B*, 82:235114, Dec 2010.

[24] N. H. Lindner, G. Refael, and V. Galitski. Floquet topological insulator in semiconductor quantum wells. *Nat. Phys.*, 7:490–495, Mar 2011.

[25] Takuya Kitagawa, Takashi Oka, Arne Brataas, Liang Fu, and Eugene Demler. Transport properties of nonequilibrium systems under the application of light: Photoinduced quantum hall insulators without landau levels. *Phys. Rev. B*, 84:235108, Dec 2011.

[26] Zhenghao Gu, H. A. Fertig, Daniel P. Arovas, and Assa Auerbach. Floquet Spectrum and Transport through an Irradiated Graphene Ribbon. *Physical Review Letters*, 107(21):216601, nov 2011.

[27] Pierre Delplace, Alvaro Gomez-Leon, and Gloria Platero. Merging of dirac points and floquet topological transitions in ac-driven graphene. *Phys. Rev. B*, 88:245422, Dec 2013.

[28] Yaniv Tenenbaum Katan and Daniel Podolsky. Modulated Floquet Topological Insulators. *Physical Review Letters*, 110(1):016802, jan 2013.

[29] Gonzalo Usaj, P. M. Perez-Piskunow, L. E. F. Foa Torres, and C. A. Balseiro. Irradiated graphene as a tunable Floquet topological insulator. *Physical Review B*, 90(11):115423, sep 2014.

[30] Arijit Kundu, H.A. Fertig, and Babak Seradjeh. Effective theory of floquet topological transitions. *Phys. Rev. Lett.*, 113:236803, 2014.

[31] Adolfo G. Grushin, Álvaro Gómez-León, and Titus Neupert. Floquet fractional chern insulators. *Phys. Rev. Lett.*, 112:156801, Apr 2014.

[32] Hossein Dehghani, Takashi Oka, and Aditi Mitra. Out-of-equilibrium electrons and the Hall conductance of a Floquet topological insulator. *Physical Review B*, 91(15):155422, apr 2015.

[33] M. A. Sentef, M. Claassen, A. F. Kemper, B. Moritz, T. Oka, J. K. Freericks, and T. P. Devereaux. Theory of Floquet band formation and local pseudospin textures in pump-probe photoemission of graphene. *Nature Comm.*, 6:7047, May 2015.

[34] Marin Bukov, Michael Kolodrubetz, and Anatoli Polkovnikov. Schrieffer-wolff transformation for periodically driven systems: Strongly correlated systems with artificial gauge fields. *Phys. Rev. Lett.*, 116:125301, Mar 2016.

[35] Martin Claassen, Chunjing Jia, Brian Moritz, and Thomas P. Devereaux. All-optical materials design of chiral edge modes in transition-metal dichalcogenides. *Nature Communications*, 7:13074, oct 2016.

[36] Jelena Klinovaja, Peter Stano, and Daniel Loss. Topological floquet phases in driven coupled rashba nanowires. *Phys. Rev. Lett.*, 116:176401, April 2016.

[37] André Eckardt. Colloquium: Atomic quantum gases in periodically driven optical lattices. *Rev. Mod. Phys.*, 89:011004, Mar 2017.

[38] Y. H. Wang, H. Steinberg, P. Jarillo-Herrero, and N. Gedik. Observation of floquet-bloch states on the surface of a topological insulator. *Science*, 342(6157):453–457, 2013.

[39] M. Aidelsburger, M. Lohse, C. Schweizer, M. Atala, J. T. Barreiro, S. Nascimbène, N. R. Cooper, I. Bloch, and N. Goldman. Measuring the Chern number of Hofstadter bands with ultracold bosonic atoms. *Nature Physics*, 11(2):162–166, dec 2015.

[40] N. Fläschner, B. S. Rem, M. Tarnowski, D. Vogel, D.-S. Lühmann, K. Sengstock, and C. Weitenberg. Experimental reconstruction of the berry curvature in a floquet bloch band. *Science*, 352(6289):1091, 2016.

[41] Gregor Jotzu, Michael Messer, Remi Desbuquois, Martin Lebrat, Thomas Uehlinger, Daniel Greif, and Tilman Esslinger. Experimental realization of the topological haldane model with ultracold fermions. *Nature*, 515:237–240, Nov 2014.

[42] Liang Jiang, Takuya Kitagawa, Jason Alicea, A. R. Akhmerov, David Pekker, Gil Refael, J. Ignacio Cirac, Eugene Demler, Mikhail D. Lukin, and Peter Zoller. Majorana fermions in equilibrium and in driven cold-atom quantum wires. *Phys. Rev. Lett.*, 106:220402, Jun 2011.

[43] Takuya Kitagawa, Matthew A. Broome, Alessandro Fedrizzi, Mark S. Rudner, Erez Berg, Ivan Kassal, Alan Aspuru-Guzik, Eugene Demler, and Andrew G. White. Energy-filtered cold electron transport at room temperature. *Nat. Comm.*, 3(882), Jun 2012.

[44] Rahul Roy and Fenner Harper. Abelian Floquet symmetry-protected topological phases in one dimension. *Physical Review B*, 94(12):125105, sep 2016.

[45] C. W. von Keyserlingk and S. L. Sondhi. Phase structure of one-dimensional interacting floquet systems. i. abelian symmetry-protected topological phases. *Phys. Rev. B*, 93:245145, Jun 2016.

[46] A. C. Potter, T. Morimoto, and A. Vishwanath. Topological classification of interacting 1d floquet phases. *Phys. Rev. X*, 6:041001, 2016.

[47] C. W. von Keyserlingk and S. L. Sondhi. Phase structure of one-dimensional interacting floquet systems. ii. symmetry-broken phases. *Phys. Rev. B*, 93:245146, Jun 2016.

[48] Dominic V. Else and Chetan Nayak. Classification of topological phases in periodically driven interacting systems. *Physical Review B*, 93(20):201103, may 2016.

[49] Dominic V. Else, Bela Bauer, and Chetan Nayak. Floquet time crystals. *Phys. Rev. Lett.*, 117:090402, Aug 2016.

[50] Vedika Khemani, Achilleas Lazarides, Roderich Moessner, and S. L. Sondhi. Phase structure of driven quantum systems. *Phys. Rev. Lett.*, 116:250401, Jun 2016.

[51] S. Choi, J. Choi, R. Landig, G. Kucsko, H. Zhou, J. Isoya, F. Jelezko, S. Onoda, H. Sumiya, V. Khemani, C. von Keyserlingk, N. Y. Yao, E. Demler, and M. D. Lukin. Observation of discrete time-crystalline order in a disordered dipolar many-body system. *Nature*, 543:221, 2017.

[52] J. Zhang, P. W. Hess, A. Kyprianidis, P. Becker, A. Lee, J. Smith, G. Pagano, I.-D. Potirniche, A. C. Potter, A. Vishwanath, N. Y. Yao, and C. Monroe. Observation of a discrete time crystal. *Nature*, 543:217, 2017.

[53] A. Quelle, C. Weitenberg, K. Sengstock, and C. Morais Smith. Driving protocol for a floquet topological phase without static counterpart. *New J. Phys.*, 19:113010, 2017.

[54] Wenchao Hu, Jason C. Pillay, Kan Wu, Michael Pasek, Perry Ping Shum, and Y. D. Chong. Measurement of a Topological Edge Invariant in a Microwave Network. *Phys. Rev. X*, 5:011012, February 2015.

[55] Fenner Harper and Rahul Roy. Floquet topological order in interacting systems of bosons and fermions. *Phys. Rev. Lett.*, 118:115301, Mar 2017.

[56] Hoi Chun Po, Lukasz Fidkowski, Takahiro Morimoto, Andrew C. Potter, and Ashvin Vishwanath. Chiral floquet phases of many-body localized bosons. *Phys. Rev. X*, 6:041070, Dec 2016.

[57] Filippo Cardano, Alessio D'Errico, Alexandre Dauphin, Maria Maffei, Bruno Piccirillo, Corrado de Lisio, Giulio De Filippis, Vittorio Cataudella, Enrico Santamato, Lorenzo Marrucci, and et al. Detection of zak phases and topological invariants in a chiral quantum walk of twisted photons. *Nature Communications*, 8:15516, Jun 2017.

[58] Ariel Sommer and Jonathan Simon. Engineering photonic floquet hamiltonians through fabry–pérot resonators. *New Journal of Physics*, 18(3):035008, 2016.

[59] M. C. Rechtsman, J. M. Zeuner, Y. Plotnik, Y. Lumer, D. Podolsky, F. Dreisow, S. Nolte, M. Segev, and A. Szameit. Photonic floquet topological insulators. *Nature*, 496:196–200, Apr 2013.

[60] Sebabrata Mukherjee, Alexander Spracklen, Manuel Valiente, Erika Andersson, Patrik Öhberg, Nathan Goldman, and Robert R. Thomson. Experimental observation of anomalous topological edge modes in a slowly driven photonic lattice. *Nature Communications*, 8:13918, 01 2017.

[61] Lukas J. Maczewsky, Julia M. Zeuner, Stefan Nolte, and Alexander Szameit. Observation of photonic anomalous floquet topological insulators. *Nature Communications*, 8:13756, 01 2017.

[62] Netanel H. Lindner, Erez Berg, and Mark S Rudner. Universal chiral quasisteady states in periodically driven many-body systems. *Physical Review X*, 7(1), 2017.

[63] Yang Peng and Gil Refael. Topological energy conversion through bulk or boundary of driven systems. *ArXiv e-prints*, 01 2018.

[64] Phillip Weinberg, Marin Bukov, Luca D'Alessio, Anatoli Polkovnikov, Szabolcs Vajna, and Michael Kolodrubetz. Adiabatic perturbation theory and geometry of periodically-driven systems. *Physics Reports*, 688:1–35, May 2017.

[65] D. J. Thouless. Quantization of particle transport. *Phys. Rev. B.*, 27:6083, 1983.

[66] Yuval Oreg, Gil Refael, and Felix von Oppen. Helical liquids and majorana bound states in quantum wires. *Phys. Rev. Lett.*, 105:177002, 2010.

[67] Alexander Tzalenchuk, Samuel Lara-Avila, Alexei Kalaboukhov, Sara Paolillo, Mikael Syvajarvi, Rositza Yakimova, Olga Kazakova, T. J. B. M. Janssen, Vladimir Fal'ko, and Sergey Kubatkin. Towards a quantum resistance standard based on epitaxial graphene. *Nat. Nano.*, 5:186–189, Mar 2010.

[68] Yasuhiro Hatsugai. Chern number and edge states in the integer quantum hall effect. *Phys. Rev. Lett.*, 71:3697–3700, Nov 1993.

[69] B. I. Halperin. Quantized hall conductance, current-carrying edge states, and the existence of extended states in a two-dimensional disordered potential. *Phys. Rev. B*, 25:2185–2190, Feb 1982.

[70] J. E. Avron, R. Seiler, and B. Simon. Homotopy and quantization in condensed matter physics. *Phys. Rev. Lett.*, 51:51–53, Jul 1983.

[71] Q Niu and D J Thouless. Quantised adiabatic charge transport in the presence of substrate disorder and many-body interaction. *Journal of Physics A: Mathematical and General*, 17:2453, 1984.

[72] Supriyo Datta. *Electronic Transport in Mesoscopic Systems*. Cambridge University Press, Cambridge, 1995.

[73] T. Voronov. *Concise Encyclopedia of Supersymmery*. Springer Netherlands, 2003.

[74] Roman M. Lutchyn, Jay D. Sau, and S. Das Sarma. Majorana fermions and a topological phase transition in semiconductor-superconductor heterostructures. *Phys. Rev. Lett.*, 105:077001, 2010.

[75] Martin Leijnse and Karsten Flensberg. Introduction to topological superconductivity and majorana fermions. *Semiconductor Science and Technology*, 27(12):124003, Nov 2012.

[76] V. Mourik, K. Zuo, S. M. Frolov, S. R. Plissard, E. P. A. M. Bakkers, and L. P. Kouwenhoven. Signatures of majorana fermions in hybrid superconductor-semiconductor nanowire devices. *Science*, 336:1003, 2012.

[77] S. M. Albrecht, A. P. Higginbotham, M. Madsen, F. Kuemmeth, T. S. Jespersen, J. Nygaard, P. Krogstrup, and C. M. Marcus. Exponential protection of zero modes in majorana islands. *Nature*, 531:206 – 209, 03 2016.

[78] Alexander Altland and Martin R. Zirnbauer. Nonstandard symmetry classes in mesoscopic normal-superconducting hybrid structures. *Phys. Rev. B*, 55:1142–1161, Jan 1997.

[79] M. Z. Hasan and C. L. Kane. *Colloquium* : Topological insulators. *Rev. Mod. Phys.*, 82:3045–3067, Nov 2010.

[80] Yoichi Ando and Liang Fu. Topological crystalline insulators and topological superconductors: From concepts to materials. *Annual Review of Condensed Matter Physics*, 6(1):361–381, 2018/04/24 2015.

[81] Masatoshi Sato and Yoichi Ando. Topological superconductors: a review. *Reports on Progress in Physics*, 80(7):076501, May 2017.

[82] F. D. M. Haldane and S. Raghu. Possible realization of directional optical waveguides in photonic crystals with broken time-reversal symmetry. *Physical Review Letters*, 100(1), 2008.

[83] Alexander B. Khanikaev, S. Hossein Mousavi, Wang-Kong Tse, Mehdi Kargarian, Allan H. MacDonald, and Gennady Shvets. Photonic topological insulators. *Nature Materials*, 12:233 EP –, 12 2012.

[84] Sabyasachi Barik, Aziz Karasahin, Christopher Flower, Tao Cai, Hirokazu Miyake, Wade DeGottardi, Mohammad Hafezi, and Edo Waks. A topological quantum optics interface. *Science*, 359(6376):666, 02 2018.

[85] Tomoki Ozawa, Hannah M. Price, Alberto Amo, Nathan Goldman, Mohammad Hafezi, Ling Lu, Mikael Rechtsman, David Schuster, Jonathan Simon, Oded Zilberberg, and Iacopo Carusotto. Topological photonics. arxiv:1802.04173, 02 2018.

[86] C. L. Kane and T. C. Lubensky. Topological boundary modes in isostatic lattices. *Nature Physics*, 10:39 EP –, 12 2013.

[87] Jayson Paulose, Bryan Gin-ge Chen, and Vincenzo Vitelli. Topological modes bound to dislocations in mechanical metamaterials. *Nature Physics*, 11:153 EP –, 01 2015.

[88] Roman Süsstrunk and Sebastian D. Huber. Observation of phononic helical edge states in a mechanical topological insulator. *Science*, 349(6243):47, 07 2015.

[89] N. P. Armitage, E. J. Mele, and Ashvin Vishwanath. Weyl and dirac semimetals in three-dimensional solids. *Reviews of Modern Physics*, 90(1), 2018.

[90] F. D. M. Haldane. Model for a quantum hall effect without landau levels: Condensed-matter realization of the "parity anomaly". *Phys. Rev. Lett.*, 61:2015, 1988.

[91] A. Kundu, M. S. Rudner, G. Refael, and N. H. Lindner. Quantized large-bias current in the anomalous floquet-anderson insulator. *arXiv:1708.05023*, 2017.

[92] Walter Kohn. Periodic thermodynamics. *Journal of Statistical Physics*, 103:417–423, 2001.

[93] Luca D'Alessio and Marcos Rigol. Long-time behavior of isolated periodically driven interacting lattice systems. *Phys. Rev. X*, 4:041048, 2014.

[94] Achilleas Lazarides, Arnab Das, and Roderich Moessner. Periodic thermodynamics of isolated quantum systems. *Phys. Rev. Lett.*, 112:150401, Apr 2014.

[95] Karthik I. Seetharam, Charles-Edouard Bardyn, Netanel H. Lindner, Mark S. Rudner, and Gil Refael. Controlled population of floquet-bloch states via coupling to bose and fermi baths. *Physical Review X*, 5(4), 2015.

[96] Iliya Esin, Mark S. Rudner, Gil Refael, and Netanel H. Lindner. Steady states and edge state transport in topological floquet-bloch systems. arxiv:1710.09404, 10 2017.

[97] D. Abanin, W. De Roeck, and F. Huveneers. A theory of many-body localization in periodically driven systems. *arXiv:1412.2752*, 2014.

[98] Achilleas Lazarides, Arnab Das, and Roderich Moessner. Fate of many-body localization under periodic driving. *Phys. Rev. Lett.*, 115(3):030402–, July 2015.

[99] C. W. von Keyserlingk, Vedika Khemani, and S. L. Sondhi. Absolute stability and spatiotemporal long-range order in floquet systems. *Phys. Rev. B*, 94:085112, Aug 2016.

[100] Marin Bukov and Anatoli Polkovnikov. Stroboscopic versus nonstroboscopic dynamics in the floquet realization of the harper-hofstadter hamiltonian. *Phys. Rev. A*, 90:043613, 2014.

[101] M. Bukov, L. D'Alessio, and A. Polkovnikov. Universal high-frequency behavior of periodically driven systems: from dynamical stabilization to floquet engineering. *Adv. in Phys.*, 64:139, 2015.

[102] G. Floquet. Sur les equations differentielles lineaires a coefficients periodiues. *Annales scientifiques*, 2:47–48, 1883.

[103] Emmy Noether and M. A. Tavel. Invariant variation problems. *Gott. Nachr.*, pages 235–237, 1918.

[104] J. K. Asboth, B. Tarasinski, and P. Delplace. Chiral symmetry and bulk-boundary correspondence in periodically driven one-dimensional systems. *Phys. Rev. B*, 90:125143, Sep 2014.

[105] R. B. Laughlin. The gauge argument for accurate quantization of the hall conductance. In: Bauer G., Kuchar F., Heinrich H. (eds) Two-Dimensional Systems, Heterostructures, and Superlattices. Springer Series in Solid-State Sciences, vol 53. Springer, Berlin, Heidelberg, 1984.

[106] Elliott Lieb and D. Robinson. The finite group velocity of quantum spin systems. *Commun. Math. Phys.*, 28:251–257, 1972.

[107] David Carpentier, Pierre Delplace, Michel Fruchart, and Krzysztof Gawedzki. Topological index for periodically driven time-reversal invariant 2d systems. *Phys. Rev. Lett.*, 114(10):106806–, March 2015.

[108] Mark Srednicki. Chaos and quantum thermalization. *Phys. Rev. E*, 50:888, 1994.

[109] Dmitry A. Abanin, Wojciech De Roeck, and François Huveneers. Theory of many-body localization in periodically driven systems. *Annals of Physics*, 372:1 – 11, 2016.

[110] D.M. Basko, I.L. Aleiner, and B.L. Altshuler. Metal-insulator transition in a weakly interacting many-electron system with localized single-particle states. *Annals of Physics*, 321(5):1126 – 1205, 2006.

[111] Arijeet Pal and David A. Huse. Many-body localization phase transition. *Phys. Rev. B*, 82:174411, 2010.

[112] Maksym Serbyn, Zlatko. Papic, and Dmitry A. Abanin. Local conservation laws and the structure of the many-body localized states. *Physical Review Letters*, 111(12), 2013.

[113] Dmitry A. Abanin, Wojciech De Roeck, and François Huveneers. Exponentially slow heating in periodically driven many-body systems. *Phys. Rev. Lett.*, 115(25):256803, December 2015.

[114] D. A. Abanin, W. De Roeck, and W. W. Ho. Effective hamiltonians, prethermalization and slow energy absorption in periodically driven many-body systems. *Phys. Rev. B*, 95(1):014112, Jan 2017. arXiv:1510.03405.

[115] Marin Bukov, Sarang Gopalakrishnan, Michael Knap, and Eugene Demler. Prethermal floquet steady states and instabilities in the periodically driven, weakly interacting bose-hubbard model. *Phys. Rev. Lett.*, 115(20):205301, 2015.

[116] Simon A Weidinger and Michael Knap. Floquet prethermalization and regimes of heating in a periodically driven, interacting quantum system. *Scientific Reports*, 7:45382, 2017.

[117] D. C. Tsui, H. L. Stormer, and A. C. Gossard. Two-dimensional magnetotransport in the extreme quantum limit. *Phys. Rev. Lett.*, 48:1559, 1982.

[118] R. B. Laughlin. Quantized hall conductivity in two dimensions. *Phys. Rev. B*, 23:5632–5633, 1981.

[119] R. B. Laughlin. Anomalous quantum hall effect: An incompressible quantum fluid with fractionally charged excitations. *Phys. Rev. Lett.*, 50:1395–1398, May 1983.

[120] Liang Fu and C. L. Kane. Topological insulators with inversion symmetry. *Phys. Rev. B*, 76:045302, Jul 2007.

[121] Markus Koenig, Steffen Wiedmann, Christoph Brüne, Andreas Roth, Hartmut Buhmann, Laurens W. Molenkamp, Xiao-Liang Qi, and Shou-Cheng Zhang. Quantum spin hall insulator state in hgte quantum wells. *Science*, 318(5851):766–770, 2007.

[122] D. Hsieh, D. Qian, L. Wray, Y. Xia, Y. S Hor, R. J. Cava, and M. Z. Hasan. A topological dirac insulator in a quantum spin hall phase. *Nature*, 452:970–974, 2008.

[123] M. Z. Hasan and C. L. Kane. *Colloquium* : Topological insulators. *Rev. Mod. Phys.*, 82:3045–3067, 2010.

[124] B. A. Bernevig and T. L. Hughes. *Topological Insulators and Supercondutors*. Princeton University Press, 2013.

[125] Netanel H. Lindner, Doron L. Bergman, Gil Refael, and Victor Galitski. Topological floquet spectrum in three dimensions via a two-photon resonance. *Phys. Rev. B*, 87:235131, Jun 2013.

[126] Thomas Iadecola, David Campbell, Claudio Chamon, Chang-Yu Hou, Roman Jackiw, So-Young Pi, and Silvia Viola Kusminskiy. Materials design from nonequilibrium steady states: Driven graphene as a tunable semiconductor with topological properties. *Phys. Rev. Lett.*, 110:176603, 2013.

[127] L.E.F. Foa Torres, P.M. Perez-Piskunow, C.A. Balseiro, and Gonzalo Usaj. Multiterminal conductance of a floquet topological insulator. *Phys. Rev. Lett.*, 113:266801, 2014.

[128] Mahmoud Lababidi, Indubala I. Satija, and Erhai Zhao. Counter-propagating edge modes and topological phases of a kicked quantum hall system. *Phys. Rev. Lett.*, 112:026805, Jan 2014.

[129] N. Goldman and J. Dalibard. Periodically driven quantum systems: Effective hamiltonians and engineered gauge fields. *Phys. Rev. X*, 4:031027, Aug 2014.

[130] Hossein Dehghani, Takashi Oka, and Aditi Mitra. Dissipative floquet topological systems. *Phys. Rev. B*, 90:195429, 2014.

[131] Paraj Titum, Netanel H. Lindner, Mikael C. Rechtsman, and Gil Refael. Disorder-induced floquet topological insulators. *Phys. Rev. Lett.*, 114:056801, 2015.

[132] Thomas Bilitewski and Nigel R. Cooper. Scattering theory for floquet-bloch states. *Phys. Rev. A*, 91:033601, 2015.

[133] Aaron Farrell and T. Pereg-Barnea. Edge-state transport in floquet topological insulators. *Physical Review B*, 93(4), 2016.

[134] Arijit Kundu, H. A. Fertig, and Babak Seradjeh. Floquet-engineered valleytronics in dirac systems. *Physical Review Letters*, 116(1), 2016.

[135] H. L. Calvo, L. E. F. Foa Torres, P. M. Perez-Piskunow, C. A. Balseiro, and Gonzalo Usaj. Floquet interface states in illuminated three-dimensional topological insulators. *Phys. Rev. B*, 91:241404, Jun 2015.

[136] K. Jimenez-Garcia, L. J. LeBlanc, R. A. Williams, M. C. Beeler, C. Qu, M. Gong, C. Zhang, and I. B. Spielman. Tunable spin-orbit coupling via strong driving in ultracold atom systems. *arXiv:1410.5364*, 2014.

[137] Takuya Kitagawa, Matthew A. Broome, Alessandro Fedrizzi, Mark S. Rudner, Erez Berg, Ivan Kassal, Alán Aspuru-Guzik, Eugene Demler, and Andrew G. White. Observation of topologically protected bound states in photonic quantum walks. *Nature Communications*, 3:882, jun 2012.

[138] Xiao-Liang Qi, Taylor L. Hughes, and Shou-Cheng Zhang. Topological field theory of time-reversal invariant insulators. *Phys. Rev. B*, 78:195424, 2008.

[139] Maryam Taherinejad, Kevin F. Garrity, and David Vanderbilt. Wannier center sheets in topological insulators. *Phys. Rev. B*, 89:115102, Mar 2014.

[140] Arijit Kundu and Babak Seradjeh. Transport signatures of floquet majorana fermions in driven topological superconductors. *Phys. Rev. Lett.*, 111:136402, 2013.

[141] Conyers Herring. Accidental degeneracy in the energy bands of crystals. *Phys. Rev.*, 52:365–373, Aug 1937.

[142] Rahul Roy and Fenner Harper. Periodic table for floquet topological insulators. arXiv:1603.06944.

[143] Allan H. Macdonald. *Quantum coherence in mesoscopic systems*. Springer, 1991.

[144] S. A. J. Wiegers, M. Specht, L. P. Lévy, M. Y. Simmons, D. A. Ritchie, A. Cavanna, B. Etienne, G. Martinez, and P. Wyder. Magnetization and energy gaps of a high-mobility 2d electron gas in the quantum limit. *Phys. Rev. Lett.*, 79:3238, Oct 1997.

[145] P Streda. Theory of quantised hall conductivity in two dimensions. *Journal of Physics C: Solid State Physics*, 15(22):L717, 1982.

[146] See supplementary online information.

[147] Fenner Harper and Rahul Roy. Stability of anomalous floquet edge unitaries. *arXiv:1609.06303*, 2016.

[148] Pedro Ponte, Anushya Chandran, Z. Papic, and Dmitry A. Abanin. Periodically driven ergodic and many-body localized quantum systems. *Annals of Physics*, 353:196–204, Nov 2014.

[149] Achilleas Lazarides, Arnab Das, and Roderich Moessner. Equilibrium states of generic quantum systems subject to periodic driving. *Phys. Rev. E*, 90:012110, Jul 2014.

[150] Pedro Ponte, Z. Papić, François Huveneers, and Dmitry A. Abanin. Many-body localization in periodically driven systems. *Phys. Rev. Lett.*, 114(14):140401–, April 2015.

[151] David A. Huse, Rahul Nandkishore, Vadim Oganesyan, Arijeet Pal, and S. L. Sondhi. Localization-protected quantum order. *Phys. Rev. B*, 88:014206, Jul 2013.

[152] B. Bauer and C. Nayak. Area laws in a many-body localized state and its implications for topological order. *J. Stat. Mech.*, 2013:P09005, 2013.

[153] V. Oganesyan and D. A. Huse. Localization of interacting fermions at high temperature. *Phys. Rev. B*, 75:155111, 2007.

[154] Soumya Bera, Henning Schomerus, Fabian Heidrich-Meisner, and Jens H. Bardarson. Many-body localization characterized from a one-particle perspective. *Phys. Rev. Lett.*, 115:046603, Jul 2015.

[155] W. De Roeck and J. Z. Imbrie. Many-Body Localization: Stability and Instability. *arXiv:1705.00756*, 2017.

[156] Anushya Chandran, Isaac H. Kim, Guifre Vidal, and Dmitry A. Abanin. Constructing local integrals of motion in the many-body localized phase. *Physical Review B*, 91(8), 2015.

[157] M. Switkes, C. M. Marcus, K. Campman, and A. C. Gossard. An adiabatic quantum electron pump. *Science*, 283(5409):1905–1908, 1999.

[158] M. D. Blumenthal, B. Kaestner, L. Li, S. Giblin, T. J. B. M. Janssen, M. Pepper, D. Anderson, G. Jones, and D. A. Ritchie. Gigahertz quantized charge pumping. *Nat Phys*, 3(5):343–347, May 2007.

[159] M. R. Buitelaar, V. Kashcheyevs, P. J. Leek, V. I. Talyanskii, C. G. Smith, D. Anderson, G. A. C. Jones, J. Wei, and D. H. Cobden. Adiabatic charge pumping in carbon nanotube quantum dots. *Phys. Rev. Lett.*, 101:126803, Sep 2008.

[160] Francesco Giazotto, Panayotis Spathis, Stefano Roddaro, Subhajit Biswas, Fabio Taddei, Michele Governale, and Lucia Sorba. A josephson quantum electron pump. *Nat Phys*, 7(11):857–861, November 2011.

[161] H.-I Lu, M. Schemmer, L. M. Aycock, D. Genkina, S. Sugawa, and I. B. Spielman. Geometrical pumping with a bose-einstein condensate. *Phys. Rev. Lett.*, 116:200402, May 2016.

[162] Shuta Nakajima, Takafumi Tomita, Shintaro Taie, Tomohiro Ichinose, Hideki Ozawa, Lei Wang, Matthias Troyer, and Yoshiro Takahashi. Topological thouless pumping of ultracold fermions. *Nat Phys*, 12(4):296–300, Apr 2016. Letter.

[163] M. Lohse, C. Schweizer, O. Zilberberg, M. Aidelsburger, and I. Bloch. A thouless quantum pump with ultracold bosonic atoms in an optical superlattice. *Nat Phys*, 12(4):350–354, Apr 2016. Article.

[164] Derek Y. H. Ho and Jiangbin Gong. Quantized adiabatic transport in momentum space. *Phys. Rev. Lett.*, 109:010601, Jul 2012.

[165] Longwen Zhou, Chong Chen, and Jiangbin Gong. Floquet semimetal with floquet-band holonomy. *Phys. Rev. B*, 94(7):075443–, August 2016.

[166] Andrew C. Potter and Takahiro Morimoto. Dynamically enriched topological orders in driven two-dimensional systems. *Phys. Rev. B*, 95:155126, Apr 2017.

[167] Rahul Roy and Fenner Harper. Floquet topological phases with symmetry in all dimensions. *Phys. Rev. B*, 95:195128, May 2017.

[168] Hoi Chun Po, Lukasz Fidkowski, Ashvin Vishwanath, and Andrew C. Potter. Radical chiral floquet phases in a periodically driven kitaev model and beyond. arXiv:1701.01440.

[169] Andrew C. Potter, Ashvin Vishwanath, and Lukasz Fidkowski. An infinite family of 3d floquet topological paramagnets. arXiv:1706.01888.

[170] Daniel W. Hone, Roland Ketzmerick, and Walter Kohn. Time-dependent floquet theory and absence of an adiabatic limit. *Phys. Rev. A*, 56:4045, 1997.

[171] K. Drese and M. Holthaus. Floquet theory for short laser pulses. *The European Physical Journal D - Atomic, Molecular, Optical and Plasma Physics*, 5:119, 1999.

[172] Vedika Khemani, Rahul Nandkishore, and S. L. Sondhi. Nonlocal adiabatic response of a localized system to local manipulations. *Nat Phys*, 11(7):560–565, July 2015.

[173] Michael Kolodrubetz, Frederik Nathan, Snir Gazit, Takahiro Morimoto, Mark Rudner, and Joel Moore. To appear shortly.

[174] P. W. Anderson. Absence of diffusion in certain random lattices. *Phys. Rev.*, 109:1492–1505, Mar 1958.

[175] N.F. Mott and W.D. Twose. The theory of impurity conduction. *Advances in Physics*, 10(38):107–163, 1961.

[176] Kartiek Agarwal, Sriram Ganeshan, and R. N. Bhatt. Localization and transport in a strongly driven anderson insulator. *Phys. Rev. B*, 96:014201, Jul 2017.

[177] Shigeki Onoda, Chyh-Hong Chern, Shuichi Murakami, Yasushi Ogimoto, and Naoto Nagaosa. Disorder-enhanced dielectric response of nanoscale and mesoscopic insulators. *Phys. Rev. Lett.*, 97:266807, Dec 2006.

[178] Chyh-Hong Chern, Shigeki Onoda, Shuichi Murakami, and Naoto Nagaosa. Quantum charge pumping and electric polarization in anderson insulators. *Phys. Rev. B*, 76:035334, Jul 2007.

[179] Waseem S. Bakr, Jonathon I. Gillen, Amy Peng, Simon Folling, and Markus Greiner. A quantum gas microscope for detecting single atoms in a hubbard-regime optical lattice. *Nature*, 462(7269):74–77, November 2009.

[180] Lawrence W. Cheuk, Matthew A. Nichols, Melih Okan, Thomas Gersdorf, Vinay V. Ramasesh, Waseem S. Bakr, Thomas Lompe, and Martin W. Zwierlein. Quantum-gas microscope for fermionic atoms. *Phys. Rev. Lett.*, 114:193001, May 2015.

[181] R. Blatt and C. F. Roos. Quantum simulations with trapped ions. *Nat Phys*, 8(4):277–284, April 2012.

[182] R. Barends, J. Kelly, A. Megrant, D. Sank, E. Jeffrey, Y. Chen, Y. Yin, B. Chiaro, J. Mutus, C. Neill, P. O'Malley, P. Roushan, J. Wenner, T. C. White, A. N. Cleland, and John M. Martinis. Coherent josephson qubit suitable for scalable quantum integrated circuits. *Phys. Rev. Lett.*, 111:080502, 2013.

[183] P. Roushan, C. Neill, Yu Chen, M. Kolodrubetz, C. Quintana, N. Leung, M. Fang, R. Barends, B. Campbell, Z. Chen, B. Chiaro, A. Dunsworth, E. Jeffrey, J. Kelly, A. Megrant, J. Mutus, P. J. J. O'Malley, D. Sank, A. Vainsencher, J. Wenner, T. White, A. Polkovnikov,

A. N. Cleland, and J. M.mal Martinis. Observation of topological transitions in interacting quantum circuits. *Nature*, 515(7526):241–244, November 2014.

[184] Hannes Bernien, Sylvain Schwartz, Alexander Keesling, Harry Levine, Ahmed Omran, Hannes Pichler, Soonwon Choi, Alexander S. Zibrov, Manuel Endres, Markus Greiner, Vladan Vuletić, and Mikhail D. Lukin. Probing many-body dynamics on a 51-atom quantum simulator. arXiv:1707.04344.

[185] Stefan Keßler and Florian Marquardt. Single-site-resolved measurement of the current statistics in optical lattices. *Phys. Rev. A*, 89:061601, Jun 2014.

[186] M. J. Rice and E. J. Mele. Elementary excitations of a linearly conjugated diatomic polymer. *Phys. Rev. Lett.*, 49:1455–1459, Nov 1982.

[187] Andrew M. Essin and J. E. Moore. Topological insulators beyond the brillouin zone via chern parity. *Phys. Rev. B*, 76:165307, Oct 2007.

[188] Adolfo G. Grushin, Álvaro Gómez-León, and Titus Neupert. Floquet fractional chern insulators. *Phys. Rev. Lett.*, 112:156801, 2014.

[189] Claudio Chamon, Eduardo R. Mucciolo, Liliana Arrachea, and Rodrigo B. Capaz. Heat pumping in nanomechanical systems. *Phys. Rev. Lett.*, 106:135504, Apr 2011.

[190] María Florencia Ludovico, Francesca Battista, Felix von Oppen, and Liliana Arrachea. Adiabatic response and quantum thermoelectrics for ac-driven quantum systems. *Phys. Rev. B*, 93:075136, Feb 2016.

[191] Luqi Yuan, Yu Shi, and Shanhui Fan. Photonic gauge potential in a system with a synthetic frequency dimension. *Optics Letters*, 41(4):741, Feb 2016.

[192] Qian Lin, Meng Xiao, Luqi Yuan, and Shanhui Fan. Photonic weyl point in a two-dimensional resonator lattice with a synthetic frequency dimension. *Nature Communications*, 7:13731 EP –, 12 2016.

[193] Tomoki Ozawa, Hannah M. Price, Nathan Goldman, Oded Zilberberg, and Iacopo Carusotto. Synthetic dimensions in integrated photonics: From optical isolation to four-dimensional quantum hall physics. *Physical Review A*, 93(4), 2016.

[194] Ulrich Weiss. *Quantum Dissipative Systems*. WORLD SCIENTIFIC, Oct 1999.

[195] K. Mølmer, Y. Castin, and J. Dalibard. Monte carlo wave-function method in quantum optics. *Journal of the Optical Society of America B*, 10(3):524, 1993.

[196] T.L. Gilbert. A lagrangian formulation of the gyromagnetic equation of the magnetic field. *Physical Review*, 100:1243, 1955.

[197] Max Born and Emil Wolf. *Principles of Optics, Cambridge University Press*. Cambridge University Press, 1999.

[198] Bastian Aurand, Stephan Kuschel, Christian Rödel, Martin Heyer, Frank Wunderlich, Oliver Jäckel, Malte C. Kaluza, Gerhard G. Paulus, and Thomas Kühl. Creating circularly polarized light with a phase-shifting mirror. *Optics Express*, 19(18):17151, Aug 2011.

[199] A Perot and C Fabry. On the application of interference phenomena to the solution of various problems of spectroscopy and metrology. *Astrophysical Journal*, 9:87, 1899.

[200] G. Hernandez. *Fabry–Pérot Interferometers*. Cambridge University Press, Cambridge, 1986.

[201] N. Ismail, C. C. Kores, D. Geskus, and M. Pollnau. Fabry-pérot resonator: spectral line shapes, generic and related airy distributions, linewidths, finesses, and performance at low or frequency-dependent reflectivity. *Optics Express*, 24(15):16366–16389, 2016.

[202] E. G. Spencer, R. C. LeCraw, and A. M. Clogston. Low-temperature line-width maximum in yttrium iron garnet. *Physical Review Letters*, 3(1):32–33, 1959.

[203] A. M. Tyryshkin, S. A. Lyon, A. V. Astashkin, and A. M. Raitsimring. Electron spin relaxation times of phosphorus donors in silicon. *Physical Review B*, 68(19), 2003.

[204] Bahadur Singh, Ashutosh Sharma, H. Lin, M. Z. Hasan, R. Prasad, and A. Bansil. Topological electronic structure and weyl semimetal in the tibise2 class of semiconductors. *Physical Review B*, 86(11), 2012.

[205] Xiangang Wan, Ari M. Turner, Ashvin Vishwanath, and Sergey Y. Savrasov. Topological semimetal and fermi-arc surface states in the electronic structure of pyrochlore iridates. *Physical Review B*, 83(20), 2011.

[206] A. A. Burkov and Leon Balents. Weyl semimetal in a topological insulator multilayer. *Physical Review Letters*, 107(12), 2011.

[207] A. A. Burkov, M. D. Hook, and Leon Balents. Topological nodal semimetals. *Physical Review B*, 84(23), 2011.

[208] Mathematical Methods for Physics and Engineering. *Riley, K. J. and Hobson, M. P. and Bence, S. J.* Cambridge University Press, 3 edition, 2006.

[209] Matthew B. Hastings and Spyridon Michalakis. Quantization of hall conductance for interacting electrons on a torus. *Communications in Mathematical Physics*, 334(1):433–471, 2015.

[210] Eugene P. Wigner. Characteristic vectors of bordered matrices with infinite dimensions. *Annals of Mathematics*, 62(3):548–564, 1955.